THÈSE DE DOCTORAT

NNT : 2025UPASF024

université PARIS-SACLAY

Study of the mechanisms of silica densification under irradiation

Etude des mécanismes de densification de la silice sous irradiation

Thèse de doctorat de l'université Paris-Saclay

École doctorale n° 571, Sciences chimiques : molécules, matériaux, instrumentation et biosystèmes(2MIB)
Spécialité de doctorat : Chimie
Graduate School : Chimie. Référent : Faculté des sciences d'Orsay

Thèse préparée dans l'unité de recherche **Institut de chimie moléculaire et des matériaux d'Orsay (Université Paris-Saclay, CNRS)**
sous la direction de **Matthieu LANCRY**, Professeur des Universités
et la direction de **Nadège Ollier**, Directrice de Recherche

Thèse soutenue à Paris-Saclay, le 27 juin 2025, par

Nadezhda SHCHEDRINA

Composition du Jury

Membres du jury avec voix délibérative

Delphine MARRIS-MORINI Professeur C2N, Université Paris Saclay	Présidente
Bruno REYNARD Directeur de recherche, ENS Lyon - CNRS	Rapporteur & Examinateur
Dominique DE LIGNY Professor Dr., Université de Erlangen	Rapporteur & Examinateur
Ekaterina BUROV Ingénieur de recherche, Saint-Gobain Recherche	Examinatrice

To my family

université PARIS-SACLAY

ÉCOLE DOCTORALE
Sciences Chimiques : Molécules, Matériaux, Instrumentation et Biosystèmes (2MIB)

Titre : Etude des mécanismes de densification de la silice sous irradiation

Mots clés : verres, silice, densification, irradiation électronique, Interactions rayonnement-matière

Résumé : Le verre de silice est prépondérant dans les dispositifs optiques et photoniques modernes grâce à son exceptionnelle transparence, sa résistance mécanique et sa faible expansion thermique. Récemment, de nouvelles applications telles que la mesure de température de haute précision et le stockage optique de données en conditions extrêmes (par exemple, température élevée et radiation) ont émergé, s'appuyant sur le traitement par laser femtoseconde (fs) pour induire des modifications structurelles spécifiques (types I, II, III et X). Cependant, ces modifications, qui induisent une densification de la silice, restent mal comprises. De plus, la possibilité de polyamorphisme de la silice complique davantage notre compréhension de ces modifications induites par irradiation. L'irradiation électronique ajoute un autre niveau de complexité, puisqu'elle peut densifier ou relaxer le verre de silice densifié et produire une phase dite « métamicte » à tres forte dose, mal caractérisée. En étudiant les changements structurels, les niveaux de densité et les mécanismes de densification à l'échelle nanométrique, ce travail vise à fournir des informations qui combleront non seulement les lacunes de notre compréhension fondamentale des mécanismes de densification de la silice sous irradiation, mais amélioreront la fiabilité et l'efficacité des technologies à base de silice. Les résultats devraient avoir des implications importantes, notamment pour les dispositifs fonctionnant dans des environnements hostiles, favorisant ainsi des avancées dans les applications photoniques.

Dans cette thèse, pour la première fois, les changements de densité induits par irradiation laser fs à l'échelle nanométrique ont été démontrés et mesurés. Les modifications de type I (changements isotropes d'indice, formation de guides d'ondes) présentent une densification de 3 à 4 %, induite par les défauts et la trempe thermique. Les modifications de type II (changements anisotropes d'indice, formation de nanoréseaux) ont montré une densification de 8 à 13 % due aux températures et pressions élevées. (10 à 15 GPa). Les modifications de type III (formation de microcavités ont révélé une densification d'environ 6 % dans les couches environnantes, reflétant une densification due aux pressions induites par choc. En outre, les modifications de type II diminuent dans les échantillons densifiés, suggérant que le volume libre est essentiel pour initier les nanoréseaux. Le volume libre intrinsèquement plus élevé de la silice explique la formation plus aisée de structures en nanoréseaux comparativement à d'autres verres.

Par ailleurs, une irradiation électronique à forte dose (5 GGy) relaxe les nanoréseaux de type II densifiés, réduisant la densité locale et la biréfringence de la structure des couches tout en préservant leur morphologie. Ceci indique de possibles changements de propriétés optiques pour des applications dans des environnements radiatifs tels que les réacteurs nucléaires ou les tokamaks.

L'étude porte sur les effets de l'irradiation électronique sur la silice et la stabilité de la phase métamicte formée par différentes voies thermomécaniques. Malgré des densités et des structures vibrationnelles identiques, l'histoire thermo-mécanique initiale de l'échantillon de silice détermine la stabilité thermique des phases métamictes obtenues sous irradiation à 11 GGy, indiquant des différences dans leurs structures internes. L'irradiation électronique modifie la stabilité thermique de la silice densifiée en rompant des liaisons et en dépolymérisant le verre, modifiant ainsi la proportion des phases amorphes de haute et basse densité dans le verre de silice densifié par des conditions de haute pression et de haute température. De plus, des températures élevées durant l'irradiation électronique influencent la dynamique de formation des défauts. À température 300–450 K, les transformations induites par l'irradiation vers la phase métamicte se produisent, et la formation de défauts s'accumule plus facilement. Lorsque T> ou égal à 600 K, elle relaxe vers une phase amorphe de basse densité.

Title : Study of the mechanisms of silica densification under irradiation

Keywords : glasses, silica, densification, laser matter interaction, electron irradiation

Abstract : Silica glass is essential in modern optical and photonics devices due to its exceptional transparency, mechanical strength, and low thermal expansion. Recently, new applications such as high-precision temperature sensing and optical data storage under extreme conditions (e.g., high temperature, radiation) have emerged, relying on femtosecond (fs) laser processing to induce specific structural modifications (Types I, II, III, and X). However, these modifications, which undergo densification, remain incompletely understood. Moreover, the possibility of polyamorphism in silica further complicates our understanding of these irradiation-induced modifications. Electron irradiation adds another level of complication, as it can densify or relax silica glass and produce a not-well-characterized metamict-like phase. By investigating the structural changes, density levels, and densification mechanisms at the nanoscale, this work aims to provide insights that will not only fill gaps in our fundamental understanding of silica glass but also pave the way for improved reliability and efficiency in silica-based technologies. The outcomes are expected to have far-reaching implications, particularly for devices operating in harsh environments, thereby driving forward advancements in photonics and optical sensor applications.

In this thesis, for the first time, density changes induced by fs laser irradiation at the nanoscale were demonstrated and measured. Type I modifications (isotropic index changes, waveguide formation) exhibited a densification of 3–4%, induced by defects and thermal quenching. Type III modifications (micro- or nanovoid formation) revealed ~6% densification in surrounding shells, reflecting densification from shock-induced pressures. Furthermore, it was found that Type II modifications decrease in densified samples, suggesting free volume is critical for seeding nanogratings. Silica's higher intrinsic free volume explains more easily formed nanograting structures compared to other glasses.

Meanwhile, high-dose electron irradiation (5 GGy) relaxes densified Type II nanogratings, reducing local density and birefringence of the layers' structure while preserving morphology. This indicates potential optical property shifts for applications in high-irradiation settings, such as nuclear reactors or Tokamaks.

By studying the effects of electron irradiation on silica and in particular the metamict phase, the structural and thermal stability of this phase obtained by different thermomechanical pathways. Despite identical densities and vibrational structures, the initial thermomechanical history of preparation determines the thermal stability of the metamict phases, indicating differences in their internal structures. Electron irradiation alters thermal stability by breaking bonds and depolymerizing the glass, shifting the proportion of high-density and low-density amorphous phases in silica glass, densified by high-pressure and high-temperature conditions. Furthermore, elevated irradiation temperatures during electron irradiation modify defect formation dynamics. At lower temperatures (300-450K), radiation-driven changes towards metamict phase happen and defect formation accumulate more readily. When the temperature is greater than or equal to 600 K, it relaxes toward a low-density amorphous phase.

CONTENU

ACKNOWLEDGMENTS

Here, I would like to thank all the people without whom this PhD adventure would not have been possible.

First, I would like to express my sincere gratitude to my supervisors, Prof. Matthieu Lancry and Prof. Nadège Ollier. I truly believe I was one of the luckiest PhD students, primarily because I had such incredible supervisors. Their support, guidance, and belief in me have been truly precious to me. Prof. Lancry always patiently answered all my questions, teaching me valuable lessons. I learned so much from our discussions, and I am deeply thankful for the many opportunities and possibilities he provided me. Prof. Ollier has also taught me a lot, guiding me through experimental procedures, and thoroughly discussing the results. Her emotional support throughout my PhD journey has been especially meaningful. I am deeply grateful to both supervisors for helping me grow as a scientist and for always believing in me.

I extend my heartfelt thanks to all collaborators who made the results presented in this thesis possible. I am grateful to the SOLEIL Synchrotron SMIS beamline team, Dr. Ferenc Borondics and Dr. Gergely Németh, for their invaluable help and support during both beamtimes, which produced significant results. My thanks also go to Dr. Olivier Cavani and Dr. Antonino Alessi for their help with the electron irradiation experiments and making high-temperature irradiation possible. I would like to thank Prof. Ludovic Bellot-Gurlet and his team from the MONARIS lab for granting me access to the Raman setup and for their assistance with measurements. I would also like to thank Dr. Thierry Deschamps and Dr. Daniel R. Neuville for kindly providing access to the density-measurement setups used in this study.

A very special thanks goes to all the MAP team members. Their support, collaborative spirit, and enjoyable atmosphere made every working day feel like a holiday. My appreciation goes to Dr. Maxime Cavillon, Prof. Bertrand Poumellec, Dr. Julien Ari, Dr. Imane Ktafi, Jun Zou, Matilde Sosa, Dr. Qiong Xie, Gladys Santandrea, Lachlan Anderson, Sébastien Bourdel, Shreyas J. Kashyap, Paul Mathieu, Dr. Jiafeng Lu. I also thank my colleagues from SP2M group, Ismail Mkinsi, Narimane Meziani, Selma Leonardi, Chuang Jia, Timothée Lauridant, Pierre Tang, Yann-Andrev Kerneur, Mathieu Loriot, and all the others, for the wonderful time spent together and the delicious dinners. Additionally, my appreciation goes to my colleagues at LSI, Charlotte Vernozy, Yeonsoo Cho, Marie Sigallon, Mahinour Mobasher, Nathalie Saouli, Mariusz Drong, Florian Aubrit, and all the others.

Warm thanks to all my dear friends who have been by my side in Paris, making my time in France incredibly enjoyable, Golshid, Sonya, Ilya, Mike, and to those scattered around the world who continuously support me despite the distance, Margo, Dasha, Lena and

Nikita, Ana and Urban, Dasha and Yvan, Sasha and Lena, Marina, Yaroslav, Lera, Julia and many others.

I warmly thank my old colleagues from Institute of Laser Technologies, especially Galina Romanova, my first scientific supervisor, who introduced me to the world of science, inspired me, and helped unlock my potential.

Most importantly, I extend my deepest gratitude to my family, whose constant support has been essential. My husband, who taught me coding, provided endless help and encouragement throughout my PhD, inspired and supported me, and helped me immensely during the thesis writing times and defense preparation. I cannot thank him enough. My parents, who always believed in me, my sister, my grandmother, and all my relatives, without their support, none of my achievements would have been possible.

GENERAL INTRODUCTION

"The only thing we require to be good philosophers
is the faculty of wonder."
— Jostein Gaarder, Sophie's World.

Motivation:

Silica glass forms the backbone of many advanced and emerging applications across optics, telecommunications, materials processing, sensor technologies, electronics, and even protective systems such as spacecraft windows. Despite its omnipresence and decades of active research, silica glass continues to present intriguing behaviors that require further investigations. Its status as a prototypical network former has made it a prime candidate for fundamental studies on mechanical response and structural rearrangements, especially under extreme conditions. Yet it regularly shows anomalous properties that set it apart from other oxide glasses.

Since the 1950-1960s, extensive work focused on the mechanical behavior of silica under quasi-static compression (e.g., using diamond anvil cells or indentation) [1] and under dynamic (shock) loading [2]. These studies revealed that silica can exist in different amorphous polymorphs, notably low-density (LDA) and high-density (HDA) forms [3], and that transitions between them can occur under specific pressures, temperatures, and conditions.

From the 1960s, the effects of electron bombardment on glass were studied with high-energy sources of the order of MeV. Silica glasses have then been much studied since the discovery of their photosensitivity to ultraviolet laser radiation in the 1980s [4]. As early as the late 1960s, a few authors began to use less energetic electron beams (of the order of keV) to study induced changes in volume and optical modifications [5]. Interestingly, high doses of irradiation were found to produce newly formed phase, known as the "metamict-like" phase, that exhibits distinct density states yet remains incompletely characterized decades after their initial discovery in 1958 [6].

A breakthrough occurred in 1996 with the discovery of 3D direct writing in silica using femtosecond (fs) lasers [7]. This technique subjects glass to strong thermo-mechanical stresses depending on the regime studied. Whatever the types of irradiation, these changes are based on the formation of point defects as well as structural modifications

including specific volume changes (observable by vibrational spectroscopy or by electronic microscopy, for example) and resulting in changes in the optical properties that can be exploited for various applications.

Depending on the energy deposited, these ultrashort pulses can induce three main types of modifications: Type I, in which an isotropic refractive index change is observed [7]; Type II, which is strongly anisotropic and produces periodic nanogratings [8]; and Type III, marked by nano- or micro-void formation surrounded by a densified shell [9]. All of these laser-induced modifications exhibit unique properties, which will be reviewed in detail in this thesis. One interesting common point is the occurrence of permanent densification in all these regimes but likely following different thermo-mechanical pathways. Yet important questions remain regarding how much densification actually takes place in laser-written zones, which physical mechanisms drive these density changes, and how such structural transformations vary across different irradiation regimes.

Among these laser-induced modifications, Type II has drawn particular attention because it reveals spontaneous nanoscale organization of the glass network, creating the smallest self-organized structures ever induced by light within the glass bulk [8], accompanied by a net volume expansion, a corresponding compressive stress field [10,11], and a controllable, thus exploitable, birefringence [12–14]. Due to the complexity involving mechanisms of excitation, feedback and reorganization of the matter, heat effects, stress field formation, mastering this phenomenon poses scientific and technological challenges before its full exploitation for various photonics applications.

Likewise, it is important to understand the behavior of both pristine and densified silica in extreme environments, such as high-dose electron irradiation, high temperatures, or a combination of both. Laser-induced Type II modifications are increasingly used in advanced optical sensors (e.g., fiber Bragg gratings and Fabry-Pérot based sensors) designed to function in nuclear reactors, fusion devices like Tokamaks, and other high-temperature, high-radiation settings reactors [15–17]. Future progress in these fields thus relies on clarifying the structural response of silica, including polyamorphic changes, defect formation, and densification mechanisms, which under the wide range of conditions it is likely to encounter in modern applications.

Goals of the thesis:

Within this context, the present PhD work forms part of a broader effort to explain how silica glass behaves and can be engineered under various irradiation conditions (light or electrons) and eventually combined to high temperature. One central objective is to deepen our understanding of polyamorphism, including the HDA-LDA transition and the emergence of metamict-like states under electron bombardment. In parallel, we

explore the full spectrum of ultrafast laser-induced modifications, from isotropic refractive-index changes (Type I) and nanograting formation (Type II) to micro-void generation (Type III), with a special focus on the mechanisms and levels of densification that occur. Through a combination of experimental and analytical approaches, the thesis aims not only to clarify the underlying thermo-mechanical and relaxation processes responsible for these structural transformations but also to leverage this knowledge for advanced optical functionalization and micromechanical applications in silica.

Organization and contribution of this thesis:

This thesis is divided into four major chapters, each addressing a key aspect of silica glass modification under electron and femtosecond laser irradiation. In details, the contents of the chapters are as follows.

Chapter I provides a review of the fundamental knowledge necessary to fully understand this thesis. It begins with an overview of silica glass, the central material studied throughout the work, highlighting its structural characteristics, including its tetrahedral SiO_4 network, intrinsic defects, and distinctive optical and vibrational properties. The chapter then explores silica glass densification, discussing various processes such as cold compression and treatments at high pressures and temperatures (HPHT), which give rise to intriguing polyamorphic transitions between low-density (LDA) and high-density (HDA) amorphous states, as well as not completely understood metamict-like phase. Additionally, this chapter addresses modifications induced by electron irradiation and ultrafast laser light, emphasizing current understanding of the modifications and highlighting open questions regarding their mechanisms, stability, and behavior under extreme conditions. Collectively, this review provides a foundation for the subsequent chapters, which further investigate these phenomena using advanced characterization methods.

Chapter II investigates the formation mechanisms, underlying nanostructure, and densification phenomena of femtosecond laser-induced nanogratings (Type II modifications) in silica glass. The first section of this chapter, based on a paper published in Materials [18], contributes to understanding how nanogratings form. The paper examines how silica densification, particularly the reduction of free volume, influences nanograting formation. This addresses the hypothesis that free volume acts as a seed for nanograting formation. Utilizing polarized optical microscopy and scanning electron microscopy (SEM), the study demonstrates that reduced free volume in silica glass significantly diminishes nanograting formation efficiency, supporting the hypothesis. The second section, based on work published in Nanoscale Advances [19], provides a detailed analysis of the intrinsic nanostructure of these laser-induced nanogratings using SEM, scanning transmission electron microscopy (STEM), high-resolution transmission electron microscopy (HRTEM), and atomic force microscopy (AFM). It reveals that

nanogratings consist of discontinuous, wavy nanoplanes composed of oblate nanopores aligned perpendicular to the laser polarization. Based on these findings and existing literature, formation mechanisms involving plasma-mediated nanocavitation processes are discussed. The final section, presented through another publication in Nanoscale Advances [20], employs advanced spectroscopic techniques, specifically scattering-type scanning near-field optical microscopy (s-SNOM) combined with synchrotron-based nano-Fourier transform infrared (nano-FTIR) spectroscopy, to directly assess nanoscale densification behind and between nanoporous layers. By analyzing shifts in the Si-O-Si asymmetrical stretching band, this study quantifies density changes comparable to those achieved by conventional HPHT treatments. Based on these findings and existing literature, densification mechanisms within the nanogratings are discussed.

Chapter III investigates the effects of electron irradiation on silica glass, focusing on polyamorphic transitions, densification, and thermal stability. The first part, based on a paper published in the Journal of Non-Crystalline Solids [21], utilizes in situ Raman spectroscopy during annealing to calculate the activation energy distribution of the densification relaxation process and to reveal the HDA-LDA transition. The paper demonstrates the presence of an HDA-LDA transition through a bimodal activation energy distribution and discusses how low-dose electron irradiation lowers thermal stability, progressively erasing the HDA phase at higher irradiation doses. The second part is based on another paper published in the Journal of Non-Crystalline Solids [22], comparing different pre-irradiation treatments and impurity levels of silica to reveal how thermo-mechanical history influences the final metamict-like state and its thermal stability. The chapter concludes with a study examining the relationship between electron irradiation dose and temperature in structural modifications of silica glass (paper submitted to the Journal of Non-Crystalline Solids). This reveals that irradiation temperatures > 600 K promote thermal annealing, leading to a monotonic decrease in compaction and suggesting a competitive interplay between the formation and temperature-driven bleaching of point defects. Together, these studies provide a comprehensive picture of how electron irradiation and thermal conditions drive structural evolution in silica glass, giving insights that are essential for developing robust, radiation-resistant optical devices.

Chapter IV focuses on densification levels and mechanisms in all main fs-laser modifications and how subsequent high-dose electron irradiation alters these structures in silica glass. It comprises two core studies: the first part, a review paper published in International Journal of Applied Glass Science, compares the state-of-the-art understanding of three main modification types and uses s-SNOM and nano-FTIR spectroscopy to quantify and compare density levels in Type I, II, and III fs-laser modifications. This analysis clarifies densification mechanisms specific to each modification, such as defect-related structural changes, thermal quenching, HPHT densification, or shock wave densification. The second part, published in Nanomaterials [23], extends this work

by exposing Type II nanogratings to high-dose (4.9 GGy) electron irradiation. This study reveals that while nanograting morphology remains unaffected, the dense interlayers relax, lowering birefringence, which is an important insight for radiation-hardened photonics and sensing applications in high-temperature or nuclear environments.

Finally, the **conclusion and perspectives section** summarizes the overall investigations regarding silica glass densification under electron and fs-laser irradiation. These results provide a useful roadmap for fabricating and designing devices using densified silica glass, particularly under fs-laser conditions, suitable for harsh environments with high irradiation.

Additional technical details are provided in the **Appendix**. Appendix 1 presents the femtosecond laser writing system. Appendix 2 explains the technical details of the electron irradiation. Appendix 3 describes the principles behind s-SNOM and nano-FTIR techniques.

Chapter I. BACKGROUND AND STATE-OF-THE-ART

I.1 INTRODUCTION

This chapter establishes the fundamental background necessary for understanding the research presented in this dissertation. This state of the art begins with a presentation of silica glass, exploring its structure and characteristic vibrational signatures. Following this, the thermomechanical properties of silica glass are discussed. The central focus of this chapter is the densification of silica glass through various methods. First, hydrostatic pressure compression is addressed, examining both room temperature and high-temperature densifications, so-called cold and hot compression, with attention to the resulting structural changes and polyamorphism phenomena. Then, the review shifts to discussing the effects of irradiation on silica glass. This section begins with electron irradiation and its effects, including the formation of metamict-like phases. Finally, femtosecond laser irradiation effects are examined, with detailed discussion of Type I, II, and III modifications and their associated densification effects in light of the current state of the art.

I.2 SILICA GLASS

Silica glass is one of the few simple materials that is extremely important in a wide variety of optical and engineering applications. It is often considered as the prototype glass network former, and it creates the basis of numerous other glass compositions. Its richness in the Earth's crust, combined with its exceptional properties (such as optical transparency, thermal stability, and chemical durability), has made it essential in modern technologies, including semiconductor devices, optical fibers, and industrial catalysis.

I.2.1 Silica glass structure

Silicon dioxide (SiO_2) is a chemical compound widely found in nature, forming a large variety of materials. There are several well-known crystalline polymorphs, such as quartz, cristobalite, tridymite, coesite, and stishovite [24]. All of them share the same fundamental Si-O tetrahedral building blocks. The key difference among the various silica polymorphs lies in how these tetrahedra are arranged and packed. In the crystalline state, these tetrahedra pack into a clear crystal lattice (Figure 1 a,b).

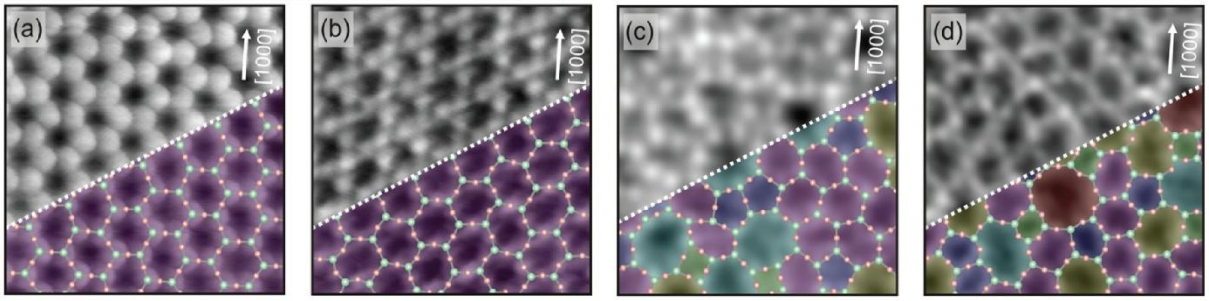

Figure 1. Atomically resolved scanning tunnelling microscopy (STM) images of crystalline and amorphous silica. (a, b) STM images of a crystalline region, showing the positions of Si atoms (a) and the arrangement of O atoms (b). (c, d) STM images of an amorphous region, with the positions of Si atoms (c) and the arrangement of O atoms (d). Adapted from [25].

Since the chemical composition SiO_2 is identical across all polymorphs, their differing physical and optical properties arise solely from variations in this network organization. As a result, each polymorph exhibits distinct values for density and refractive index, presented in Figure 2. A key observation from Figure 2 is the strong linear dependence of the refractive index on the density of the polymorph. The slope of this dependence ($dn = 0.44\, d\rho/\rho$ cm^3/g) aligns well with the Lorentz-Lorenz relation (discussed further in Section I.3.4).

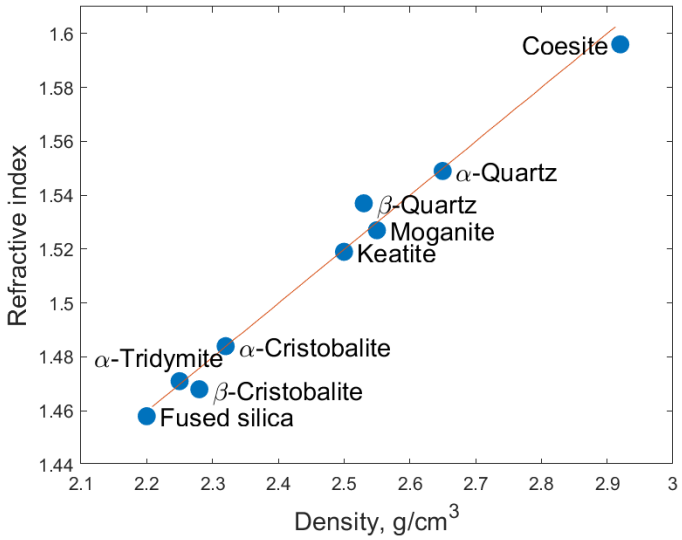

Figure 2. Dependency of the refractive index on the density of different silica polymorphs. Adopted from PhD thesis of K. Mishchik [26].

Based on the X-ray and neutron diffraction studies [27], the amorphous form of silica (known as silica glass) does not have any long-range structural order like all glasses [28], as illustrated by the scanning tunnelling microscopy (STM) images in Figure 1 c,d. However, it maintains the same tetrahedral coordination of silicon and oxygen found

in the crystalline forms (Figure 3) i.e. a short-range order is preserved.

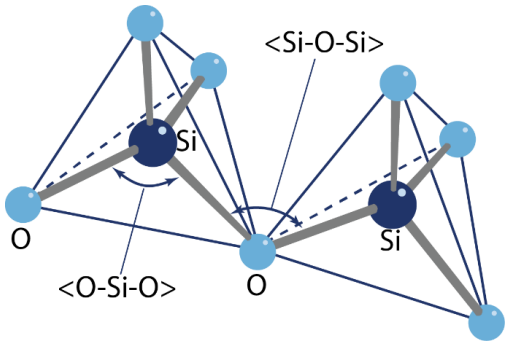

Figure 3. Schematic representation of the SiO_2 tetrahedral network. Each Si atom is surrounded by four O atoms. The angles between O and Si atoms (O-Si-O) and between neighbouring Si atoms connected through an O bridge (Si-O–Si) define the overall network geometry.

For this tetrahedral building unit, the typical Si-O bond length is approximately 1.608-1.62 Å [29,30], and the internal O-Si-O bond angles are close to the ideal tetrahedral value of 109.47°. These tetrahedra are connected between each other with shared "bridging" oxygen atoms, forming the Si-O-Si linkage with an angle around 144°. In addition, typical nearest-neighbour O-O distances are about 2.50-2.65 Å, while the Si-Si distance is approximately 3.12 Å [28,31]. The formed amorphous silica network is both continuous and random in structure, opposed to its crystalline phases.

These tetrahedral building units link into closed n-membered $(Si\text{-}O)_n$ rings, forming the medium-range order of the silica network. In crystalline silica, the ring sizes are mostly 6- and 8-membered, they form the periodic lattice structure [24]. However, in amorphous silica, the ring sizes vary more widely, typically ranging from 3 to 10 members [32–34], with the most common sizes being 6- and 7-membered rings. The distribution of these rings depends on the thermomechanical history of the silica glass. This variable ring size distribution creates interstitial voids or "free volume" within the network, which provides pathways for potential structural rearrangements during densification processes i.e. silica glass is intrinsically porous but at the sub-nm scale.

I.2.2 Point defects in silica glass

The SiO_2 tetrahedral network represents the ideal, yet disordered framework of amorphous silica. However, in addition to the natural randomness of the silica glass, the presence of intrinsic defects, dopants (e.g. GeO_2), and impurities (e.g. Cl, OH) creates an additional level of structural or chemical disorder. Compared with crystalline quartz, silica glass has a significantly higher efficiency in generating point defects and even has other defect types [27,34]. This difference comes from the amorphous nature of silica, with "strained bonds" (due to small-numbered rings) acting as precursors for the creation of silicon and oxygen dangling bonds.

I.2.2.1 Frenkel-type defects (vacancy-interstitial type)

The defects in silica glass are typically classified into groups based on their structural nature. The first category includes Frenkel-type defects, which involve vacancy-interstitial pairs analogous to those in crystalline materials (see Figure 4 for vacancy-interstitial defects observed in SiO_2).

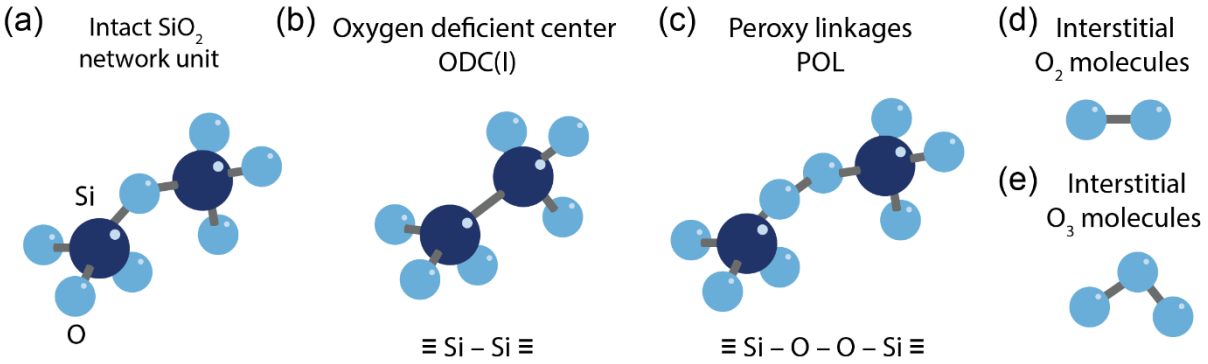

Figure 4. Vacancy-interstitial type defects observed in silica glass: (a) intact SiO_2 network unit, (b) oxygen deficient center (ODC(I)), (c) peroxy linkages (POL), (d) interstitial O_2 molecules, and (e) interstitial O_3 molecules.

The oxygen deficient center, ODC(I), also known as the neutral oxygen vacancy (or Si-Si bond defect [35]), appears when an oxygen atom is missing from the network (Figure 4 b). In its absence, the two neighbouring silicon atoms form a direct bond, resulting in a ≡ Si – Si ≡ configuration. This defect has an absorption band around 7.6 eV [36] and is typically diamagnetic due to the absence of unpaired electrons. ODC(I) often forms as a result of radiation effects [37] and is commonly observed in oxygen-deficient silica [34].

The peroxy linkages (POL) form in the silica network when two silicon atoms are connected through two oxygen atoms (≡Si–O–O–Si≡) (Figure 4 c). This defect is diamagnetic and challenging to detect optically due to its low oscillator strength and the strong background absorption from dangling bonds in the UV-VUV region [34]. However, it can be selectively generated through the photolysis of interstitial O_2 using an F_2 laser [38].

Interstitial oxygen molecules (O_2) are commonly introduced during the synthesis of oxygen-rich silica (Figure 4 d). They can also be incorporated by thermal diffusion or generated by high-dose irradiation. Although not typical Frenkel defects, interstitial O_2 exhibits distinct spectral features. For instance, when present above approximately $5\times10^{17}\,cm^{-3}$, a narrow line at $1549\,cm^{-1}$ in Raman or infrared (IR) absorption spectra, which shifts towards higher wavenumbers under pressure [39]. The PL peak for O_2 in silica is approximately at 1273 nm, in the near-IR region [34].

Interstitial ozone molecules (O_3) have been identified by an absorption band peaking

near 4.8 eV in irradiated oxygen-rich silica (Figure 4 e). Although this band nearly coincides with that of dangling oxygen bonds, spectroscopic analysis has confirmed its association with O_3 [34].

I.2.2.2 Dangling bond-type defects

The next major group of defects in silica glass consists of dangling bond-type defects (see Figure 5).

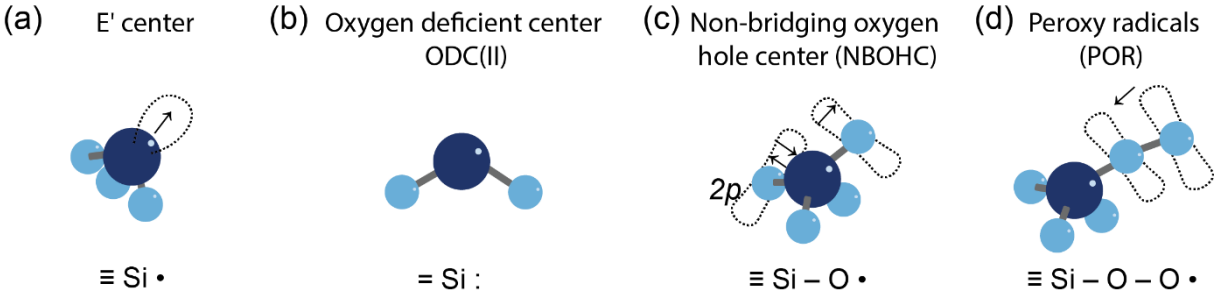

Figure 5. Dangling bond-type defects in silica glass: (a) E' center, (b) oxygen deficient center ODC(II), (c) non-bridging oxygen hole center (NBOHC), and (d) peroxy radical (POR).

E' centers are defects formed where a silicon atom is bonded to only three oxygen atoms (Figure 5 a), leaving a dangling bond with an unpaired localized electron (≡Si•) [36]. This silicon dangling bond gives rise to a strong absorption band at 5.8 eV, while no photoluminescence (PL) is observed. As a paramagnetic defect, the E' center exhibits a magnetic response that can be detected by electron paramagnetic resonance (EPR) [36]. Since their initial discovery, more than ten variants of E' centers have been identified (with E'γ-center being the most abundant) [34,40–43]. It is typically formed by radiation or mechanical stress that breaks Si–O bonds in the silica network.

ODC(II) forms under oxygen-poor conditions during synthesis and consists of a twofold-coordinated silicon atom (represented as =Si:) (Figure 5 b) [44]. This defect exhibits absorption bands at 3.15 eV, 5.05eV, 6.9 eV and is diamagnetic [34,36]. ODC(II) exhibits emission bands peaking at approximately 280 nm and 460 nm [34]. It is commonly present in all irradiated or oxygen-deficient silica glasses.

Non-bridging oxygen hole center (NBOHC) forms when a regular ≡Si–O–Si≡ bond breaks, leaving behind a dangling oxygen bond (≡Si–O•) with an unpaired electron (Figure 5 c) [27,34]. This paramagnetic defect was first identified through its EPR signal [45] and is a main contributor to the visible-to-near UV absorption spectrum, with characteristic absorption bands at 2.0 eV and 4.8 eV [34]. NBOHCs exhibit PL with an emission band peaking at approximately 650 nm. NBOHCs are primarily generated under irradiation through the breaking of strained Si–O bonds [46] and peroxy linkages [47] or, more efficiently, by the dissociation of silanol (≡Si–O–H) groups, following the reaction [34,48]:

$$\equiv Si-O-H \rightarrow \equiv Si-O\bullet + H\bullet$$

Peroxy radicals (POR) are defects characterized by oxygen species with an unpaired electron (≡Si–O–O•) (Figure 5 d). These paramagnetic defects can be characterized by EPR [45,49] and exhibit an absorption band at 5.4 eV on silica surfaces [34]. POR can form through the reaction of interstitial O_2 with silicon dangling bonds or via the irradiation-induced breaking of peroxy linkages [50]. They can also be generated during the glass fabrication process, such as in the drawing of optical fibers [51].

I.2.2.3 Transient defects and impurities

In addition to dangling bond defects and vacancy-interstitial defects, silica glass also has transient defects, such as self-trapped holes (STH) and self-trapped excitons (STE). These defects have a short lifetime, are formed under excitation, and can either relax back to the original structure or lead to permanent modifications in the network.

Self-trapped holes (STHs) are paramagnetic, metastable defects in silica that exist in two forms STH_1 and STH_2. In STH_1 the hole is localized in a single bridging oxygen atom, while in STH_2 the hole is shared between two oxygen atoms in the same SiO_4 tetrahedron. In bulk silica, the corresponding absorption bands are located at around 2.6 eV and 2.16 eV for STH_1 and STH_2, respectively [52].

Self-trapped excitons (STEs) are electron-hole pairs that become localized due to distortions in the silica network, often involving the displacement of an oxygen atom [53]. They have two main optical absorption bands at 4.2 eV and 5.3 eV [54]. STEs can relax by emitting light (with luminescent band at about 2.0 and 2.3 eV) or decay without emission. STEs contribute to the formation of E' centers and NBOHCs [55].

There are also impurities introduced during silica fabrication (see section I.2.3), which significantly influence its optical and structural properties. One example is the presence of hydroxyl groups, particularly **silanol (SiOH) groups**, which have an absorption band above 7.4 eV [56] and can promote the formation of additional defects. The incorporation of interstitial H_2 ("hydrogen loading") helps to suppress the increase of defects by saturating dangling Si or O bonds [57]. However, while hydrogen loading reduces the creation of dangling bonds, it can lead to an increased formation of oxygen vacancies [58]. Another hydrogen-related defect is the **H(I) center**. This paramagnetic defect is similar to the Si E' center, except that one oxygen atom is replaced by hydrogen. The H(I) center exhibits an optical absorption band at 4.9 eV [34], with no corresponding luminescence. Additionally, other **impurities**, such as chlorine, which is typically introduced during synthetic silica production, can be present in silica glass and are undesirable, especially for optical fibers, due to their UV absorption properties [59]. More recently, paramagnetic fluorine-related defects were identified in heavily F-doped silica as E'(F) centers, which are silicon dangling bonds modified by a neighboring Si-F bond [60].

The absorption bands associated with the main silica glass defects are summarized in Figure 6.

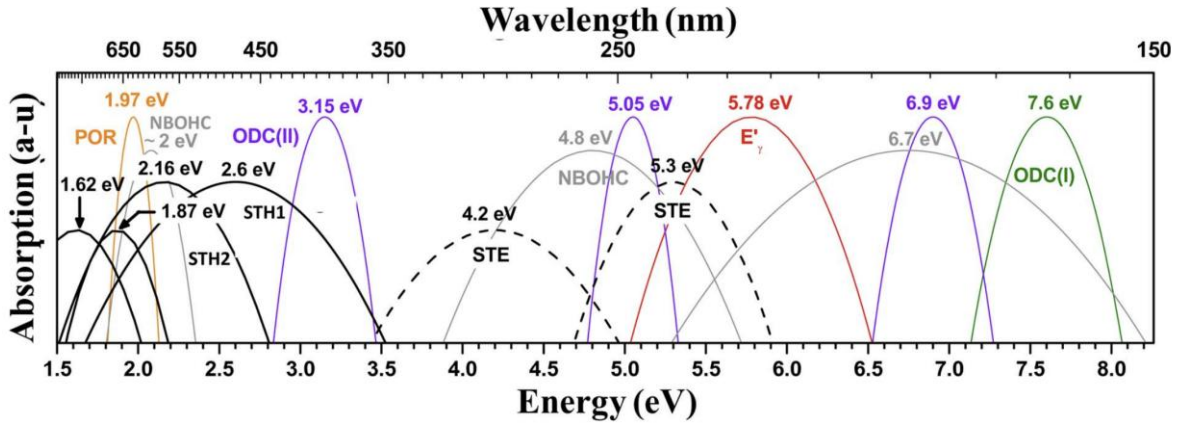

Figure 6. Absorption bands of the main transient and permanent point defects in silica glass. Cited from [61].

I.2.3 Types of silica glass and manufacturing process

Silica glass manufacturing begins with the selection of raw materials and heat sources. The raw materials are typically either natural crystalline quartz (or high-quality glassmaking sand) or liquid compounds, such as tetraethylorthosilicate (TEOS), halides, or siloxanes. The heat treatment can be achieved either electrically (using electric arcs, resistance and induction heaters, or high frequency plasma discharges) or through chemical combustion (using hydrogen-oxygen or methane-based flames).

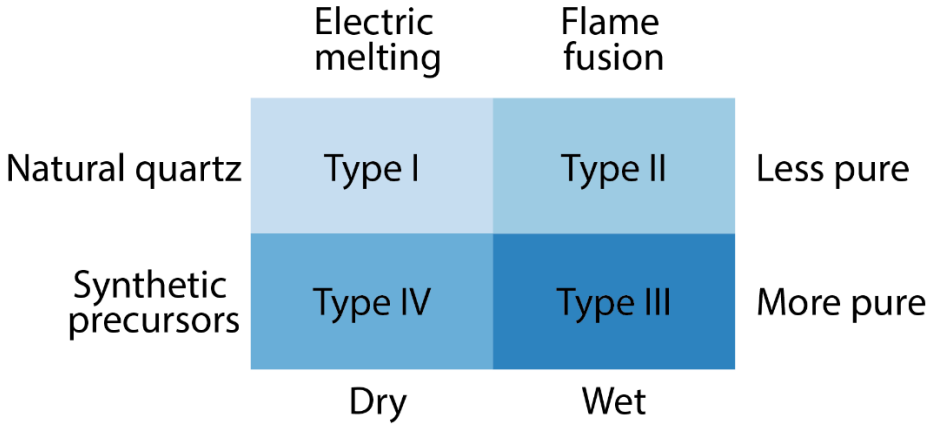

Figure 7. Classification of silica glass types based on raw material source (natural quartz vs. synthetic precursors), manufacturing method (electric melting vs. flame fusion), hydroxyl content (dry vs. wet), and purity level.

There are 4 main types of silica glass, each defined by its raw material source and fabrication method (Figure 7) [33,62].

Type I is traditionally known as "fused quartz" and is produced from natural quartz or beneficiated sand. In this process, the quartz is melted using electric fusion under vacuum or inert gas conditions. The resulting glass is "dry" (with less than 200 ppm OH). However, it typically exhibits higher metallic impurities (approximately 30–100 ppm aluminum and about 4 ppm sodium by weight). This method is widely used for making crucibles, rods, and tubing.

Type II, also referred as "fused quartz", is developed as an outgrowth of early innovations in glassmaking. This method involves the continuous deposition of molten quartz granules onto a hot, rotating mandrel, where they sinter into a dense ingot or "boule." The absence of crucible contact reduces metallic impurities compared to Type I, but the flame environment introduces a higher OH content (typically 150–400 ppm).

Type III. This method ("fused silica") employs a flame (or vapor-phase) hydrolysis process [63,64], in which silicon tetrachloride ($SiCl_4$) vapor is introduced into a hydrogen- or methane-oxygen flame. The key reaction is:

$$SiCl_4 + 2\ H_2O \rightarrow SiO_2 + 4\ HCl$$

Here, water generated by the combustion of hydrogen or methane serves as the hydrolysis agent. A fraction of that water also becomes incorporated into the glass network as SiOH. Consequently, the resulting glass is considered "wet," typically containing 600-1200 ppm of hydroxyl groups. In the flame, fine (< 50 nm) amorphous silica "soot" particles form [65] and are subsequently sintered into transparent glass. Because the process avoids the use of a crucible, metallic impurities are kept to minimal levels. Deposition rates have improved over the years, making this method scalable for larger production. Additionally, because $SiCl_4$ is used as the precursor, Type III synthetic silica commonly contains 1000-3000 ppm of chlorine. In contrast, natural quartz typically has chlorine content below 0.15 ppm.

Type IV. A variation of the vapor-phase oxidation process, Type IV uses a water vapor-free gas stream (often in a plasma torch [66]) to oxidize the silica precursor (for example, $SiCl_4$). This type is also known as "fused silica". The process produces a "dry" silica with less than 20 ppm OH and impurity levels similar to those in Type III. This method is particularly suited for applications requiring extremely low hydroxyl content.

Due to variations in impurity content and hydroxyl concentration, types of silica glass exhibit distinct selective properties and characteristic differences in their network structure. In this thesis, experiments were conducted using Suprasil CG and Suprasil F300, both classified as Type III silica glass. Suprasil F300, in addition to undergoing an intermediate drying step during manufacturing [67] that reduces its OH content to below 1 ppm (rendering it a "dry" variant compared to the "wet" Suprasil CG), is characterized by ultra-low total metallic impurities (< 1 ppm) and a chlorine content of 1000–3000 ppm. This relatively high chlorine concentration results in a slight shift of

the UV-absorption edge to the longer wavelength region and affects the viscosity of the glass.

I.3 Optical properties and vibrational signature of silica glass

I.3.1 Fundamentals of the Lorentz oscillator model

The Lorentz oscillator model is essential for describing silica glass's optical properties and vibrational signature, as it quantitatively links the resonant behaviour of vibrational bands to the material's frequency-dependent dielectric response [68]. In general, the Lorentz oscillator model provides a classical description of how bound electrons in a material respond to an external electric field. In this model, an electron is considered to be bound to an atomic nucleus by a restoring force, similar to a mass attached to a spring (Figure 8). When an external electric field E is applied, the electron cloud is displaced relative to the nucleus, resulting in oscillatory motion around its equilibrium position. This model extends to various oscillators, such as bound electrons in atoms or crystal bands, weakly bound impurity centers in polymers and dielectrics, optical phonons, vibrational modes in polyatomic polar molecules, exciton-impurity complexes, plasma oscillations, and other polarization processes, whose effects on a material's optical properties can be described in an analogous manner.

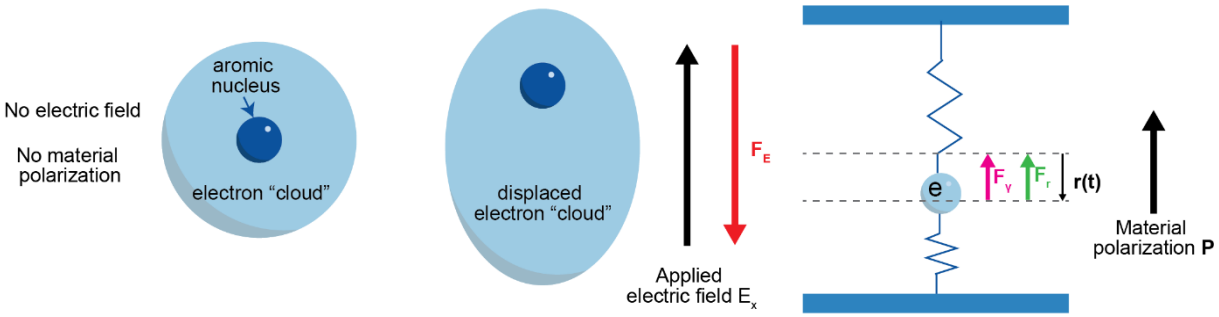

Figure 8. Lorentz oscillator model illustrating electron cloud displacement under an applied electric field, leading to material polarization. The right diagram represents the electron as a harmonic oscillator with restoring F_r, damping F_γ, and driving force F_E.

The motion of the electron is governed by three forces (Figure 8). A restoring force F_r that pulls the electron back toward equilibrium, analogous to a spring. A damping force F_γ that accounts for energy loss due to interactions with the surrounding medium. A driving force F_E is exerted by the applied electric field, which displaces the electron.

Mathematically, the equation of motion for an oscillating electron can be written as:

$$m\frac{d^2\vec{r}}{dt^2} = \overrightarrow{F_r}(\vec{r}) + \overrightarrow{F_\gamma}(\vec{v}) + \overrightarrow{F_E}(\vec{E}) = -C\vec{r} - m\gamma\frac{d\vec{r}}{dt} - \overrightarrow{E_L}e^{-i\omega t} \qquad (1)$$

where m is the effective mass of the electron, γ is the damping coefficient (related to energy dissipation), C is the restoring force constant, and $\overrightarrow{E_L}e^{-i\omega t}$ represents the external driving force. Since the applied field causes the electron to oscillate, and using

equation (1), the electric dipole moment can be described as

$$\vec{p} = -e\vec{r} = \frac{e^2}{m}\frac{1}{\omega_0^2-\omega^2-i\gamma\omega}\overrightarrow{E_L}, \quad (2)$$

where the square of the resonance frequency is $\omega_0^2 = \frac{C}{m}$.

The response of a material to an external electric field is frequency-dependent. This behavior is characterized by the atomic polarizability $\alpha(\omega)$, which describes how a bound electron cloud deforms under an oscillating electric field. The atomic polarizability is given by:

$$\alpha(\omega) = \frac{P_0}{\varepsilon_0 E_L} = \frac{e^2}{\varepsilon_0 m}\frac{1}{\omega_0^2-\omega^2-i\gamma\omega}. \quad (3)$$

The macroscopic response of a material to an electric field originates from the polarization of individual atoms. So, the total polarization P in a material is related to the atomic polarizability $\alpha(\omega)$. The relationship between polarizability and electric susceptibility depends on whether the material is a rarified medium (gas) or a solid.

For a rarified medium, such as a gas, with atomic number density N (and atoms are well separated), the polarization P is the sum of the individual dipole contributions:

$$P = \varepsilon_0\chi(\omega)E_L = \varepsilon_0 N\alpha. \quad (4)$$

Thus, the electric susceptibility is:

$$\chi(\omega) = N\alpha = \frac{Ne^2}{\varepsilon_0 m}\frac{1}{\omega_0^2-\omega^2-i\gamma\omega} = \frac{\omega_p^2}{\omega_0^2-\omega^2-i\gamma\omega}, \quad (5)$$

where the plasma frequency is

$$\omega_p^2 = \frac{Ne^2}{\varepsilon_0 m}.$$

Moving forward, the dielectric function $\varepsilon(\omega)$ describes how a material interacts with an external electromagnetic field. It is directly related to the electric susceptibility $\chi(\omega)$:

$$\varepsilon(\omega) = 1 + \chi(\omega) = 1 + \frac{\omega_p^2}{\omega_0^2-\omega^2-i\gamma\omega}. \quad (6)$$

So, we see that the dielectric function $\varepsilon(\omega)$ is a complex function, and it can be separated into real and imaginary parts (Figure 9 a):

$$\varepsilon'(\omega) = 1 + \frac{\omega_p^2(\omega_0^2-\omega^2)}{(\omega_0^2-\omega^2)^2+\gamma^2\omega^2}, \quad (7)$$

$$\varepsilon''(\omega) = \frac{\omega_p^2\gamma\omega}{(\omega_0^2-\omega^2)^2+\gamma^2\omega^2}, \quad (8)$$

where ε' (real part) influences the phase velocity of light in the material (dispersion) and ε'' (imaginary part) quantifies the energy loss from the electromagnetic wave (absorption).

The response of the material to the external electric field is determined by the dielectric response function ε, while the propagation of electromagnetic waves within material is

determined by the complex refractive index n. The refractive index n is related to the dielectric function ε by:

$$n = \sqrt{\boldsymbol{\varepsilon}} = n' + in'' = \sqrt{\varepsilon' + i\varepsilon''}. \tag{9}$$

Expanding this relation gives (Figure 9 b):

$$n' = \sqrt{\frac{\varepsilon' + \sqrt{\varepsilon'^2 + \varepsilon''^2}}{2}}, \tag{10}$$

$$n'' = \sqrt{\frac{-\varepsilon' + \sqrt{\varepsilon'^2 + \varepsilon''^2}}{2}}. \tag{11}$$

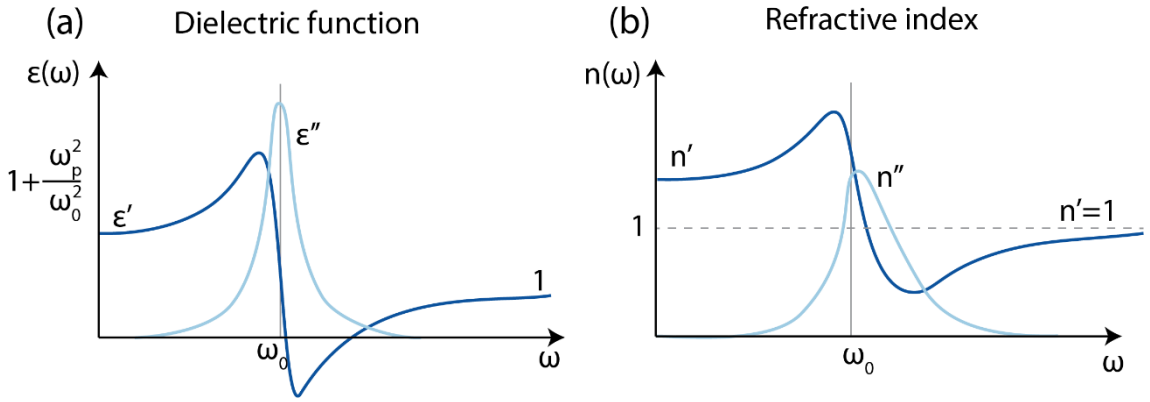

Figure 9. Lorentz oscillator model for 1 oscillator: (a) Frequency dependence of the real (ε') and imaginary (ε'') parts of the dielectric function. (b) Corresponding real (n') and imaginary (n'') parts of the refractive index.

As can be seen from the Figure 9, at low frequencies ($\omega \ll \omega_0$), n' is large (slow light propagation) and absorption is minimal. Near resonance ($\omega \approx \omega_0$), both dispersion and absorption become pronounced. For $\omega \gg \omega_0$, n' approaches 1, and the material becomes nearly transparent.

In dense materials such as solids, the local electric field $\overrightarrow{E_L}$ experienced by an atom differs from the applied field $\overrightarrow{E_0}$ due to contributions from nearby dipoles. For a cubic crystal, it can be approximately written as:

$$E_L = E_0 + \frac{P}{3\varepsilon_0}. \tag{12}$$

where P is the polarization density. Because of this correction, the polarization for atoms with polarizability α_j and number density N_j is given by:

$$P = \varepsilon_0 \sum_j N_j \alpha_j E_L. \tag{13}$$

After rearrangement, the effective susceptibility becomes:

$$\chi = \frac{\sum_j N_j \alpha_j}{1 - \frac{1}{3}\sum_j N_j \alpha_j}. \tag{14}$$

Then we can use the Clausius-Mossotti relation, which connects the microscopic polarizability of individual atoms to the macroscopic dielectric constant ε of the material:

$$\frac{\varepsilon-1}{\varepsilon+2} = \frac{1}{3\varepsilon_0}\sum_j N_j \alpha_j. \quad (15)$$

For a homogeneous system where all atoms are similar (i.e., they have the same polarizability), these local interactions lead to a shift in the resonance frequency. The modified resonance frequency is expressed as:

$$\omega_0^2 = \frac{C}{m} - \frac{Ne^2}{3m\varepsilon_0}. \quad (16)$$

And the dielectric constant then can be represented again as in equation (6).

I.3.2 Optical constants and dielectric function in silica glass

Although there are resemblances between the measured optical response of SiO_2 and the predictions from simple Lorentz oscillators, important differences arise because the primary absorption in the infrared region is due to vibrational (phonon) transitions rather than electronic ones [69]. We need to consider a polar diatomic molecule: the permanent dipole moment can be modulated by thermal agitation, which periodically stretches or shrinks the interatomic bond. This process is similar to the electron-based oscillations as shown in Figure 8, but here the dipoles pre-exist and are driven by collective vibrations (phonons) across the material. These phonons can be either transverse optical (TO) modes, where ionic displacements are perpendicular to the direction of propagation, or longitudinal optical (LO) modes, with displacements along the propagation direction [68,70]. Even in non-crystalline solids, these modes interact coherently with IR electromagnetic waves. As a first approximation, these displacements are often modelled with Lorentz oscillators, where the resonance frequency corresponds to the natural vibrational frequency of the TO mode [68].

Talking about these properties for silica glass, we can note the following. In the example below [70], thin films of SiO_2 were studied, which exhibit properties similar to amorphous silica glass. Reflectance and absorbance spectra were measured, and from these measurements, the optical constants were derived. The resulting optical constants for a-SiO_2 are shown in Figure 10 a. Then, using the correspondence between refractive index and the dielectric function (Eq. 9), the dielectric function was calculated, and its real and imaginary parts were plotted in Figure 10 b.

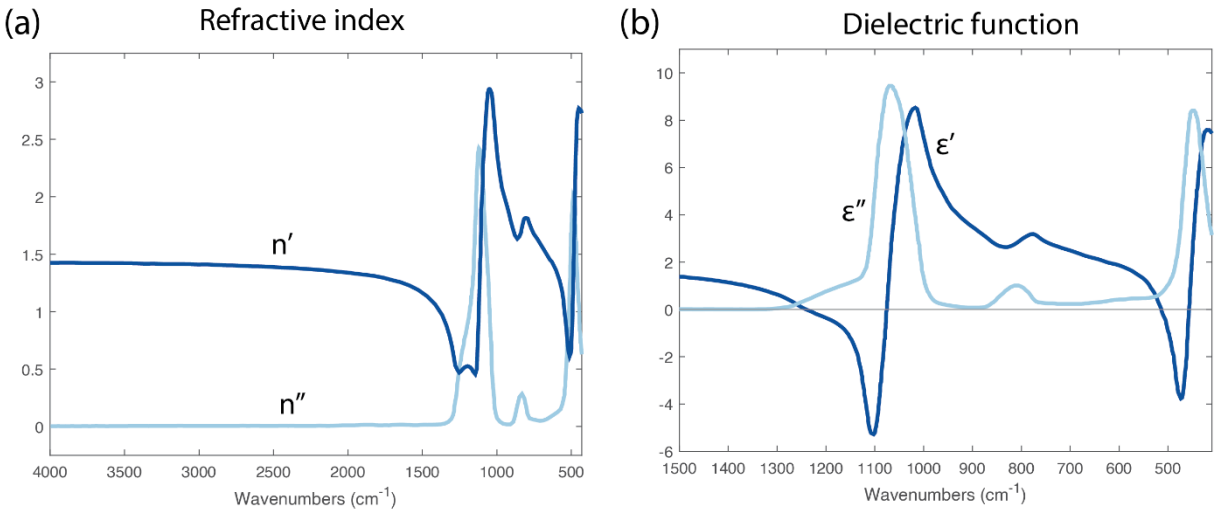

Figure 10. Refractive index (a) and dielectric function (b) of silica glass as a function of wavenumber. Adapted from [70].

There are two spectral regions where the real part of the dielectric function (ε′) becomes negative, each corresponding to a prominent peak in the imaginary part (ε′′). Between these two regions, ε′ remains positive and only a low-intensity band appears in ε′′. The three absorption bands observed in the ε′′ are associated with characteristic vibrations of bridging oxygen relative to the axis joining two neighboring silicon atoms: rocking at ~450 cm^{-1}, symmetrical stretching at ~810 cm^{-1}, and asymmetrical stretching with a main maximum at ~1070 cm^{-1} [71].

In amorphous systems, each of these modes still exhibits 2 contributions: corresponding TO and LO branches, where the LO modes generally shift to higher frequencies due to additional restoring forces along the direction of wave propagation. This splitting is evident in more detailed analyses of energy-loss functions, emphasizing the role of phonon dispersion in silica glass.

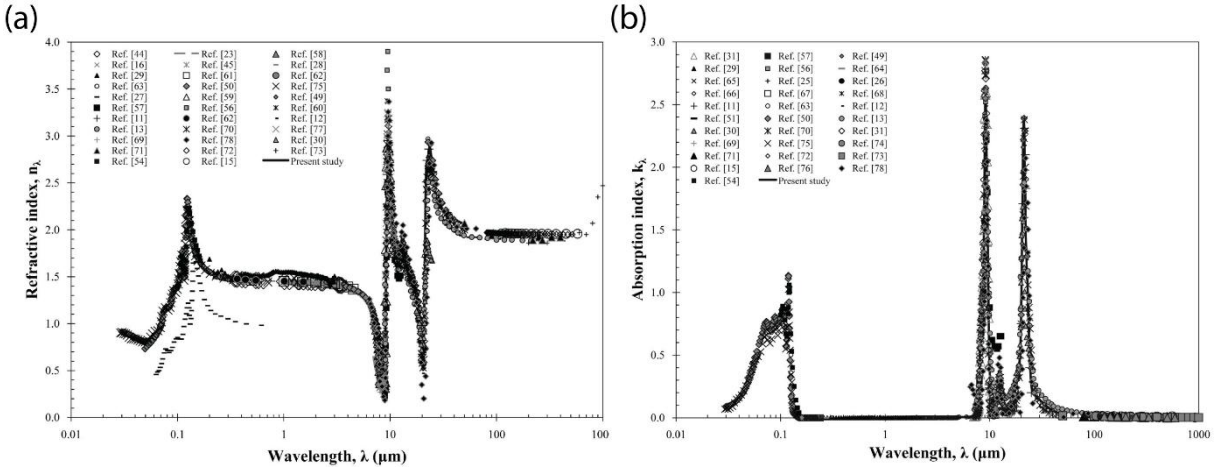

Figure 11. Real n' (a) and imaginary n'' (b) parts of the complex refractive index of silica glass over a broad spectral range, compiled from various experimental studies as reported in [72].

In addition to the IR absorption from vibrational transitions, silica glass also shows significant absorption in the ultraviolet (UV) region due to electronic transitions across its wide bandgap. The optical bandgap of amorphous SiO_2 is typically around 8–9 eV, corresponding to wavelengths below about 150–160 nm [63,72]. As a result, while silica glass is highly transparent in the visible and near-IR regions, its transmittance drops sharply in the vacuum-UV (so-called VUV) due to these electronic absorption processes. To illustrate the full spectral behavior of silica glass, Figure 11, from [72], presents the refractive index (n') and absorption index (n'') over a wide wavelength range, summarizing data from multiple experimental studies.

I.3.3 Vibrational spectroscopy of silica glass

I.3.3.1 IR spectroscopy of silica glass

Taking all the points discussed above into account, we see that IR spectroscopy is a powerful tool for probing the vibrational signature of silica glass, offering valuable insights into its short-range atomic order and the structure of its amorphous network. Early IR studies of glasses often relied on transmission measurements of powdered samples dispersed in alkali halide pellets. However, this approach was sensitive to artifacts such as ion exchange, hydrolysis, and spectral distortions [68]. So, the measured phonon frequency often deviated from the expected IR-active TO mode and instead appeared intermediate between the TO and LO vibrational modes [71]. Alternatively, samples had to be extremely thin (sometimes below 10 μm) to obtain reliable transmission data. These limitations were overcome with the advent of IR reflectance spectroscopy, which enables direct analysis of polished bulk samples without inducing structural alterations [68,70]. As a result, accurate mid- to far-infrared spectra can be obtained. Notably, the absorption band near 1100 cm^{-1} and the reflection band near 1120 cm^{-1} are both coming from the asymmetric stretching vibration of the Si-O bond and can be converted from one to another using the Kramers-Kronig transformation [73].

A typical IR reflection spectrum of silica glass can be seen in Figure 12. IR reflection spectroscopy of silica glass reveals a broad spectral feature in the 100-1500 cm^{-1} region. As mentioned earlier, there are three distinct bands reflected in the IR spectra of silica glass: rocking vibration at **480 cm^{-1}**, symmetrical stretching vibration at **790 cm^{-1}**, and asymmetrical stretching vibration with a main maximum at typically **1100-1130 cm^{-1}** [71,74,75], which is often accompanied by a shoulder around 1200 cm^{-1}; the main peak is generally attributed to the TO mode, while the shoulder reflects the LO component arising from Coulomb interactions [70].

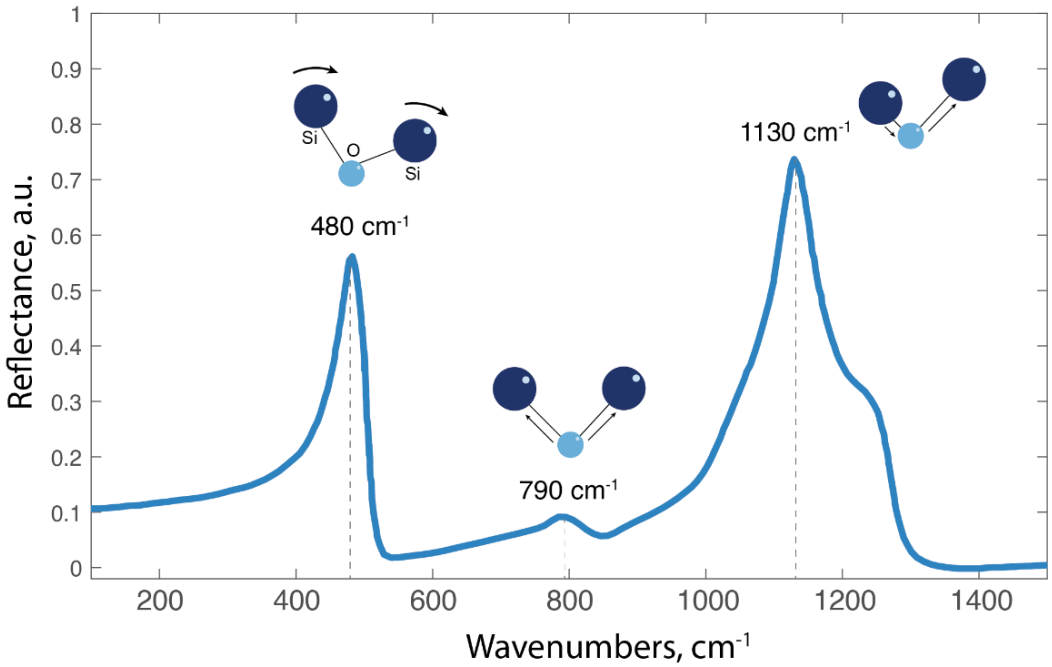

Figure 12. Typical IR reflection spectrum of pure silica glass and main vibrational modes in IR. Data for the spectrum was taken from [68]

The asymmetric stretching vibration of the Si-O-Si bond ($\boldsymbol{\nu_{as}^{Si-O-Si}}$) is the most prominent and structurally significant feature in the IR spectrum of silica glass. This key band is highly sensitive to the changes in the average Si-O-Si bond angle [73,76] and serves as an excellent probe of the local atomic arrangement. More specifically, the band shifts to higher frequencies with an increase in the average Si-O-Si bond angle in the glass structure [77,78]. In both pure and doped silica glasses, an increase in fictive temperature, accompanied by densification, produces a clear shift toward lower wavenumbers in the IR absorption peak tied to this asymmetric stretching vibration, and this shift provides a practical means of building calibration curves that connect the peak position to the glass's thermal history (i.e., the fictive temperature) [75,79,80].

I.3.3.2 Raman spectroscopy of silica glass

Raman spectroscopy is another powerful analytical technique for examining the structural properties of materials, including silica glass. In this method, a monochromatic laser beam excites vibrational modes within the sample. The inelastic scattered light having a positive or negative frequency shift (anti-Stokes or Stokes Raman shift) tells us about the material's vibrational "fingerprint" [81]. In Raman spectroscopy, each band is characterized by its position (it correlates with specific vibrational modes), full width at half maximum measured (FWHM) (usually related to an inhomogeneous broadening indicative of structural and chemical disorder), and intensity or integrated area, which tells about population-weighted contribution of a vibrational mode. Together, these characteristics give information about the local-to-

medium-range order of the material.

A typical Raman spectrum of pristine silica glass (Figure 13) shows seven main bands relative to different vibrational modes.

Around **50-100 cm^{-1}** (not visible here), the boson peak is located, which is a universal feature of disordered glasses. The origin of the boson peak in silica glass is attributed to the partial destruction of acoustic plane waves at nanometer wavelengths, leading to an excess of low-frequency vibrational modes, particularly hybrid vibrations that combine the rocking and shifting of rigid SiO_4 tetrahedra. These modes appear near the Ioffe-Regel crossover frequency, where sound waves lose their ability to travel as coherent plane waves [82].

At around **440 cm^{-1}**, the main Raman band is generally associated with oxygen motion within the SiO_2 tetrahedral network [83]. More specifically, it corresponds to the bending vibration of the Si–O–Si bond, with oxygen atoms moving perpendicular to the Si–Si axis [76]. This vibrational mode primarily arises from atomic movements in rings composed of five or more SiO_2 tetrahedral units, effectively representing a superposition of modes from larger ring structures [76,84].

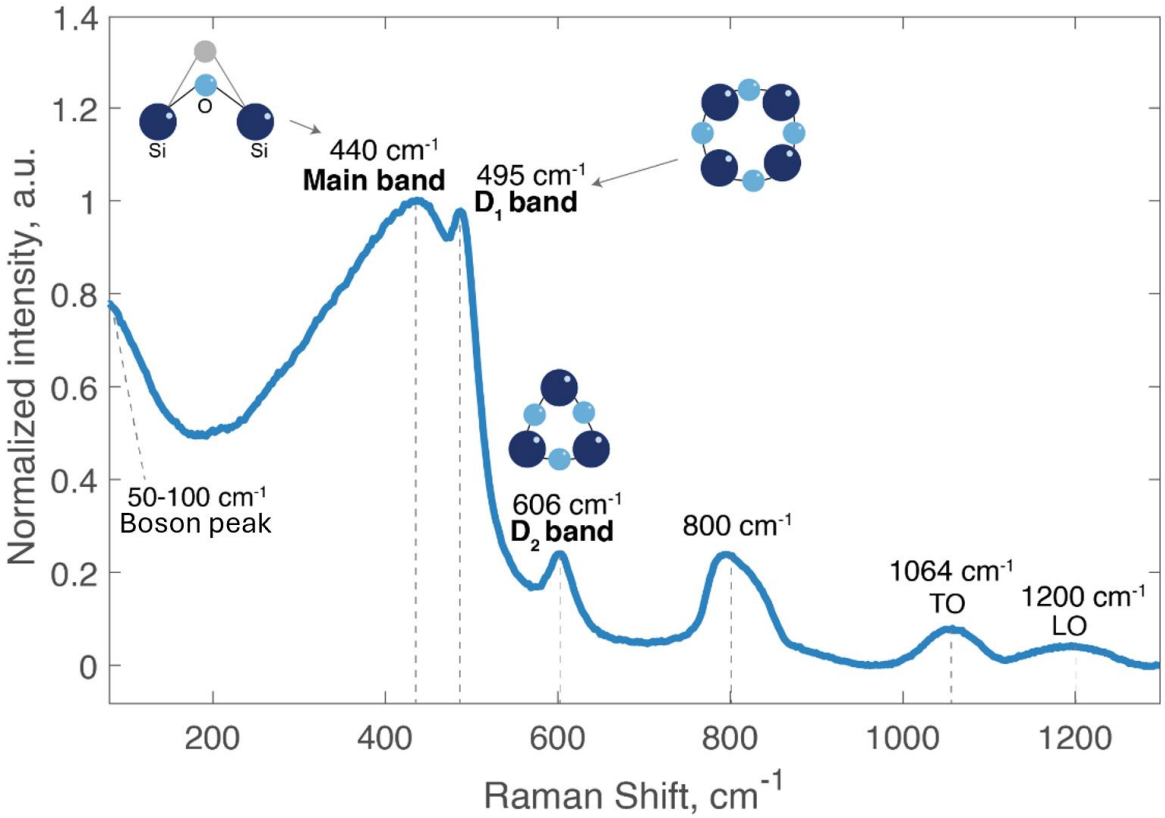

Figure 13. Typical Raman spectrum of pure silica glass and main vibrational modes.

Bands near **495 cm^{-1} and 606 cm^{-1}** are associated with the "breathing" motions of oxygen atoms in silica ring structures [81,85,86]. The band around 495 cm^{-1}, known as the D_1 band, arises from the oxygen atoms "breathing" in four-membered rings. The band near 606 cm^{-1}, referred to as the D_2 band, is attributed to planar three-membered rings [85,87]. These assignments are supported, for example, by observations in the silica polymorph coesite, where a closely related peak near 500 cm^{-1} is present due to its structure being predominantly composed of four-membered rings [88]. The validation also comes from vibrational simulations and molecular dynamics studies [86,89].

The band near **800 cm^{-1}** band is attributed to a symmetric stretching motion of the bridging oxygen atom with a significant displacement of the Si atom [76,86].

Finally, Raman peaks at **1064 and 1200 cm^{-1}** are attributed to Si–O stretching motions [70,81]. When a vibration is both Raman and IR active, it is polar and can undergo LO and TO splitting due to Coulomb interactions. This effect results in the observed doublet at 1064 and 1200 cm^{-1} [71].

I.3.4 Lorentz–Lorenz equation and density

While IR and Raman spectroscopy provide insights into the vibrational properties, structure, and connection to density in silica glass, the refractive index can also serve as an indicator of density changes. The refractive index n of a medium is linked to its density through the Lorentz–Lorenz equation [90], which is derived from the Clausius–Mossotti relation. One common form of the equation is:

$$\frac{n^2-1}{n^2+2} = \frac{N\boldsymbol{\alpha}}{3\boldsymbol{\varepsilon}_0} = \frac{4\boldsymbol{\pi}}{3}\frac{\boldsymbol{\alpha}}{V}, \tag{17}$$

Where N is the number density, α is the molecular polarizability, ε_0 is the vacuum permittivity, and V is the molecular volume.

By differentiating this relation, we obtain an expression for the relative change in the refractive index Δn in terms of the relative changes in polarizability and molecular vo--lume:

$$\frac{\boldsymbol{\Delta} n}{n} = \frac{(n^2-1)(n^2+2)}{6n^2}\left(\frac{\boldsymbol{\Delta\alpha}}{\boldsymbol{\alpha}} - \frac{\boldsymbol{\Delta} V}{V}\right). \tag{18}$$

Defining the parameter

$$\boldsymbol{\Omega} = \frac{\boldsymbol{\Delta\alpha}/\boldsymbol{\alpha}}{\boldsymbol{\Delta} V/V},$$

the above expression can be rearranged as:

$$\boldsymbol{\Delta} n = \frac{(n^2-1)(n^2+2)}{6n}(\boldsymbol{\Omega}-1)\frac{\boldsymbol{\Delta} V}{V} = \frac{(n^2-1)(n^2+2)}{6n}(\boldsymbol{\Omega}-1)\frac{\boldsymbol{\Delta}\rho}{\rho}. \tag{19}$$

This equation shows that, for small deformations, the change in refractive index is directly related to both the fractional change in molecular volume and density. In cases such as isotropic densification, the refractive index increases if the polarizability does not decrease proportionally (i.e., when $\Omega < 1$).

Empirically, the actual change in polarizability with compaction is determined by matching equation 19 to experimental data. For example, thermal and pressure treatments give $\Omega \approx 0.19$ [78], while UV-irradiated samples produce $\Omega \approx 0.23$ [91]. Similar values of about 0.22 and 0.23 have been reported for γ-irradiated [92] and neutron-irradiated [6] glasses, respectively. Higher values of Ω correspond to smaller refractive index changes per unit densification. Figure 14 illustrates how the refractive index evolves with density for these experimentally derived Ω values, alongside the theoretical predictions evaluated at a wavelength of 632 nm.

Using Equation 19 and n=1.459 for silica in the green-light range gives the relationship $dn = 0.43\, d\rho/\rho$, which aligns well with the slope $dn = 0.44\, d\rho/\rho$ from Figure 2 (Section I.2.1) with the refractive indices of various silica polymorphs against their densities.

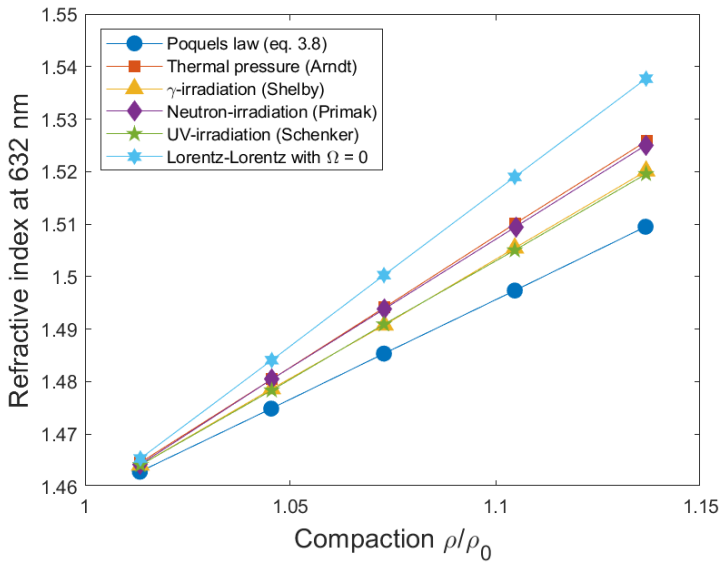

Figure 14. Comparison of the densification data for different experimental methods: thermal and pressure [78], UV-irradiated [91], γ-irradiated [92], neutron-irradiated [6]. Adopted from PhD thesis of F. Durr [93].

I.4 THERMOMECHANICAL BEHAVIOR AND DENSIFICATION OF SILICA GLASS

Silica glass is known for its exceptional qualities, which largely come from its high purity and strong bonding. Its resistance to common chemicals is accompanied by a high softening point, minimal thermal expansion, high thermal shock resistance, and notable optical clarity over a wide spectrum, as was mentioned earlier. Nevertheless, silica glass also exhibits several unusual behaviors [94]. For example, its thermal

expansion coefficient is negative below approximately 80 to 100 °C, while it remains positive at higher temperatures [33]. Unlike most glasses, its equilibrium density decreases following heat treatment within the transformation range, and its elastic moduli increase above 190 °C [94]. Additional anomalous characteristics will be discussed alongside other property descriptions. This section examines how the glass structure influences its overall thermomechanical behavior.

I.4.1 Thermomechanical properties of silica glass

Silica, like all glasses, is an amorphous solid that exhibits a glass transition at dedicated temperature called the glass transition temperature (T_g). The glass transition is a gradual process in which the atomic motion within the liquid progressively slows upon cooling, forming a solid-like state. However, this state preserves the structural disorder of the original liquid, preventing crystallization due to fast cooling [95]. Above T_g, the glass can be shaped or annealed to relieve internal stresses, whereas below T_g, its rigid structure maintains stability and resistance to deformation. The cooling rate strongly affects T_g, with rapid cooling ("quenching") leading to higher observed transition temperatures compared to slower cooling. Natural silica glasses tend to exhibit T_g values around 1200 °C, whereas many synthetic variants present slightly lower T_g values of approximately 1100 °C. This difference is primarily attributed to changes in water and hydroxyl group content; higher levels of these components, as found in type III silica glasses, reduce the viscosity and enhance molecular mobility, thereby shifting T_g to lower temperatures [62].

Viscosity characterizes a fluid's internal resistance to flow, where with greater viscosity the flow slows down. Small amounts of dopants or impurities disrupt the Si–O–Si network and thereby lower viscosity. The viscosity of silica glass is similarly sensitive not only to the chemical composition but also to the glass thermal history, thus its fictive temperature. Thermal history, in turn, influences the fictive temperature (T_f), defined as the temperature at which a given glass structure would be in equilibrium if rapidly heated or cooled to that temperature [95]. By knowing both the actual temperature (at the moment) and the glass fictive temperature it is possible to accurately describe the glassy state. For instance, one study notes that a silica sample with a fictive temperature of 1400 °C exhibits a viscosity of approximately 1 TPa·s at 1700 °C, whereas a similar sample with a fictive temperature closer to 1000 °C reaches the same viscosity at around 1320 °C [33].

When the glass is densified at high temperature and pressure, however, the fictive temperature alone does not fully account for the structure. In such cases, an additional order parameter, fictive pressure P_f, is needed. When a silica glass is pressurized at a temperature below its glass transition temperature for a sufficiently long time, subse-

quently cooled under pressure, and then depressurized at room temperature, the structure "freezes in" not only the treatment temperature but also the treatment pressure [80,96].

Below T_g, the high viscosity of silica glass strengthens its structural stability and shapes how it responds to mechanical stress. Main elastic properties such as Young's modulus, the shear modulus, and Poisson's ratio define this response. At 25 °C, vitreous silica commonly displays a Young's modulus of around 73 GPa, a shear modulus near 31 GPa, and a Poisson's ratio of about 0.17. Deviations can arise due to density variations (as will be discussed further), as a higher density slightly reduces the elastic modulus and increases the Poisson's ratio [62]. Uniquely among many glass types, the elastic moduli of vitreous silica actually rise with temperature, peaking around 1100–1200 °C, where they can exceed room-temperature values by approximately 10% [94,97].

In addition, silica glass features a notably low coefficient of thermal expansion (CTE) - approximately $0.55 \times 10^{-6}\,K^{-1}$ near room temperature, which grants its high dimensional stability during heating and cooling. Manufacturers typically cite linear expansion coefficients within the 0-300 °C range of about $5.4 \times 10^{-7}\,K^{-1}$ to $5.6 \times 10^{-7}\,K^{-1}$ [33]. Thermal history also further influences the thermal expansion behavior: samples equilibrated at different fictive temperatures and then quenched in water show that lower fictive temperatures increase negative thermal expansion [33]. As the fictive temperature rises, the structure becomes more densified, causing a correspondingly lighter thermal response.

The density of transparent vitreous silica is approximately 2.20 g/cm^3, making it lower than those crystalline phases of silicon dioxide, such as quartz (2.65 g/cm^3) [33]. The density of silica glass varies depending on its hydroxyl content and fictive temperature, with higher hydroxyl concentrations and lower fictive temperatures generally leading to a decrease in density [98]. Despite sharing the same short-range bonding structure as its crystalline phases, silica glass possesses a significant amount of interstitial volume, allowing for densification under specific conditions.

I.4.2 Silica glass densification

Numerous studies have investigated the high-pressure behavior of silica glass, revealing that its response and degree of compaction depend on temperature, pressure, and the duration of these conditions [1].

I.4.2.1 Cold compression

At room temperature and within lower pressure ranges (up to 6-10 GPa), silica glass primarily exhibits elastic behavior, meaning that any deformation remains fully reversible [99,100]. Notably, its elastic moduli (Young's modulus, the bulk modulus, and the

shear modulus) initially decreases with pressure up to approximately 2-4 GPa before increasing at higher pressures [101,102].

At higher pressures (8-9 GPa at room temperature), silica glass undergoes permanent deformation. Initially discovered by compressing thin glass discs between cobalt-tungsten alloy plates under quasi-static loading [103], this phenomenon, called densification, demonstrates a permanent increase in density after pressure exceeds a threshold. Studies using both uniaxial and hydrostatic compression via diamond anvil cells (DAC) have shown that the densification rate increases with pressure until a second, saturation threshold is reached, at which point the glass reverts to elastic behaviour [104].

Under room temperature conditions, this "cold compression" of silica glass leads to an irreversible polyamorphic transition above 8-9 GPa (first threshold) [99], with maximum densification of approximately 21% after compression at 20-25 GPa (second threshold) [102,104] resulting in a density of about 2.65 g/cm^3 [1,105,106] (Figure 15). This effect is attributed to the closure of free volumes as atomic structures rearrange to optimize packing [1], achieving a volume similar to that of crystalline quartz while remaining amorphous.

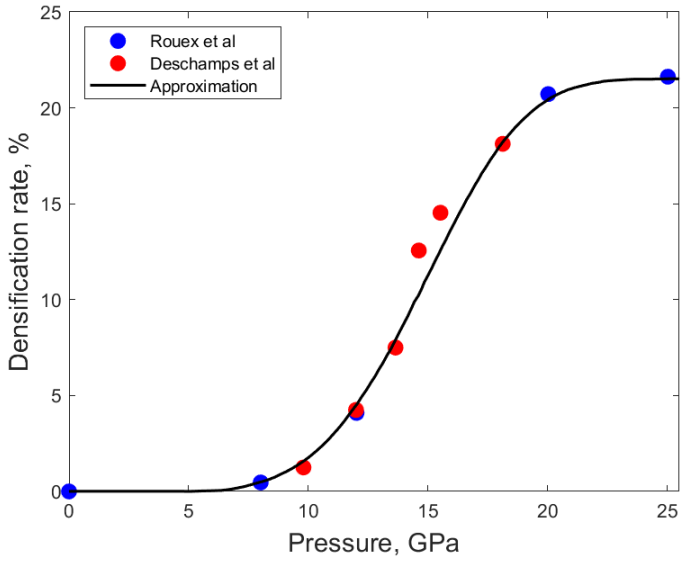

Figure 15. Densification rate as a function of pressure during cold compression of silica glass. Data from [105,106]. Adopted from PhD thesis of C. Dereure [107].

I.4.2.2 High Pressure High Temperature densification (hot compression)

Because glass is often considered as a frozen liquid due to its high viscosity, temperature has a significant influence on both its structure and behavior, especially near the glass transition. As temperature rises, the increased atomic mobility facilitates structural rearrangements under pressure. As a result, significant densification can be realized at lower pressures when conducted at higher temperatures [3,108–110], a process

referred to as "hot-compression" or High-Pressure, High-Temperature (HPHT) densification. This effect is clearly illustrated in Figure 16, which shows the densification of silica glass as a function of quench pressure at different temperatures.

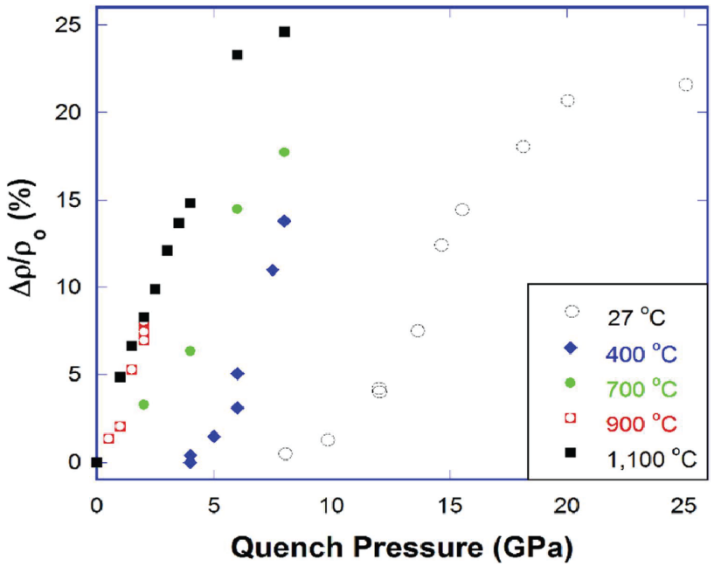

Figure 16. Density changes in silica glass as a function of quench pressure at various temperatures. Cited from [108].

One of the earliest demonstrations of this effect was reported by Mackenzie [1], who showed that raising the temperature while applying high pressure notably enhances the densification of silica glass, indicating that thermal energy plays an important part in enabling structural rearrangements. Although pressure and shear remain essential factors, added thermal energy increases atomic mobility within the glass network, thereby promoting more efficient shear-induced compaction.

MacKenzie [1] also has demonstrated that the application of shear stress during compression promotes a higher densification rate for a given hydrostatic pressure. The experiments were conducted using compression cells with different pressure-transmitting media (alumina and silver chloride). The alumina cell generates more shear than the silver chloride one. Under two different pressure-temperature conditions (6 GPa at 400 °C for the alumina cell and 8 GPa at 300 °C for the silver chloride cell), the densification rate in the alumina setup was found to be twice as high as that in the silver chloride cell. A comparable effect is observed when comparing different compression setups. For instance, DAC generally induces less shear than Belt press, so Belt press can achieve higher densification rates under equivalent pressure-temperature conditions.

Guerette et al. [3,108] subjected silica glass samples to hot compression at 1100 °C with pressures up to 8 GPa, achieving an approximately 25 % increase in density compared to the pristine silica glass. The resulting structural characteristics differed considerably

from those produced by cold compression alone, highlighting the distinct effects of elevated temperature on densification pathways.

Similarly, Martinet et al. [109] compared silica samples subjected to both cold compression (10–26 GPa at room temperature) and compression at temperatures up to 1020 °C. They found that a density of 2.5 g/cm³ required only 5 GPa and 750 °C under hot-compression conditions, while cold compression demanded pressures of about 16 GPa to reach the same density.

Concerning the structure, Zanatta et al. [111] demonstrated that silica densified under HPHT conditions retains its short-range tetrahedral units while undergoing significant medium-range structural evolution. Their positron annihilation lifetime spectroscopy data suggest that interstitial free volume reduction, rather than coordination change, dominates the densification process. It has been shown that the density changes from about 2.2 g/cm^3 to 2.67 g/cm^3 lead to a decrease in void volume from 60 Å^3 to 10-15 Å^3. However, short-range structure is also affected by the densification. Devine et al. [112], using electron spin resonance hyperfine splitting from E′ centers, observed that a 24 % increase in density is accompanied by about a 5° reduction in Si-O-Si bridging angles around defect sites, as well as a small but measurable increase in Si-O bond lengths (from 1.618 to 1.623 Å).

I.4.2.3 Structural differences between silica glass densified with CC and HPHT conditions

Although silica glass can reach similar density levels through both CC and HPHT compression, their resulting structures differ in slight yet significant ways [108–110]. One of the most direct indicators of these differences lies in the Raman spectra. Shifts, FWHM, and intensity of the main band and D_1 and D_2 bands reflect variations in ring configurations, bond angles, and overall network strain [84,108,109].

As an example, Figure 17 presents the Raman spectra of samples with similar densities (2.3 g/cm^3 on Figure 17a and 2.5 g/cm^3 on Figure 17 b) obtained under HPHT conditions using a Belt Press and under CC conditions using DAC.

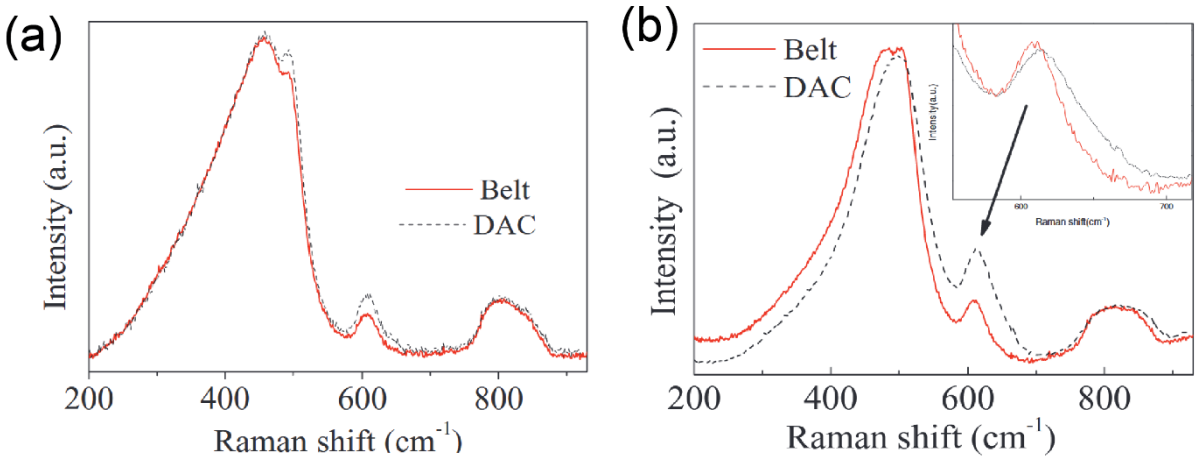

Figure 17. Raman spectra of silica glass densified to similar densities: (a) 2.3 g/cm^3 and (b) 2.5 g/cm^3, obtained by Belt Press (HPHT) and Diamond Anvil Cell (CC). Cited from [109].

Under HPHT conditions, the main Raman band narrows and shifts to approximately 495 cm^{-1} with increasing quench pressure, indicating a reduction in the mean Si–O–Si bond angle and a more constrained angular distribution [108,109,113]. For 20% densification, simulations suggest that the Si–O–Si angle decreases by approximately 4° to 5° [84]. Although cold-compressed samples also exhibit a band shift toward higher frequencies (up to 530 cm^{-1}), the shift per unit density is more pronounced for CC than for HPHT [108], as clearly seen in Figure 13b. This observation points to a more strained framework in room-temperature compactions, as there is less capacity for the glass network to reorganize and relieve stress [1,84,108,109].

Furthermore, both cold and hot compression lead the D_1 peak to shift to higher frequencies, likely due to slight deformation of the ring structures [108]. In cold-compressed silica, however, the D_1 line merges with the main band once the density exceeds about 2.45-2.50 g/cm^3 [106,109,114]. In contrast, HPHT compression generally shows a smaller shift of the D_1 band position, and it does not merge that distinctly with the main band [108,113]. The fact that the D_1 band partially overlaps with the main band without significantly broadening suggests that the 4-membered rings breathing vibrations remain somewhat independent from the rest of the network [84].

The D_2 band also shifts to higher frequencies under both CC and HPHT densification [108,109]. However, the intensity of the band grows more quickly in CC samples [109]. Cold-compressed silica can exhibit nearly triple the intensity of the D_2 band compared to similarly dense HPHT samples (Figure 17 b), reflecting the minimal opportunity for structural relaxation at room temperature [109]. Correspondingly, D_2 band broadening is more pronounced after CC, implying more deformation and bond-angle dispersion within the three-membered rings. Under HPHT conditions, the D_2 line area remains essentially unaffected by density increases, and the intensity stays close to that observed in pristine silica glass [109]. This happens due to higher temperatures facilitating structural rearrangements that limit the formation of highly strained rings

[84,109]. Additionally, the intensity of the D_2 band in pure silica glass has been found to increase with rising fictive temperature, which in turn leads to higher density [79,115]. It has been suggested that fictive temperature may be a more suitable variable for describing variations in the D_2 band, rather than density alone [114]. However, as was mentioned in Section I.4.1, for the densified under pressure glasses, one must also consider the fictive pressure parameter.

Even though the D_2 band is associated with the most compact silica network structure of 3-membered rings, a lower D_2 intensity does not necessarily indicate a lower density. As one study suggests [116], two 6-membered rings could transform into one 3-membered ring and one 9-membered ring. While the 3-membered ring suggests a more compact local configuration, the larger 9-membered ring introduces additional free volume that can lead to expansion. In other words, creating 3-membered rings may simultaneously generate voids, making difficult the direct relationship between D_2 intensity and overall density. Furthermore, the D_2 band exhibits an anomalous response during thermal annealing, initially increasing and only then decreasing through relaxation processes [3,21,116–118]. This behavior, which will be discussed in the following section, supports the idea that a higher D_2 intensity does not directly equate to a higher density. In this regard, a concept known as "topological pruning" can be discussed, where applying sufficient pressure and temperature removes small, unstable rings and larger voids from the silica network. Recent experiments by Ono et al. [119] show that hot-compressed silica around ~1 GPa and 1800 °C undergoes a "pruning" of its mid-range structure, with 3-membered rings and large voids collapsing simultaneously. This transformation significantly lowers the D_2 band intensity (and thereby Rayleigh scattering) without necessarily producing a proportional increase in overall density.

Beyond local structural distinctions, CC and HPHT densified silica also exhibit evident differences in their intermediate-range order. In HPHT densified silica, the first sharp diffraction peak (FSDP) appears both narrower and more intense than in CC sample with same density [108]. This suggests a more homogeneous network arrangement for HPHT silica, showing again how high temperatures produce a more uniform reconfiguration of the silicate network compared to the relatively heterogeneous structure formed during room-temperature compression [113]. According to Onodera et al. [110], CC and HPHT silica glasses show different structures, with the correlation length for the HPHT sample being approximately 60% longer than that of the CC one. This indicates a more extended ordering of tetrahedral SiO_4 units in the HPHT glass.

Furthermore, CC and HPHT densified samples can have differences in mechanical properties. For instance, at same density increases of 15 %, HPHT densified silica typically exhibits a higher bulk modulus than CC silica (Figure 18). For HPHT conditions from 0 to 8 GPa, the Young's modulus of silica glass rises from 72 to 123 GPa (a 71 % increase), and the shear modulus grows from 32 to 50 GPa (61 %), well outpacing the roughly

25 % increase in density. Such findings confirm that elevated temperatures not only promote a more uniform structural reorganization but also enhance the overall stiffness of the resulting densified glass [108].

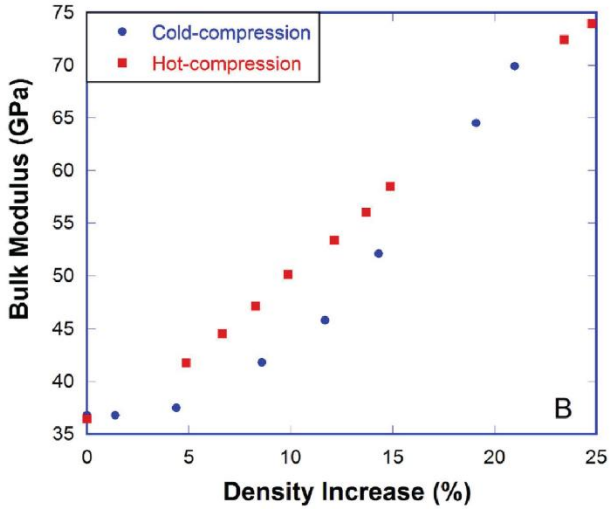

Figure 18. Bulk modulus as a function of density increase of silica glass from CC and HPHT densification. Cited from [108].

I.4.2.4 Shock-wave densification

Another way to densify silica glass is through shock wave interaction, which leads to structural differences due to a distinct compression mechanism. Shock wave densification occurs when high-velocity impacts or explosions generate supersonic pressure waves propagating in the material and causing rapid and extreme compression. During this process, both pressure and temperature rise sharply, creating a transient high-pressure, high-temperature state. Unlike static compression, the shock wave induces a non-equilibrium state, where the material undergoes rapid densification. After the shock passes, the material experiences thermal relaxation as the elevated temperature persists for a short period, enabling further structural reorganization and, in many cases, permanent densification.

The shock compression behaviour of fused silica is typically characterised by three distinct pressure regimes [120]. Initially, an elastic regime is observed, extending up to approximately 8-9 GPa. Following this, a highly compressible region, spanning roughly 10 to 35 GPa, is encountered and is notable for substantial densification of the glass. Within this region, studies indicate that the degree of densification generally increases with escalating shock pressures, often reaching a maximum at a certain pressure before potentially declining at even higher pressures due to the influence of post-shock residual temperatures (up to 8000 K [121]) causing partial annealing [120,122]. This trend is presented on Figure 19.

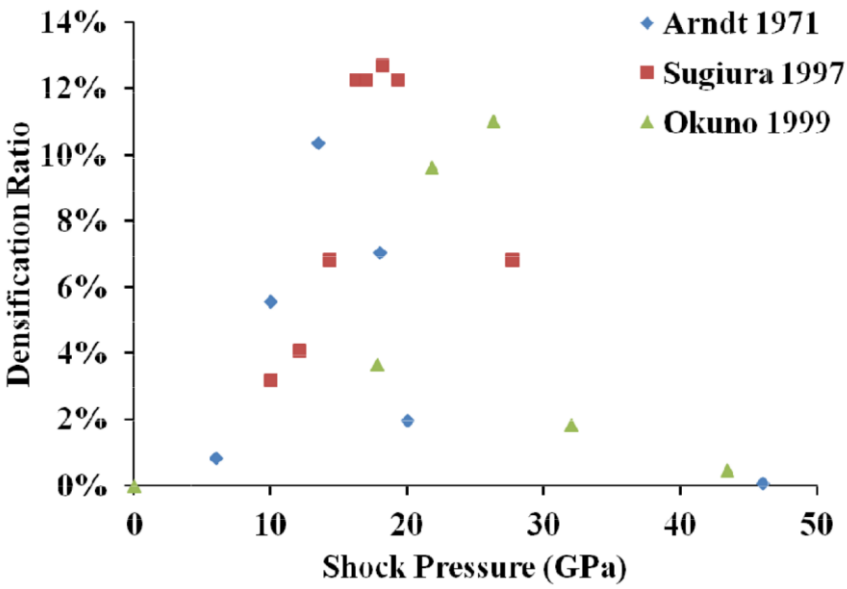

Figure 19. Densification rate of silica after shock impact as a function of shock pressure. Extracted from PhD thesis of C. Dereure [107], data based on [2,122,123].

Although the dynamics of the densification are different, structurally, the densification is similar to HPHT densified silica glass. Densification under shock load is attributed to structural rearrangements within the silica network, involving a reduction in the average Si-O-Si bond angle and modifications in the population and small and medium-sized rings [122]. Beyond the highly compressible region, above approximately 35 GPa, there is a transition to a dense, low compressibility phase. In situ X-ray diffraction studies have identified this high-pressure phase could be polycrystalline stishovite, a denser crystalline form of SiO_2 [120].

Researchers also use laser-induced shocks as another method to generate the high pressures and loading conditions comparable to hypervelocity impacts, offering the advantage of enabling the recovery of samples for detailed post-mortem analysis of the resulting damage and structural modifications [124,125]. For example, a study on fs-laser densification used effects of shock waves generated by two spatially separated focused beams, acting as quasi-simultaneous "pressure-wave emitters" [125].

I.4.2.5 Optical properties of densified silica glass

Optical properties of densified silica glass undergo systematic modifications as the structure compacts [78]. One of the most notable effects is the linear increase in refractive index with density (Figure 20 a), which is directly linked to changes in the mean polarizability of the glass network. As the glass densifies, the refractive index measured at the sodium D-line (589.3 nm) increases proportionally with density.

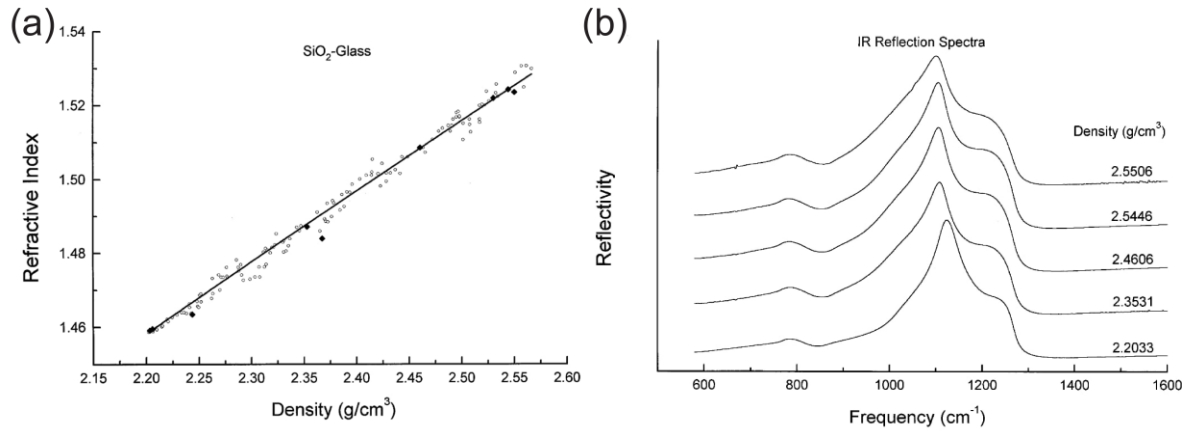

Figure 20. (a) Relationship between density and refractive index (at 589.3 nm) of silica glasses. (b) IR reflection spectra of the silica glasses with different densities. Adopted from [78].

IR spectroscopy further illustrates the structural changes caused by densification (Figure 20 b). In densified silica glasses, the main IR band near 1100 cm^{-1}, associated with the asymmetric stretching of the Si–O–Si bridges (as was reviewed in section I.3.3.1), shifts linearly to lower frequencies as density increases. This behaviour is quantitatively expressed by the following correlations:

$$\nu_R = (1332 \pm 13) - (95 \pm 5)\rho \quad (17)$$

for the reflectance spectra, and

$$\nu_A = (1270 \pm 16) - (74 \pm 7)\rho \quad (18)$$

for absorption spectra.

Here, ν_R and ν_A represent the resonance frequencies (in cm^{-1}) obtained from IR reflection and absorption measurements, respectively, while ρ is the glass density. The negative slopes of these equations indicate that as the glass becomes denser, the vibrational frequency of the Si-O-Si bonds decreases. Owing to its sensitivity to structural changes and density, the position of the Si-O asymmetric stretching band is also widely used to monitor the fictive temperature (T_f) in silica glasses and optical fibers [73,75,79].

I.4.2.6 Thermal relaxation of densified silica glass

It is important to study how densified silica glass behaves when subjected to heat treatment, so, during thermal relaxation. In glassy systems, relaxation is a fundamental process through which the material evolves toward an equilibrium state. Thermal relaxation can reveal the reverse transformation (opposite effect to the densification), providing a valuable perspective on the mechanisms behind structural rearrangements [116]. It is also crucial from an industrial point of view, as understanding how densified silica glass relaxes under working temperatures can provide the design of reliable, stable glass components. The relaxation of densified silica glass is, however, far from

straightforward. It strongly depends on factors such as the compression pathway, the initial density reached during densification, and the subsequent annealing temperature [3,126].

The density of densified silica glass decreases monotonically during thermal relaxation [127]. This decrease in density is consistent with observations from FSDP measurements, which indicate an increase in the characteristic distance of the intermediate-range order during relaxation [116]. However, the underlying structural changes relax in a more complicated way. For example, Arndt et al. observed non-monotonous behavior in the refractive index of densified silica during annealing at 600-800°C [127]. This indicates that macroscopic density measurements alone cannot fully capture or represent the complexity of the relaxed glass network [117]. For example, as discussed in the previous section, CC and HPHT silica glasses can have the same densities but exhibit distinct Raman spectral signatures.

There is also an anomalous behavior during thermal relaxation involving the Raman D_2 band. It was found that, counterintuitively, D_2 intensity initially increases before eventually decreasing as the glass relaxes [3,116–118]. This short rise points to a transitory structural state, wherein 3-membered rings temporarily appear more prior to the network's eventual return toward its low-density configuration. Such behavior indicates the polyamorphism of silica glass.

HPHT compressed silica has higher thermal stability than samples produced via cold compression. In particular, HPHT silica maintains its densified structure at significantly higher temperatures (up to 650–700 °C), as confirmed by in-situ Brillouin scattering experiments [108]. In contrast, cold-compressed silica begins structural relaxation at lower temperatures (100–150 °C), indicating a lower stability of its network and the presence of the internal stresses. Cornet et al. [117] estimated the activation energy for relaxation in HPHT silica as 255 ± 45 kJ/mol (around 289 ± 21 kJ/mol, according to Höfler et al. [126]), while for CC silica suggested values were centered around 145 kJ/mol.

I.4.2.7 Silica polyamorphism

In general, polyamorphism refers to the phenomenon where a material can exist in two or more distinct amorphous phases, with the potential for transitions between them. This concept was initially introduced to explain the negative melting slope observed in water and extended to the glassy state of water, leading to the identification of three different amorphous forms of ice [128,129].

Early research on polyamorphism in silica glass mentioned its occurrence in compressed silica glass. Grimsditch et al. in 1980s first mentioned another 'amorphous polymorph' after observing irreversible structural changes in silica glass subjected to plastic compression at a pressure of 17 GPa [130]. Nowadays, polyamorphism in silica glass is typically discussed in terms of transitions between Low-Density Amorphous (LDA) and High-Density Amorphous (HDA) forms, each characterized by distinct ring topologies, density, and stability [3,102,116,117,131]. A helpful way to visualize these transformations is using the potential energy landscape, which depicts the possible configurational states available to a system and the energy barriers separating them (Figure 21). For silica glass, the potential energy landscape is hypothesized to feature multiple "megabasins," each corresponding to a separate amorphous structure [3,131].

For pressures near ambient, the most stable minimum is associated with LDA silica. Under higher pressures, the glass can enter basins corresponding to HDA states. As was discussed earlier, depending on the compression pathway, HDA silica can be obtained through CC, resulting in c-HDA, or through HPHT, making h-HDA. Because silica's densification pathways are highly sensitive to conditions such as shear stress, compression rate, and temperature, numerous metastable HDA states may appear in experiments [3]. It has also been suggested that silica glass under pressure can consist of coexisting LDA and HDA domains, with their relative proportions depending directly on the maximum pressure and conditions applied during densification [102].

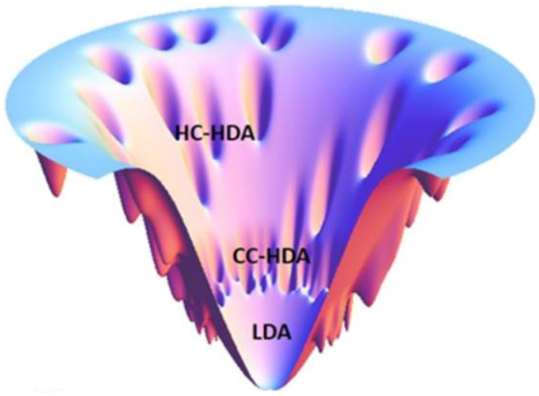

Figure 21. Schematic potential energy landscape for amorphous silica. Cited from [3].

Thermal relaxation is a way to observe the reverse transitions from HDA to LDA. The fact that HPHT silica is more thermally stable than CC silica indicates that h-HDA has higher energy barriers needed to overcome to revert fully to LDA [3]. In CC samples, relatively low thermal energy near room temperature is often enough to start reverting the network to LDA. Notably, HDA to LDA transitions occur continuously without cracking or loss of mechanical integrity, showing the gradual nature of the structural relaxation [3]. One of the examples of amorphous-amorphous transition during thermal relaxation is, how was mentioned earlier, unexpected D_2 band intensity increase (so the

increase in 3-membered ring number) during isothermal annealing of compacted silica under both conditions (CC and HPHT) shown by Cornet et al. [117], whereas density decreases. In their following study [116], they further investigated this question and, using in situ X-ray scattering studies, have revealed that during thermal annealing, densified silica glass passes through a transient, disordered state. This state is characterized by a pronounced maximum in structural heterogeneities, shown by peaks in the FSDP width and SAXS intensity, which indicates the transition between HDA and LDA forms. The transient state represents an activated passage between the HDA and LDA megabasins, requiring the system to overcome significant energy barriers.

Recent experiments on pre-densified silica (by HPHT) by Courtois et al. [131] showed that the elastic limit is directly linked to glass density, rather than to the thermomechanical history used to achieve this density. In other words, silica glasses with similar densities have identical elastic limits, regardless of whether densification occurred with CC or by HPHT. They report elastic limits of approximately 14.4 GPa and 16.5 GPa for silica glasses HPHT pre-densified by ~10% and ~16%, respectively. This closely matches the elastic limits observed for similarly dense CC silica glasses (about 14 GPa and 16.2 GPa, respectively). Moreover, authors suggest that once compressed beyond roughly 20 GPa at room temperature, all silica glasses converge to the same high-density amorphous structure (c-HDA). Authors propose that this 'erasure' of the glass's thermodynamic history suggests that the energy barriers separating the various amorphous states vanish above a certain threshold pressure, leaving only one stable amorphous basin in the potential energy landscape.

I.5 IRRADIATION OF SILICA GLASS

Silica glass is widely used in optical devices exposed to high levels of ionizing radiation, such as nuclear reactors, space missions, and high-energy physics facilities [16,132] (the most exposed ones are usually optical fibers).

Gamma or X-rays, neutrons, electrons, and ions can induce both transient and permanent changes in the silica structure. Understanding these effects is crucial for ensuring the performance and stability of silica under extreme conditions, making it significant for both fundamental studies and applied technologies.

Structurally, irradiation disrupts the silica network through bond breakage, atomic displacements, and localized reorganization, producing several interconnected changes. These include alterations in density, the generation of point defects, and modifications of optical and mechanical properties. The extent and nature of these changes depend on the type and energy of the incident radiation (e.g., neutrons, electrons, protons, heavy ions) [133,134].

I.5.1 Silica glass structure under electron irradiation

Electron irradiation primarily causes damage through ionization processes and associated Coulombian interactions, owing to electrons' low mass. The bulk of damage arises from bond breaking via ionization and creation of point defects [135–137]. By contrast, neutron and heavy ion irradiation involve both electronic and nuclear interactions that can result in atomic displacements (knock-on effects) [133,138].

Despite these differing mechanisms, irradiation-induced processes eventually disrupt Si-O-Si bonds and create defect centers, thereby influencing the glass's structural disorder [135–137]. Nevertheless, short-range order remains remarkably stable, as silica largely keeps its fourfold coordination regardless of irradiation conditions [135]. Molecular dynamics simulations though suggested a rare appearance of fivefold-coordinated silicon atoms resulting from displacement cascades [139].

Medium-range order is more significantly affected through changes in angular distributions and ring statistics under significant irradiation dose (from GGy for electrons). A decrease in the average Si-O-Si angle and a reduction of its distribution can be seen from Raman spectroscopy through shifts and narrowing of the main band [140]. While this is true for non-densified silica glass, densified glasses exhibit relaxation behavior under irradiation [141]. As a result, their Raman signature displays the opposite trend, with broadening of the main band, as seen on Figure 22 a. Furthermore, there are increased intensities in the D_1 and D_2 Raman bands (true for both non-densified and pre-densified silica glass), and molecular dynamics simulations which confirm the formation of 3- and 4-membered rings under irradiation [139,140,142]. There is also a shift of the boson peak to higher frequencies with the increase of irradiation (reported for neutron and ion irradiated silica), indicating reduced medium-range order and enhanced structural disorder [143–145].

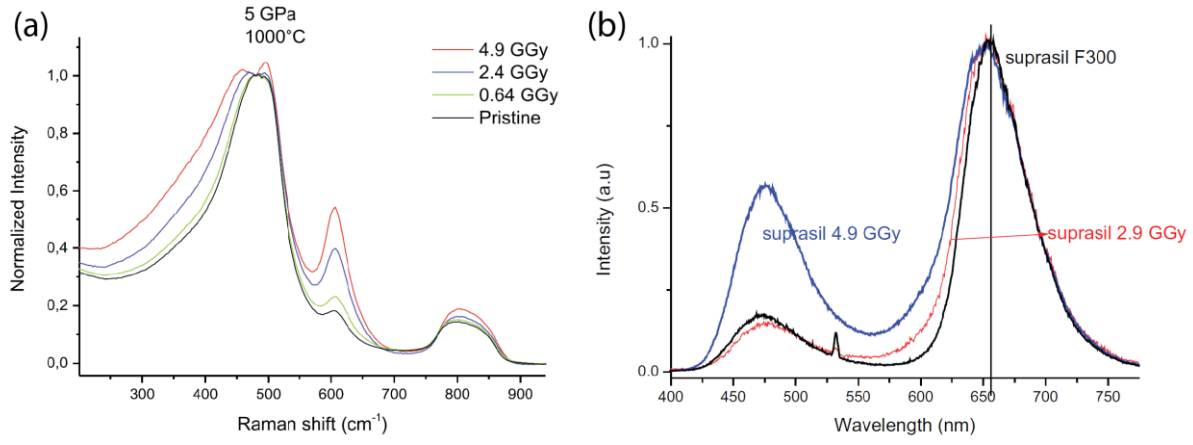

Figure 22. (a) Raman spectra evolution with the integrated dose of electron irradiated densified silica glass under HPHT conditions of 5 GPa 1000 °C. Cited from [141]. (b) PL spectra under 266 nm laser excitation for non-densified silica glass unirradiated and electron irradiated at 2.9 and 4.9 GGy. Cited from [146].

I.5.2 Defects formation

Irradiating silica glass can create several intrinsic point defects, including oxygen vacancies (E′ centers), NBOHC, ODC (see Figure 22 b) and peroxy radicals [145,147–150]. The formation and annealing of these defects are influenced by factors such as OH content and density, with densified silica typically showing both enhanced defect generation and reduced defect mobility [145,147]. In silica fibers, radiation-induced defects similarly produce new absorption bands and scattering centers, which manifest as increased radiation-induced attenuation (RIA) and can destabilize the performance of fiber-based sensing or data-transmission systems [151]. It has been suggested by Buscarino et al. [137,152,153] that electron irradiation can lead to an inhomogeneous restructuring of the silica matrix, and based on EPR studies, that there are locally formed defect-rich regions within the silica glass, resulting in a structurally inhomogeneous state. Their findings suggest an irradiation-induced structural modifications and local densification around defect centers like E′ centers [137,152]. They further support their hypothesis by a two-component model proposed for the IR absorption band at 2260 cm^{-1}, with distinct Si–O–Si groups in pristine and irradiation-densified regions [153].

Furthermore, irrespective of starting density, electron-densified silica exhibits an enhanced population of NBOHC alongside stronger green luminescence [141,146,154]. The exact origin of green luminescence is still debated, but in silica glass, it refers to an emission band observed around 540 nm, typically enhanced in glasses that have been densified either by high-pressure and temperature treatment or by high-dose electron irradiation [146].

I.5.3 Silica densification under electron irradiation

Among the various structural alterations, the densification (and associated refractive index variations) of silica glass is one of the most studied yet intriguing ones. Early work by W. Primark showed that neutron irradiation induces a rapid initial density increase, saturating at around 3% [6]. Interestingly, similar saturation values of around 3-4% have been reported under various irradiation conditions, including ions, neutrons, electrons, and UV photons [4,91,135,155–157]. This densification is commonly attributed to the formation of point defects [149,158]. Therefore, point defect creation and densification drive further structural rearrangements, such as decreased bonding angles and shifts in ring statistics [135,148].

I.5.4 The Metamict-like phase

High-dose irradiation can induce a distinct phase of silica glass, known as the metamict-like phase, which is formed under neutron, ion, or electron irradiation [134,136,159]. Borrowed from geological terminology, “metamict” traditionally describes minerals rendered amorphous by irradiation; it was also applied to quartz

damaged through radioactive decay, reflecting its disordered, post-irradiation state [6,160]. Because silica glass subjected to extremely high neutron irradiation doses (~$2 \cdot 10^{20}$ neutrons/cm^2) exhibited a vibrational signature similar to irradiated quartz [161], this glass is similarly termed metamict or metamict-like. Figure 23 presents the Raman spectra of the metamict-like phase obtained from quartz and silica glass.

Upon sufficient exposure, silica gets a relatively stable state with a characteristic density of about 2.26 g/cm^3 [118].

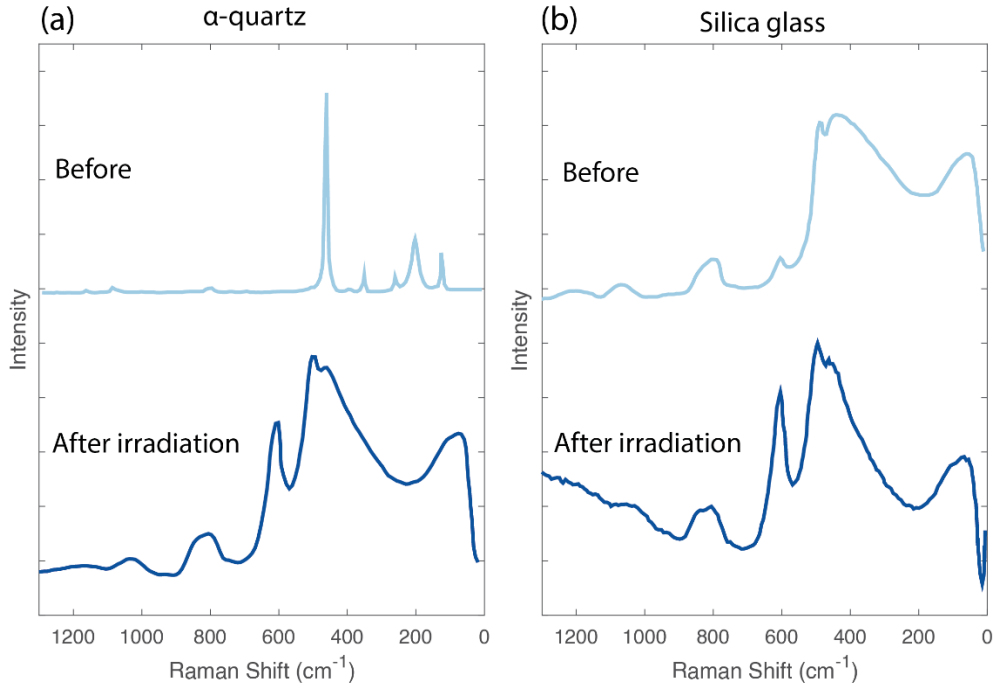

Figure 23. Comparison of Raman spectra for the metamict-like phase obtained from quartz and silica glass after neutron irradiation at 2×10^{20} n/cm2. (a) Initial spectrum of α-quartz and spectrum after irradiation; (c) Initial spectrum of silica glass and spectrum. Adopted from [161].

Upon sufficient exposure, silica gets a relatively stable state with a characteristic density of about 2.26 g/cm^3 [118]. Interestingly, regardless of a silica sample's initial density or the irradiation method, high-dose exposure consistently drives the material toward a uniform density near 2.26 g/cm^3 [118,154]. This trend is clearly illustrated in Figure 24 c, which shows density evolution data for silica under various irradiation conditions.

As mentioned earlier, Primak first reported this phenomenon in 1958, followed by other scientists, demonstrating that heavily neutron-irradiated quartz and silica converged in both density and vibrational signature [6,161–163]. However, electron diffraction, SEM, and EPR investigations [138,164,165] show that metamict phases may vary depending on the original polymorph (quartz, cristobalite, tridymite) and the irradiation conditions (fast neutrons or electrons).

In silica glass irradiated with 2.5 MeV electrons up to 11 GGy, both non-densified and densified samples ultimately exhibit similar EPR spectra and comparable E' defect concentrations upon saturation [166]. These E' centers share similar line shapes, intensities, and hyperfine parameters, although their formation kinetics differ. In non-densified silica, defect density rises gradually with dose [137], showing no rapid saturation. By contrast, pre-densified silica saturates more quickly, presumably because its compact network, formed under high-pressure conditions, restricts the migration and interaction of defect sites. Additionally, interstitial O_2 is saturated in metamict like phase and destroyed with further irradiation [166], whereas non-densified silica supports a more constant formation of O_2.

Speaking about Raman signature, under electron irradiation, the D_2 band increases with increasing dose; however, once density reaches approximately 2.26 g/cm^3, the correlation breaks down, making the metamict-like phase the one with the highest D_2 band intensity [140–142] (Figure 24 a,b).

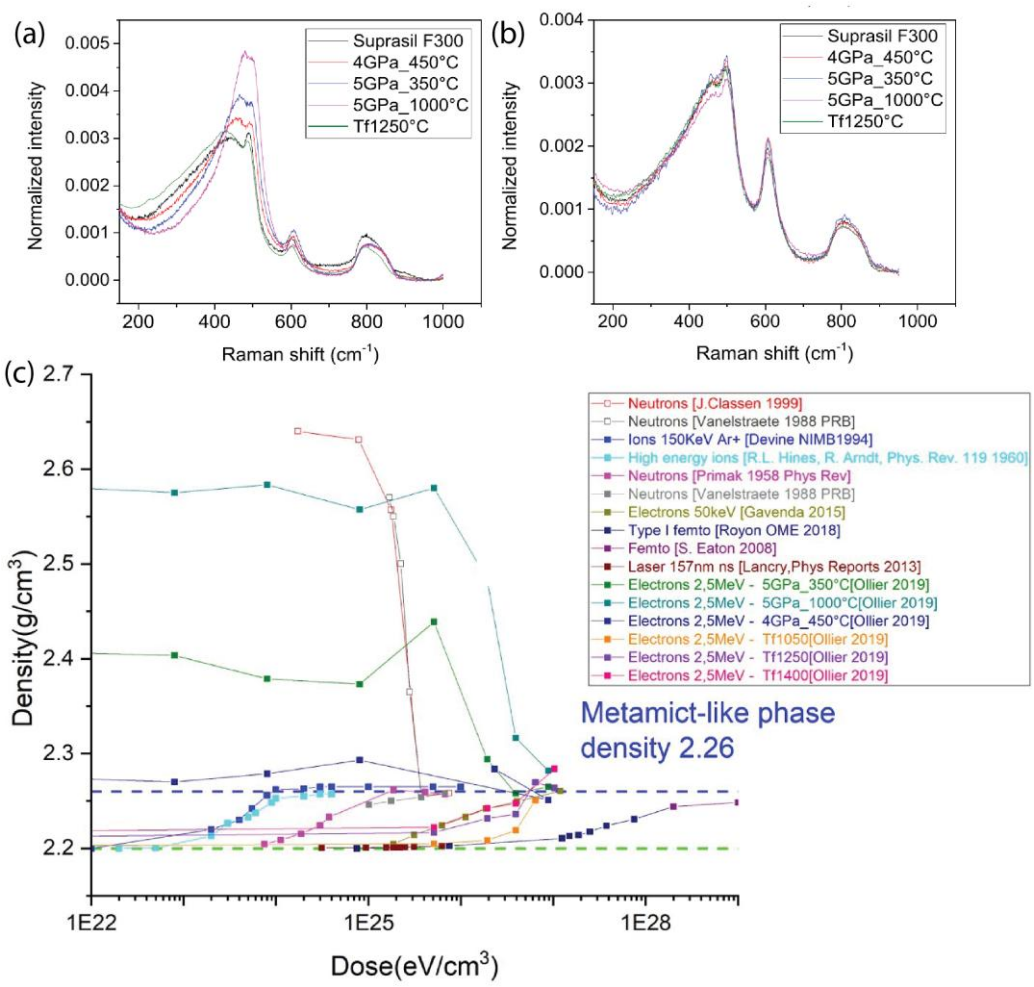

Figure 24. (a) Raman spectra of HPHT and a reference silica non-densified sample – pristine and (b) spectra after 11 GGy of electron irradiation. Cited from [154]. (c) Evolution of silica glass density as a function of irradiation dose for different irradiation types. Cited from [118].

Recent work by Mobasher et al. [118] further underscores that silica glass after electron irradiation has a Raman spectrum that does not fully revert to its original state even after high-temperature annealing. These findings suggest that relaxed metamict-like silica glass, despite returning to its pre-irradiation density, remains structurally different from pristine silica and has higher configurational disorder.

I.6 LASER IRRADIATION OF SILICA GLASS

Silica glass can also be modified through laser irradiation. While UV laser irradiation is similar to mechanisms described in the previous section and typically results in modifications not exceeding 3% especially using ns or ps UV lasers, IR ultrashort (femtosecond, or fs) laser irradiation produces different effects. In particular, fs laser irradiation can induce 3D localized modifications within the silica glass thanks to non-linear photoionization processes. To fully understand the structural reorganization and densification caused by fs laser irradiation, it is necessary to outline the underlying mechanisms of laser-glass interactions.

I.6.1 The basics of light-matter interactions and underlying nonlinear effects

In dielectric media such as silica glass, the behavior of electromagnetic waves is determined by how the material responds to the electric field of the light.

The starting point is the wave equation, derived from Maxwell's equations, which governs how the electric field $\vec{E}$ of the laser propagates through silica glass:

$$\nabla^2\vec{E} - \frac{1}{c^2}\frac{\partial^2\vec{E}}{\partial t^2} = \mu_0\frac{\partial^2\vec{P}}{\partial t^2} \tag{19}$$

where $\nabla^2\vec{E}$ represents the spatial variation of the electric field, showing how it changes across the glass; $\frac{1}{c^2}\frac{\partial^2\vec{E}}{\partial t^2}$ describes the temporal oscillation of the field in a vacuum, where c is the speed of light; $\mu_0\frac{\partial^2\vec{P}}{\partial t^2}$ is the material's response with the polarization $\vec{P}$, with μ_0 being the magnetic permeability.

At high intensities, this response is nonlinear, meaning that the material's polarization $\vec{P}$ does not simply scale with the electric field but includes additional contributions that become significant:

$$\vec{P} = \varepsilon_0\left(\chi^{(1)}\vec{E} + \chi^{(2)}\vec{E}^2 + \chi^{(3)}\vec{E}^3 + \cdots\right) = \vec{P}^{(1)} + \vec{P}^{(2)} + \vec{P}^{(3)} + \cdots = \vec{P}_L + \vec{P}_{NL} \tag{20}$$

where $\chi^{(i)}$ is the susceptibility and $\vec{P}^{(i)}$ is the polarization of order *i* where according to the classical description of non-linear optics [54-56], the vector polarization is the sum of linear polarization $\vec{P}_L = \vec{P}^{(1)}$ and non-linear polarization $\vec{P}_{NL} = \vec{P}^{(2)} + \vec{P}^{(3)} + \cdots$

In centrosymmetric materials like silica glass, the second-order susceptibility

$\chi^{(2)}$ vanishes due to symmetry considerations, making the third-order nonlinearity (associated with $\chi^{(3)}$) the dominant nonlinear contribution. This leads to an effective expression for the polarization:

$$\vec{P} = \varepsilon_0 \left[n_0^2 \left(1 + \frac{3}{4} \frac{\chi_{eff}^{(3)}}{n_0^2} \left| \vec{E} \right|^2 \right) - 1 \right] \vec{E} \tag{21}$$

where $n_0^2 = \chi_{eff}^{(1)} + 1$ is the linear refractive index and the intensity-dependent term modifies the refractive index

$$n = n_0 + n_2 I = n_0 \left(1 + \frac{3}{4} \frac{\chi_{eff}^{(3)}}{n_0^2} \left| \vec{E} \right|^2 \right)^{\frac{1}{2}} \tag{22}$$

being the nonlinear refractive index, where $I = \varepsilon_0 c n_0 \left| \vec{E} \right|^2$ is the laser intensity. This modification of the refractive index is at the heart of the optical Kerr effect.

The optical Kerr effect induces self-focusing of the beam. For a Gaussian beam, the central part, having higher intensity, experiences a larger refractive index than the periphery. This creates a lens-like effect (often termed a "Kerr lens"), which can focus the beam. When the beam power exceeds a certain threshold, defined as the critical power self-focusing becomes significant. The interaction between self-focusing, induced by the Kerr effect, and the focusing provided by any external optical system (lens focusing) can be further delineated by boundary conditions that account for both effects. When self-focusing dominates, the beam converges until a dynamic equilibrium is reached between Kerr-induced focusing, diffraction, and, at high intensities, defocusing due to plasma generation. This equilibrium results in a filament, which is a narrow, high-intensity channel that can propagate over long distances without significant divergence.

I.6.2 Femtosecond laser–silica interactions

The interaction between fs lasers and matter is studied extensively, however, not yet fully understood, as it consists of multiple processes, including ionization, non-thermal and thermal effects (sometimes cumulative from pulses to pulses), and various relaxation pathways including structural or phase transformations. The response of silica glass to intense, ultrashort laser pulses can be categorized into three primary stages [167]: electronic excitation [168] (femtosecond timescale), thermalization (up to 10's picoseconds), relaxation (nanoseconds to microseconds) followed by permanent modifications.

During electronic excitation, electrons in the material absorb energy from the laser, resulting in ionization [167]. In silica, this process typically involves multiphoton absorption due to its large bandgap (~9 eV), which exceeds the energy of individual photons (e.g., 1–3 eV in the near-infrared range). As a result, the material is normally transparent at the irradiation wavelength, allowing light to transport into the bulk. At low

intensities, single-photon absorption is insufficient to bridge this bandgap. However, under high-intensity conditions, the laser field can overcome the electronic band structure, enabling energy transfer to the electronic system and, subsequently, to the material itself. This process, known as photoionization, involves several possible mechanisms: multiphoton, tunnelling, or avalanche ionization (see

Figure 25). However, it was demonstrated that multiphoton ionization is the dominant mechanism in silica glass (requiring 6 photons) [169]. For pulse durations below 200 fs, neither tunnel ionization nor avalanche ionization is observed [169,170].

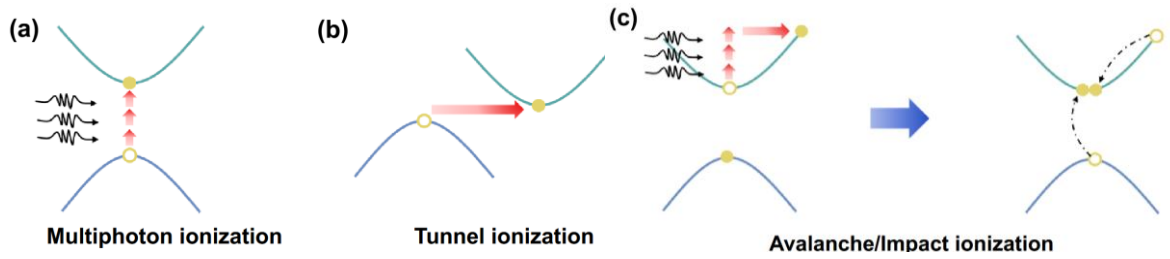

Figure 25. Illustration of three photoionization processes: (a) multiphoton ionization, (b) tunnel ionization and (c) avalanche or impact ionization. Cited from [171].

Once electrons are excited into the conduction band, they continue to absorb additional photons in a process called electron heating. The energy absorbed by these electrons is then transferred to the lattice (i.e., phonons) within approximately ten picoseconds, leading to localized heat generation. As these conduction-band electrons accumulate, a dense free-electron plasma forms (above or below the critical plasma density, depending on laser parameters). This plasma redistributes part of its energy through electron-phonon coupling, creating high temperature and pressure gradients. Experimental measurements using time-resolved Raman spectroscopy indicate that local temperatures can reach thousands of degrees Celsius in silica and silicate glasses [172].

After a few nanoseconds, heat begins to diffuse outward from the focal volume. At sufficiently low rates [173], the material returns to ambient temperature within a few microseconds, avoiding heat accumulation. However, at high energies, additional processes, such as non-thermal ionic motion, can induce permanent structural changes. Shockwaves on the order of several tens of GPa have been confirmed [174], and even higher pressures are predicted under more extreme focusing conditions [175]. Under such intense conditions, phenomena including expansion, stress formation [10,176–178], cavitation, micro-explosions, densification, expansion, recrystallization, and chemical migration [167,179–181], as well as the formation of point defects [182], which exhibit absorption in the UV and vacuum UV spectral ranges.

I.6.3 Heat effects

Building on the earlier discussion about plasma formation and the subsequent energy transfer from electrons to the lattice, we now consider the role of heat diffusion in shaping the final material transformations.

The characteristic time for dissipating deposited energy from the focal volume is often estimated by the diffusion time τ_D, given by $\tau_D = \frac{\omega_0}{2D}$, where ω_0 is the focal radius and D is the thermal diffusivity of the material [183]. The diffusivity D is defined by

$$D = \frac{\kappa}{\rho C_P}$$

with κ being the thermal conductivity, ρ - the density, and C_P - the specific heat capacity. In fused silica, for instance, a typical single-pulse modification using a numerical aperture (NA) of about 0.5 extends roughly 1 µm in width, giving a diffusion time on the order of 1 µs to evacuate 2/3 of the heart but it takes about 10 µs to go back to room temperature depending on the deposited energy.

When the pulse period τ_p is shorter than the thermal diffusion time τ_D, the focal volume will experience stepwise heating under repeated exposure, referred to as heat accumulation process [168,173,184]. To evaluate the significance of heat accumulation relative to the pulse period, one can define the parameter $R_\tau = \frac{\tau_p}{\tau_d}$ [185].

Heat accumulation is minimal or negligible when $R_\tau > 10$ [186]. When the repetition rate is low (e.g., <100 kHz for silica), R_τ is high, each laser pulse deposits energy that dissipates before the next pulse arrives, preventing significant thermal accumulation. The material thus returns to near-ambient temperature on the timescale of microseconds, implying that each pulse modifies the material independently. However, incubation effects arising from successive pulses can alter the material response, particularly at low repetition rates and low numerical apertures (NA ≈ 0.25), resulting in a reduced damage threshold and an increase in the refractive index [187–189]. These effects stem from the progressive accumulation of point defects, which modify the absorption characteristics, and the activation of additional energy-deposition mechanisms beyond conventional electron–phonon coupling [190]. The concentration of these defects depends on the initial defect density, the number of pulses, and the number of atomic sites available for modification.

At high repetition rates (>0.1 MHz in silica), so R_τ is low, next pulses arrive before the material can cooled down to room temperature, leading to a pulse-to-pulse thermal accumulation up to a steady state regime resulting in an expansion of the heat-affected zone much beyond the focal volume and eventually to permanent modifications if the surrounding temperature is higher than a transformation one (e.g. fictive temperature, crystallization temperature, etc.) [168,173]. Simulations confirm that local melting can

occur and drives this process, with subsequent resolidification and densification, contributing to the observed refractive index changes [173]. However, one can also observe solid-solid transformations like localized crystallization [191,192]. For example, the correspondence between the laser-modified Raman D_2 band and fictive temperature values demonstrated that the local fictive temperature can exceed the pristine level (~940 °C) and reach up to 1700 °C [193] within the so-called type I regime (see next section). Additionally, time-resolved micro-Raman studies indicate that at pulse energies around 2 µJ, peak temperatures in silica may approach 5000 K [172].

I.6.4 Volume modifications in silica glass

Ultrashort laser pulses can induce a broad range of structural changes in the volume of glasses, primarily determined by how effectively the light energy is transferred to the material [180]. Nowadays the laser induced modifications are categorized as "Types" (e.g., Types I, II, III, A, X, or combinations thereof), each linked to distinct levels of energy deposition and resulting in different structural outcomes and related optical properties [167,194].

In silica, there exist main regimes of transformation, which can be separated by three "damage thresholds" (T1, T2, T3) [195]. Below the first threshold ($T1 \approx 0.085 \pm 0.015$ µJ/pulse for pure silica at 800 nm, 160 fs, 0.5 NA, 100 kHz), the induced refractive index changes are transient and short-lived, producing no permanent modifications. Between thresholds T1 and T2 (with $T2 \approx 0.31$ µJ/pulse under the same irradiation conditions), a stable and isotropic refractive index modification (**Type I**) emerges [196]. When pulse energies exceed T2 but remain below T3 ($T3 \approx 4$ µJ/pulse), the refractive index change become strongly anisotropic (**Type II**), characterized by the formation of nanogratings [8] causing significant form birefringence [14,197]. Above threshold T3, the material undergoes micro-explosions, resulting in nano- or micro-void formation with densified shell around (**Type III**) [198]. The key stages leading to these structural transformations and resulting modification types are schematically illustrated in Figure 26

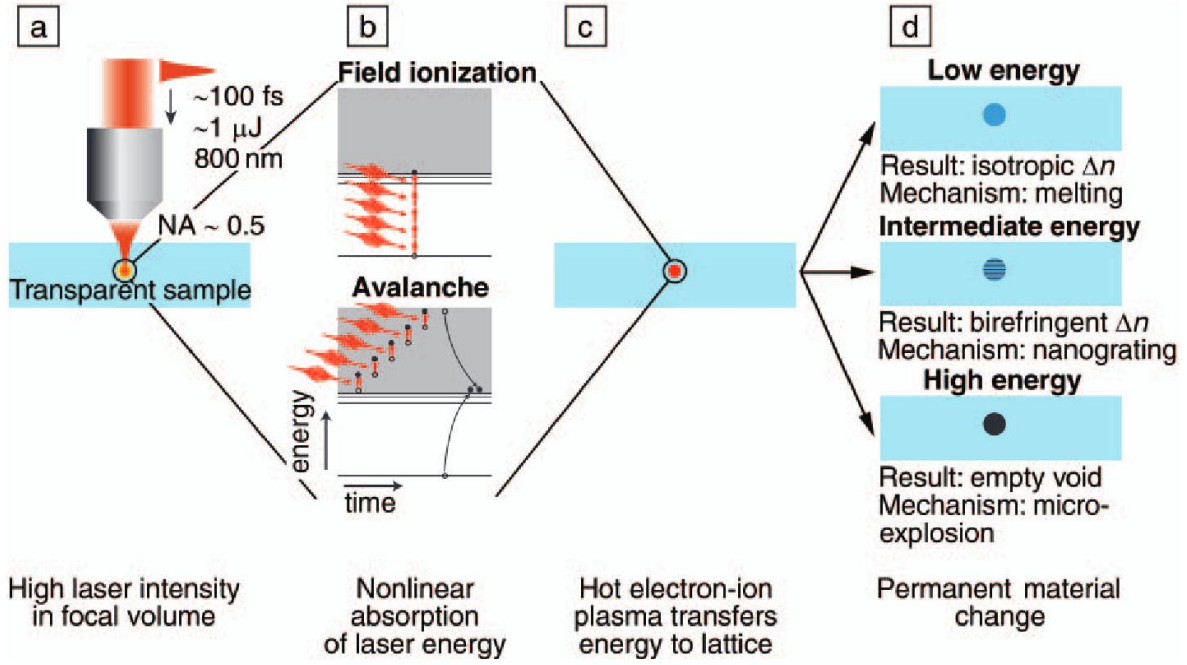

Figure 26. Schematic representation of the key stages in fs laser-induced structural modifications within bulk transparent materials. (a)–(c) A high-temperature electron-ion plasma is generated in the focal volume via nonlinear absorption of intense fs laser pulses. (d) The types of the resulting structural modifications in silica volume depend on the deposited energy. Cited from [180].

The nature of these modifications depends strongly on both the laser parameters [195], including pulse energy, duration, repetition rate, wavelength, polarization state, numerical aperture, depth of focus, and scanning speed. These modification regimes can be distinctly identified when pulse durations are shorter than approximately 200 fs [197,199,200]. At longer pulse durations, the stable Type I modifications processing window becomes significantly narrower, making it challenging to achieve stable isotropic index change under multi-pulse conditions.

Another interesting type of transformation recently identified in silica is known as "Type X" [201–203]. This modification is characterized by the formation of oblate nanopores (with the diameters below 50 nm [203,204]) and typically occurs at low pulse densities with pulse durations exceeding approximately 220 fs. Counterintuitively, reducing the deposited energy density (achieved by increasing the scanning speed) can actually enhance the magnitude of Type X (as well as Type I) modifications in silica glass. This effect is attributed to the non-local nature of the interaction between light and matter [205]. Type X has a very high transparency up to 99 % in visible spectrum, however, at the same time, it exhibits lower retardance values (up to 50 nm) that leads to the necessity of multilayers writing [206]. The birefringence of Type X is usually in the order of 10^{-4} to 10^{-3} [201,206]).

I.6.5 Type I modifications

The first effect observed in silica glass subjected to sufficiently intense laser irradiation above a threshold T1 (categorized as Type I modifications) is a reduction in optical transmission. This phenomenon has been documented across a broad spectrum of wavelengths, from infrared to blue [207,208] and even UV range [209], indicating fundamental structural alterations within the glass matrix associated with point defects centers.

In general, Type I modifications present isotropic changes in refractive index while maintaining minimal structural alterations [7,196] (see

Figure 27 a). These modifications produce permanent refractive index changes associated with increased density, as will be explained further, with high transparency and higher thermal stability compared to UV-induced modifications. However, still their thermal stability is moderate, with complete erasure occurring within 30 minutes at temperatures of 1000°C [210]. In silica glass, the maximum observed refractive index change for Type I (Δn) typically falls between $3\text{-}6\times10^{-3}$ [196,211]. Usually, type I modifications are achieved by using lower energy densities, visible or near-infrared laser wavelengths, and shorter pulse durations, typically less than 10 ps. Recent studies have demonstrated that utilizing multiscan approach can significantly enhance refractive index contrast, achieving values up to 10^{-2} [212]. The highest value of $\Delta n = 2.2\times10^{-2}$ [213] was achieved using high repetition rate regimes resulting in a different heating-cooling profile and a significant heat-affected zone. However, this approach introduces complications, including additional material damage and increased light scattering.

The refractive index contrast (Δn) observed in Type I regime comes from several distinct mechanisms, including volumetric modifications Δn_V, surrounding stress fields (inside and outside of the light affected zone), and the formation of point defects Δn_D. The contribution from point defects can be quantified using the Kramers-Kroning relation, though its magnitude remains relatively modest (around 10^{-4}) [214–217]. Within Type I modifications, the mains defects are E' centers, NBOHC, and defects associated with green luminescence [218,219] (see

Figure 27 c). These defects can be completely erased through thermal treatment, for example, at a 2-hour annealing at 450°C [220,221]. Type I demonstrate quite low optical losses, with most absorption bands concentrated in the UV and VUV, while light scattering remains little [220]. The volumetric contribution (Δn_V) comes from several processes occurring during laser irradiation. These include rapid thermal quenching, the development of high localized pressures during ultrashort timescales, progressive bond breakage, or combinations of these mechanisms that result in glass restructuring and densification in silica or expansion in some others glasses [167,222]. The resulting

permanent refractive index modification correlates directly with the relative volume change (ΔV/V) and glass polarizability changes **Ω** of the material through the Lorentz-Lorenz relationship as detailed in previous Section I.3.4.

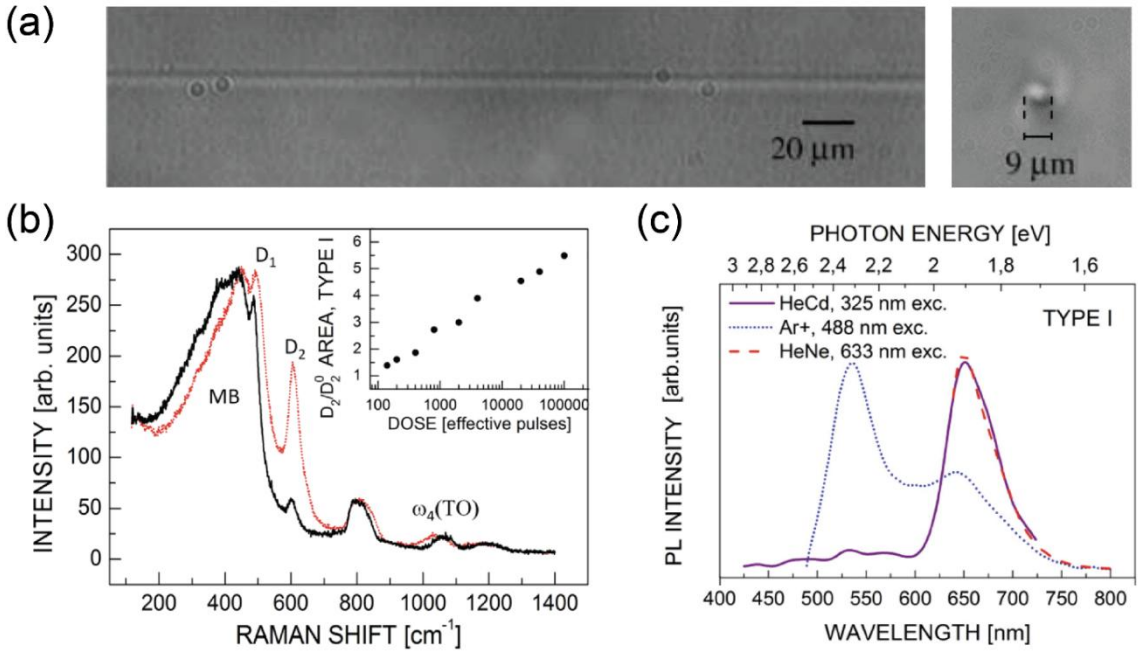

Figure 27. (a) Type I modification inscribed in silica using 1 µJ fs-pulse energy (adapted from [219]). (b) Raman spectra of pristine silica (black curve) and Type I modified silica (red dotted curve), with the inset displaying the relative D_2 band area as a function of irradiation dose. (c) Normalized PL spectra recorded in Type I modifications under 633 nm (red line), 488 nm (blue line), and 325 nm (purple line) excitation (b and c adapted from [179]).

From the vibrational spectroscopy point of view, structural changes in Type I modifications were characterized through Raman and FTIR micro-spectroscopy. Raman analysis (see

Figure 27 b) of laser-modified regions reveals a narrowing of the main band's FWHM and increase in intensity of the D_1 and D_2 bands [219,222–224], indicating decrease in the average Si-O-Si angle and a moderate increase in small-numbered rings, linked to the densification. Further evidence of structural reconfiguration appears in the Si-O-Si antisymmetric stretching band, which shifts toward lower frequencies, indicating increased glass density from alterations in inter-tetrahedral Si-O-Si bridges [78,79]. FTIR analysis of Type I modifications has documented a 6 cm^{-1} shift in the primary IR band peaking around 1120 cm^{-1} [225], signifying localized glass densification in SiO_2 (about 3%).

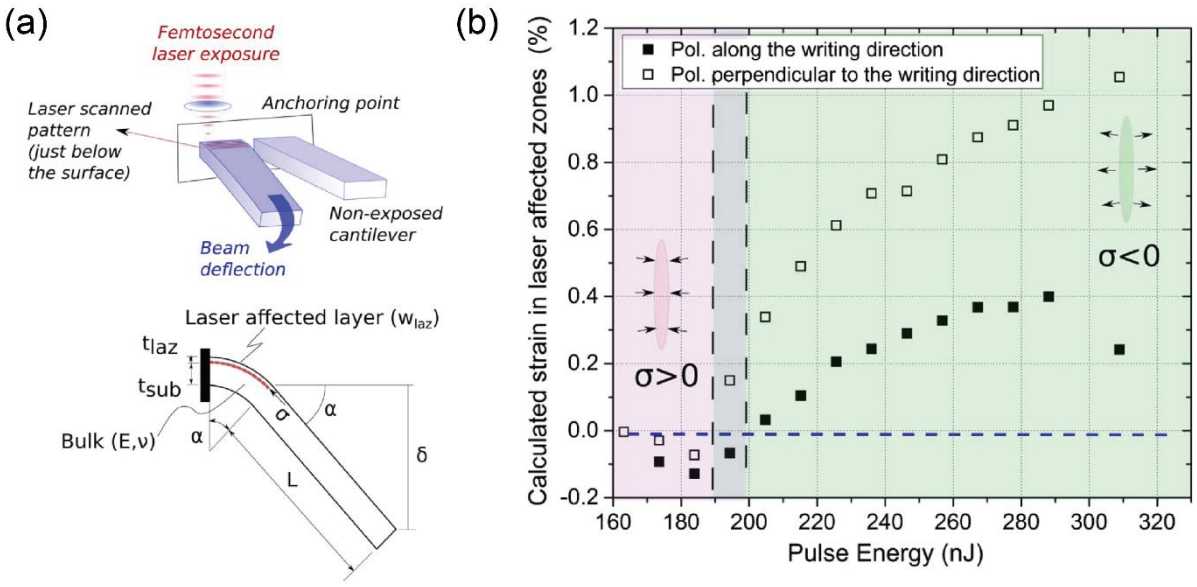

Figure 28. (a) Schematic representation of the cantilever-based technique employed to measure volume changes induced by fs laser irradiation. The cantilever structures are exposed to a fs beam near the top surface through a series of closely spaced parallel lines. (b) Cantilever deflection measurements following exposure to 150 fs laser pulses, showing variations with increasing pulse energy for both polarization states. Adopted from [176].

Also, permanents strain and related elastic response may affect the local mechanical characteristics. For instance, cantilever deflection (Figure 28) experiments by Bellouard et al. have demonstrated upward sample bending correlating with localized volume reduction and an equivalent average tensile stress of approximately 40 MPa [176] in post-mortem measurements. Nanoindentation studies reveal a substantial 2-3 GPa increase in local Young's modulus, elevating from approximately 72 GPa in pristine silica to 74–75 GPa within modified zones [226].

The collective evidence from refractive index measurements, spectroscopic analysis, and mechanical property measurements confirms permanent densification in Type I modifications. The suggested mechanism can be briefly explained: the energy transfer from free electrons to the glass network generates extreme localized temperatures, reaching several thousand degrees [173] at the focal point, constrained by thermal conduction limitations [227,228], and accompanied by high pressure development. This extreme thermal environment can increase the glass fictive temperature by several hundred degrees above its pristine value [79]. The subsequent rapid cooling process effectively "freezes" these configurations, resulting in permanent structural transformations [62,219,222], making the thermal densification is predominant compared to point defects formation.

I.6.6 Type II modifications

Type II modifications (known as nanogratings) exhibit a pronounced anisotropic change in the refractive index of glass. This effect primarily originates from form birefringence [12,13], with additional contributions from stress-induced birefringence that depend on the laser writing geometry [10,11,229]. In some cases, the refractive index shift can be as large as -2×10^{-2} [212,230], and these modifications are remarkably thermally stable, surviving annealing at temperatures up to 1000 °C for over two hours [210,231–233], with even longer-term stability observed in fiber Bragg gratings [210] and bulk silica [233].

The key to this birefringent behavior lies in the nanograting structure itself [8,14]. Nanogratings are composed of alternating periodic layers: one consisting of oblate nanopores [19,234] and the other of a densified material. These layers are arranged perpendicular to the laser beam polarization [8,230], as illustrated on Figure 29. This specific orientation results in a negative uniaxial birefringent response, where the fast axis aligns parallel and the slow axis perpendicular to the polarization direction [230]. This was first shown by early work by Bricchi et al. in 2004 [230], who demonstrated that the sub-wavelength periodicity of these structures effectively makes them behave as uniaxial, linearly birefringent materials. Unlike intrinsic birefringence, which is linked to the anisotropic distribution of molecules, the form birefringence of nanogratings comes from the orderly alignment of nanolayers with a refractive index contrast compared to the interlayer material.

Consequently, light polarized parallel to these interfaces experiences a higher refractive index, leading to a measurable phase difference between the two perpendicular polarizations. Notably, the magnitude of this effect can be tuned by adjusting the periodicity of the nanogratings, allowing for the extraction of ordinary (n_o) and extraordinary (n_e) refractive indices under linear approximations and assuming a uniaxial birefringence [230,235]. In addition to the contribution from form birefringence, the total birefringent response in Type II modifications is also influenced by stress-induced effects [236,237], coming from permanent volume changes during laser writing (a net volume expansion of the porous nanolayers), as well as by point defects and the densified background material [20].

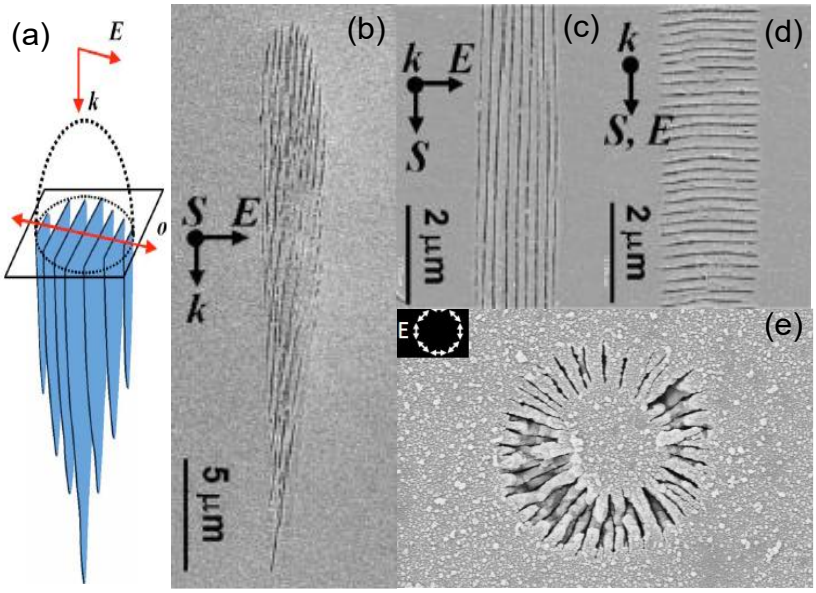

Figure 29. (a) Schematic representation of nanogratings within a laser track cross-section. (b)-(e) SEM of nanogratings inscribed 65 µm beneath the surface with linear polarization oriented perpendicularly. Extracted from PhD thesis of Q. Xie [238].

Optically, these modifications have high visible-spectrum transparency (approximately 74% transmission at 550 nm [239]) and a laser damage threshold near 0.31 ± 0.05 µJ/pulse for pure silica (under conditions of 800 nm wavelength, 160 fs pulse duration, 0.5 NA, and 100 kHz repetition rate) [195]. However, imperfections in the nanogratings can cause anisotropic light scattering, with 10-50% of the incident light being scattered in the visible range [220]. Furthermore, these structures display linear dichroism [220,239] along with engineered circular effects such as optical rotation and circular dichroism [239,240], highlighting their potential for advanced photonic applications.

I.6.6.1 Nanogratings formation mechanisms

The mechanisms leading to the formation of periodic nanostructures (often called nanogratings) in the volume of transparent dielectrics is still a subject of debate, but it can be outlined in several steps, presented on Figure 30.

Initially, inhomogeneities exist or arise within the dielectric, suggested to be present from the beginning or generated during laser irradiation. The literature proposes that these inhomogeneities serve as seeds for nanoplasma formation. Subsequent interference of scattered waves on seeds [242] leads to the spatio-temporal structuring that forms nanogratings.

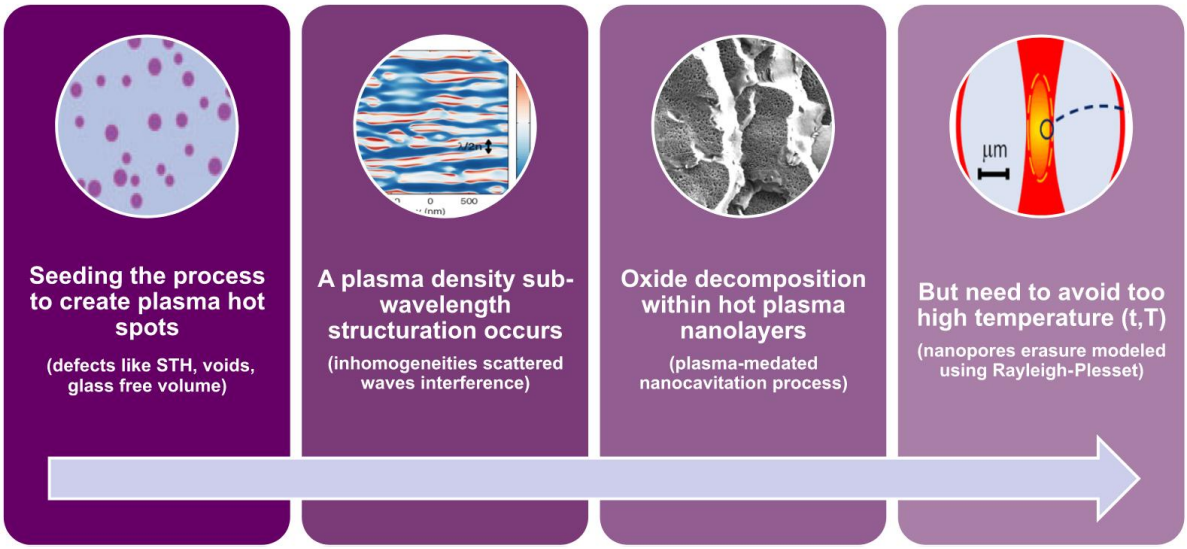

Figure 30. Schematic representation of the formation mechanism of nanogratings. Cited from [241].

Possible sources include defects (transient or otherwise, such as self-trapped excitons and self-trapped holes) or color centers [19,203,243,244], nanoscale inhomogeneities [245,246]. Recently, it has been demonstrated that nanostructure formation can be intentionally seeded by creating initial modifications in the fused silica [247]. Gribaudo et al. presented a two-step approach in which fs laser pulses are first used to create nanovoids, serving as seeds for subsequent nanoplane formation. During a second laser exposure at lower energy, these prefabricated seeds induce near-field enhancement, enabling the controlled growth of nanoplanes. Similarly, another example is the formation of a single isolated nanoplane in porous silica prepared from phase-separated alkali-borosilicate glass [248–250].

The widespread model for nanograting formation nowadays is based on nanoplasmonic phenomena [244,251,252]. In this theory, the generation of "defects" inside silica matrix is followed by the formation of inhomogeneous plasma. Under multipulse irradiation, local plasma hotspots develop into spherical nanoplasmas. Because of polarization-sensitive field enhancement at the boundaries of the plasma, the initially spherical plasma spots become elongated. When the electron concentration remains below the critical density, the electric field becomes amplified, driving the formation of nanoplanes through a multipulse process. This results in a periodic structure with a spacing of $\lambda/2n$. However, if the plasma density becomes too high, field enhancement at the "poles" dominates, preventing nanogratings from forming.

A recent refinement of this nanoplasmonic model incorporates randomly distributed inhomogeneities, seeding the process [246]. As the concentration of these seeds increases, two types of perpendicular nanoplanes appear. At lower seed concentrations,

low spatial frequency planes (period ~λ/n) emerge from interference between the incident beam and scattered light. At higher seed concentrations, the collective scattering of multiple nanoplasmas becomes dominant, producing a highly ordered high spatial frequency pattern (period ~λ/2n). Further increases in seed concentration can reduce the spacing until the nanoplanes merge, resulting in uniformly distributed plasma across the irradiated region.

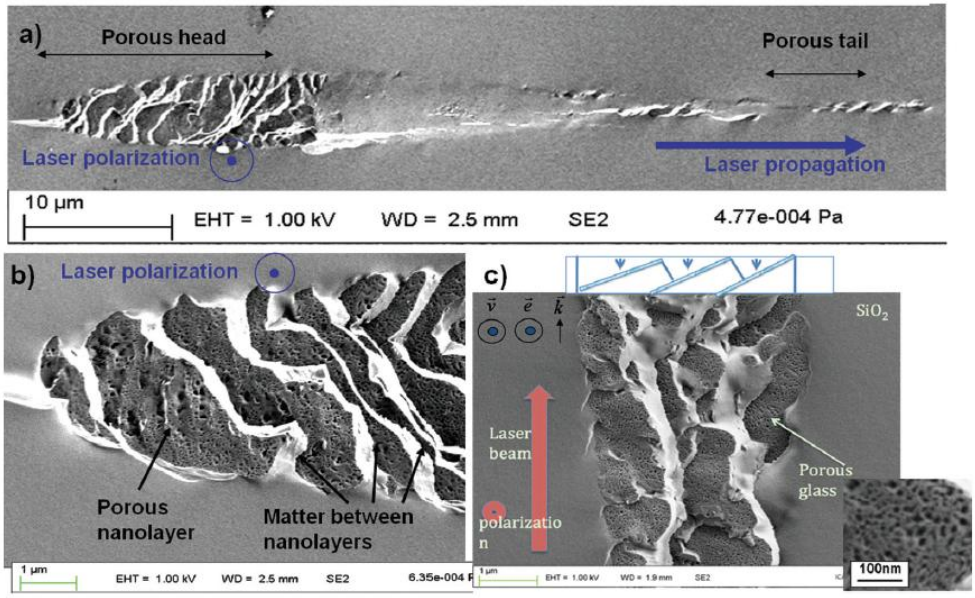

Figure 31. SEM images of laser track cross-sections. (a) Full laser track with laser polarization aligned parallel to the scanning direction; (b)-(c) close-up views of the nanoporous regions. Images adapted from Lancry et al. [234]. Extracted from PhD thesis of Q. Xie [238].

Speaking about the nature of the layers, some studies report fracture-like features, while others observe oxygen depletion [8]. Recent investigations using SEM suggest that nanogratings consist of alternating "uniform" and porous glass layers [234,253,254] (see Figure 31). By cleaving the sample along the nanograting planes, it is possible to observe small interior structures under a field-emission electron microscope, features that would otherwise be hidden beneath a conductive coating.

One proposed mechanism attributes nanopore formation to SiO_2 decomposition into understochiometric silica $SiO_{2(1-x)} + x.O_2$. This happens by electronic heating, which expels ionized oxygen atoms [234], with a strain mechanism [255] that have recently been refined as a plasma mediated nanocavitation process [256]. As seen using Raman spectroscopy, the oxygen atoms accumulate in interstitial sites, but also inside nanopores, as confirmed by Raman spectroscopy. In silica, typical nanopore diameters range from 10 nm to 30 nm, and small-angle X-ray scattering measurements corroborate the nanoporous structure [254,257,258]. However, nanogratings formation would be suppressed if nanopores become unstable during irradiation, for example, due to excessive temperatures (typ 3000-3500°C for 10's ns) at high repetition rates [185,259].

I.6.6.2 Structure of Type II modifications

In Type II modifications, the contribution of point defects to the overall refractive index contrast and birefringence is typically minor. Although there are some main defects, such as E′ centers [260] and NBOHC, similar to those observed in Type I modifications, resulting from the decay of self-trapped excitons [243,261]. Type II structures additionally exhibit other defect types, including ODC and O_2. NBOHC can react with E′ centers at critical concentrations to form ODC(II) [195,227,262]. E′ centers and ODC can be bleached relatively quickly (30 minutes of annealing at 600°C) [263], while NBOHC defects can be removed for example after annealing for 10 hours at 300 °C) [264]. Even after full defect bleaching, the overall birefringence in the visible to near-IR spectral range reduces by less than 5% [220], confirming that photo-induced defects are a minor contributor to the observed birefringence compared to structural factors.

From a vibrational spectroscopy perspective, Raman spectra of nanogratings in silica glass show increased D_1 and D_2 band intensities, a reduced FWHM of the main band, and the presence of O_2 molecules. Raman spectroscopy has also served as a tool to estimate densification in Type II modifications [125,176,223,224,236,263]. For example, by comparing Raman signatures to HPHT treated samples, densification levels of about 8% have been reported [224]. Other studies, using local density indicators such as D_2 band intensity or the R-band FWHM, estimate a post-irradiation glass density of 2.25–2.27 [263]. However, the D_2 band intensity becomes less reliable above densities of 2.3, due to its non-monotonous evolution i.e. a decreasing trend beyond that "returning" point [141]. More recent work has investigated pressures in the tens of gigapascals caused by fs-laser-induced shock waves, based on changes in silica's Raman signature [125]. However, because Type I modifications exhibit a relatively homogeneous structure, techniques like Raman and classical FTIR are well-suited for their analysis. Type II, on the other hand, features a layered composite nanostructure, making nanoscale characterization using the same methods more challenging.

Similarly to Type I, micro-cantilever deflection measurements have been employed to investigate specific volume changes and mechanical properties in Type II modifications [176,236,265,266]. Unlike Type I modifications, which exhibit upward deflection due to densification and volume reduction, Type II modifications produce downward deflection as a result of nanopore formation and net volume expansion [176,236], as illustrated on Figure 28. These observations reveal a stress-state inversion in silica glass [176], where the dense, Type I-like interlayer material possesses an elevated Young's modulus (around 80 GPa), while the porous layers exhibit significantly lower modulus [176,265,266]. Moreover, the coefficient of thermal expansion (CTE) varies with modification type: densified (Type I) zones show a decrease in CTE, whereas Type II exhibits a contrary trend compared to pristine silica [265]. In addition, Type II modifications display a reduction in the temperature coefficient of elasticity (TCE) of more than 50%,

attributed to submicron densified layers within the nanograting structure [267]. A recent grid nano-indentation study further revealed a bimodal stiffness distribution along laser-affected regions, featuring a porous zone where nanogratings form and a more densified zone deeper along the laser track [268].

I.6.7 Type III modifications

Type III modifications (above threshold T3) are distinguished by the formation of nano or micro-voids within materials subjected to extremely high energy deposition [9,269–271]. Morphological investigations employing SEM [173,176] have documented void dimensions ranging from 100 to 900 nm, as seen on the example on Figure 32 a. These dimensions are influenced by focusing conditions and laser parameters, and their length can be precisely engineered to create complex objects, including gradient-index metaphotonic structure [272].

At these high energy input levels, the material undergoes a localized micro-explosion phenomenon, resulting in void formation surrounded by a densified shell structure. These modifications demonstrate remarkable thermal resilience. For example, high-temperature annealing experiments reveal that voids experience shrinkage between 1050°C and approximately 1150°C, followed by expansion and deformation at temperatures exceeding 1200°C, while the surrounding densified shell maintains its structural integrity [273] (see Figure 32 d). This exceptional thermal stability presents significant advantages for applications requiring materials to preserve their properties under extreme thermal conditions, such as sensors for structural health monitoring, components for laser additive manufacturing processes, and materials for nuclear applications [262,274,275].

Similar to Type I and Type II modifications, Raman spectroscopic analysis confirms the densification, which in case of Type III modification is localized in shells surrounding micro-voids in Type III modifications in both SiO_2 and GeO_2 glasses [276]. Complementary investigations utilizing quantitative phase microscopy (QPM) in optical fibers have revealed negative phase variations within the void regions contrasted by positive variations in surrounding areas, providing further evidence of densified matter formation and permanent strain [273,277] (Figure 32 b and c). Additionally, AFM combined with s-SNOM measurements at 1130 cm^{-1} clearly attribute this positive phase shell to localized material densification [273].

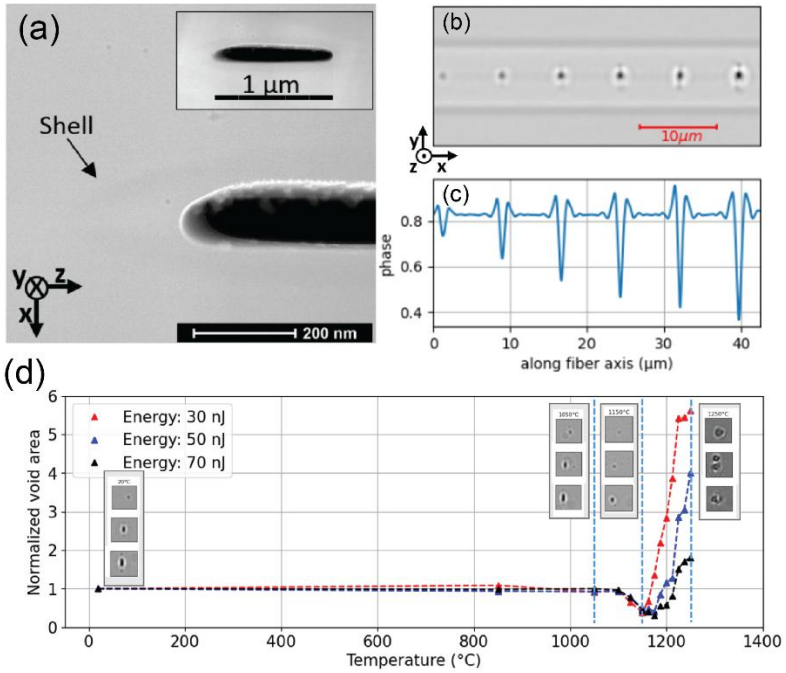

Figure 32. (a) TEM image of a microvoid inscribed in the Ge-doped silica fiber core. (b) Quantitative phase image showing six microvoids in a silica fiber. (c) Phase profile across the fiber core, passing through the center of the microvoids. (d) Normalized area evolution of three microvoids inscribed at 30 nJ, 50 nJ, and 70 nJ during a 30-minute stepwise isochronal thermal annealing up to 1250 °C. Adopted from [273].

The mechanisms underlying these structural transformations have evolved through several theories. For example an early model explaining micro-void formation attributed it to a Coulomb explosion [269,278]. When the density of electronic excitations reaches extreme levels, electrostatic repulsion between ions surpasses their binding energies, forcing ions into interstitial positions. However, subsequent analysis suggests this scenario is improbable under typical irradiation conditions.

Today's understanding involves a more complex process: energy absorbed within a confined volume generates intense pressure gradients, launching a spherical shock wave that compresses surrounding material while simultaneously initiating a rarefaction wave that reduces density at the energy deposition center [279]. This shock wave continues propagating outward until the pressure behind it approaches the Young's modulus of the material (reaching magnitudes up to 200 GPa), at which point it stabilizes and forms permanent structural modifications [175,280–283].

I.7 APPLICATIONS

The fundamental properties of densified silica glass, described in previous sections, show intriguing structural transformations and behaviors. Beyond the fundamental interest of these modifications, densified silica's unique properties, such as its refractive index, mechanical strength, and radiation response, make it extremely valuable for practical applications. Fs laser processing offers a convenient way to induce localized

density changes in silica, introducing it to a range of technological opportunities. Over the last two decades, fs-laser modifications have found use in a variety of fields, including birefringent optical elements [284–286], 3D geometric phase optics, 5D optical data storage [231,287], highly selective chemical etching (e.g. using HF or hot KOH), the development of optical fibers with sensors designed to withstand harsh environments [288,289], and many others [171].

Because fs-laser inscription of nanogratings in silica glass produces form birefringence, it can be employed to fabricate various polarization-manipulating components, such as polarization diffraction gratings, birefringent Fresnel zone plates, and waveplates [15]. These elements allow precise control of light polarization and are integral to numerous optical systems. Furthermore, the birefringent nanostructures induced by fs lasers can be tailored to generate geometric phase optical components, including radially polarized vortex converters and Airy beam converters [241]. By carefully adjusting laser parameters, one can create space-variant birefringence profiles that enable complex phase modulation.

An interesting example of fs laser induced modification is optical data storage, made with Type II or Type X modifications in silica glass [206,241]. In such systems, data is recorded by local inscriptions of the modifications in the bulk of glass and then read by detecting how these modifications affect light propagation. Advanced methods, like 5D optical data storage, can encode up to seven bits in a single point (voxel) by varying coordinates, but also properties such as birefringence and orientation of the nanostructures resulting in 5 dimensions storage. Thanks to the remarkable thermal stability of fs-laser modifications, data stored in this manner can endure harsh conditions and has a “seemingly unlimited lifetime” at room temperature [231].

One of the most prominent applications of densified silica glass is the fabrication of fiber Bragg grating (FBGs) sensors, which often rely on Type II or Type III modifications due to their optical properties and high thermal stability [15,16]. These gratings are formed by periodically inscribing refractive index changes into silica fibers, forming a Bragg structure that selectively reflects specific wavelengths in response to variations in strain, temperature, or pressure.

Fs laser inscribed FBGs exhibit excellent thermal stability, making them suitable for high-temperature sensing, and are therefore particularly attractive for pressure and temperature monitoring in applications like aircraft engines, laser additive manufacturing, Tokamaks and next-generation sodium-cooled nuclear reactors [15–17]. Conventional FBGs fabricated using UV-laser phase-mask techniques generally operate below 450 °C. However, many applications demand reliable operation at temperatures ranging from 400 °C to 1800 °C. In these environments, fs-laser-inscribed FBGs stand out for their ability to remain stable beyond 1000 °C in silica-core optical fibers [15].

Another critical area involves high-radiation environments, such as space (exposed to X-rays, gamma rays, protons, heavy ions, and electrons), nuclear facilities (gamma rays, neutrons), and nuclear waste storage [17,132]. The radiation dose rate and doses in these settings vary considerably, from mGy levels in medical applications to GGy within nuclear reactor cores, and even MGy per second in laser fusion facilities. In space, total doses can reach up to 10 kGy. Nevertheless, as explained in earlier sections, electron and neutron irradiation can alter the refractive index, optical properties, and density of glass, causing radiation-induced attenuation and radiation-induced compaction, which in turn shift the Bragg wavelengths.

Moreover, combining high temperature with radiation poses unique challenges: while elevated temperatures may partially anneal some radiation-induced damage, more measurements are needed to fully understand the dynamic behavior [17,132]. For example, for next-generation sodium-cooled nuclear reactors, which operate at around 580 °C and involve significant neutron flux and gamma radiation up to GGy cumulated dose, FBG sensors are being explored for real-time temperature monitoring.

I.8 Conclusion

In this chapter, the fundamental properties of silica glass were reviewed, including its structural features, common defects, and the thermomechanical and optical behaviors. Beginning with an overview of amorphous silica's tetrahedral network and characteristic vibrational signatures, we covered the mechanisms driving densification under hydrostatic pressure, both cold compression or high pressure high temperature compression. It was described how polyamorphism arises from these different compression pathways, with the structural distinctions between HDA and LDA amorphous silica. Additionally, it was shown that electron and laser irradiations can further alter the silica network, resulting in densification, defect formation, and, at high doses, the development of a metamict-like phase.

Yet, there are many questions remaining, for example, about HDA-LDA transition, especially under electron irradiation. The metamict-like phase, which forms under high-dose irradiation, also show the polymorphic nature of silica glass but remains incompletely characterized. Further question comes about how electron irradiation at elevated temperatures might modify or accelerate these amorphous-amorphous transformations, even though such conditions are directly relevant for nuclear applications.

At the same time, there are questions about the structural modifications induced by ultrashort-pulse lasers. Depending on the laser parameters, silica can have isotropic index change (Type I), porous nanogratings (Type II), or micro/nano-void formation with densified shell (Type III). The seeding mechanisms for these nanostructures, as well

as their densification levels, are still under debate, particularly for Type II modifications at the nanoscale. Another question is how nanogratings might behave in radiative environment, a question with direct implications for many applications.

All these open questions are addressed throughout this PhD dissertation.

Chapter II. STUDY OF FS LASER-INDUCED TYPE II MODIFICATIONS IN SILICA GLASS: MECHANISMS, STRUCTURE, DENSIFICATION

II.1 INTRODUCTION

Having discussed the densification processes in silica glass and the mechanisms of fs laser irradiation, the attention of this chapter will be on the unique birefringent fs-laser Type II modifications known as nanogratings. As shown earlier, these structures possess extraordinary properties that enable many advanced optical or micro-mechanical applications. Yet several open questions remain, as outlined at the end of the previous chapter. In this part of the thesis, we will study some aspects about nanogratings formation (with a focus on the connection with density of silica glass), examine their nanoscale structure, explore methods to measure the density at the nanometer scale, and finally address what drives densification.

First, the aim is to fill a gap in understanding of nanograting formation. Literature suggests that the "seeds" of nanogratings are local inhomogeneities in the dielectric constant. We hypothesize that such inhomogeneities correspond to the free volume in the glass network. This idea matches criteria such as size of inhomogeneities and necessary the "sign" of the dielectric constant i.e. lower than the background material in the most accurate models. To test this hypothesis, we subjected silica samples to HPHT treatments (up to 5 GPa, 1000 °C) prior to laser inscription, thereby reducing drastically the available free volume [111]. Polarized optical microscopy probing the photo-induced birefringence, along with SEM imaging, revealed that the formation of nanogratings is significantly suppressed as the glass density increases. These observations illustrate the role of free volume, suggesting it acts as a "precursor" to nanocavitation and periodic plasma organization, two processes essential for nanograting formation.

Next, we characterize the internal nanostructure of nanogratings in silica glass using SEM, scanning transmission electron microscopy (STEM), high-resolution transmission electron microscopy (HRTEM), and atomic force microscopy (AFM). By examining nanogratings from various orientations, we show that each layer consists of oblate nanopores in a wavy, discontinuous arrangement. We investigate how the nanograting period depends on the pulse density and, in light of our own data as well as prior studies, discuss deeply how nanogratings are formed through a plasma-mediated nanocavitation mechanism.

Finally, we examine how fs-laser inscription restructures silica glass at the nanoscale in type II modifications, nanogratings. Our goal is to quantify their density and clarify the origin of densification. For this, we employ advanced spectroscopic techniques:

scattering-type near-field optical microscopy (s-SNOM) combined with nanoscale Fourier transform infrared spectroscopy (nano-FTIR) using synchrotron radiation. Applying these methods, we directly observe for the first time, at nanoscale resolution, the densification of glass between nanoporous layers. By monitoring the shifts in the primary infrared vibrational band of the silicate network (the Si-O-Si stretching), we detect densification levels of the interlayer material on the order of 8-13%. Lastly, we discuss the mechanisms behind such elevated density levels in nanogratings, integrating our findings with the existing literature.

II.2 THE EFFECT OF COMBINING FEMTOSECOND LASER AND ELECTRON IRRADIATION ON SILICA GLASS

materials

MDPI

Article

Impact of Glass Free Volume on Femtosecond Laser-Written Nanograting Formation in Silica Glass

Nadezhda Shchedrina [1,2,*], Maxime Cavillon [1], Julien Ari [1], Nadège Ollier [2] and Matthieu Lancry [1,*]

[1] Institut de Chimie Moléculaire et des Matériaux d'Orsay, Université Paris-Saclay, Avenue des Sciences, 91400 Orsay, France; maxime.cavillon@universite-paris-saclay.fr (M.C.); julien.ari@universite-paris-saclay.fr (J.A.)

[2] Laboratoire des Solides Irradiés, École Polytechnique-CEA-CNRS, 91128 Palaiseau Cedex, France; nadege.ollier@polytechnique.edu

* Correspondence: nadezhda.shchedrina@universite-paris-saclay.fr (N.S.); matthieu.lancry@universite-paris-saclay.fr (M.L.)

Abstract: In this study, we investigate the effects of densification through high pressure and temperature (up to 5 GPa, 1000 °C) in the making of nanogratings in pure silica glass, inscribed with femtosecond laser. The latter were monitored through retardance measurements using polarized optical microscopy, and their internal structure was observed under scanning electron microscopy. We reveal the difficulty in making nanogratings in densified silica glasses. Based on this observation, we propose that free volume may be a key precursor to initiate nanograting formation.

Keywords: fs-laser; type II modifications; nanogratings; silica glass; densified glass; free volume

Citation: Shchedrina, N.; Cavillon, M.; Ari, J.; Ollier, N.; Lancry, M. Impact of Glass Free Volume on Femtosecond Laser-Written Nanograting Formation in Silica Glass. *Materials* **2024**, *17*, 502. https://doi.org/10.3390/ma17020502

Academic Editor: Vlassios Likodimos

Received: 9 December 2023
Revised: 14 January 2024
Accepted: 18 January 2024
Published: 20 January 2024

1. Introduction

The variety of femtosecond (fs) laser-induced modifications in glass paves the way for a multitude of structural alterations initiated through the nonlinear absorption of laser pulse energy. The nature of these modifications in optical glasses varies based on the laser-writing parameters, and they are classified in the literature into three main types [1]. Type I modifications can be observed as smooth and homogeneous changes in the refractive index at lower energy. Early studies demonstrated the potential of fs-lasers to induce 3D refractive index profiling in silica glass, a foundational step in creating waveguides [2]. Type II modifications are distinguished by an anisotropic change in the refractive index. Under specific pulse duration, frequency, and energy conditions, a strong form birefringence appears, which originates from periodic lamellar nanostructures oriented perpendicular to the laser polarization [3]. At higher laser intensities, Type III modifications occur, marked by the formation of nano/micro-voids with a densified shell due to localized micro-explosions.

Of particular interest are Type II modifications, associated with the formation of nanogratings. Fs-laser-induced nanogratings find expansive applications in several technological domains. They play a central role in the creation of long-term optical data storage devices [4,5], thermal optical sensors [6,7], and microfluidics [8,9]. Importantly, they are also employed in the fabrication of various optical elements, including waveguides, light polarization converters [10,11], and other birefringent elements [12]. Despite the broad scope of their applications, a comprehensive understanding of the mechanisms behind nanograting formation in glass remains to be achieved. This is crucial, as it impacts their fabrication and, consequently, the optimization of their use in various technological contexts.

Central to the nanograting formation process is the phenomenon of multiphoton ionization, wherein photon absorption facilitates energy transfer from the incident light to the solid glass structure [13]. As the laser intensity exceeds specific thresholds, it results in the generation of plasma, characterized by a high-density free-electron cloud [14]. Interference between the incident laser light and scattered light from the inhomogeneities

in the glass matrix results in periodic modulations in the electron plasma concentration, leading to nanostructural changes in the glass [15]. Simultaneously, plasma hotspots evolve into elongated nanoplasma regions because of local field enhancement, which occurs perpendicular to the polarization [16]. These nanoplasma regions are "forced-arranged" by light into distinct periodic patterns, oriented in a direction orthogonal to the laser's polarization vector. Finally, plasma-mediated oxide decomposition occurs, resulting in nanolayers made of an assembly of oblate nanopores [17,18].

While there is an understanding of the mechanisms behind nanograting formation, determining the exact precursors in glass remains a debated topic in the field of laser–matter interactions. One hypothesis [19] posits that the inception of nanogratings does not have any pre-existing precursors. Instead, modeling studies suggest that the initial laser pulse generates nanopores or nanovoids, which subsequently influence the light organization [15,20]. An alternative theory [21] emphasizes the role of point defects and color centers as the initial precursors for nanograting formation. These defects are hypothesized to be either intrinsic, pre-existing within the material, or extrinsically induced by the initial laser pulse (e.g., STHs [22]).

Building upon the existing theories of nanograting formation, our current research introduces a hypothesis that emphasizes the significance of free volume in the nanograting seeding process. Free volume in glass refers to sub-nanometer-scale voids or spaces within its amorphous structure [23–26]. In silica glass, this free volume is significant given the inherent arrangement of silicon and oxygen atoms, which creates a 3D network of n-membered rings with notable interstitial spaces [27]. The density of silica glass inversely correlates with its free volume; as the glass becomes denser through processes like high-pressure, high-temperature (HPHT) treatment, its free volume decreases [25]. In silica glass, its density or specific volume can be reduced by up to 22% under high pressure (HP) [28], highlighting its intrinsic porous nature at the sub-nanometer scale and its high initial free volume. This perspective could explain why materials like silica [14] and germanium dioxide [29], which inherently possess large free volumes in their networks, demonstrate a pronounced ability to form nanogratings compared with most other glass [30].

This paper presents, for the first time, an investigation of nanograting writing in pristine silica glass compared with densified silica glass subjected to high-pressure, high-temperature (HPHT) conditions. Prior studies have extensively explored the properties of densified glass through techniques such as Raman spectroscopy [31], X-ray diffraction [32], Brillouin scattering [33], and positron annihilation spectroscopy (PAS) [25], which have demonstrated a reduction in glass free volume indicators such as void size and rings statistics. By utilizing fs-laser writing in four different silica glass samples, each with a distinct density, and varying both pulse energy and pulse density followed by birefringence measurements, we strive to gain insights into how density and inherent interstitial voids affect the dynamic of nanograting formation. This exploration contributes to our broader understanding of the mechanisms behind nanograting creation and their potential optimization across various applications.

2. Materials and Methods

The material used for this study was Synthetic Fused Silica SK-1300 glass (OHARA GMbH, Hofheim, Germany), fabricated with the vapor axial deposition process (OH < 200 ppm). The silica samples used in our experiments were cylindrical in shape, with a diameter of 3.95 mm and a thickness of approximately 3 mm. A schematic representation of these samples is included in the insert of Figure 1. Densification of the silica glass was achieved using a high-temperature, high-pressure belt press [34]. The selected pressure and temperature conditions were chosen based on the literature [34] to provide a range of densities from 2.2 to 2.6, with the highest one being close to α-quartz density. Consequently, four samples were prepared: pristine silica and three densified samples (4 GPa at 450 °C, 5 GPa at 350 °C, and 5 GPa at 1000 °C); the densities of these samples were determined to be 2.203 ± 0.001, 2.317 ± 0.007, 2.408 ± 0.013, and 2.609 ± 0.006, respectively, where the

error represents the standard deviation from three separate measurements. The density measurements were conducted using the Archimedean sink–float method, measuring the samples' weights in air (m_a) and when submerged in toluene (m_l). We employed the equation $d = (m_a \times \rho_{toluene})/(m_a - m_l)$ to calculate the density, where $\rho_{toluene}$ is the density of toluene, determined by its temperature-dependent equation (density (T) = $0.8845 - 0.9159 \times 10^{-3} \times T + 0.368 \times 10^{-6} \times T_2$, T in °C) [35]. Considering the optical properties of densified silica, it has been observed that the refractive index generally scales up with increased density in silica glass [36]. As for the optical bandgap, only minor changes (typically less than 5–10%) can be observed in densified silica. This can be inferred from calculations conducted on crystalline polymorphs of silica [37].

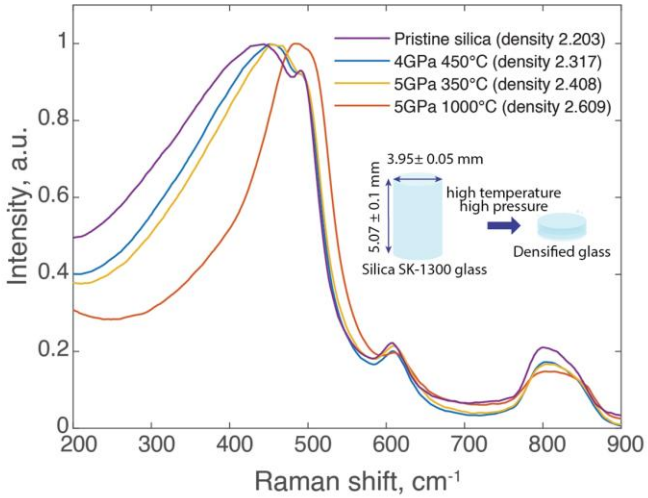

Figure 1. Raman scattering spectra of silica glass samples alongside a schematic representation of the densification process.

This study employed an fs-laser system (Satsuma, Amplitude Systemes Ltd., Pessac, France) operated at 1030 nm, with a repetition rate of 10–100 kHz and a pulse duration of around 300 fs. The chosen repetition rate (10–100 kHz) was low enough to avoid any pulse-to-pulse heat accumulation effects. The laser beam was focused 200 µm beneath the sample surface using a 0.6 NA aspheric lens. The laser-writing process was conducted at a scanning speed of 0.1 mm/s, with energy ranging from 0.05 µJ to 2 µJ. In a second set of experiments, the scanning speed was decreased from 5 to 0.005 mm/s to achieve a range of pulse density between 2 to 50,000 pulses/µm. The pulse density was calculated from the scanning speed and the repetition rate using the formula $N = f/v$, where N is the number of pulses per micron, f is the repetition rate in kHz, and v is the scanning speed in mm/s. During the laser-writing procedure, the sample was moved along the X-axis. The laser light was linearly polarized and set in two orientations (writing configurations) parallel (Xx) and perpendicular (Xy) to the laser-writing direction.

The formed optical modifications were examined using an Olympus BX51 polarized optical microscope (Olympus Corporation, Tokyo, Japan) in transmission mode. To measure the optical retardance, which is proportional to the linear birefringence, induced by fs-laser direct writing, we employed the Sénarmont compensator technique [38]. A quarter-waveplate is oriented at 45° to the axis of the linearly polarized light entering the microscope. As light passes through the birefringent sample, it undergoes a phase shift, resulting in elliptically polarized light. The rotating analyzer is then adjusted to achieve extinction, and its angle, θ, is rotated directly proportional to the retardance, following the relation $R = (\lambda \cdot \theta)/180$, where λ is the probe wavelength in nm, and R is the relative retardance or optical path difference in nm. The measurements represent mean values,

averaging from a series of three independent measurements. Data fitting was performed as a guide to the eye for Figures 2 and 3, using an asymptotic exponential function:

$$R = a \times \left(1 - exp\left(-\frac{x}{b}\right)\right), \quad (1)$$

where R is the retardance, x represents the input variable (either pulse energy or number of pulses per micron), and a and b are the fitting parameters. Additionally, we used a full wave-plate to determine the slow/fast axis orientation. This method also helps to visually confirm the dependence of the birefringence orientation with the writing laser's polarization.

To analyze the cross-sections of the laser tracks, cleaved samples were examined using a field emission gun scanning electron microscope (FEG-SEM, ZEISS SUPRA 55 VP, Zeiss, Oberkochen, Germany) to study their morphology. Prior to laser irradiation, Raman spectroscopy measurements were taken using an externally doubled diode laser from Spectra-Physics, operating at an excitation wavelength of 488 nm, with a 1200 L/mm grating, a slit width of 50 µm, and power of 28.5 mW. Spectra were normalized by the total integrated area.

3. Results

In this study, we employed a set of four silica glass samples, one of which was pristine, while the remaining three were subjected to densification via a belt press technique. The densification process, executed under varying conditions of temperature and pressure using the same HPHT method for all samples, reliably generated distinct densities. The variation in free volume can be indirectly assessed through molar volume, expressed as $\frac{M}{\rho}$ (where M is molar mass, and ρ is density). Applying this to our samples indicates a molar volume decrease of approximately 4.9%, 8.5%, and 15.6% for densified samples 4 GPa 450 °C, 5 Gpa 350 °C, and 5 Gpa 1000 °C, respectively, when compared with the pristine glass with a molar volume of 27.27 cm^3/mol. Positron annihilation spectroscopy (PAS) studies have demonstrated that the HPHT densification process significantly impacts void size in the silica network, linearly reducing the average void volume from 65 $Å^3$ to as small as 10 $Å^3$ with a densification of 22% [25]. A schematic representation illustrating the densification process and the dimensions of the samples is provided in the insert of Figure 1.

The Raman spectra of the four samples were obtained and are presented in Figure 1. Notable differences were observed in the spectral shapes between the densified samples and the pristine sample. In our observations, the R-band at 440 cm^{-1} in the densified samples notably shifted toward higher frequencies, and concurrently, the full width at half maximum (FWHM) of this R-band was observed to decrease. These changes indicate reduced average Si-O-Si angles, consistent with the increased density of the silica glass [31]. The densification process compacts the structure of silica glass, causing silica tetrahedra to tilt closer to each other and reducing the available volume between the atoms. This results in a more uniform and, thus, narrower range of Si-O-Si bond angles. The uniformity in bond angles restricts the vibrational frequency range of the Si-O-Si bonds, which is reflected as a sharper and more defined Raman band in our spectral analysis. Variations in the intensities of the D_1 and D_2 Raman bands, which are linked to local density indicators, were also noted.

Two distinct experimental series were conducted to investigate nanograting formation. In the first series, the pulse count remained constant as the energy varied between 0.05 µJ and 2 µJ. The laser-writing parameters and this energy range were chosen based on prior research [39] and our focus on Type II fs-laser-induced structures, which are associated with nanograting formation and result in a permanent form birefringence. The second series maintained a constant energy while varying the pulse count from 2 to 50,000 pulses per micron. Subsequent optical retardance measurements were performed on the laser-written structures in each sample type. In the experiment with energy variation, Figure 2 illustrates

the retardance values within the irradiated areas inside the laser tracks across differing pulse energies for the four types of samples.

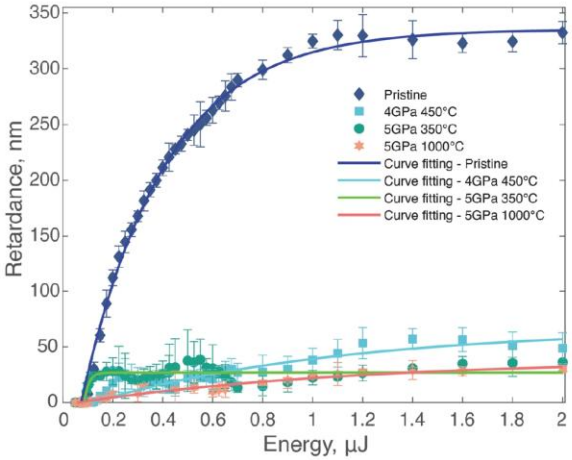

Figure 2. Mean retardance of laser-written structures plotted against pulse energy. Experimental conditions: λ = 1030 nm; τ = 250 fs; f = 100 kHz; v = 100 µm/s, resulting in a pulse density of 1000 pulses/µm and energy, E, varying from 0.05 to 2 µJ.

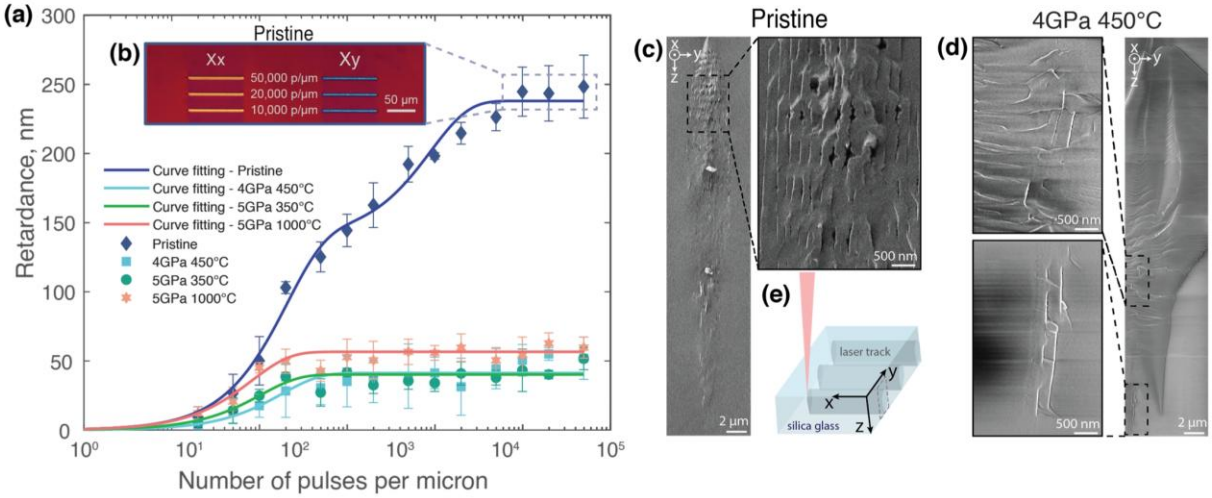

Figure 3. (**a**) Mean retardance of laser-written structures plotted against a number of pulses per micron. Experimental conditions: λ = 1030 nm, τ = 350 fs, E = 1 µJ, f = 10–100 kHz, and v = 0.002–5 mm/s for a pulse density from 2 to 50,000 pulses/µm. (**b**) Optical microscope image of laser-written structures using a crossed polarizer and analyzer and a full retardation waveplate inserted at 45°, indicating the orientation of the slow axis for pristine sample. (**c**) SEM images of a cross-section of the laser track (1000 pulses/µm, 1 µJ, Xy writing configuration) in the pristine sample and (**d**) in the 4 GPa 450 °C sample. (**e**) Scheme of the sample orientation for the SEM analyses.

The lowest observed energy yielding a non- or low-birefringent optical contrast marks the Type I threshold (if any). In addition, the orientation of the stress-induced birefringence within this Type I regime remains independent of the writing polarization orientation. In contrast, Type II corresponds to a non-zero birefringence (here, an optical retardance) whose slow/fast axis orientation is quasi-linearly dependent on writing laser polarization, thus indicating nanograting formation [40], which we initially detect using the full waveplate technique and further confirmed with SEM. To precisely determine this threshold, we

incrementally increased energy in very small steps (ranging from 0.015 µJ to 0.075 µJ) at the lower energy range (from 0.05 µJ to 0.125 µJ). This approach ensured a precise determination of the threshold energy, beyond which, we increased the step size (0.025 µJ to 0.2 µJ) for practicality in measurements. For the pristine sample, the threshold energy was approximately 0.125 µJ. The retardance then rapidly increased to around 330 nm at 1 µJ, beyond which, it stabilized. Different degrees of densification in silica glass only subtly influence the threshold energy (around +/−0.02 µJ). However, they exhibited fluctuating but generally low retardance levels (typ. below 50 nm), with values notably below those of the pristine silica sample.

For the subsequent experiment, an energy of 1 µJ was selected, as this value represented a plateau in retardance for all samples. The focus was shifted to varying the number of pulses per micron, as previous studies have demonstrated that higher pulse densities lead to more pronounced nanograting formation with a lower period [15,41]. Here, the retardance within the irradiated areas in the pristine sample initially increased gradually, reaching a value of around 30 nm at 10 pulses per micron. It then exhibited a more pronounced increase, peaking at approximately 270 nm at 50,000 pulses per micron (Figure 3a). In contrast, the retardance values within the irradiated areas of the densified samples remained substantially lower, not surpassing 55 nm.

In both experimental conditions, indirect evidence of nanograting formation was observed in the pristine samples. In Figure 3b, an optical micrograph using a full waveplate displays the behavior of the pristine silica glass sample. The full waveplate adds a fixed optical path difference, which results in the emergence of interference-based colors [42]. These images reveal the neutral axes of the birefringence: the orange (Xx writing configuration) and blue (Xy writing configuration) colors correspond to the orientation of the birefringence's fast and slow axes, respectively, relative to the laser polarization. In Figure 3b, the clear contrast between orange and blue serves as an indirect confirmation of nanograting formation since it demonstrates the formation of a birefringence whose orientation is polarization-dependent [3]. Indeed, the change in color directly correlates to the 90° rotation of the birefringence slow axis when the writing laser's polarization is rotated by 90°. Contrastingly, no such evidence of nanograting formation was observed in the densified sample. In the densified samples, the laser tracks appear uniformly colored despite the writing configuration, signaling the absence of ordered nanogratings while stress-induced birefringence is still present.

To complement this view, SEM micrographs in Figure 3c,d provide a comparative cross-sectional analysis of the nanogratings in two silica glasses, respectively, 4 GPa 450 °C and the pristine glass. For the pristine sample (Figure 3c), images reveal an ordered array of nanolayers, consistent with expectations for laser tracks written with 1000 pulses per micron at an energy of 1 µJ in the Xy writing configuration. Here, the laser polarization is perpendicular to the laser-writing direction, resulting in nanogratings that are vertically aligned within the laser track. However, it should be noted that some tilt in the nanogratings can occur because of variations in the local material response [43]. In contrast, Figure 3d displays the cross-section in densified silica glass (4 GPa 450 °C), where the nanogratings' periodicity appears quite disrupted. Only a few vertical nanolayers can be observed, which are visible in the magnified images of Figure 3c, highlighting the "negative effect" of densification on nanograting organization. Furthermore, horizontal striations are visible in the SEM micrographs (Figure 3d) along the cracks, which are typical fracture facies due to strain relaxation in cleaved samples.

Returning to the dependence of retardance on pulse energy, a more detailed analysis reveals correlations with the density of the studied samples. For instance, Figure 4a presents the dependency of the maximum retardance value on the density of the samples. For the pristine silica, this value is notably high (332 nm), while for the densified samples, it remains considerably lower, reaching a minimum (34 nm) for the most densely packed glass (5 GPa at 1000 °C). A similar trend is observed when examining the slope of the curve at the origin (up to 0.2 µJ), as shown in Figure 4b. The slope at the origin of the retardance kinetics

curve in Figure 4b, measured just above the threshold energy, serves as an indicator of the material's initial photosensitivity. This parameter reflects the efficiency of nanograting formation at the onset, revealing the relative ease of imprinting nanogratings in the glass according to its initial density.

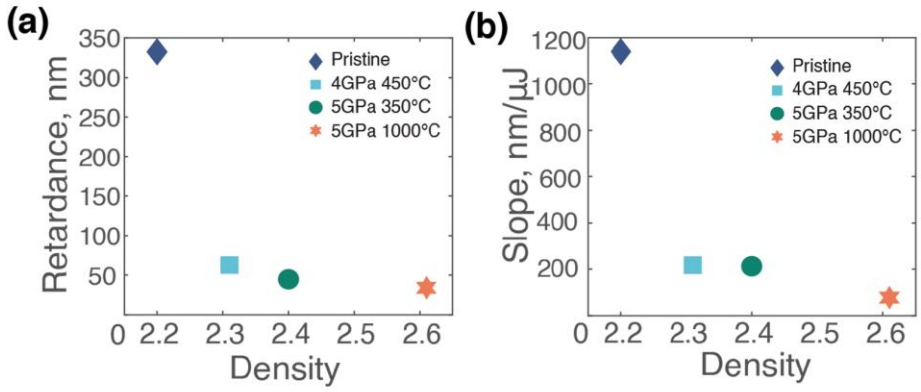

Figure 4. Analysis of retardance for the set of samples with varying energy: (**a**) plot of the maximum retardance for each sample against the density of the samples; (**b**) plot of the slope of the curve at the origin (up to 0.2 μJ) for each sample against the density of the samples.

4. Discussion

In this section, we explore the initial steps of nanograting formation, focusing on the role of glass density and underlying structure in silica glass.

According to the prevailing theory, nanograting formation initiates with dielectric constant inhomogeneities that serve as process precursors or seeds, and which also play a role in scattering centers in the glass matrix. Within this model [15,20], incident light interacts with scattering centers in the glass structure, leading to multiple scattered wave interferences. Within the interference pattern, these seeds, in turn, generate spherical nanoplasma hotspots because of increased plasma density. As the process evolves, the influence of light polarization reshapes this nanoplasma into an oblate shape [16]. For seeds with a lower dielectric constant compared with the surrounding material, the local field enhancement results in the maxima perpendicularly to light polarization, whereas it is the reverse for a higher dielectric constant [15,44]. Through the plasma-mediated nanocavitation process, nanopores are created that, over numerous laser pulses, eventually merge to form nanolayers [15]. Nanogratings in the glass consistently form perpendicular to light polarization.

The literature suggests various potential seeds, either native to the glass or induced by laser pulses. Modeling studies of bulk nanogratings are usually based on a low dielectric constant seed as an initial "nanovoid" [15,20]. Some studies have suggested point defects like E'; ODC; and, generally, color centers [21], as well as transient defects like self-trapped electrons (STEs) [18,45] and self-trapped holes (STHs) [22] as seeds. In discussing potential precursors, we must consider the necessity of a lower change in the refractive index to facilitate the plasma field enhancement perpendicularly to light polarization. Notably, most point defects, as well as STEs, are unlikely candidates, as they contribute to a positive change in the local refractive index. Another counterargument against the presumption of point defects acting as seeds comes from observations concerning HPHT densification, which increases the initial concentration of defects such as E' centers and ODCs [46]. Nevertheless, as described above, we evidenced that the formation of nanogratings remains notably suppressed in highly densified glass, indicating a less efficient generation process. Recent studies have considered the potential role of STHs as seeds for nanograting formation [22]. However, certain intrinsic characteristics of STHs cast doubt on their feasibility as seeds. Primarily, the size of STHs, approximately 1 Å, makes them too small to function effectively as scattering centers. Moreover, some studies indicate a lower stability of STHs

in neutron-irradiated or in densified silica, particularly at room temperature, compared with pristine silica [47]. Hypothetically, this should instead facilitate nanograting formation in densified silica because of the accumulation of more stable STHs between laser pulses.

Our research introduces a new hypothesis highlighting the role of free volume and inherently related voids as precursors for nanograting formation. This aligns with the observed ease of nanograting formation in silica, a glass material characterized by a very high free volume. The efficiency is even more pronounced in nanoporous silica forms like aerogels [48], which require fewer pulses to form high birefringence given their increased free volume. So, we suggest that the initial sub-nanometer or -nanoscale porosity (the so-called glass free volume) of the glass plays a role as a low-density (low dielectric constant) seed, initiating the scattered waves that lead to the plasma spatial organization, namely, an arrangement of regularly spaced hot plasma layers. Then, oxide decomposition occurs [17] within these hot plasma nanolayers, resulting in nanograting imprinting. According to current models [15], the concentration of these "nanopores" significantly influences the nanograting-seeding process, resulting in a shorter average period for the nanogratings. The pore size is also an important factor; numerical models have successfully used voids of up to 10 nm [15,20]. Experimentally, it has been observed that nanogratings are more easily imprinted in nanoporous sol–gel silica provided that nanopores are not too big [48,49].

Conversely, multicomponent glasses such as aluminoborosilicate glasses, with their denser networks and lower free volume, exhibit narrower processing windows for nanograting formation, partly attributable to their reduced free volume [39]. First one needs to consider that the chemical composition, particularly the addition of B and Al atoms in silicate glasses, leads to a less "open" glass network, translating into a lower free volume, as indicated by a higher atomic packing density [50]. Secondly, the free volume model also offers a comprehensive framework for understanding the relationship between glass viscosity, T, and dependence, especially in the temperature range, from the glass transition temperature (T_g) up to the melting temperature (T_m) [51]:

$$\eta = \eta_0 \exp\left(\frac{BV_0}{V_f}\right), \tag{2}$$

where η is glass viscosity, V_f is the free volume, V_0 is the volume of a molecule, and η_0 and B are constants. According to this model, free volume, V_f, can be represented by the equation:

$$V_f = V - V_0 = \frac{V_0(T - T_0)}{T_0}, \tag{3}$$

where V is the total volume, and T_0 is a critical temperature. From an experimental point of view, in silica-based glasses, T_0 is typically much smaller compared with aluminoborosilicate glasses such as commercial varieties like B33, AF32, BK7, etc. This difference in T_0 translates into a significantly lower-free-volume aluminoborosilicate, which can be directly correlated with its reduced ability to form nanogratings. Indeed, the processing window for nanograting formation has two boundaries: the lower energy bound is influenced by the glass's free volume (seeding the process), while the upper limit, defined by the maximum energy beyond which no more nanogratings survive, is less directly but still related to free volume through the glass viscosity (T) and the laser heating–cooling profile. While nanoporous layers can be generated through plasma-mediated nanocavitation, at higher energies or repetition rates, these nanolayers can be erased by subsequent heat pulses within a few 10s of nanoseconds, as modeled in our recent studies [52].

We hypothesize that free volume and, thus, the resulting voids are primordial in determining both the plasma spatial organization and the nanocavitation process. As previously mentioned, varying density from 2.203 to 2.609 yields a molar volume reduction of up to 15.6%. The literature indicates that a 22% density increase can shrink the void size to below 10 Å^3, a stark contrast to the 65 Å^3 of pristine silica [25,41]. This agrees with the Raman spectroscopy results (Figure 1), which reveal notable shifts in the R-band

toward higher frequencies in densified samples along with a decreased FWHM, indicating a reduction in average Si-O-Si angles, signifying increased glass density [31,47]. This compaction results in a narrower Si-O-Si bond angle range, as reflected in more defined Raman bands. The shift in the D_2 peak toward higher frequencies further corroborates this densification [34].

In our investigations of silica with varying densities, we manipulated energy levels and pulse numbers to assess their impact on nanograting formation. Utilizing the maximum value and slope of the retardance curve as indicators, we found marked differences between pristine and densified samples. While the threshold energy remained quite consistent across all samples, densified samples exhibited significantly lower retardance values (Figures 2 and 3a). In the results shown in Figure 2, the minimal differences in optical retardance between the densified samples, as compared with the more pronounced retardance in the pristine sample, can primarily be attributed to the high degree of densification across all samples. The degree of densification in this study is higher than the metamict phase threshold of silica, where further densification through any kind of irradiations becomes ineffective [53]. In contrast, more significant differences are expected in samples with densities ranging from 2.20 to 2.27, i.e., below the metamict phase density.

As illustrated in Figure 4, both maximum retardance and slope values decreased with increasing density. Contrary to the well-formed nanogratings in the pristine samples, the densified counterparts tend to avoid the generation of nanogratings, as evidenced by our SEM analysis (Figure 3c,d). The observed lower retardance could potentially stem from a reduced number of seeds, which would also imply fewer nanopores generated per unit volume. The background birefringence in the highest densified sample can be attributed to the stress-induced birefringence. Meanwhile, the reduced slope indicates a change in the underlying mechanism itself, specifically hinting at a decreased energetic efficiency in facilitating the decomposition of glass oxide, subsequently leading to the reduced generation of nanopores and, likely, molecular oxygen. Indeed, the generation of nanogratings inherently involves the formation of molecular oxygen [17], a process that appears to be more difficult in densified silica. Recent studies [41] have evidenced a diminished capacity to generate molecular oxygen in densified silica during electron irradiation. This aligns well with our findings; the challenging nature of initiating molecular oxygen formation and creating associated defects, such as Frenkel defects, seems to inhibit the successful generation of nanogratings in densified samples.

As suggested above, glass free volume could serve as a primary seed for the nanocavitation process. The rapid transition from nanoplasma hotspots into nanopores is driven by swift temperature transfer to phonons and local thermal expansion, which effectively imprints oblate nanopores [18]. These nanopores' shapes and orientations are largely influenced by the incident light's polarization, supporting a plasma-mediated over a thermo-mediated nanocavitation process. Recent findings [54] have validated this by demonstrating spherical nanopore formation under circular polarization. For nanocavitation, primary conditions are required: a quick process that surpasses thermal diffusion and acoustic wave relaxation and a significant localized strain coupled with a pressure drop potentially due to local electrostriction [55].

5. Conclusions

By employing fs-laser writing on silica glass samples with varied densities, we demonstrated that the tendency for nanograting formation is inversely related to the material's densification. Densified samples exhibited significantly lower retardance values and slopes, revealing a diminished efficiency in nanograting generation. This provides novel insights into the role of glass free volume as a crucial precursor of nanograting formation. Void-related free volume may serve as an ideal seed owing to its size and lower refractive index, thereby facilitating the formation of nanoplasma hotspots and subsequent nanogratings that consistently align perpendicularly to light polarization. Our suggested mechanism may coherently explain why silica glass or GeO_2, which naturally possesses a high free

volume, facilitates nanograting formation more efficiently than other types of glass. The relationship between free volume and nanograting efficiency could guide the engineering of materials (e.g., nanoporous dedicated materials) with tailored optical properties, paving the way for improved applications in advanced photonic systems.

Author Contributions: Conceptualization, M.L.; methodology, M.L.; validation, N.S., M.C., N.O. and M.L.; formal analysis, N.S. and M.L.; investigation, N.S. and J.A.; resources, M.L.; writing—original draft preparation, N.S.; writing—review and editing, N.S., M.C., N.O. and M.L.; visualization, N.S.; supervision, M.L.; project administration, M.L.; funding acquisition, M.L. All authors have read and agreed to the published version of the manuscript.

Funding: This research was funded by Agence Nationale de la Recherche (ANR), FLAG-IR Project, award number ANR-18-CE08-0004-01, and REFRACTEMP project, award number ANR-22-CE08-0001-01.

Institutional Review Board Statement: Not applicable.

Informed Consent Statement: Not applicable.

Data Availability Statement: Data are contained within the article.

Conflicts of Interest: The authors declare no conflicts of interest.

References

1. Itoh, K.; Watanabe, W.; Nolte, S.; Schaffer, C.B. Ultrafast Processes for Bulk Modification of Transparent Materials. *MRS Bull.* **2006**, *31*, 620–625. [CrossRef]
2. Davis, K.M.; Miura, K.; Sugimoto, N.; Hirao, K. Writing Waveguides in Glass with a Femtosecond Laser. *Opt. Lett.* **1996**, *21*, 1729–1731. [CrossRef] [PubMed]
3. Bricchi, E.; Klappauf, B.G.; Kazansky, P.G. Form Birefringence and Negative Index Change Created by Femtosecond Direct Writing in Transparent Materials. *Opt. Lett.* **2004**, *29*, 119–121. [CrossRef] [PubMed]
4. Zhang, J.; Gecevičius, M.; Beresna, M.; Kazansky, P.G. Seemingly Unlimited Lifetime Data Storage in Nanostructured Glass. *Phys. Rev. Lett.* **2014**, *112*, 033901. [CrossRef] [PubMed]
5. Rowstron, A. Rethinking Data Storage for the Zettabyte Cloud Era: The Journey from Metal to Glass. In Proceedings of the Advanced Photonics 2018 (BGPP, IPR, NP, NOMA, Sensors, Networks, SPPCom, SOF), Zurich, Switzerland, 2–5 July 2018; OSA: Washington, DC, USA, 2018.
6. Mihailov, S.; Grobnic, D.; Hnatovsky, C.; Walker, R.; Lu, P.; Coulas, D.; Ding, H. Extreme Environment Sensing Using Femtosecond Laser-Inscribed Fiber Bragg Gratings. *Sensors* **2017**, *17*, 2909. [CrossRef] [PubMed]
7. Wang, Y.; Cavillon, M.; Ballato, J.; Hawkins, T.; Elsmann, T.; Rothhardt, M.; Desmarchelier, R.; Laffont, G.; Poumellec, B.; Lancry, M. 3D Laser Engineering of Molten Core Optical Fibers: Toward a New Generation of Harsh Environment Sensing Devices. *Adv. Opt. Mater.* **2022**, *10*, 2200379. [CrossRef]
8. Bellouard, Y.; Said, A.; Dugan, M.; Bado, P. Fabrication of High-Aspect Ratio, Micro-Fluidic Channels and Tunnels Using Femtosecond Laser Pulses and Chemical Etching. *Opt. Express* **2004**, *12*, 2120–2129. [CrossRef] [PubMed]
9. Hnatovsky, C.; Taylor, R.S.; Simova, E.; Rajeev, P.P.; Rayner, D.M.; Bhardwaj, V.R.; Corkum, P.B. Fabrication of Microchannels in Glass Using Focused Femtosecond Laser Radiation and Selective Chemical Etching. *Appl. Phys. A Mater. Sci. Process.* **2006**, *84*, 47–61. [CrossRef]
10. Lu, J.; Dai, Y.; Li, Q.; Zhang, Y.; Wang, C.; Pang, F.; Wang, T.; Zeng, X. Fiber Nanogratings Induced by Femtosecond Pulse Laser Direct Writing for In-Line Polarizer. *Nanoscale* **2019**, *11*, 908–914. [CrossRef]
11. Beresna, M.; Gecevičius, M.; Kazansky, P.G.; Gertus, T. Radially Polarized Optical Vortex Converter Created by Femtosecond Laser Nanostructuring of Glass. *Appl. Phys. Lett.* **2011**, *98*, 201101. [CrossRef]
12. Beresna, M.; Gecevičius, M.; Kazansky, P.G. Ultrafast Laser Direct Writing and Nanostructuring in Transparent Materials. *Adv. Opt. Photonics* **2014**, *6*, 293. [CrossRef]
13. Mao, S.S.; Quéré, F.; Guizard, S.; Mao, X.; Russo, R.E.; Petite, G.; Martin, P. Dynamics of Femtosecond Laser Interactions with Dielectrics. *Appl. Phys. A Mater. Sci. Process.* **2004**, *79*, 1695–1709. [CrossRef]
14. Shimotsuma, Y.; Kazansky, P.G.; Qiu, J.; Hirao, K. Self-Organized Nanogratings in Glass Irradiated by Ultrashort Light Pulses. *Phys. Rev. Lett.* **2003**, *91*, 247405. [CrossRef] [PubMed]
15. Rudenko, A.; Colombier, J.-P.; Itina, T.E. From Random Inhomogeneities to Periodic Nanostructures Induced in Bulk Silica by Ultrashort Laser. *Phys. Rev. B.* **2016**, *93*, 075427. [CrossRef]
16. Bhardwaj, V.R.; Simova, E.; Rajeev, P.P.; Hnatovsky, C.; Taylor, R.S.; Rayner, D.M.; Corkum, P.B. Optically Produced Arrays of Planar Nanostructures inside Fused Silica. *Phys. Rev. Lett.* **2006**, *96*, 057404. [CrossRef] [PubMed]
17. Lancry, M.; Poumellec, B.; Canning, J.; Cook, K.; Poulin, J.-C.; Brisset, F. Ultrafast Nanoporous Silica Formation Driven by Femtosecond Laser Irradiation. *Laser Photon. Rev.* **2013**, *7*, 953–962. [CrossRef]

18. Xie, Q.; Shchedrina, N.; Cavillon, M.; Poumellec, B.; Lancry, M. Nanoscale Investigations of Femtosecond Laser Induced Nanogratings in Optical Glasses. *Nanoscale Adv.* **2023**, *6*, 489–498. [CrossRef]
19. Rudenko, A.; Colombier, J.-P.; Höhm, S.; Rosenfeld, A.; Krüger, J.; Bonse, J.; Itina, T.E. Spontaneous Periodic Ordering on the Surface and in the Bulk of Dielectrics Irradiated by Ultrafast Laser: A Shared Electromagnetic Origin. *Sci. Rep.* **2017**, *7*, 12306. [CrossRef]
20. Buschlinger, R.; Nolte, S.; Peschel, U. Self-Organized Pattern Formation in Laser-Induced Multiphoton Ionization. *Phys. Rev. B Condens. Matter Mater. Phys.* **2014**, *89*, 184306. [CrossRef]
21. Taylor, R.; Hnatovsky, C.; Simova, E. Applications of Femtosecond Laser Induced Self-Organized Planar Nanocracks inside Fused Silica Glass. *Laser Photon. Rev.* **2008**, *2*, 26–46. [CrossRef]
22. Lei, Y.; Shayeganrad, G.; Wang, H.; Sakakura, M.; Yu, Y.; Wang, L.; Kliukin, D.; Skuja, L.; Svirko, Y.; Kazansky, P.G. Efficient Ultrafast Laser Writing with Elliptical Polarization. *Light Sci. Appl.* **2023**, *12*, 74. [CrossRef]
23. Chen, S.; Xu, D.; Zhang, X.; Chen, X.; Liu, Y.; Liang, T.; Yin, Z.; Jiang, S.; Yang, K.; Zeng, J.; et al. Reversible Linear-Compression Behavior of Free Volume in a Metallic Glass. *Phys. Rev. B.* **2022**, *105*, 144201. [CrossRef]
24. Liao, B.; Wu, S.-Y.; Yang, L. Free Volume: An Indicator of the Glass-Forming Ability in Binary Alloys. *AIP Adv.* **2017**, *7*, 105101. [CrossRef]
25. Zanatta, M.; Baldi, G.; Brusa, R.S.; Egger, W.; Fontana, A.; Gilioli, E.; Mariazzi, S.; Monaco, G.; Ravelli, L.; Sacchetti, F. Structural Evolution and Medium Range Order in Permanently Densified Vitreous SiO_2. *Phys. Rev. Lett.* **2014**, *112*, 045501. [CrossRef] [PubMed]
26. Ojha, P.K.; Rath, S.K.; Sharma, S.K.; Sudarshan, K.; Pujari, P.K.; Chongdar, T.K.; Gokhale, N.M. Free Volume of Mixed Cation Borosilicate Glass Sealants Elucidated by Positron Annihilation Lifetime Spectroscopy and Its Correlation with Glass Properties. *J. Power Sources* **2015**, *273*, 937–944. [CrossRef]
27. Onodera, Y.; Kohara, S.; Salmon, P.S.; Hirata, A.; Nishiyama, N.; Kitani, S.; Zeidler, A.; Shiga, M.; Masuno, A.; Inoue, H.; et al. Structure and Properties of Densified Silica Glass: Characterizing the Order within Disorder. *NPG Asia Mater.* **2020**, *12*, 85. [CrossRef]
28. Deschamps, T.; Kassir-Bodon, A.; Sonneville, C.; Margueritat, J.; Martinet, C.; de Ligny, D.; Mermet, A.; Champagnon, B. Permanent Densification of Compressed Silica Glass: A Raman-Density Calibration Curve. *J. Phys. Condens. Matter* **2013**, *25*, 025402. [CrossRef] [PubMed]
29. Zhang, F.; Zhang, H.; Dong, G.; Qiu, J. Embedded Nanogratings in Germanium Dioxide Glass Induced by Femtosecond Laser Direct Writing. *J. Opt. Soc. Am. B* **2014**, *31*, 860. [CrossRef]
30. Yao, H.; Xie, Q.; Cavillon, M.; Dai, Y.; Lancry, M. Materials Roadmap for Inscription of Nanogratings inside Transparent Dielectrics Using Ultrafast Lasers. *Prog. Mater. Sci.* **2024**, *142*, 101226. [CrossRef]
31. Poe, B.T.; Romano, C.; Henderson, G. Raman and XANES Spectroscopy of Permanently Densified Vitreous Silica. *J. Non-Cryst. Solids* **2004**, *341*, 162–169. [CrossRef]
32. Guerette, M.; Ackerson, M.R.; Thomas, J.; Yuan, F.; Bruce Watson, E.; Walker, D.; Huang, L. Structure and Properties of Silica Glass Densified in Cold Compression and Hot Compression. *Sci. Rep.* **2015**, *5*, 15343. [CrossRef] [PubMed]
33. Guerette, M.; Ackerson, M.R.; Thomas, J.; Watson, E.B.; Huang, L. Thermally Induced Amorphous to Amorphous Transition in Hot-Compressed Silica Glass. *J. Chem. Phys.* **2018**, *148*, 194501. [CrossRef] [PubMed]
34. Martinet, C.; Kassir-Bodon, A.; Deschamps, T.; Cornet, A.; Le Floch, S.; Martinez, V.; Champagnon, B. Permanently Densified SiO_2 Glasses: A Structural Approach. *J. Phys. Condens. Matter* **2015**, *27*, 325401. [CrossRef] [PubMed]
35. Lide, D.R. *CRC Handbook of Chemistry and Physics*, 82nd ed.; CRC Press: Boca Raton, FL, USA, 2001; ISBN 9780849304828.
36. Tan, C.Z.; Arndt, J.; Xie, H.S. Optical Properties of Densified Silica Glasses. *Phys. B Condens. Matter* **1998**, *252*, 28–33. [CrossRef]
37. Güler, E.; Uğur, G.; Uğur, Ş.; Güler, M. A Theoretical Study for the Band Gap Energies of the Most Common Silica Polymorphs. *Chin. J. Phys.* **2020**, *65*, 472–480. [CrossRef]
38. Delly, J.G. Sénarmont Compensation: How to Accurately Measure Small Relative Retardations (0-1λ). Available online: https://www.mccrone.com/mm/measure-small-retardation-senarmont-compensation/ (accessed on 20 November 2023).
39. Xie, Q.; Cavillon, M.; Poumellec, B.; Pugliese, D.; Janner, D.; Lancry, M. Application and Validation of a Viscosity Approach to the Existence of Nanogratings in Oxide Glasses. *Opt. Mater.* **2022**, *130*, 112576. [CrossRef]
40. Poumellec, B.; Lancry, M.; Chahid-Erraji, A.; Kazansky, P.G. Modification Thresholds in Femtosecond Laser Processing of Pure Silica: Review of Dependencies on Laser Parameters [Invited]. *Opt. Mater. Express* **2011**, *1*, 766. [CrossRef]
41. Ollier, N.; Reghioua, I.; Cavani, O.; Mobasher, M.; Alessi, A.; le Floch, S.; Skuja, L. Probing Densified Silica Glass Structure by Molecular Oxygen and E′ Center Formation under Electron Irradiation. *Sci. Rep.* **2023**, *13*, 13657. [CrossRef]
42. The First Order (Full Wave) Retardation Plate. Available online: https://www.olympus-lifescience.com/en/microscope-resource/primer/techniques/polarized/firstorderplate/ (accessed on 10 January 2024).
43. Dai, Y.; Ye, J.; Gong, M.; Ye, X.; Yan, X.; Ma, G.; Qiu, J. Forced Rotation of Nanograting in Glass by Pulse-Front Tilted Femtosecond Laser Direct Writing. *Opt. Express* **2014**, *22*, 28500–28505. [CrossRef]
44. Rudenko, A.; Mauclair, C.; Garrelie, F.; Stoian, R.; Colombier, J.P. Light Absorption by Surface Nanoholes and Nanobumps. *Appl. Surf. Sci.* **2019**, *470*, 228–233. [CrossRef]
45. Richter, S.; Jia, F.; Heinrich, M.; Döring, S.; Peschel, U.; Tünnermann, A.; Nolte, S. The Role of Self-Trapped Excitons and Defects in the Formation of Nanogratings in Fused Silica. *Opt. Lett.* **2012**, *37*, 482–484. [CrossRef] [PubMed]

46. Beresna, M.; Gecevičius, M.; Kazansky, P.G.; Taylor, T.; Kavokin, A.V. Exciton Mediated Self-Organization in Glass Driven by Ultrashort Light Pulses. *Appl. Phys. Lett.* **2012**, *101*, 053120. [CrossRef]
47. Devine, R.A.B. Macroscopic and Microscopic Effects of Radiation in Amorphous SiO2. *Nucl. Instrum. Methods Phys. Res. B* **1994**, *91*, 378–390. [CrossRef]
48. Cerkauskaite, A.; Drevinskas, R.; Rybaltovskii, A.O.; Kazansky, P.G. Ultrafast Laser-Induced Birefringence in Various Porosity Silica Glasses: From Fused Silica to Aerogel. *Opt. Express* **2017**, *25*, 8011. [CrossRef] [PubMed]
49. Stopkin, S.I.; Lipatiev, A.S.; Fedotov, S.S.; Lipatieva, T.O.; Mikhailov, Y.V.; Lotarev, S.V.; Sigaev, V.N. Direct Laser Writing of High Retardance Structures in Nanoporous Glass. In Proceedings of the International Conference on Advanced Laser Technologies (ALT), Samara, Russia, 18–21 September 2023; Federal State Budgetary Institution of Science Federal Research Center, AM Prokhorov Institute of General Physics of the Russian Academy of Sciences: Moscow, Russia, 2023; p. 155.
50. Liu, P.; Januchta, K.; Jensen, L.R.; Bauchy, M.; Smedskjaer, M.M. Competitive Effects of Free Volume, Rigidity, and Self-adaptivity on Indentation Response of Silicoaluminoborate Glasses. *J. Am. Ceram. Soc.* **2020**, *103*, 944–954. [CrossRef]
51. Ojovan, M.I. Viscosity and Glass Transition in Amorphous Oxides. *Adv. Condens. Matter Phys.* **2008**, *2008*, 1–23. [CrossRef]
52. Xie, Q.; Cavillon, M.; Poumellec, B.; Lancry, M. Upper Temperature Limit for Nanograting Survival in Oxide Glasses: Publisher's Note. *Appl. Opt.* **2023**, *62*, 7156. [CrossRef]
53. Mobasher, M.; Lancry, M.; Lu, J.; Neuville, D.; Bellot Gurlet, L.; Ollier, N. Thermal Relaxation of Silica Phases Densified under Electron Irradiation. *J. Non Cryst. Solids* **2022**, *597*, 121917. [CrossRef]
54. Sakakura, M.; Lei, Y.; Wang, L.; Yu, Y.-H.; Kazansky, P.G. Ultralow-Loss Geometric Phase and Polarization Shaping by Ultrafast Laser Writing in Silica Glass. *Light Sci. Appl.* **2020**, *9*, 15. [CrossRef]
55. Poumellec, B.; Cavillon, M.; Lancry, M. Electrostatic Interpretation of Phase Separation Induced by Femtosecond Laser Light in Glass. *Crystals* **2023**, *13*, 393. [CrossRef]

II.3 NANOSCALE INVESTIGATIONS OF FEMTOSECOND LASER INDUCED NANOGRATINGS IN OPTICAL GLASSES

Nanoscale Advances

ROYAL SOCIETY OF CHEMISTRY

PAPER

View Article Online
View Journal | View Issue

Cite this: *Nanoscale Adv.*, 2024, **6**, 489

Nanoscale investigations of femtosecond laser induced nanogratings in optical glasses

Qiong Xie, Nadezhda Shchedrina, Maxime Cavillon, Bertrand Poumellec and Matthieu Lancry*

Femtosecond (fs) laser irradiation inside transparent materials has drawn considerable interest over the past two decades. More specifically, self-assembled nanogratings, induced by fs laser direct writing (FLDW) inside glass, enable a broad range of potential applications in optics, photonics, or microfluidics. In this work, a comprehensive study of nanogratings formed inside fused silica by FLDW is presented based on high-resolution electron microscopy imaging techniques. These nanoscale investigations reveal that the intrinsic structure of nanogratings is composed of oblate nanopores, shaped into nanoplanes, regularly spaced and oriented perpendicularly to the laser polarization. These nanoporous layers are forced-organized by light, resulting in a pseudo-organized spacing at the sub-wavelength scale, and observed in a wide range of optical glasses. In light of the current state of the art, we discuss the imprinting of nanoporous layers under thermomechanical effects induced by a plasma-mediated nanocavitation process.

Received 6th September 2023
Accepted 18th November 2023

DOI: 10.1039/d3na00748k

rsc.li/nanoscale-advances

Introduction

When a femtosecond (fs) laser beam is focused inside a glass material such as silica, the light is nonlinearly absorbed through multiphoton, tunneling and avalanche ionization mechanisms. These complex light/matter interactions lead to the formation of permanent modifications inside, and sometimes around, the irradiated volume. The transformations, while being a function of both glass composition and laser parameters, yield typical transformations classified into regimes, including (i) positive or negative refractive index modifications (commonly called type I),[1] (ii) formation of volume nanogratings (NGs) (at the root of form birefringence and labeled type II),[2,3] and (iii) nanovoid-like structures.[4] The NGs are believed to be the smallest self-organized structures ever created by light in the volume of a transparent material.

The focus of this work is on NGs, which have found use in various fields and applications such as health,[5] optical data storage,[6–8] optofluidics,[9,10] sensors in harsh environments[11,12] and a wide range of optical components like 3D optical waveguides, 3D geometric phase optics,[13] and polarizing optical devices.[14,15] Porous NGs and related strong birefringence are a spectacular manifestation of a light controlled glass decomposition, and have been primarily reported in pure silica[16] and slightly doped silica glasses.[17,18] Unlike surface ripples,[19] NGs were initially found only in a handful of materials: fused silica, sapphire, tellurium oxide, ULE glass and alkali-free aluminoborosilicate glasses.[20–23] From this list, silica is the material of choice to induce NGs. It brings a wide range of optical functionalities, coupled with high thermal and chemical stability, ease of nanoplasma initiation,[13,24] and its ability to form nanopores (high viscosity values over a wide temperature range *i.e.* a so-called "long glass"), as opposed to other optical glasses,[25] thereby offering significant industrial potential as the backbone of many today's photonics applications. Several studies on NG formation were conducted on multicomponent silicate glasses doped with germanium, phosphorus or titanium.[26] NGs were also found in porous silica prepared from phase-separated alkali-borosilicate glass by removing the borate phase in a hot acid solution.[27]

The importance of understanding NG formation mechanisms lies in the ability to reliably reproduce and potentially scale up the production of NGs, as well as to gain a deeper fundamental understanding of the complex light–matter interactions involved. Numerous research groups have investigated mechanisms behind the formation of self-organized nanogratings, providing valuable frameworks for advancing related scientific inquiries. At the nanoscale, Shimotsuma *et al.*[28] showed contrast NGs (around 20 nm width and periodicity from 140 to 320 nm) in back-scattered electron imaging corresponding to atomic density contrast. Chemical analysis by Auger spectroscopy revealed that these variations could correspond to oxygen depletion and related density modulation.[29] Hnatovsky *et al.*[30,31] reported the presence of nano-cracks and raised questions about whether these NGs can best be described as highly modified regions of differing materials (*e.g.* through bond breaking accumulation) or

Institut de Chimie Moléculaire et des Matériaux d'Orsay, CNRS-Université Paris Sud, Université Paris Saclay, Bât. 410, 91405 Orsay, France. E-mail: matthieu.lancry@universite-paris-saclay.fr

as some nanovoids. Regardless of the precise mechanistic explanation of nanoplanes (nanoplasma,[32] photon–plasmons interference,[33] plasmon–polaritons[34] or complex self-organization similar to a Turing structure), Lancry *et al.* observed that nanoplanes undergo a glass decomposition coupled with oxygen release.[35] Asai *et al.* observed a similar feature in GeO_2 glass[36] reinforcing the theory of the suggested decomposition process in these oxide glasses. This nanoporosity has been confirmed recently by Richter *et al.* using small angle X-ray scattering,[37] revealing the formation of elongated nanopores. In 2014 [38] and 2018,[19,39,40] the self-organization process was suggested to be seeded by nanoscale inhomogeneities such as voids and a nanocavitation mechanism was proposed. In 2013, the formation of SiO_{2-x} nanocrystals within nanoplanes was reported,[41] which could be in agreement with oxide decomposition.[42] In a second publication, the same group did not report nanocrystals but instead revealed that damaged nanoplanes contain randomly dispersed nanopores with a bimodal size distribution.[43] However, it appears that the use of HF etching degrades the quality of the observations and there are still no reliable nanoscale observations of NGs.

In this paper, we analyze NGs and related nanopore formation inside silica glass using transmission electron microscopy imaging and atomic force microscopy (AFM) techniques. We explored various geometries to probe not only the assembly of nanolayers but also their internal nanostructures. Through high-resolution imaging, we observed a nanoscale assembly of oblate nanopores constituting the nanolayers. Their long axis is found perpendicular to the light polarization while the average periodicity is decreased with the pulse number. These results are then discussed within the framework of a plasma-mediated nanocavitation process and generalized to a wide range of optical glasses.

Experimental details

The imprinting of NGs in the bulk of fused silica (Suprasil type-I) was performed using a 1030 nm mode locked Yb^{3+} doped fiber laser system (Satsuma, Amplitude Systemes Ltd.). The emitting laser delivered pulses of 250 fs at 100 kHz. Additionally, an aspheric lens (numerical aperture NA = 0.6) was used to focus the laser beam below the sample surface. Due to the minimization of spherical aberration, a laser track was inscribed at a depth of 200 μm. When the laser is translating along *X* and the linear polarization lying along *x*, we define it as "*Xx* writing" (or "*Xy* writing" for a polarization along the *y* axis). Then by moving the sample along the +*X*-axis with a scanning speed of 100 μm s^{-1}, a series of adjacent lines being 5 mm long were inscribed. The pulse energy was fixed to either 0.5 μJ or 1 μJ, that is, above the NG formation threshold.[44] Under these conditions, a strong form birefringence appears due to the presence of porous NGs. For completeness, the optical retardance was measured using a quarter waveplate technique and found to be on the order of 200 nm.[45]

To observe the NG nanostructure, each irradiated sample was cleaved using a diamond pen as shown in Fig. 1. Following this, the laser track cross-sections were analyzed by field emission gun scanning electron microscopy (FEG-SEM ZEISS SUPRA 55 VP) for studying the surface morphology. Furthermore, thin samples were prepared using a focus ion beam (FIB) instrument (Zeiss Neon 60, current 50 pA, accelerating voltage 30 kV) to extract slices of NG regions embedded in fused silica glass with a thickness under 50 nm. Here, we used a commercial TOPCON 002B electron microscope (200 kV with a resolution of 0.18 nm). Note that various geometries were employed as sketched in Fig. 1 *i.e.*, through transversal (*XY* plane) and longitudinal (*XZ* plane) views.

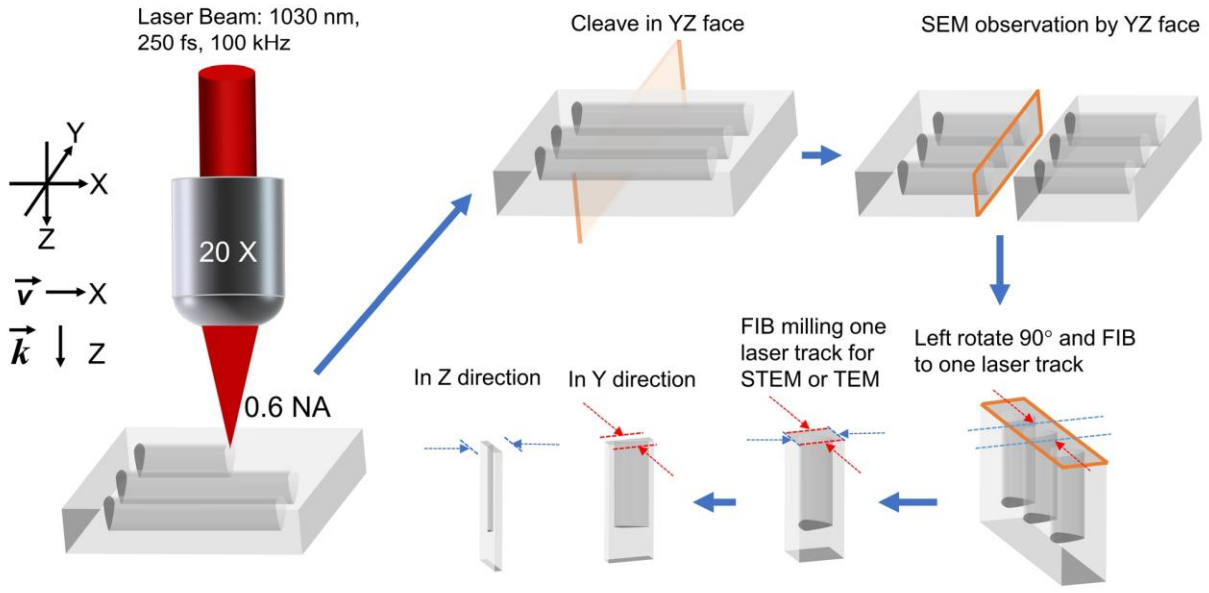

Fig. 1 Scheme of FLDW and sample cleaving orientation for subsequent electronic microscopy (SEM, STEM, and TEM) analyses.

Finally, scanning transmission electron microscopy (STEM) and high-resolution transmission electron microscopy (HR-TEM) were employed to analyze the internal nanostructures of NGs.

Results

After the FLDW step and before being sliced using the FIB technique, the cleaved samples were observed under a SEM. The resulting cross-sections are shown in Fig. 2 for both *Xx* and *Xy* writing configurations. The darker regions correspond to the nanopores (see Fig. 2(a)) and nanoplanes (see Fig. 2(b)). The gray and white parts correspond to the materials between nanoplanes and nanopores.[46] Fig. 2(a) corresponds to the inside of the nanoplanes that reveal a nanoporous material due to ultrafast oxide decomposition.[46] In addition, Fig. 2(b) exhibits the sub-wavelength periodicity of the nanoplanes (around $\lambda/2n$ with λ and n being the laser wavelength and the glass refractive index, respectively) along the laser track cross-section and oriented perpendicularly to the laser polarization orientation *Y*. The non-uniformity of the nanoplanes visible from Fig. 2(b) is detailed and discussed in the later analysis of TEM and STEM imaging.

To observe the NGs in the transverse view (*i.e.*, in the *XY* plane as indicated by the blue rectangles from Fig. 2), the samples were prepared using a FIB milling process as already described. The resulting morphology of the nanoplanes within the *XY* plane is shown in Fig. 3, with Fig. 3(a) serving as a guide for the reader. In these TEM micrographs, the bright regions are attributed to the fluctuations of the effective electronic thickness of laser-irradiated SiO_2. The bright lines are thinner regions and likely correspond to the nanoplanes and nanopores. The dark regions correspond to the material situated between nanoplanes. From **E** or **v** (*X*) direction, the nanoplanes exhibit an average period, labeled Λ, of 297 ± 14 nm (Fig. 3(c) and (d)). We observe that the nanoplanes are not perfectly aligned perpendicular to **v** or **E** and can present some tilt or wavy appearance. The white porous parts of the nanolayers appear to be several hundred nm long, discontinuous but connected by lamellas of weaker density along *Y* (perpendicularly to the polarization direction). In Fig. 3(e)–(g), the nanostructures are displayed with higher magnification. Nanopores clearly appear as the brightest part of the nanoplanes. They are aligned along each other but quite distributed in size and merging into some whiter matter lamellae like in Fig. 3(e). Based on TEM micrographs of Fig. 3(e)–(g), the nanoporous layer thickness exhibits variable values, averaged to 18 ± 12 nm. The size variation of the nanopores along the *Y* direction ranges from 36 to 56 nm. These observations are consistent with SEM observations in Fig. 2(a), and in agreement with the literature.[46]

In the aforementioned representation where **E** is parallel to **v**, the nanoplanes are thus aligned along **k**(*Z*) and *Y* directions in SEM or TEM observations. Now by selecting an additional slice by FIB milling identified by the red selection in Fig. 2(a), observations in the longitudinal view (*i.e.*, *XZ* plane) become possible. Corresponding micrographs are provided in Fig. 4(b)–(d). Fig. 4(a) serves as a guide for the reader. Along the *X* direction, which corresponds to either the **E** or **v** direction, the measured period Λ and thickness of the observed nanoplanes are around 296 ± 20 nm and 14 ± 2 nm, respectively. The observed nanoplanes showed discontinuities such as partially formed in the **k**(*Z*) direction and it appears pseudo-periodic as first observed in Fig. 2(b). Additionally, from Fig. 4(d) one can observe that both the shape and contrast of the nanoplanes are not homogeneous. The brighter parts correspond to more nanopores superimposed, or larger nanopores, and this is schematically visualized in Fig. 4(a). These overall nanoscale observations align with SEM images in Fig. 2(b), which contain nanopores and with a periodicity along *Z*. This process was attributed to an exciton–polariton-mediated light-organization

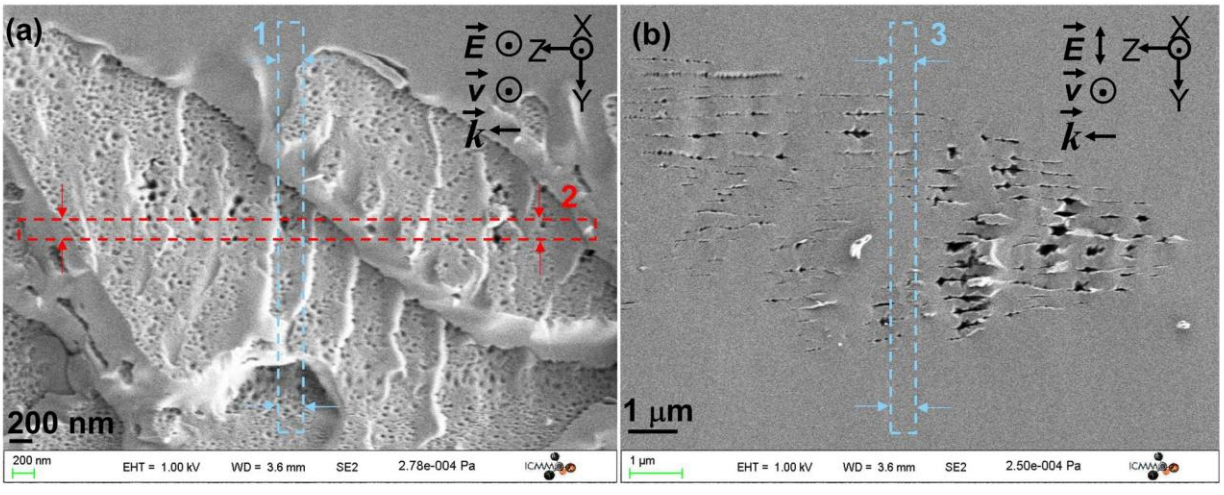

Fig. 2 SEM micrographs of (a) nanopores (*Xx* writing) and (b) nanoplanes (*Xy* writing). The red arrows in the *Y* direction and blue ones in the *Z* direction are the directions of FIB milling for TEM sample preparation (typical slice thicknesses are smaller than 50 nm). The numbers 1–3 correspond to the 3 slices extracted by FIB and subsequently observed.

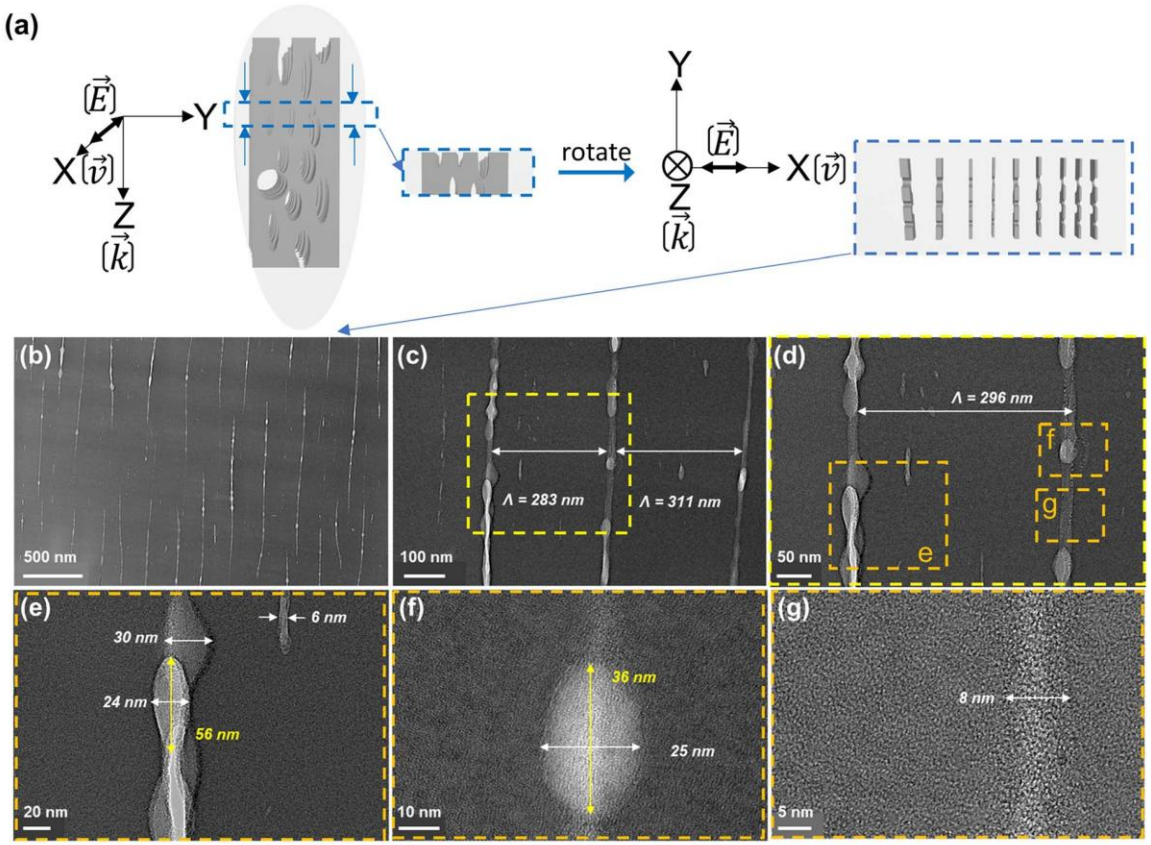

Fig. 3 (a) Geometry of the *XY* slice extracted by the FIB milling process. (b–g) TEM micrographs from Fig. 2(a) in blue arrows and *XY* plane observation with different size magnifications. The writing configuration is *Xx*.

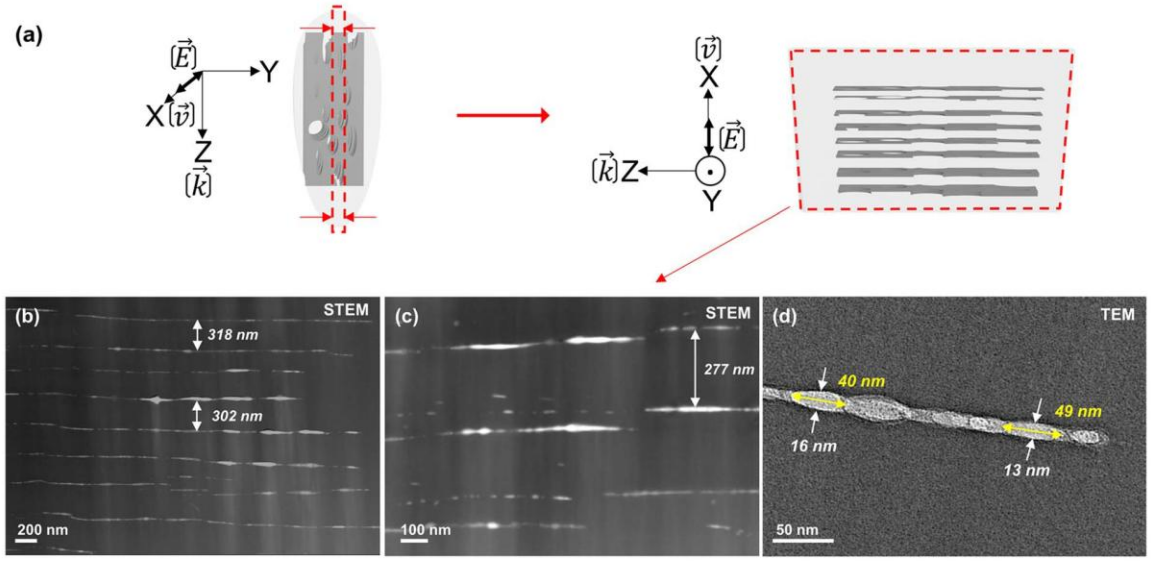

Fig. 4 (a) Schematic of the FIB milling process for extracting the *XZ* slice (see red arrows in Fig. 2(a)). (b and c) STEM and (d) TEM micrographs. The writing configuration is *Xx*.

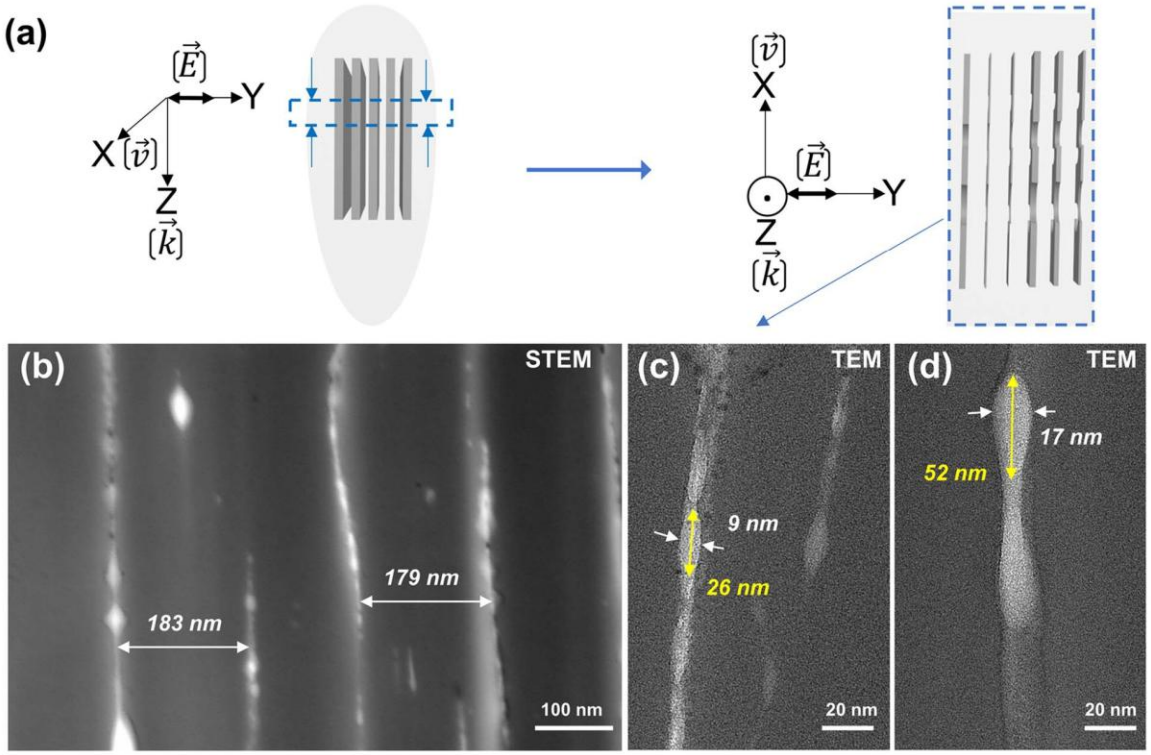

Fig. 5 (a) The schematic of the FIB milling process. (b) STEM and (c and d) TEM micrographs from Fig. 2(b) (nanoplanes) in blue arrows in *XY* plane observation. The writing configuration is *Xy*.

effect in glass similar to the exciton pattern formation effect observed in cold exciton gases.[34]

Now, changing again our point of view, the results in Fig. 5 represent the *XY* face by taking a sample slice along the blue arrows as sketched in Fig. 2(b). In this configuration, the nanoplanes are aligned along $\mathbf{k}(Z)$ and $\mathbf{v}(X)$ directions. In the $\mathbf{E}(Y)$ direction, the period and thickness of the nanoplanes are respectively 181 ± 4 nm and 13 ± 4 nm. The assembly of sub-wavelength nanolayers has a shorter period than for *Xx* configuration in agreement with the literature.[47] However, the dimensions of the nanopores are similar to the one observed for the *Xx* configuration. The nanoplanes exhibit a wavy shape along the $\mathbf{v}(X)$ direction as observed in Fig. 3 and 4.

To investigate NG formation in a multipulse regime, we investigated by SEM the step-by-step nanoscale modifications when pulse density is progressively varied from 1 to 2×10^5 pulses per μm. The resulting SEM micrographs are provided in Fig. 6 and highlight the transformation morphology occurring for a perpendicular writing configuration (*i.e.*, *Xy*). The pulse energy was fixed to 0.5 μJ. At a pulse density of 1 pulse per μm, only isotropic index changes are detected by optical microscopy and SEM reveals no specific nanostructure other than a slight contrast related to volume change. At lower pulse densities, between 2 and 10 pulses per μm, we detect a topographic contrast and interestingly some kind of nanopores that evolve into elongated ones (1–2 μm in length and 180–220 nm wide) as pulse density increases. The upper part of Fig. 6 shows atomic force microscopy (AFM) images obtained using intermittent contact mode. Besides the conventional surface topography image (left inset), the cantilever is driven close to a system resonance, to give reasonable amplitude for the oscillation and also to provide phase information, as shown in the right inset of Fig. 6. In particular the phase signal is sensitive to properties of the tip–sample interaction, and may reveal "mechanical information" about the surface such as elasticity, viscosity or adhesion. The observations reveal that the single elongated nanolayer seen below on the SEM micrograph is effectively made of an assembly of nanopores.

At higher pulse densities, these nanopores merge, thus creating some apparently long and thin (typ. 20–30 nm) nanolayers in agreement with the above HR-TEM results. Finally, as the number of nanolayers increases, their average spacing Λ decreases for pulse densities higher than 100 pulses per μm and reaching up to 2×10^5 pulses per μm in agreement with the literature.[48] Such quantitative evolution measured in SiO_2 is shown in the inset of Fig. 7.

Discussion

From the above HR-TEM and STEM imaging analysis, we can probe the 3D nanostructure of fs-imprinted NGs in silica. We can observe an array of oblate nanopores, which have a long axis oriented both along **k** and perpendicularly to **E**. The thickness of the nanolayers ranges from 6 to 30 nm and their extension perpendicularly to the laser polarization could reach a few μm or more. As shown in Fig. 6, under a multipulse regime, these

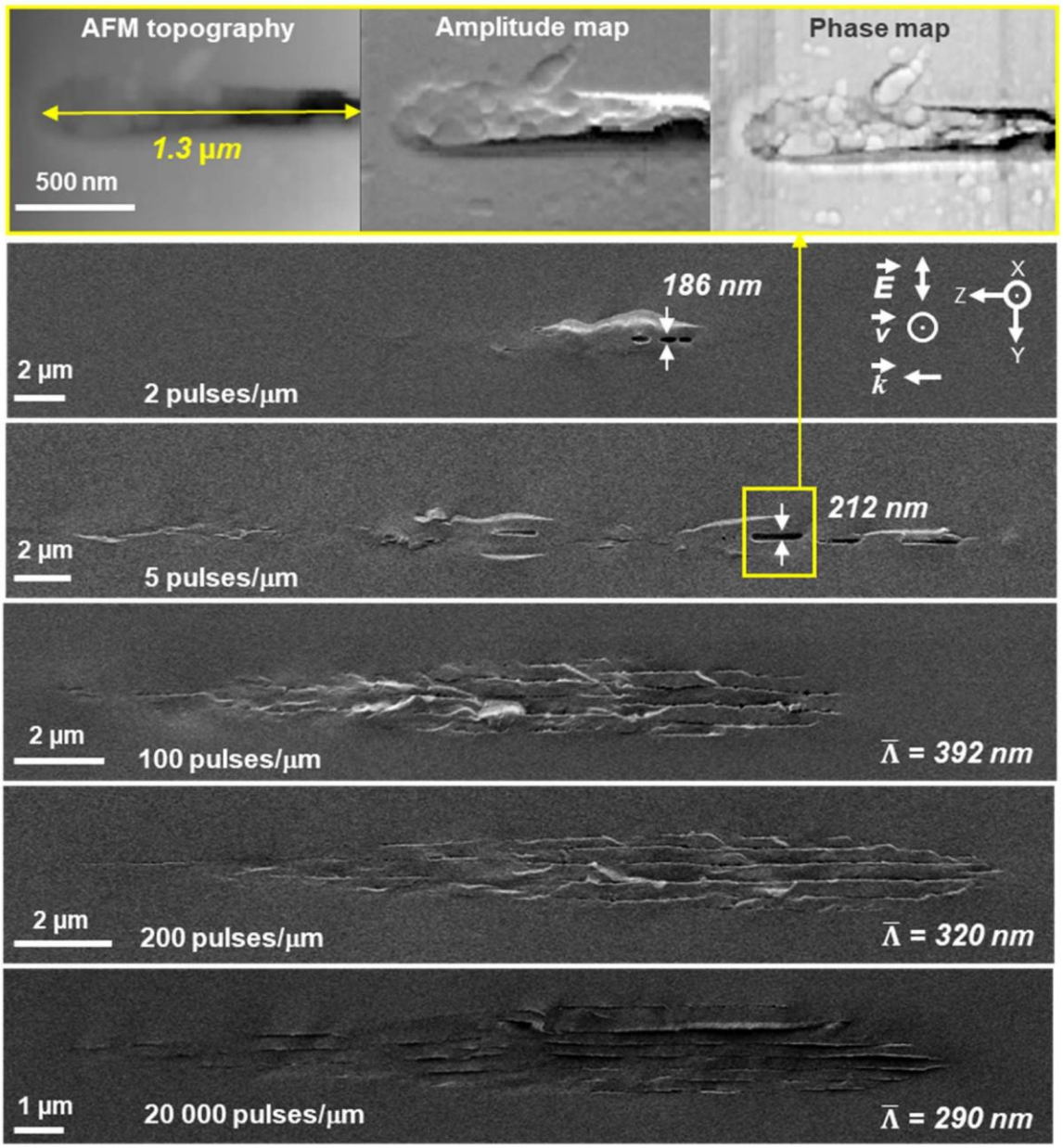

Fig. 6 AFM intermittent contact mode and SEM secondary electron images of laser track cross-section according to pulse density expressed in pulses per µm. The laser parameters were: 0.5 µJ per pulse, 1030 nm, 300 fs, 0.6 NA, 100 kHz and *Xy* configuration.

nanolayers are made of oblate nanopores that obviously "self-align" along each other to create these nanoplanes over quite long distances, as observed in the literature over the last two decades.[28] We can also observe a subwavelength ordering resulting in an average periodicity, perpendicular to **E**, on the order of 290–390 nm depending on the writing configuration.

Based on these results and on the reported mechanisms of the NG formation in the overall literature, we suggest that NGs are imprinted through a plasma-mediated nanocavitation process with a spatial ordering due to scattered wave interference,[38,49] which is described below.

The first step would be that some inhomogeneities of dielectric constant seed the process. These inhomogeneities (or seeds) could either be already present in the pristine glass or be photo-induced by the first pulse(s). Following these first instants, a spherical nanoplasma forms, stimulated by plasma density or temperature and evolves into an oblate-shaped nanoplasma over several pulses. This plasma-mediated process has been suggested in the literature. For example, Taylor R. *et al.*[50] suggested in 2008 that the presence of defects or color centers might seed the plasma, creating locally and easily ionized "nanospots" creating high plasma density. In the

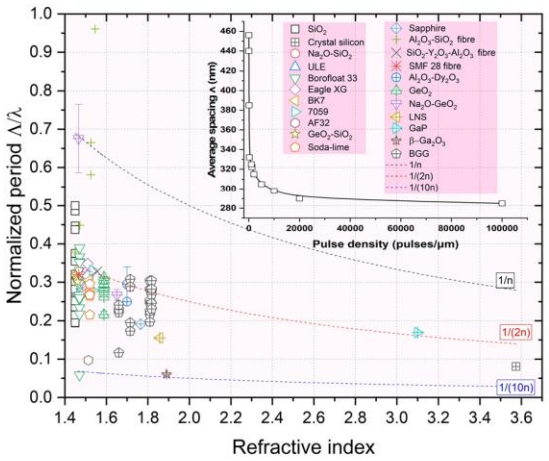

Fig. 7 Normalized period Λ/λ of the overall investigated glasses in the literature including commercial glasses *vs.* refractive index, *n*, measured at 550 nm. The laser wavelength λ used in the various experiments was typically between 515 and 1030 nm. Data were extracted from the following ref. 17, 20, 23–26, 45, 48 and 54–67.

model developed by Bhardwaj *et al.*,[51] the period Λ of nanogratings was assumed to remain between λ/n and $\lambda/2n$ and a period initially to be independent of pulse energy. However, the period was shown to decrease continuously with the number of laser pulses[52,53] but also when playing with the chemical composition such as doped SiO_2 (ref. 26) or in multicomponent glasses.[23,24] This is clearly illustrated in Fig. 7 where we summarized the normalized period Λ/λ *vs.* refractive index reported in the overall literature including a wide range of commercial glasses.

In 2014 Buschlinger R. *et al.*[38] conducted finite-difference time-domain (FDTD) modeling of plasma spatial structuration to investigate the periodicity of the NGs. These originated from the randomly distributed nanometer-size inhomogeneity that seeded the plasma structure. Due to the interference between scattered and incident light, the plasma owns a spatial structuration and grows against the direction of the light polarization. In 2016 A. Rudenko *et al.*[68] developed a numerical model to explain the formation of periodic volume NGs from random inhomogeneities with varying concentration and laser parameters. The contribution of an interplay of the physical processes (*e.g.*, the interference between the incident and the scattered waves, multiple scatterings, local field enhancement, and accumulation processes driven by multiphoton ionization) reinforced in the formation of NGs. Importantly, the period of NGs was found to scale down with growing pulse number, which in turn relies on scattering originating from nanoscale inhomogeneities. Following the above views, we suggest that nanogratings are not self-organized or self-assembled through diffusion-reaction mechanisms like Turing structures but rather "forced aligned" by the light pattern itself. In addition, the authors suggested the presence of some kinds of nanovoids, 0.6 nm average diameter, that are initiating the process. However, what seeds the process is not yet fully elucidated. It could be point defects (like self-trapped excitons (STEs) or self-trapped holes (STHs)), where the valence band possesses high energy and can easily be excited, some voids generated by the first pulse or even some glass-free volume that is already "available" in the pristine glass. Moreover, it exhibits a quite regular structure in the short range, with some *n*-membered rings creating well-known porosity at the sub-nm scale.[69] This is even reinforced in nanoporous sol–gel silica where the pulse number needed to imprint NGs was observed to be smaller,[70] when increasing the glass free volume.

From Fig. 3(c) and 4(c), we can observe some short (typ. <50 nm) but always oblate nanopores (with a long axis along **k** and perpendicular to **E**) with a thickness much smaller than 5 nm. They appear to be dispersedly distributed, but sometimes start to align along each other. When increasing the number of pulses, we can expect having more seeds (*e.g.*, some first nanopores or some STH) generated by the first pulses. This, in turn, leads to additional scattering centers resulting in a smaller periodicity based on the scattered wave interference model suggested by A. Rudenko *et al.*[68] and in agreement with F. Zimmermann *et al.*[48] who reported a decrease in NG period. It's worth mentioning that there are many "small size nanopores" between the long and well-arranged ones revealing the emergence, and growth, of new nanolayers like in Fig. 3(c) and 4(c). These are some kinds of "seeds" that will grow and merge (see Fig. 6) with neighboring nanopores to become a new porous nanolayer when increasing the number of pulses. According to the suggested "memory effects" involved in the mechanism of nonlinear ionization, new inhomogeneities are generated from pulse to pulse resulting in additional multiple scattering thus organizing the plasma distribution. It assumes that the pulse density is proportional to the concentration of the inhomogeneity.[68] As the pulse density increases, new plasma nanoplanes are generated "here and there" between the pre-existing ones following the light pattern. The imprinted nanolayers are initially made of elongated nanopores that grow from pulse-to-pulse and merge resulting in new nanolayers. Finally, from pulse to pulse, this will lead to a reduction of the average spacing $\bar{\Lambda}$ of the nanogratings as observed in the inset of Fig. 7.

The second step would be plasma formation and the local field enhancement resulting in ellipsoid (oblate) nanoplasma hot spot (high electron plasma density or energy) formation. Indeed, and even for a single pulse, the disordered spherical nanoplasma would evolve into an ellipsoidal shape and become oblate perpendicularly to the laser linear polarization. This occurs because the laser electric field triggers an asymmetric growth of the nanoplasma.[50] In contrast, for a circular polarization the nanoplasma hot spots should remain symmetric, resulting in spherical nanopores as has been observed in the type X regime.[13] Then in a multipulse view, there is an evolution of the oblate nanoplasmas into nanoplanes as shown in "post-mortem" experiments in Fig. 6.[53] The lengths of the oblate voids, whose direction is perpendicular to **E**, increase as the pulse number increases in agreement also with observations made in the type X regime.[13] From Fig. 4 one can also notice that such step by step nanopore growth also creates a longitudinal

component since nanopores are also "elongated" along the laser beam direction (**k**) and self-aligned to form nanoplanes.

The third step would be the energy transfer between electrons and phonons resulting in localized heat distribution at the nanoscale. Indeed, the modification of transparent glasses with wide bandgap dielectrics is induced rapidly by fs laser pulses through a multiphoton ionization (MPI) within a few femtoseconds. The electron plasma produced by MPI heats the media by electron–lattice coupling. Here we first assume no heat accumulation either considering a single pulse or multiple pulses in this process. The low heat capacity of electrons allows them to be easily heated to extremely high temperatures, but the glass matrix (the lattice) initially remains "cold" due to the relatively long electron–phonon relaxation time, typically 10 ps in SiO_2. After this time, the lattice will finally heat up, by a few 1000s of °C but this is a local effect. Indeed, after the free electron plasma energy is transferred to the lattice, the spatial distribution of the temperature is quite the same as the one of the plasmas because the timescale (<1 nanosecond) is too short to have some significant heat diffusion (on the order of the μs). In that sense, this is a plasma-mediated process, and the temperature distribution is the image of plasma 3D nanostructuration or the plasma "map".[46]

The fourth step would be the strain creation due to the temperature difference, between the nanoplasma hot spot and the background, resulting in a local thermal expansion. While the heat diffuses inside the material, the silicon–oxygen bonds would elongate and the glass specific volume expand within a time scale shorter than the characteristic acoustic relaxation time (typ. 500 ps in silica glass)[25] thus creating a moderate shock wave. So at a short time scale, there exists a localized nanostrain, which distributes ellipsoidally as a mirror image of the temperature map. This in turn will initiate the nanocavitation process at these specific locations. Indeed, a decrease of the local pressure would be created due to the formation of a rarefaction zone behind the "shock wave". Once this "negative pressure" difference develops between the "pore nuclei" and surrounding materials,[46] nanopores are imprinted at the image of the plasma ellipsoidal nanostructuration where the nanocavitation process starts. Finally, the formation of nanopores was observed in most oxide glasses[20,24,25,63,66,71–73] thus revealing that the glass oxide decomposition process occurred in all these compositions, highlighting in such a way that this is a general mechanism.

In this process it seems that nanopores may not have the chance to grow from a spherical shape but rather ellipsoid like the nanoplasma distribution itself for a linear polarization whereas a circular polarization would induce substantially spherical nanopores and thus no/low birefringence.[74] Following this view, type X is in fact the early birth of nanograting formation mostly observed for a low number of pulses and low energy. These type X modifications refer to oblate (for linear or elliptical polarization) nanopores with low birefringence and ultralow optical losses.[13] In this mechanism, the small nanopore diameters that are quite randomly arranged result in a decrease of the Rayleigh scattering and thus low optical losses offering exciting prospects for applications. For example, these type X modifications were exploited for achieving a 5D optical storage with high data capacity and long lifetime in fused silica[75] or to imprint ultralow loss 3D geometric phase optics.[13]

Conclusions

We investigated some nanoscale aspects of the formation of self-assembled porous nanogratings in oxide glasses. Oblate nanopores populate some array of non-continuous nanoplanes, which grow perpendicularly to the laser polarization direction and along the laser propagation direction. Some tiny elongated nanopores were also found between the long and fully-grown nanoplanes. These nanopores will grow and merge in a multipulse regime, resulting in a pulse-to-pulse decrease of the average periodicity much below $\lambda/2n$ as reviewed in this paper. The plasma-mediated nanocavitation model discussed the formation of these "light forced-organized" (rather than self-organized) sub-wavelength NGs in a multipulse view. Our tentative interpretation supported by HR-TEM and STEM investigations proposes an overall framework for NG formation. This mechanism is useful to guide future experiments to explore the interaction between laser and optical materials, along with enabling one to better control NG formation and its generalization in any kind of optical glasses.

Author contributions

Conceptualization, M. C. and M. L.; funding acquisition, B. P., M. C. and M. L.; investigation, Q. X., N. S.; methodology, Q. X., M. C. and M. L.; project administration, M. L.; resources, M. L.; supervision, M. L.; validation, Q. X.; visualization, Q. X. and M. C.; writing—original draft, Q. X.; writing—review & editing, Q. X., N. S., M. C., B. P. and M. L. All authors have read and agreed to the published version of the manuscript.

Conflicts of interest

There are no conflicts to declare.

Acknowledgements

This research was funded by Agence Nationale de la Recherche (ANR), FLAG-IR project, award number ANR-18-CE08-0004-01; and REFRACTEMP project, award number ANR-22-CE08-0001-01. Qiong Xie acknowledges the China Scholarship Council (CSC) for the funding of her PhD fellowship, no. 202007040018. We acknowledge the support of the SMIS beamline from synchrotron SOLEIL.

References

1 K. Davis, K. Miura, N. Sugimoto and K. Hirao, *Opt. Lett.*, 1996, **21**, 1729–1731.
2 Y. Shimotsuma, P. G. Kazansky, J. R. Qiu and K. Hirao, *Phys. Rev. Lett.*, 2003, **91**, 247405.

3 J. Lu, Y. Dai, Q. Li, Y. Zhang, C. Wang, F. Pang, T. Wang and X. Zeng, *Nanoscale*, 2019, **11**, 908–914.
4 C. Schaffer, A. Brodeur, N. Nishimura and E. Mazur, *Proc. SPIE*, 1999, **3616**, 143.
5 L. He, K. Sheehy and W. Culbertson, *Curr. Opin. Ophthalmol.*, 2011, **22**, 43–52.
6 E. N. Glezer, M. Milosavljevic, L. Huang, R. J. Finlay, T. H. Her, J. P. Callan and E. Mazur, *Opt. Lett.*, 1996, **21**, 2023–2025.
7 A. Podlipensky, A. Abdolvand, G. Seifert and H. Graener, *Appl. Phys. A: Mater. Sci. Process.*, 2005, **80**, 1647–1652.
8 M. Watanabe, H. Sun, S. Juodkazis, T. Takahashi, S. Matsuo, Y. Suzuki, J. Nishii and H. Misawa, *Jpn. J. Appl. Phys.*, 1998, **37**, L1527–L1530.
9 C. Monat, P. Domachuk and B. Eggleton, *Nat. Photonics*, 2007, **1**, 106–114.
10 Y. Bellouard, A. Said, M. Dugan and P. Bado, *Opt. Express*, 2004, **12**, 2120–2129.
11 Y. Wang, M. Cavillon, J. Ballato, T. Hawkins, T. Elsmann, M. Rothhardt, R. Desmarchelier, G. Laffont, B. Poumellec and M. Lancry, *Adv. Opt. Mater.*, 2022, **10**, 2200379.
12 S. J. Mihailov, *Sensors*, 2012, **12**, 1898–1918.
13 M. Sakakura, Y. Lei, L. Wang, Y. H. Yu and P. G. Kazansky, *Light Sci. Appl.*, 2020, **9**, 15.
14 K. M. Davis, K. Miura, N. Sugimoto and K. Hirao, *Opt. Lett.*, 1996, **21**, 1729–1731.
15 R. Nielsen, A. Boltasseva, A. Kristensen, S. Bozhevolnyi, V. Volkov, I. Fernandez Cuesta and A. Klukowska, presented in part at *Advanced Fabrication Technologies for Micro/Nano Optics and Photonics*, San Jose, California, USA, 2008.
16 S. Richter, M. Heinrich, S. Döring, A. Tünnermann, S. Nolte and U. Peschel, *J. Laser Appl.*, 2012, **24**, 042008.
17 M. Lancry, J. Canning, K. Cook, M. Heili, D. R. Neuville and B. Poumellec, *Opt. Mater. Express*, 2016, **6**, 321–330.
18 Y. Shimotsuma, S. Kubota, A. Murata, T. Kurita, M. Sakakura, K. Miura, M. Lancry and B. Poumellec, *J. Am. Ceram. Soc.*, 2017, **100**, 3912–3919.
19 A. Rudenko, J.-P. Colombier, S. Höhm, A. Rosenfeld, J. Krüger, J. Bonse and T. E. Itina, *Sci. Rep.*, 2017, **7**, 12306.
20 Y. Wang, S. Wei, M. R. Cicconi, Y. Tsuji, M. Shimizu, Y. Shimotsuma, K. Miura, G. D. Peng, D. R. Neuville, B. Poumellec and M. Lancry, *J. Am. Ceram. Soc.*, 2020, **103**, 4286–4294.
21 Y. Shimotsuma, K. Hirao, J. R. Qiu and K. Miura, *J. Non-Cryst. Solids*, 2006, **352**, 646–656.
22 S. Richter, D. Möncke, F. Zimmermann, E. I. Kamitsos, L. Wondraczek, A. Tünnermann and S. Nolte, *Opt. Mater. Express*, 2015, **5**, 1834–1850.
23 S. S. Fedotov, R. Drevinskas, S. V. Lotarev, A. S. Lipatiev, M. Beresna, A. Čerkauskaitė, V. N. Sigaev and P. G. Kazansky, *Appl. Phys. Lett.*, 2016, **108**, 071905.
24 Q. Xie, M. Cavillon, D. Pugliese, D. Janner, B. Poumellec and M. Lancry, *Nanomaterials*, 2022, **12**, 2986.
25 Q. Xie, M. Cavillon, B. Poumellec, D. Pugliese, D. Janner and M. Lancry, *Opt. Mater.*, 2022, **130**, 112576.
26 S. Richter, C. Miese, S. Döring, F. Zimmermann, M. J. Withford, A. Tünnermann and S. Nolte, *Opt. Mater. Express*, 2013, **3**, 1161–1166.
27 Y. Liao, Y. Shen, L. Qiao, D. Chen, Y. Cheng, K. Sugioka and K. Midorikawa, *Opt. Lett.*, 2013, **38**, 187–189.
28 Y. Shimotsuma, P. G. Kazansky, J. Qiu and K. Hirao, *Phys. Rev. Lett.*, 2003, **91**, 247405.
29 Y. Shimotsuma, P. Kazansky, J. Qiu and K. Hirao, *Phys. Rev. Lett.*, 2003, **91**, 247405.
30 C. Hnatovsky, R. Taylor, P. Rajeev, E. Simova, V. Bhardwaj, D. Rayner and P. Corkum, *Appl. Phys. Lett.*, 2005, **87**, 014104.
31 C. Hnatovsky, R. Taylor, E. Simova, V. Bhardwaj, D. Rayner and P. Corkum, *Opt. Lett.*, 2005, **30**, 1867–1869.
32 P. Rajeev, M. Gertsvolf, C. Hnatovsky, E. Simova, R. Taylor, P. Corkum, D. Rayner and V. Bhardwaj, *J. Phys. B: At., Mol. Opt. Phys.*, 2007, **40**, S273.
33 P. G. Kazansky, E. Bricchi, Y. Shimotsuma and K. Hirao, presented in part at *Conference on Lasers and Electro-Optics/ Quantum Electronics and Laser Science Conference and Photonic Applications Systems Technologies*, Baltimore, Maryland, 2007.
34 M. Beresna, M. Gecevičius, P. G. Kazansky, T. Taylor and A. V. Kavokin, *Appl. Phys. Lett.*, 2012, **101**, 053120.
35 M. Lancry, B. Poumellec, J. Canning, K. Cook, J. Ä. Poulin and F. Brisset, *Laser Photon. Rev.*, 2013, **7**, 953–962.
36 T. Asai, Y. Shimotsuma, T. Kurita, A. Murata, S. Kubota, M. Sakakura, K. Miura, F. Brisset, B. Poumellec and M. Lancry, *J. Am. Ceram. Soc.*, 2015, **98**, 1471–1477.
37 S. Richter, A. Plech, M. Steinert, M. Heinrich, S. Döring, F. Zimmermann, U. Peschel, E. B. Kley, A. Tünnermann and S. Nolte, *Laser Photon. Rev.*, 2012, **6**, 787–792.
38 R. Buschlinger, S. Nolte and U. Peschel, *Phys. Rev. B: Condens. Matter Mater. Phys.*, 2014, **89**, 184306.
39 A. Rudenko, H. Ma, V. P. Veiko, J.-P. Colombier and T. E. Itina, *Appl. Phys. A: Mater. Sci. Process.*, 2017, **124**, 63.
40 A. Rudenko, J. P. Colombier and T. E. Itina, *Phys. Chem. Chem. Phys.*, 2018, **20**, 5887–5899.
41 V. Oliveira, S. P. Sharma, P. Herrero and R. Vilar, *Opt. Lett.*, 2013, **38**, 4950–4953.
42 C. M. Pépin, E. Block, R. Gaal, J. Nillon, C. Hoenninger, P. Gillet and Y. Bellouard, *arXiv*, 2018, preprint, arXiv:1806.10802, DOI: **10.48550/arXiv.1806.10802**.
43 S. P. Sharma, V. Oliveira, P. Herrero and R. Vilar, *J. Appl. Phys.*, 2014, **116**, 053106.
44 B. Poumellec, M. Lancry, A. Chahid-Erraji and P. G. Kazansky, *Opt. Mater. Express*, 2011, **1**, 766–782.
45 Y. Wang, S. Wei, M. Cavillon, B. Sapaly, B. Poumellec, G.-D. Peng, J. Canning and M. Lancry, *Appl. Sci.*, 2021, **11**, 600.
46 M. Lancry, B. Poumellec, J. Canning, K. Cook, J.-C. Poulin and F. Brisset, *Laser Photon. Rev.*, 2013, **7**, 953–962.
47 R. Buividas, M. Mikutis and S. Juodkazis, *Prog. Quant. Electron.*, 2014, **38**, 119–156.
48 F. Zimmermann, A. Plech, S. Richter, A. Tünnermann and S. Nolte, *Appl. Phys. Lett.*, 2014, **104**, 211107.
49 A. Rudenko, J. P. Colombier, T. E. Itina and R. Stoian, *Adv. Opt. Mater.*, 2021, **9**, 2100973.

50 R. Taylor, C. Hnatovsky and E. Simova, *Laser Photon. Rev.*, 2008, **2**, 26–46.
51 V. R. Bhardwaj, E. Simova, P. P. Rajeev, C. Hnatovsky, R. S. Taylor, D. M. Rayner and P. B. Corkum, *Phys. Rev. Lett.*, 2006, **96**, 057404.
52 F. Zimmermann, A. Plech, S. Richter, A. Tünnermann and S. Nolte, *Laser Photon. Rev.*, 2016, **10**, 327–334.
53 R. Desmarchelier, B. Poumellec, F. Brisset, S. Mazerat and M. Lancry, *World J. Nano Sci. Eng.*, 2015, **5**, 115–125.
54 S. E. Wei, Y. Wang, H. Yao, M. Cavillon, B. Poumellec, G. D. Peng and M. Lancry, *Sensors*, 2020, **20**, 762.
55 S. V. Lotarev, S. S. Fedotov, A. I. Kurina, A. S. Lipatiev and V. N. Sigaev, *Opt. Lett.*, 2019, **44**, 1564–1567.
56 M. Cavillon, M. Lancry, B. Poumellec, Y. Wang, J. Canning, K. Cook, T. Hawkins, P. Dragic and J. Ballato, *J. Phys.: Photonics*, 2019, **1**, 042001.
57 J. Wang, X. Liu, Y. Dai, Z. Wang and J. Qiu, *Opt. Express*, 2018, **26**, 12761–12768.
58 S. Lotarev, S. Fedotov, A. Lipatiev, M. Presnyakov, P. Kazansky and V. Sigaev, *J. Non-Cryst. Solids*, 2018, **479**, 49–54.
59 Y. Nakanishi, Y. Shimotsuma, M. Sakakura, M. Shimizu and K. Miura, presented in part at the *Laser-Based Micro- and Nanoprocessing XII*, San Francisco, California, United States, 2018.
60 P. Dragic, M. Cavillon and J. Ballato, *Int. J. Appl. Glass Sci.*, 2017, **9**, 421–427.
61 J. Cao, B. Poumellec, L. Mazerolles, F. Brisset, A.-L. Helbert, S. Surble, X. He and M. Lancry, *J. Am. Ceram. Soc.*, 2017, **100**, 115–124.
62 Y. Shimotsuma, T. Sei, M. Mori, M. Sakakura and K. Miura, *Appl. Phys. A: Mater. Sci. Process.*, 2016, **122**, 122.
63 S. Mori, K. Torataro, S. Yasuhiko, S. Masaaki and M. Kiyotaka, *J. Laser Micro/Nanoeng.*, 2016, **11**, 87–90.
64 M. Lancry, F. Zimmerman, R. Desmarchelier, J. Tian, F. Brisset, S. Nolte and B. Poumellec, *Appl. Phys. B: Lasers Opt.*, 2016, **122**, 66.
65 M. Mori, Y. Shimotsuma, T. Sei, M. Sakakura, K. Miura and H. Udono, *Phys. Status Solidi A*, 2015, **212**, 715–721.
66 T. Asai, Y. Shimotsuma, T. Kurita, A. Murata, S. Kubota, M. Sakakura, K. Miura, F. Brisset, B. Poumellec, M. Lancry and J. Ballato, *J. Am. Ceram. Soc.*, 2015, **98**, 1471–1477.
67 W. Dirk, G. Jens, B. Nelli and H.-S. Herbert, *Opt. Express*, 2008, **16**, 1517–1522.
68 A. Rudenko, J.-P. Colombier and T. E. Itina, *Phys. Rev. B*, 2016, **93**, 075427.
69 R. H. Doremus, *Glass Science*, Wiley, 1973.
70 A. Cerkauskaite, R. Drevinskas, A. O. Rybaltovskii and P. G. Kazansky, *Opt. Express*, 2017, **25**, 8011–8021.
71 H. Yao, Q. Xie, M. Cavillon, D. R. Neuville, D. Pugliese, D. Janner, Y. Dai, B. Poumellec and M. Lancry, *Opt. Express*, 2023, **31**, 15449–15460.
72 H. Yao, R. Zaiter, M. Cavillon, B. Sapaly, F. Calzavara, P. Delullier, T. Cardinal, Y. Dai, B. Poumellec and M. Lancry, *Ceram. Int.*, 2021, **47**, 34235–34241.
73 F. Zhang, H. Zhang, G. Dong and J. Qiu, *J. Opt. Soc. Am. B*, 2014, **31**, 860–864.
74 Y. Lei, G. Shayeganrad, H. Wang, M. Sakakura, Y. Yu, L. Wang, D. Kliukin, L. Skuja, Y. Svirko and P. G. Kazansky, *Light: Sci. Appl.*, 2023, **12**, 74.
75 H. Wang, Y. Lei, L. Wang, M. Sakakura, Y. Yu, G. Shayeganrad and P. G. Kazansky, *Laser Photon. Rev.*, 2022, **16**, 2100563.

II.4 Nano-FTIR spectroscopy reveals SiO_2 densification within fs-laser induced nanogratings

Nanoscale Advances

ROYAL SOCIETY OF CHEMISTRY

PAPER

View Article Online
View Journal

Cite this: DOI: 10.1039/d4na00409d

Nano-FTIR spectroscopy reveals SiO_2 densification within fs-laser induced nanogratings†

Nadezhda Shchedrina, *[ab] Gergely Nemeth,[c] Ferenc Borondics,[c] Nadege Ollier[b] and Matthieu Lancry[a]

This study explores the structural transformations induced by femtosecond (fs) laser inscriptions in glass, with a focus on type II modifications (so-called nanogratings), crucial for advanced optical and photonic technologies. Our novel approach employs scattering-type scanning near-field optical microscopy (s-SNOM) and synchrotron radiation nanoscale Fourier-transform infrared spectroscopy (nano-FTIR) to directly assess the nanoscale structural changes in the laser tracks, potentially offering a comprehensive understanding of the underlying densification mechanisms. The results reveal the first direct nanoscale evidence of densification driven by HP-HT within fs-laser inscribed tracks, characterized by a significant shift of the main infrared (IR) vibrational structural band of silica glass. It reveals moreover a complex interplay between type I and type II modifications.

Received 15th May 2024
Accepted 5th August 2024

DOI: 10.1039/d4na00409d

rsc.li/nanoscale-advances

1 Introduction

Femtosecond (fs) laser modifications in glass have gained significant attention in material processing, enabling 3D localized modifications at the nanoscale with widespread implications for optical and photonic technologies. These modifications manifest as type I, type II, or type III, dependent on the energy deposition and thus laser processing parameters.[1] Type I alters the refractive index quite isotropically; type II, referred to as nanogratings, introduces a strong linear birefringence; and type III creates nano/micro-voids with a densified shell.

Among these, type II modifications and underlying nanogratings have become a crucial component in the development of optical and photonic technologies. Owing to their unique linear and circular birefringence[2] and high thermal stability,[3,4] nanogratings are used across a broad spectrum of applications, such as 3D optical waveguides,[5] birefringent devices,[6–8] advancements in long lifetime optical data storage,[3,9] temperature sensors,[10,11] and high-temperature structural health monitoring.[12]

Focusing a fs-laser beam onto glass, such as silica, initiates nonlinear absorption through multiphoton, tunneling, and avalanche ionization mechanisms, resulting in permanent structural modifications.[13] As the laser intensity surpasses a certain threshold, multiphoton ionization generates a plasma with a high-density electron cloud.[14] The interference between the incident laser light and light scattered from inhomogeneities of the dielectric constant results in periodic modulations of the electron plasma density and temperature. Such modulations and the evolution of plasma hotspots into elongated nanoplasma regions, driven by local field enhancement, facilitate the emergence of nanogratings.[15] Oriented perpendicular to the laser's linear polarization, these nanogratings comprise structured layers of oblate nanopores.[16,17] Despite advances in understanding nanopore formation, the material between these layers, assumed to be densified, remains less understood. Exploring the occurrence of densification and the structural changes within this interlayer material is vital for a full grasp of nanograting mechanisms.

There are several studies focusing on the texture, composition, and properties of the material between fs-laser induced nanogratings. Some experimental investigations have provided indirect evidence of densification within these regions. Following the discovery of nanogratings, studies to understand induced negative uniaxial birefringence revealed significant densification.[18] Researchers observed an average increase of the refractive index between nonporous layers through the analysis of its directional changes using polarized probe light.

Raman spectroscopy was similarly employed for assessing densification in femtosecond laser-inscribed tracks.[19–24] Using Raman spectroscopy, Bellouard *et al.*[20] reported an 8% densification in glass subjected to fs laser processes by drawing comparisons with high-pressure, high-temperature (HPHT) treated samples, indicating a significant alteration in the

[a]Institut de Chimie Moléculaire et des Matériaux d'Orsay (ICMMO), Université Paris-Saclay, CNRS, Bât. 410, 91405 Orsay, France. E-mail: nadezhda.shchedrina@universite-paris-saclay.fr

[b]Laboratoire des Solides Irradiés, École Polytechnique, CNRS, CEA/DRF/IRAMIS, Institut Polytechnique de Paris, 91128 Palaiseau Cedex, France

[c]SMIS Beamline, SOLEIL Synchrotron, L'Orme des Merisiers, 91190 Saint Aubin, France

† Electronic supplementary information (ESI) available. See DOI: https://doi.org/10.1039/d4na00409d

material's structure. Further studies,[22] correlating the D2 band intensity and FWHM of the R-band with samples densified by HPHT or HPHT followed by high-energy, high-dose electron irradiation, estimated the post-irradiation glass density to be around 2.25–2.27. However, it should be noted that the D2 band intensity, while increasing linearly with density up to a threshold (around a density of 2.3), may not serve as a definitive density estimator in SiO_2, as it decreases for densities beyond this point.[25]

Another recent study on fs-laser densification delved into the effects of shock waves generated by two spatially separated focused beams, acting as quasi-simultaneous "pressure-wave emitters".[23] This method, using the same approach of silica's Raman signature analysis, estimated the pressure from laser pulses to reach tens of GPa. However, the Raman spectroscopy results, although insightful for densification estimates, reveal the complexity of analyzing the entire laser track due to its composite structure, comprising porous nanolayers and densified interlayers.

Another method to examine the material changes within laser-inscribed tracks involves measuring the volume change and mechanical properties through micro-cantilever deflections.[21,24,26,27] Type I modifications typically result in volume reduction and material densification, as evidenced by micro-cantilevers moving upwards. Type II modifications cause micro-cantilevers to move downwards due to nanopore expansion. These studies indicate that femtosecond lasers can control a stress-state inversion in bulk fused silica, leading to either stress increase or decrease.[21] Notably, the material between porous layers shares characteristics with type I modifications, suggesting a denser structure with a higher Young's modulus than pristine silica.[21,27] Further, while porous layers display a significantly lower Young's modulus, interlayer material exhibits an increased Young's modulus of about 80 GPa[26,27] suggesting a local densification.

All these findings provide indirect but solid evidence of densification in fs-laser modified regions, however without nanoscale spatial resolution. Despite advances in characterizing fs-laser induced nanogratings, a direct, nanoscale understanding of the densification process remains elusive. Current methods offer a composite view that obscures the magnitude of densification, leaving the specific mechanisms, whether thermal, mechanical, thermo-mechanical, or defect accumulation, quite speculative. Techniques like scanning electronic microscopy (SEM) and atomic force microscopy (AFM) provide nanoscale imaging but fail in revealing the densification process. This gap underscores the need for approaches capable of directly assessing the densification at the nanoscale, which could significantly advance our understanding of the underlying mechanisms. This study utilizes scattering-type scanning near-field optical microscopy (s-SNOM) and synchrotron radiation nanoscale Fourier-transform infrared spectroscopy (nano-FTIR), tools for unveiling the spectral signature of densification at the nanoscale. These methodologies offer unique insights into the densification occurrence and potential underlying mechanisms within type II modifications.

2 Experimental details

The nanogratings were imprinted in type II silica glass (Suprasil CG, Heraeus) utilizing a fs fiber laser with a wavelength of 1030 nm (Satsuma, Amplitude Systemes Ltd, Pessac, France). The laser emitted pulses at a duration of 250 fs, with a repetition rate of 100 kHz. An aspheric lens with a numerical aperture of 0.6 was used to focus the laser beam at a depth of 200 μm below the surface. The scanning speed varied from 0.005 to 0.8 mm s^{-1} to achieve a range of pulses density values from 1.3 to 20 000 pulses per mm. The laser light was linearly polarized and set in two orientations, parallel (*Xx* configuration) and perpendicular (*Xy*) to the laser writing direction, creating a series of lines with pulse energies exceeding the nanograting threshold (namely 0.3 μJ in our conditions) as schematically described in Fig. 1a.

Post-inscription, the sample was cleaved along the *z*–*y* plane to analyze the cross-section of the laser tracks, see Fig. 1b. Subsequently, the cross-sections were examined using field emission gun scanning electron microscopy (FEG-SEM, ZEISS SUPRA 55 VP, Zeiss, Oberkochen, Germany) to investigate the surface morphology and to construct a detailed map to assist subsequent IR measurements at the synchrotron.

Infrared analyses were conducted at the SMIS beamline of the Synchrotron Soleil in Saint Aubin, France. To characterize the nanostructural modifications (Fig. 1c), we employed scattering-type Scanning Near-field Optical Microscopy (s-SNOM). s-SNOM is a combination of AFM and optical microscopy. It utilizes a metal-coated AFM tip illuminated by focused light. The incident light creates the optical near field that is localized to the apex of the tip. When the tip is brought into close proximity of the sample, the near-field interaction results in scattered light. By measuring both the amplitude and the phase of the scattered light s-SNOM is capable of retrieving the complex optical properties of the sample.[28]

The instrument at SMIS (IR-neaSCOPE, Attocube system AG, Haar, Germany) was used in two different modes. First, taking advantage of the broadband synchrotron radiation nanoscale Fourier-transform infrared spectroscopy (nano-FTIR) was used to collect both infrared near-field amplitude and phase spectra from various sections. This allows identifying optimal wavelengths for subsequent s-SNOM single-wavelength imaging by a built-in quantum cascade laser (QCL). In all the measurements the AFM operated in tapping mode and the optical signal was demodulated at the second harmonic of the tip oscillation frequency.[28]

The main feature of the silica glass infrared spectrum originates from the collective asymmetric stretching vibration of Si–O–Si subunits of its structure.[29] This infrared active phonon band is located between 900 and 1300 cm^{-1}. This strong excitation has its signature both in the amplitude and the phase response. After initial examinations, a wavenumber of 1130 cm^{-1} was chosen from the high wavenumber/frequency edge of the phonon peak for its sensitivity to spectral shifts attributed to fs-laser induced structural changes.

3 Results

To investigate the densification of the interlayer material within type II modification, it is important to examine the early stages,

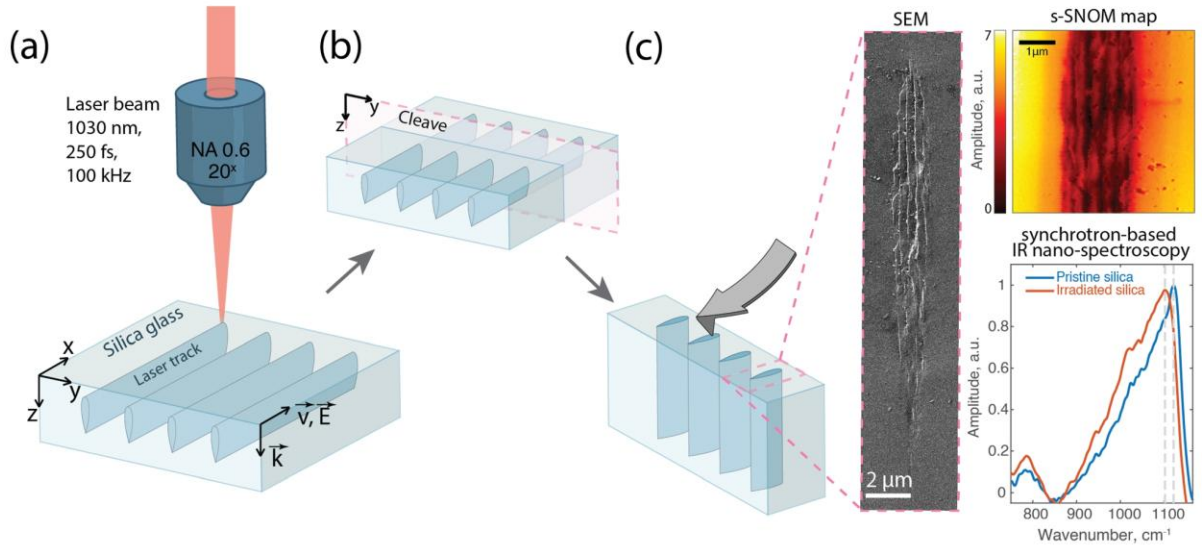

Fig. 1 Fabrication and characterization of fs-inscribed laser tracks in silica glass. (a) Laser writing process. (b) Cleaving of the sample for cross-sectional access. (c) Morphological and structural characterization using SEM, s-SNOM amplitude mapping, and synchrotron-based nano-FTIR spectroscopy. Insets show the SEM image and s-SNOM amplitude map illustrating the cross-section of the laser track (200 pulses per micron), as well as nano-FTIR amplitude spectra of both pristine and irradiated areas.

the energy threshold of formation during the absence of nanogratings and low birefringence. Therefore, we employed a variation in pulse density, starting from 2 pulses per micron, to capture the initial phase of nanograting development, sometimes related to type X in the literature.[5] The laser inscription was performed on silica glass, which was prepared as outlined in the experimental section, and subsequently cleaved and examined using FEG-SEM.

Fig. 2 shows a laser track inscribed with 2 pulses per micron in an *Xx* (perpendicular) configuration. The SEM image (Fig. 2a) reveals the morphology of the laser track, highlighting topographical changes at the track's head, including the emergence of slightly elongated (along *z*) nanopores. On the other hand, the tail of the track appears flat. This observation is corroborated by the AFM image (Fig. 2b), which similarly depicts topological alterations at the head with no significant changes in the tail, except at the very end. It is important to mention the presence of contaminants along the sides of the laser track, attributable to residual dust due to the cleaving process. This contamination is unrelated to the intrinsic structure of the sample.

Subsequently, we utilized s-SNOM imaging and nano-FTIR spectroscopy to obtain IR maps of the laser tracks. Through near-field amplitude mapping at 1130 cm^{-1}, pronounced structural modifications were found as shown in Fig. 2c. Visual examination of the color map distinctly highlighted an extensive area, revealing significant fs-laser induced structural transformations in the silica glass, changes that elude detection by SEM and AFM analyses. Within the irradiated track, the reflectance amplitude at 1130 cm^{-1} was notably reduced in comparison to the unaltered surrounding regions. This observation is additionally confirmed in the cross-sectional profile inset in Fig. 2c. This reduction likely indicates a shift of the IR main band of silica glass to lower wavenumbers, as 1130 cm^{-1} is positioned on the higher-frequency side, or right side, of this band. Similar observations were made in the phase map, which showed significant phase variations within the laser-affected

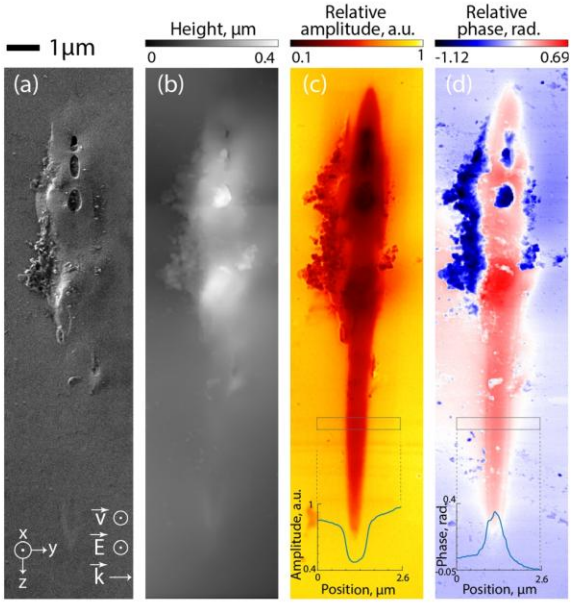

Fig. 2 (a) SEM image of a track written with 2 pulses per micron; (b) AFM surface topography; (c) 2D map of near-field scattered amplitude at 1130 cm^{-1}; inset: cross-section profile indicating amplitude decrease across the laser track; (d) near-field phase map measured at 1130 cm^{-1}.

area, typically displaying an increase in the relative phase at 1130 cm^{-1} inside the irradiated volume (see Fig. 2d).

Further analysis of the laser track, particularly in the upper area with few nanopores, is presented in Fig. 3a and b, in close-up near-field amplitude and phase maps. We conducted nano-FTIR measurements, along a specified line across this image. Fig. 3e and f display two spectra at points 1 and 2, respectively, outside of the laser track and inside. The spectroscopy data showed significant shifts in peak positions, signaling strong material densification.[30,31] Notably, the Si–O–Si asymmetric stretching band of silica $\nu_{as}^{Si-O-Si}$, associated with a peak at around 1120 cm^{-1}, shifted to lower wavenumbers by more than 14 cm^{-1} in the irradiated region, moving from 1121 to 1107 cm^{-1} (Fig. 3e). In the phase spectra displayed in Fig. 3f, we see similar modifications, consistent with the alterations observed in the amplitude spectra. To accurately track phase spectral changes, we analyzed the wavenumber at 80% of the phase maximum, as the peak itself was a bit noisy, denoting a shift of the low wavenumber shoulder from 1124 to 1111 cm^{-1}. Additional amplitude and phase spectra at several other points along this laser track are provided in the ESI in Fig. SI_1.†

The $\nu_{as}^{Si-O-Si}$ shift along line profiles related to amplitude spectra (Fig. 3c) and the one related to the phase measured at 80% of the maximum (Fig. 3d) both reveal a strong and reliable material modification. Starting outside the laser track, the amplitude peak position is stable, representing the unmodified material. Progressing into the laser track, there is a consistent shift of the peak towards lower wavenumbers down to 1103 cm^{-1}, with the maximum at the track's center. The slight variation near the center suggests an influence of pores, indicating a small alteration in material density. As the profile extends beyond the track's midpoint, the peak positions rise again, denoting a reduced densification towards the track's periphery. The observed trends in the amplitude peak positions are mirrored in the phase profile, which displays a similar pattern of variation across the laser track. The amplitude and phase spectra used to plot these profiles are provided in ESI Fig. SI_2.†

Turning to well-imprinted type II modifications, we investigate a laser track inscribed with 200 pulses per micron in an *Xy* (parallel) configuration, where sufficient pulse density allows for the formation of nanogratings. These are clearly evidenced by the SEM image in the inset of Fig. 1c. Fig. 4a and b provide a detailed view with IR amplitude and phase maps of this laser track. Synchrotron nano-FTIR measurements, conducted along the indicated line in these maps, reveal the nanogratings' structural changes.

Fig. 4c presents the spectral position of the amplitude peak along a cross-sectional line within nanogratings. Starting inside of the laser track at the peak position at 1111 cm^{-1}, a pattern of fluctuating peak positions emerges, decreasing and increasing in correspondence with the nanogratings' alternating interlayers (around 1112 cm^{-1}) and nanoporous layers. The lowest points (around 1095 cm^{-1}) in the graph represent the areas where the nanogratings are densified at the highest degree, near the porous nanolayers. The overall trend appears to oscillate with a periodicity *L*, corresponding to the spacing of the nanogratings of approximately 310 nm. As seen in Fig. 4d, this oscillatory pattern is replicated in the quantitative phase profile revealing a higher phase within interlayers that appear in red on the phase map. The amplitude and phase spectra used to plot these profiles are provided in ESI Fig. SI_3.†

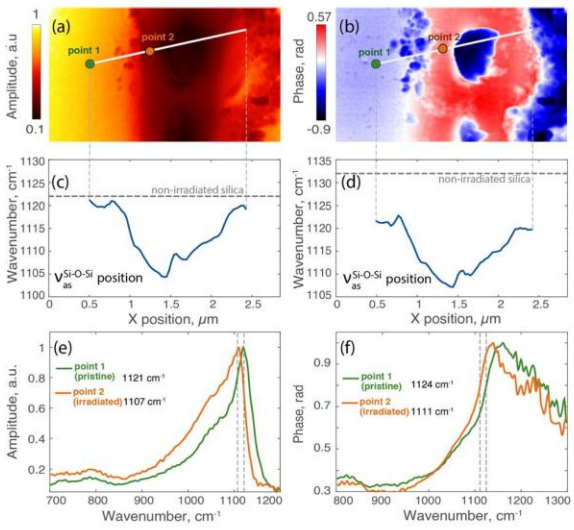

Fig. 3 The laser track written with 2 pulses per micron: (a) near-field amplitude map at 1130 cm^{-1}; (b) near-field phase map at 1130 cm^{-1}; (c) amplitude peak position and (d) phase peak position (measured at 80% of its maximum) along the line profile; (e) synchrotron nano-FTIR amplitude and (f) phase spectra for pristine material and irradiated area inside of the laser track.

4 Discussion

This study advances the current understanding of femtosecond laser-induced modifications in glass, revealing intricate patterns of densification within a laser track. These findings provide the first direct nanoscale evidence of densification within fs-laser inscribed laser tracks, characterized by an interplay of structural modifications such as the formation of

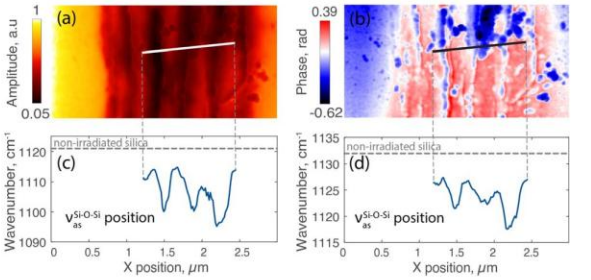

Fig. 4 The laser track written with 200 pulses per micron: (a) near-field amplitude map at 1130 cm^{-1}; (b) near-field phase map at 1130 cm^{-1}; (c) amplitude peak position and (d) phase peak position (measured at 80% of its maximum) along the line profile.

porous nanogratings within a background of densified matter. At the early birth of nanogratings *e.g.* within the type X regime, these structural changes are indicative of a mixed modification regime, blending type I and type II processes, and offer a deeper insight into the mechanisms driving the laser-induced modifications observed.

Prior to this work, there was no direct evidence of densification between layers or surrounding nanopores, with most existing results relying on microscale data that average the overall composite nanostructure, where densification has been indirectly inferred based on various hypotheses. However, these investigations have been crucial in providing important estimations and formulating hypotheses that have laid the groundwork for the understanding of fs-laser induced modifications. Previous studies have underscored the utility of Raman spectroscopy and other analytical techniques in elucidating the densification phenomena induced by fs-laser irradiation in silica glass. For instance, pioneering work utilizing scanning thermal microscopy alongside Raman spectroscopy has illuminated the localized densification. These investigations reported an approximate 8% increase in densification and suggested that the densification mechanism involved the development of high pressures.[20] Further exploration into nanogratings *via* mechanical and optical assessments has supported the hypothesis about the densification of the material. Techniques measuring micro-cantilever deflections have illustrated a change in volume and mechanical properties for type I and type II modifications with tensile stress in type I and compressive stress in type II modifications in bulk fused silica.[21,24,26,27]

This study employs nano-FTIR spectroscopy to delve into the structural nuances of type X and type II modifications within silica glass. IR spectroscopy is a great tool for probing the internal structure of glass, such as the intertetrahedral Si–O–Si asymmetric stretching vibration band near around 1120 cm^{-1}.[32] This spectral feature is instrumental in elucidating the molecular architecture of the glass network, as shifts in this band's position are indicative of alterations in network density, bond angles, and bond lengths. A displacement toward lower wavenumbers denotes a compaction of the network structure, characterized by shorter Si–O bond lengths, a signature of densification.[31,33–36] The bending mode around 780–800 cm^{-1} is less sensitive than stretching modes due to its intrinsic nature, as the bending vibration is "more internal" and has a lower vibration amplitude, making it less responsive to changes in parameters such as density, stress, or fictive temperature.[37] This contrasts with the Si–O–Si asymmetric stretching mode response that has been studied and exploited extensively.[31]

In amorphous SiO_2, a significant shift in the asymmetric stretching vibration band was observed under high-dose (10^{13} cm^{-2}) ion bombardment, moving from 1078 cm^{-1} to 1044 cm^{-1}.[38] This shift is attributed to the silica reaching a so-called metamict phase, which is also characterized by an increased presence of 3 and 4-membered rings. However, this does not imply a higher density of the material, as the density of the metamict phase consistently remains at 2.27 and it has been shown that a higher number of 3-membered rings do not always correspond to a higher overall material density.[25]

Another study utilizing FTIR spectroscopy on silica glass demonstrated that the variations in the glass fictive temperature result in slight shifts of $\nu_{as}^{Si-O-Si}$ by only 3 cm^{-1} increase[31,36] accompanied by a slight densification close to 2% assuming a 400 °C increase in the fictive temperature.

In contrast, a comparable shift to those observed in our findings was demonstrated in another study, where the main band frequency decreases linearly with an increase in density.[30] Notably, a frequency shift of 30 cm^{-1} was observed for silica subjected to HPHT treatment, resulting in a density increase to 2.55 under densification conditions of 5 GPa pressure and 800 °C temperature. The relationship between IR reflection spectra and density is summarized by the linear dependence:

$$\nu_{as}^{Si-O-Si} = (1332 \pm 13) - (95 \pm 5)\rho, \quad (1)$$

where $\nu_{as}^{Si-O-Si}$ is the evaluated resonance frequency near 1120 cm^{-1}, and ρ is the glass density.[30]

In our case, as seen in Fig. 3 and 4, IR spectra exhibit a pronounced shift in this band towards lower wavenumbers. For laser tracks inscribed at a density of 200 pulses per micron, spectral analysis reveals a shift from 1121 cm^{-1} in unirradiated silica to a minimum of 1095 cm^{-1} inside the laser track close to a nanoporous layer, with the interlayer material exhibiting values ranging around 1112 cm^{-1}. Consequently, this represents a shift of up to 26 cm^{-1} near within these nanogratings. Using (eqn (1)), we can estimate the laser irradiated silica's density to be 2.495 ± 0.190 for these highly densified regions while the interlayer material correlates with a density of 2.316 ± 0.183. Similarly, for the laser track inscribed with 2 pulses per micron, the minimum peak position in the middle of the track is 1104 cm^{-1}, corresponding to a density of 2.400 ± 0.186. The magnitude of these shifts underscores the clear evidence of the densification process not only between nanolayers but all along the laser track and likely around nanopores themselves.

On one hand, our study reveals a complex interplay between type I and type II modifications. At a low pulse density of 2 pulses per micron, we observe the early stages of nanograting formation (so-called type X nanopores) within a surrounding densified matrix, indicative of the onset of the nanocavitation process but within a type I-like background or "bed". When the pulse density is increased to 200 pulses per mm, the foundational densification remains relatively stable, while the nanogratings start to develop in a pulse-to-pulse mechanism. This observation points to a densification process that may precede (from previous pulses) but also accompany the formation of nanogratings as suggested earlier.[20]

On the other hand, IR spectra shift within laser tracks and the densification levels estimated are like those achieved through HPHT treatments. This suggests that the densification mechanism involved a combination of high dynamic pressure and high temperature. Indeed, the observed densification and $\nu_{as}^{Si-O-Si}$ shift cannot be attributed solely to thermal effects, as high-temperature quenching (*i.e.* glass fictive temperature increase) alone cannot achieve high levels of densification in

SiO_2 (typ. limited around 3%).[31,36] Therefore, the necessity of high pressure becomes evident. However, similarly, the densification level observed cannot be entirely attributed to high pressure. The rapid timescale of femtosecond laser processes implies that without accompanying heat, the pressure alone would not result in significant densification, underscoring the necessity of a combined thermo-mechanical mechanism for the observed changes.

High temperatures facilitate rapid and efficient densification along the laser track, following the laser beam's shape and thermal profile. Densification is not limited to areas around nanopores but extends throughout the laser track, reflecting the energy deposition and the plasma distribution. This process, initiated by a swift temperature increase from light–matter interaction, results in thermal expansion and the generation of a strain wave. Within the type II regime, this strain wave is characterized by a compression wave ahead, fostering densification and a rarefaction wave behind that may trigger the nanocavitation process.[17]

To bridge these observations with a semi-quantitative view of the mechanism, it is essential to estimate the involved pressure. Real-time polariscopic observations have recently confirmed the generation of moderate shockwaves with supersonic velocities, approximately 6 km s^{-1}, during fs-laser modifications in silica on a picosecond timescale.[39] Then a transition to acoustic waves occurs within nanoseconds. At the picosecond scale, stress levels reach the gigapascal range, around 10 GPa, corroborating simulation data.[40] Using data from the mechanics field, the static high-pressure Hugoniot curve provides a theoretical yet experimentally validated framework to estimate pressure from densification in the silica.[41–44] Previously, by examining shifts in the main band, we determined a density of approximately 2.5. Employing the Hugoniot curve, this translates to an estimated pressure of around 7 GPa. On the other hand, drawing on correlations between densification ratio and shock wave pressure,[45] the densification ratio of approximately 13.6% translates into an estimated pressure of around 14 GPa. Meanwhile, recent investigations, through comparisons of Raman spectra of densified silica by shock waves generated by two spatially separated focused fs-beams with compressive hydrostatic loading experiments, have estimated the development of dynamic strains with pressures around 13–15 GPa shortly after irradiation.[23] These overall estimations, ranging from 7 to 14 GPa, highlight the interplay between high pressure and high temperature in driving the densification process of the material within laser tracks resulting in the observed type II fs-modifications.

5 Conclusions

In conclusion, our study employing IR s-SNOM and nano-FTIR has unveiled new insights into the nanoscale densification mechanisms within femtosecond laser-induced nanogratings in silica glass. We have demonstrated the first direct evidence of nanoscale densification, both characterized by a significant shift in the Si–O–Si asymmetric stretching band and the corresponding amplitude and phase contrast around 1130 cm^{-1}. We estimated densities inside the laser tracks of approximately 2.4–2.5. This demonstrates a densification "bed" behind the nanogratings, suggesting that the underlying mechanism for glass densification during nanograting formation is quite similar to high temperature high pressure SiO_2 compression. These insights significantly enrich our understanding of fs-laser-induced nanogratings and pave the way for optimizing their fabrication for specific optical applications.

Data availability

The data supporting this article have been included as part of the ESI.† Additional data are available upon request from the authors.

Author contributions

Writing – original draft, N. Shchedrina; writing – review and editing, N. Shchedrina, G. Nemeth, F. Borondics, N. Ollier, M. Lancry; visualization, N. Shchedrina; data curation, N. Shchedrina and G. Nemeth; formal analysis, N. Shchedrina; investigation, N. Shchedrina, G. Nemeth, N. Ollier, and M. Lancry; validation, G. Nemeth, F. Borondics, N. Ollier, and M. Lancry; methodology, G. Nemeth and M. Lancry; resources, F. Borondics and M. Lancry; supervision, N. Ollier and M. Lancry; conceptualization, M. Lancry; funding acquisition, M. Lancry. All authors have read and agreed to the published version of the manuscript.

Conflicts of interest

There are no conflicts to declare.

Acknowledgements

This research was funded by Agence Nationale de la Recherche (ANR), Project REFRACTEMP (no. ANR-22-CE08-0001-01). We acknowledge the support of the SMIS beamline from synchrotron SOLEIL.

Notes and references

1 K. Itoh, W. Watanabe, S. Nolte and C. B. Schaffer, *MRS Bull.*, 2006, **31**, 620–625.
2 Y. Lei, G. Shayeganrad, H. Wang, M. Sakakura, Y. Yu, L. Wang, D. Kliukin, L. Skuja, Y. Svirko and P. G. Kazansky, *Light: Sci. Appl.*, 2023, **12**, 74.
3 J. Zhang, M. Gecevičius, M. Beresna and P. G. Kazansky, *Phys. Rev. Lett.*, 2014, **112**, 033901.
4 Y. Wang, M. Lancry, M. Cavillon and B. Poumellec, *Opt. Lett.*, 2022, **47**, 1242–1245.
5 M. Sakakura, Y. Lei, L. Wang, Y.-H. Yu and P. G. Kazansky, *Light: Sci. Appl.*, 2020, **9**, 15.
6 M. Beresna, M. Gecevičius and P. G. Kazansky, *Adv. Opt. Photonics*, 2014, **6**, 293.
7 M. Beresna, M. Gecevičius, P. G. Kazansky and T. Gertus, *Appl. Phys. Lett.*, 2011, **98**, 201101.

8 J. Lu, Y. Dai, Q. Li, Y. Zhang, C. Wang, F. Pang, T. Wang and X. Zeng, *Nanoscale*, 2019, **11**, 908–914.
9 A. Rowstron, *Advanced Photonics 2018 (BGPP, IPR, NP, NOMA, Sensors, Networks, SPPCom, SOF)*, Washington, D.C., 2018.
10 S. Mihailov, D. Grobnic, C. Hnatovsky, R. Walker, P. Lu, D. Coulas and H. Ding, *Sensors*, 2017, **17**, 2909.
11 Y. Wang, M. Cavillon, J. Ballato, T. Hawkins, T. Elsmann, M. Rothhardt, R. Desmarchelier, G. Laffont, B. Poumellec and M. Lancry, *Adv. Opt. Mater.*, 2022, **10**, 2200379.
12 G. C. Kahandawa, J. Epaarachchi, H. Wang and K. T. Lau, *Photonic Sens.*, 2012, **2**, 203–214.
13 S. S. Mao, F. Quéré, S. Guizard, X. Mao, R. E. Russo, G. Petite and P. Martin, *Appl. Phys. A: Mater. Sci. Process.*, 2004, **79**, 1695–1709.
14 Y. Shimotsuma, P. G. Kazansky, J. Qiu and K. Hirao, *Phys. Rev. Lett.*, 2003, **91**, 247405.
15 V. R. Bhardwaj, E. Simova, P. P. Rajeev, C. Hnatovsky, R. S. Taylor, D. M. Rayner and P. B. Corkum, *Phys. Rev. Lett.*, 2006, **96**, 057404.
16 M. Lancry, B. Poumellec, J. Canning, K. Cook, J.-C. Poulin and F. Brisset, *Laser Photonics Rev.*, 2013, **7**, 953–962.
17 Q. Xie, N. Shchedrina, M. Cavillon, B. Poumellec and M. Lancry, *Nanoscale Adv.*, 2024, **6**, 489–498.
18 E. Bricchi, B. G. Klappauf and P. G. Kazansky, *Opt. Lett.*, 2004, **29**, 119–121.
19 J. W. Chan, T. Huser, S. Risbud and D. M. Krol, *Opt. Lett.*, 2001, **26**, 1726–1728.
20 Y. Bellouard, E. Barthel, A. A. Said, M. Dugan and P. Bado, *Opt. Express*, 2008, **16**, 19520.
21 Y. Bellouard, A. Champion, B. McMillen, S. Mukherjee, R. R. Thomson, C. Pépin, P. Gillet and Y. Cheng, *Optica*, 2016, **3**, 1285.
22 Y. Wang, M. Cavillon, N. Ollier, B. Poumellec and M. Lancry, *Phys. Status Solidi*, 2021, **218**, 2100023.
23 A. Radhakrishnan, J. Gateau, P. Vlugter and Y. Bellouard, *Opt. Mater. Express*, 2022, **12**, 2886.
24 A. Champion and Y. Bellouard, *Opt. Mater. Express*, 2012, **2**, 789.
25 N. Ollier, M. Lancry, C. Martinet, V. Martinez, S. Le Floch and D. Neuville, *Sci. Rep.*, 2019, **9**, 1227.
26 P. Vlugter, E. Block and Y. Bellouard, *Phys. Rev. Mater.*, 2019, **3**, 053802.
27 P. Vlugter and Y. Bellouard, *Phys. Rev. Mater.*, 2020, **4**, 023607.
28 N. Ocelic, A. Huber and R. Hillenbrand, *Appl. Phys. Lett.*, 2006, **89**, 101124.
29 R. J. Bell, N. F. Bird and P. Dean, *J. Phys.*, 1968, **1**, 299–303.
30 C. Z. Tan, J. Arndt and H. S. Xie, *Phys. B*, 1998, **252**, 28–33.
31 M. Lancry, E. Régnier and B. Poumellec, *Prog. Mater. Sci.*, 2012, **57**, 63–94.
32 E. I. Kamitsos, *Mod. Glass Charact.*, 2015, 1–42.
33 H. Liu, H. Kaya, Y.-T. Lin, A. Ogrinc and S. H. Kim, *J. Am. Ceram. Soc.*, 2022, **105**, 2355–2384.
34 M. Tomozawa, J.-W. Hong and S.-R. Ryu, *J. Non-Cryst. Solids*, 2005, **351**, 1054–1060.
35 A. Agarwal and M. Tomozawa, *J. Non-Cryst. Solids*, 1997, **209**, 166–174.
36 A. Agarwal, K. M. Davis and M. Tomozawa, *J. Non-Cryst. Solids*, 1995, **185**, 191–198.
37 A. Geissberger and F. L. Galeener, *Phys. Rev. B: Condens. Matter Mater. Phys.*, 1983, **28**, 3266.
38 K. Awazu, S. Ishii, K. Shima, S. Roorda and J. L. Brebner, *Phys. Rev. B: Condens. Matter Mater. Phys.*, 2000, **62**, 3689–3698.
39 A. Mouskeftaras, O. Koritsoglou, G. Duchateau and O. Utéza, *Conference on Lasers and Electro-Optics/Europe (CLEO/Europe 2023) and European Quantum Electronics Conference (EQEC 2023)*, Technical Digest Series, Optica Publishing Group, 2023, paper cm_10_4.
40 R. Beuton, B. Chimier, J. Breil, D. Hébert, K. Mishchik, J. Lopez, P. H. Maire and G. Duchateau, *Appl. Phys. A: Mater. Sci. Process.*, 2018, **124**, 1–10.
41 H. Sugiura, K. Kondo and A. Sawaoka, *J. Appl. Phys.*, 1981, **52**, 3375–3382.
42 C. S. Alexander, L. C. Chhabildas, W. D. Reinhart and D. W. Templeton, *Int. J. Impact Eng.*, 2008, **35**, 1376–1385.
43 J. Wackerle, *J. Appl. Phys.*, 1962, **33**, 922–937.
44 R. Renou, L. Soulard, E. Lescoute, C. Dereure, D. Loison and J.-P. Guin, *J. Phys. Chem. C*, 2017, **121**, 13324–13334.
45 H. Sugiura, R. Ikeda, K. Kondo and T. Yamadaya, *J. Appl. Phys.*, 1997, **81**, 1651–1655.

II.5 CONCLUSION

This chapter has explored how fs laser-induced nanogratings form in silica glass, examined their nanostructure, and investigated the accompanying density changes.

First, through polarized optical microscopy and SEM, we demonstrated that a material's tendency to form nanogratings can be directly linked to its free volume. Densified samples exhibited notably lower retardance and reduced slope values (as functions of pulse energy and pulse count), reflecting a diminished ability to form nanogratings. This provides novel insights into the role of glass free volume as a crucial precursor for nanograting formation. Voids related to free volume at sub-nm scale may serve as an ideal seed owing to its size and lower refractive index, thereby facilitating the formation of nanoplasma hotspots and subsequent nanogratings that consistently align perpendicular to light polarization. This agrees with recent findings showing that laser-induced nanostructures in fused silica can be seeded by creating a primary void (typically > 100 nm in diameter), which then allows the nanoplane to develop further under lower energy levels [247]. The suggested mechanism coherently explains why silica glass, which naturally possesses a high free volume, facilitates nanograting formation more efficiently than other types of glass. The relationship between free volume and nanograting efficiency could guide the engineering of materials (e.g. nanoporous dedicated materials) with tailored optical properties, paving the way for improved applications in advanced photonic systems.

Subsequently, structural analyses using SEM, HR-TEM, and STEM revealed that nanogratings are composed of oblate nanopores "aligned along each other's" but in non-continuous, revealing wavy nanoplanes perpendicular to the laser polarization and along the propagation direction. Between the larger nanoplanes, smaller, elongated nanopores were observed, indicating a dynamic growth and merging process under multiple pulses. This pulse-to-pulse evolution lowers the grating period well below $\lambda/2n$. Our observations support a plasma-mediated nanocavitation model, in which nanogratings are more accurately described as "light-forced organized," rather than purely self-organized, on a multipulse timescale.

Finally, employing advanced spectroscopic methods, specifically s-SNOM combined with nano-FTIR, we have, for the first time, directly quantified nanograting densification at the nanoscale. IR band shifts in the Si-O-Si asymmetrical stretching mode indicate densification levels on the order of 8–13%, like those achieved through conventional HPHT compression. This shows how fs-laser irradiation can act as a confined HPHT micro-reactor in silica glass. Furthermore, our results uncover a complex interplay between Type I and Type II modifications, suggesting that a densified "background" aarises prior to nanograting formation. Collectively, these insights deepen our understanding of how fs-laser pulses change glass at the nanoscale, thereby offering insights for refining fabrication techniques and improving optical devices that depend on precisely engineered refractive index distributions and controlled birefringence.

Chapter III. EFFECTS OF ELECTRON IRRADIATION ON THE STRUCTURE AND STABILITY OF SILICA GLASS

III.1 INTRODUCTION

This chapter presents an investigation of how electron irradiation affects silica glass, focusing on the questions of the polyamorphism, transitions between HDA and LDA, activation energy distributions along thermal relaxation of densified silica, and the formation of the metamict-like phase under very high doses (11 GGy) of 2.5 MeV electrons. It further delves into how elevated temperatures, yet sub-T_g, during electrons irradiation alter both the point defects generation and the densification or its relaxation kinetics.

In the first section, we examine the HDA-LDA transition that occurs during the thermal relaxation of densified silica. Here, in situ Raman spectroscopy during isothermal annealing is used to track the evolution of the D_2 band, a key indicator of three-membered rings and thus local density. A master-curve approach is applied to derive the activation energy distribution, which provides a quantitative measure for the thermal stability of densified states. By comparing densified silica samples subjected to different doses (0, 10^7 Gy, and 11 GGy), we show how even moderate irradiation can significantly lower the central activation energy and thus alter the stability of HDA phase; at very high doses, HDA phase is effectively "erased" beyond our detection limit.

The second part of the chapter shifts to metamict-like silica formed under high-dose irradiation (11 GGy). Although all samples converge to a similar density of about 2.26, we demonstrate that the initial silica structure and impurities play crucial roles in the resulting structure and overall thermal stability. Specifically, silica samples prepared via HPHT treatment and then irradiated have higher thermal stability than the silica samples irradiated without densification. The OH-content of the silica glass also affects the resulted metamict-like state. Raman, FTIR, and PL analyses highlight that, despite achieving comparable densities, the differences in pre-irradiation processing and impurity content lead to distinct defect signatures and relaxation behaviors.

Finally, we investigate the influence of high temperature (range from 300 K to 1000 K) during irradiation. By tentatively isolating the contributions of dose and temperature, we show that elevated temperatures can suppress certain defect centers and modify the densification of silica or relaxation rates. At lower temperatures (300-450 K), the structure of silica glass moves toward metamict-like state, thought the rate slows down with the rise of the temperature. However, with the increase of temperature (from 600 K) the thermal effects dominate over irradiation dose leading to relaxation. This observation is essential for applications where silica experiences both high-radiation fields and high temperatures (e.g., nuclear reactor environments).

III.2 INVESTIGATING DENSIFICATION PROCESSES OF AMORPHOUS SILICA PHASES THROUGH ACTIVATION ENERGY DISTRIBUTION

Journal of Non-Crystalline Solids 617 (2023) 122491

Contents lists available at ScienceDirect

Journal of Non-Crystalline Solids

journal homepage: www.elsevier.com/locate/jnoncrysol

Investigating densification processes of amorphous silica phases through activation energy distribution

N. Shchedrina [a,b,*], N. Ollier [b], M. Mobasher [b], M. Lancry [a]

[a] Institut de Chimie Moléculaire et des Matériaux d'Orsay, CNRS, Université Paris Saclay, Orsay 91405, France
[b] Laboratoire des Solides Irradiés, École polytechnique-CEA-CNRS, Cedex, Palaiseau 91128, France

ARTICLE INFO

Keywords:
Silica glass
Polyamorphism
Densification
Electron irradiation
Metamict phase
Thermal relaxation
Activation energy

ABSTRACT

We investigated thermal stability of silica glass that underwent high-temperature (HT), high-pressure (HP) densification followed with electron irradiations. We performed isothermal annealing and *in situ* Raman spectroscopy to observe changes in the silica structure. By determining the activation energy distributions at the root of the densification process, we aimed to gain insights into the relaxation pathway of densified silica and its relationship with the structural properties. Of particular interest we observed a non monotonous behavior of D_2 band in Raman spectra in HP-HT samples exposed at low dose $\leq 10^7$ Gy, which we attribute to presence of a specific phase of silica glass known as the high-density amorphous phase. Our study highlights the impact of irradiation on the ratio between high-density amorphous and low-density amorphous phases, and on relative activation energy distributions. These findings have important implications for development of high-performance optical devices based on silica densification for a wide range of applications.

1. Introduction

Silica glass is an essential material with a broad range of applications due to its unique optical, thermal, and mechanical properties. The structure of silica glass can be tailored through densification, resulting in altered properties such as increased refractive index [1] or a decreased Rayleigh scattering coefficient attributed to a reduction in the size of density fluctuations [2]. This enables its use in advanced applications like Bragg grating writing and high-precision temperature sensors operating in harsh environments [3]. Densification of silica can be achieved via high-pressure techniques [4–6] or irradiation [7,8]. Nevertheless, establishing a straightforward relationship between densification pathways, rates, and specific structural alterations (e.g., Si-O-Si angles, ring statistics, free volume [9], void size [2]) remains obscure. Due to the complexity involving mechanisms of excitation, feedback and reorganization of the matter, stress field formation, mastering phenomenon of densification poses scientific and technological challenges.

As a result, the fundamental question of polyamorphism in silica glass [10,11] has gained significant attention due to its potential impact on the material's properties and applications. Indeed silica glass can undergo reversible transformations between different amorphous modifications with varying short-range order structures and densities under high pressure [4,5,7,12,13]. The existence of low-density amorphous (LDA) and high-density amorphous (HDA) phases, and their coexistence under certain conditions, is widely discussed such as the transition from HDA to LDA during annealing [5,13]. Polyamorphism was often addressed in densified silica samples under High Pressure but rarely under irradiation. It is true that densification under irradiation never exceeds 5 % [7,14]. However, "high-dose" irradiation (e.g. 11 GGy with 2.5 MeV electrons) can lead to the formation of a metamict like phase in SiO_2 [8]. This phase exhibits a similar structure, Raman signature, and density of 2.26 g/cm^3 to the metamict phase resulting from quartz amorphization under neutron irradiation [15]. However, the relationship between this metamict phase of "medium density" and LDA or HDA phases is not well understood.

To investigate this question, Raman spectroscopy is a powerful tool for monitoring structural changes in silica glass. The main band in silica Raman spectra corresponds to the bending motion of SiO_2-tetrahedra involving n-membered rings ($n \geq 5$) and gives indication of the average Si-O-Si angle. The D_1 and D_2 bands at respectively 490 and 605 cm^{-1} originate from the collective breathing motion of oxygen atoms within the 3-membered and 4-membered rings respectively [16]. The densification signature of glass, often correlated with Raman bands D_1 and D_2,

* Corresponding author.
E-mail address: nadezhda.shchedrina@universite-paris-saclay.fr (N. Shchedrina).

https://doi.org/10.1016/j.jnoncrysol.2023.122491
Received 12 May 2023; Received in revised form 16 June 2023; Accepted 28 June 2023
Available online 10 July 2023

has been extensively investigated in previous studies. In pure silica glass, these bands' intensities tend to increase with the macroscopic density of the glass [17–19]. However, there are cases where D bands do not monotonously correlate with the macroscopic density [20–22], as observed in Ge-doped silica subjected to thermal treatments [23] or in high pressure-high temperature conditions (HP-HT) silica irradiated by electrons [22]. Moreover, several studies have reported non monotonous increase in the D_2 band intensity during the thermal relaxation of densified silica, whereas the sample relaxed towards pristine silica structure [5,12,13,21]. It should be noted that the same ring structures and bond angles can exist across different local densities within an amorphous network. Thus, while D bands can serve as local density indicators, reflecting local structures, they may not necessarily correlate with bulk densities.

In the following, we will thus investigate the thermal relaxation of silica densified under various conditions (HP-HT and electrons irradiation) using Raman spectroscopy. D_2 band has been chosen to follow the densification relaxation pathway. We seek to contribute to a deeper understanding of densified silica glass, estimating the underlying activation energy distribution [17,24], and phase transitions, including the coexistence of LDA and HDA phases and transitions between them when electrons irradiation occurs.

2. Experimental details

In this study, type III silica rods made of Heraeus Suprasil F300HQ with a high Cl (typ. 2000-2500 ppm) and low OH content (<1 ppm) were used. The densification process was carried out under high pressure-high temperature conditions (HP-HT) of 5 GPa and 1000°C using a belt press [6]. Samples were then subjected to high-energy electron irradiation at 2.5 MeV, integrating doses of 11 GGy or 10^7 Gy using the SIRIUS facility (LSI/CEA/Ecole Polytechnique). Irradiation at 11 GGy results in a silica metamict-like phase [5]. Throughout the remainder of the text, we will refer to these samples as " 5 GPa_1000°C 11 GGy", "5 GPa_1000°C 10^7 Gy," and "5 GPa_1000°C". An unirradiated sample is taken as reference for comparison ("5 GPa_1000°C").

Density measurements were conducted using the Archimedean-based sink-float method using toluene as the immersion liquid. Prior thermal relaxation, mass densities for "11 GGy", "10^7 Gy," and "5 GPa_1000°C" samples were 2.26, 2.50, and 2.59 g/cm^3, respectively. *In situ* Raman spectra were then monitored during the isothermal annealing process using a Linkam heating stage. The "5 GPa_1000°C 11 GGy" and "5 GPa_1000°C" samples were annealed at 825°C, 885°C, and 950°C, while the "5 GPa_1000°C 10^7 Gy" sample was annealed at 850°C, 900°C, and 975°C. These annealing temperatures were selected to ensure measurable erasure at each temperature, a complete erasure at the highest temperature after 18 hours, and sufficient overlap of the corresponding activation energies to facilitate the further determination of a master curve. The choice of temperatures and duration was further informed by preliminary step isochronal annealing [21].

Raman spectra were recorded every 3-5 minutes for first 2 hours and 15-minutes intervals for next 16 hours. Raman spectra were collected with a Horiba LabRam HR 800 spectrometer, utilizing a 600 lines/mm grating, Peltier-cooled CCD detector, and an Ar^+ laser at 458 nm excitation. The laser power at the sample was approximately 18 mW. For data analysis, a Matlab algorithm was employed to extract the D_2 band amplitude. Spectra were normalized by the total integrated area, and the D_2 band amplitude was obtained by fitting the background within 550-650 cm^{-1} range using polynomial functions and determining the maximum of the fitted curves. In the following, the activation energy error, calculated considering time and temperature uncertainties, is estimated to remain lower than 0.01 eV, while the error bar for normalized D_2 amplitude is determined to remain within 5%.

3. Results

In this section, we present the approach and analysis to extract the activation energy distributions for the investigated samples. The determination of activation energy distribution is a well-established method for predicting the lifetime and thermal stability of various optical properties [25]. This is especially important for disordered materials such as glasses, where many processes are distributed [26]. To investigate the internal structural changes in polyamorphous silica, we utilized the VAREPA (VAriable REaction PAthways) framework [25]. In principle, this allows rationalizing the thermal stability of any optical or structural property. In the following we will use data derived from accelerated aging and fed a model based on 1st-order Arrhenius kinetics, which is thermally activated with activation energy distributed according to a temperature and time-independent function. For this, we can use the demarcation energy, E_d, which is the boundary between achieved and non-achieved reactions for a given temperature (T) and time (t) couple. As described in [25], the following formula can be used:

$$\boldsymbol{E_d = k_B T \ln(k_0 t)} \tag{1}$$

where E_d is demarcation energy (eV), k_B is Boltzmann constant (eV/K), T is annealing temperature (K), k_0 is the constant rate of the densification relaxation (s^{-1}), t is the annealing time (s). If all hypotheses are fulfilled, a master curve can be obtained by plotting the total content of a reaction product against the defined demarcation energy. In a glassy material, the densification process or its relaxations occurs with a distribution of activation energies noted g(E) rather than just a single activation energy barrier. To estimate this distribution, the first derivative of the master curve according to E_d can be used. From an experimental point of view, we selected the D_2 band intensity as a local density indicator and to assess the related thermal stability. In addition, we assume that the formation or destruction of 3-membered rings, associated with the D_2 band, represents an elementary one-step reaction closely related to the densification speciation namely the occurrence of HDA or LDA.

To investigate the changes in the D_2 band intensity, we performed *in vivo* Raman spectroscopy measurements during isothermal annealing. As a general trend the Raman spectra evolution over time revealed a change in D_2 band intensity associated with a broadening and an upshift of the R-band for all samples. Fig. 1 exemplifies the Raman spectra at 850°C at fixed times for sample "5 GPa_1000°C 10^7 Gy", with an inset showing the D_2 band. Notably, the D_2 intensity reveals a non monotonous behavior during the first 15 minutes. This is also observed in non-irradiated HP-HT sample (during first 100 minutes) in agreement with the literature [5,13,21]. Conversely, for HP-HT samples, irradiated at 11 GGy, the decrease in D_2 intensity was monotonous throughout the annealing for all temperatures.

The extracted D_2(t,T) band intensities were compared to the final D_2 value corresponding to last measurements at the highest temperature $D_2(\infty,T_{max})$. This assumes that the HP-HT silica is fully relaxed at the end of the annealing process at 975°C which is confirmed by comparing its Raman spectra to pristine silica. Then the differences were normalized relative to their initial values D_2(0,T). This allows defining a normalized transformation rate calculated using the following Eq. (2):

$$\mathbf{D}_{2_{\mathrm{norm}}}(\mathbf{t},\mathbf{T}) = \frac{\boldsymbol{D}_{2\ (t,T)} - \boldsymbol{D}_{2}\ (\infty, \boldsymbol{Tmax})}{\boldsymbol{D}_{2\ T}(0,\mathbf{T}) - \boldsymbol{D}_{2}\ (\infty, \boldsymbol{Tmax})} \tag{2}$$

Here, $\boldsymbol{D}_2\ (\infty, \boldsymbol{Tmax})$ is estimated considering a full relaxation of the densified state post an extended annealing at the highest temperature (i.e. after 18 hours). The corresponding Raman spectrum was also compared as been similar to the one of pristine silica.

Isotherms were plotted for each sample to observe changes in the normalized D_2 transformation rate over time and then to further determine the distribution of activation energy of the densification process. The evolution of the D_2 transformation rate, $D_{2\ \mathrm{norm}}$ (t, T), as a function of annealing time for the 5 GPa_1000°C 10^7 Gy sample is shown

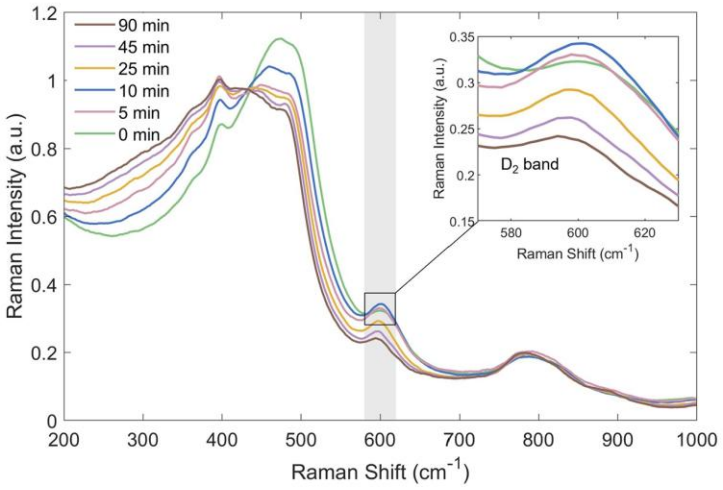

Fig. 1. Evolution of Raman spectra during isothermal annealing at 850°C of HP-HT SiO_2 sample irradiated at 10^7 Gy at different annealing times.

in Fig. 2. The D_2 transformation rates for each temperature exhibit similar trends. For temperatures 825 and 885°C, there is a small increase in D_2 transformation rates during the first 5-10 minutes, followed by a rapid decrease in the next 150 minutes and then a slower decrease over the entire duration of the remaining annealing process. For the 950°C temperature, a similar trend is observed but without the initial increase in the D_2 transformation rate. Notably, this transition towards trend to saturation occurs more rapidly for the highest and slowly for the lowest annealing temperatures.

First, we assumed a constant relaxation rate of the densification reaction corresponding to k_0 (expressed in s^{-1}) set to 1 and plotted the $D_{2\ norm}(E_d)$ evolution as a function of the demarcation energy using Eq. (1). As expected, the resulting curves did not overlap. To collapse the three isotherms into a single curve called the master curve, it was necessary to determine the best value of k_0 (Fig. 3).

Using least squares optimization, we obtained a parabolic graph of chi-square χ^2 as a function of k_0, which allowed us to find its optimal value. The optimal reaction rate was determined to be $k_0 = 2 \times 10^8\ s^{-1}$ for the 10^7 Gy SiO_2 sample. We estimated the experimental uncertainties to derive confidence intervals for k_0. We have included this interval in the inset in Fig. 3 for the sample 5 GPa_1000°C 10^7Gy. Using the 63% confidence interval, we obtained the optimized value of k_0 within the range of $2 \times 10^7\ s^{-1}$ to $2 \times 10^9\ s^{-1}$. Finally, we plotted the resulting curves in Fig. 3 using the optimized value of k_0 showing a collapse of data sets into a single curve. This so-called master curve represents the activation process for any temperature and time, allowing us to predict the behavior of the densified samples under different conditions and providing a comprehensive representation of the system's behavior for local density indicators, namely D_2 here.

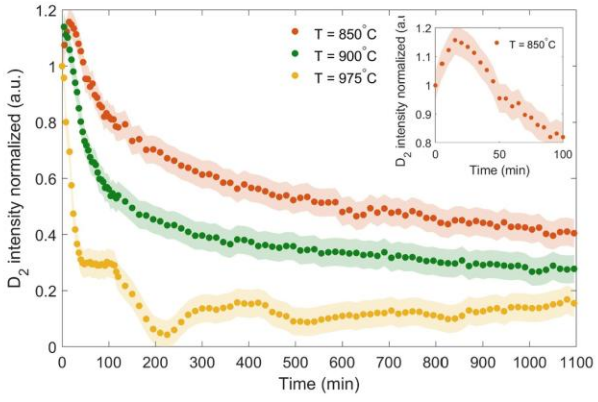

Fig. 2. Isotherms of normalized D_2 intensity, $D_{2\ norm}(t, T)$, as a function of annealing time at different temperatures (825, 885, and 950°C) for densified silica irradiated at 10^7 Gy. Inset: A zoomed-in view of the first 100 minutes of annealing time at 825°C. The filled areas represent the standard deviation.

At this point, it should be noted that the first Raman spectra (thus, the first point on the isotherms), at t = 0 min, was collected after the sample had reached the target temperature. So, samples had been relaxing for the time during which the stage was heating (with rate of approximately 200°C/minute), which can lead to an offset in the E_d calculation. Thanks to the existence of the master curve, data can thus be corrected by estimating the equivalent time during the heating slope up to reaching the chosen annealing temperature, using the equation:

$$\mathbf{t}_{eq\ 2} = (t_2 - t_1) + \frac{1}{\mathbf{k_B}} * \left(\mathbf{k}_0 * \mathbf{t}_{eq\ 1}\right)^{\left(\frac{T_1}{T_2}\right)}, \tag{4}$$

where t_1 and t_2 are heating time along the discretized slope (so t_2-t_1 is the heating duration at T_2), T_1 and T_2 are corresponding temperatures to t_1 and t_2, $t_{eq\ 1}$ and $t_{eq\ 2}$ are equivalent time at respective T. Parameters t_1 and t_2 represent time intervals associated with incremental temperature increases (e.g. discretizing the heating slope by steps of 2°C). Therefore, t_1 and t_2 increment in a way that each time step corresponds to a step-rise in temperature. For sample "5 GPa_1000°C 10^7 Gy", we estimated that heating the sample up to 850°C with rate 3.2°C/s corresponds to approximately a $t_{eq\ final}$ of 17 seconds at the target temperature of 850°C.

As observed in Fig. 4, the master curve for sample "5 GPa_1000°C 10^7 Gy" shows two sections of different trends. A first increase starts around 2.3 eV and increases by 20 % of the initial in $D_{2\ norm}(t,T)$ value. The second section starts from 2.5 eV and corresponds to a drastic decrease of in $D_{2\ norm}(t,T)$ down to zero. This non monotonous behavior suggests that annealing curve is composed of at least two terms, but with the same value of k_0 revealing a complex distribution. Finally, we fitted the curve using two sigmoid components seen as two additive contributions of D_2, using the following equation:

$$\boldsymbol{D}_2\ (\boldsymbol{E_d}) = \frac{1+\boldsymbol{m}}{1+\exp\left(-\frac{2\sqrt{\pi}\ (E_d - E_1)}{FWHM_1}\right)} - \frac{\boldsymbol{m}}{1+\exp\left(-\frac{2\sqrt{\pi}\ (E_d - E_2)}{FWHM_2}\right)} \tag{5}$$

In this equation, m represents the relative contribution to the overall curve, E_i is the central energy, and $FWHM_i$ is the width of the

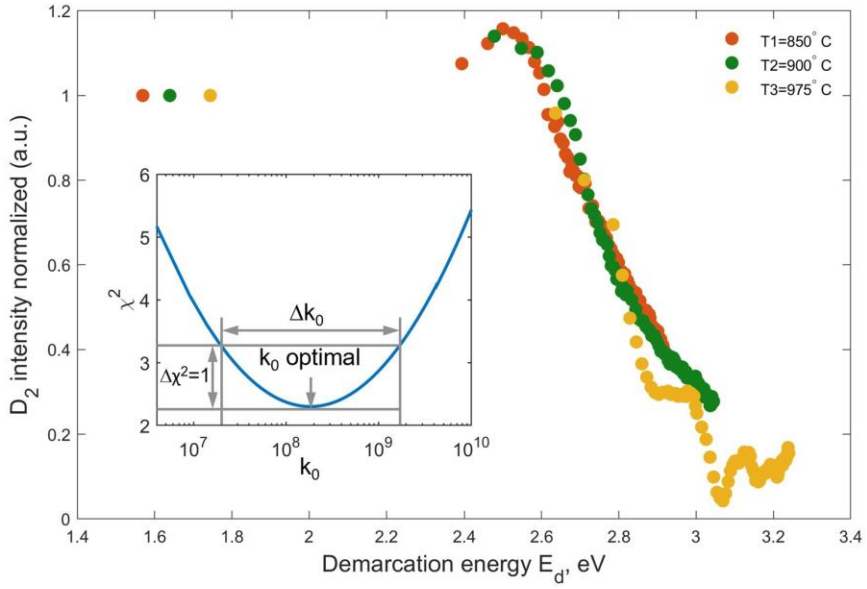

Fig. 3. Normalized D_2 intensity as a function of the demarcation energy with best k_0, i.e., the master curve, insert: the confidence interval Δk_0 at 63.8% for k_0 as a function of χ^2.

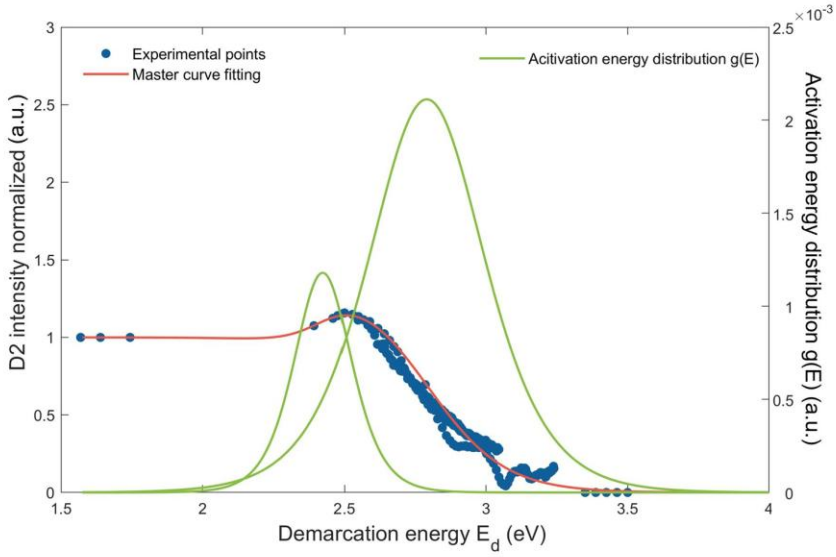

Fig. 4. Normalized D_2 peak intensity as a function of the demarcation energy E_d and the for sample 5 GPa_1000°C 10^7 Gy.

distribution. For sample "5 GPa_1000°C", there is a similar master curve shape with two contributions. In contrast, for sample "5 GPa_1000°C 11 GGy", we observed a monotonous decay according to the demarcation energy without any apparent increase. Therefore, we fitted the data using a single sigmoidal component. The overall fitting parameters are presented in Table 1.

To further study the physicochemical reactions, which are responsible for process of structural changes linked to densification, the erasure reaction owing variable pathways with a distribution g(E) has been derived from the master curve and presented in Fig. 4 for sample "5 GPa_1000°C 10^7 Gy". Following this view, we have performed a mathematical decomposition of the normalized distribution g(E) using two

Table 1
The fitting parameters used in equations 5 and 6 for samples "5 GPa_1000°C 11 GGy", "5 GPa_1000°C 10^7 Gy," and "5 GPa_1000°C"

Sample	E_1 (eV)	$FWHM_1$ (eV)	E_2 (eV)	$FWHM_2$ (eV)	m
5GPa 1000°C 11 GGy	3.109 ± 0.003	0.514 ± 0.002	-	-	0
5GPa 1000°C 10^7 Gy	2.791 ± 0.002	0.482 ± 0.002	2.425 ± 0.007	0.019 ± 0.002	1.358 ± 0.007
5GPa 1000°C	4.549 ± 0.002	0.443 ± 0.006	4.226 ± 0.007	0.020 ± 0.004	1.808 ± 0.006

components. Based on previous work [18], we assume that each component can be described as the derivative of a sigmoidal function. Now by comparing the bimodal distribution in Fig. 4 and those obtained in other samples using the same methodology (Fig. 5), we can assimilate each function to the overall densification process. The first function represents the pathway through a kind of transitory state with a narrow distribution (around $3k_BT$ i.e., 0.24 eV), centered at 2.42 eV. Then the second function (FWHM=0.48 eV) is attributed to the major contribution which should be erased around $E_1 = 2.79$ eV. For the "5 GPa_1000°C" unirradiated sample, the center value both distributions are shifted towards higher energy: 4.22 eV, with a FWHM of 0.25 eV for first distribution; 4.55 eV, with a FWHM of 0.44 eV for the second one.

For "5 GPa_1000°C 11 GGy", the high dose irradiation results in a single component distribution centered 2.87 eV with a FWHM of 0.59 eV.

4. Discussion

We investigated the thermal stability of two densified silica samples first subjected to HPHT (5 GPa, 1000°C) then to subsequent electrons irradiation (10^7 Gy and at high dose 11 GGy) and compared with the unirradiated one (5 GPa, 1000°C). The density values for the unirradiated, 10^7 Gy irradiated, and 11 GGy irradiated samples were 2.59 g/cm^3, 2.50 g/cm^3, and 2.26 g/cm^3, respectively. Activation energy distribution analysis aimed to explore densified silica glass relaxation pathways and its relationship with the local density indicators that we followed using Raman spectroscopy. Specifically, we observed a non monotonous evolution of the D_2(t,T) transformation rate during the first minutes of annealing in both unirradiated (5 GPa_1000°C) and low-dose irradiated (5 GPa_1000°C 10^7 Gy) silica, likely indicating the formation of higher number of 3-membered rings whereas R-band follows a monotonous decay. While the D_2 band has been often used as a macroscopic densification indicator, it is important to remember that amorphous networks can present a range of densities for the same number of ring structures and bond angles. The D_1 and D_2 bands measure local structures and while they often correlate with local densities, they need not correspond directly with bulk densities. Consequently, the observed non-monotonic behavior of the D_2 band is not inconsistent with a continuous decrease in density during the relaxation processes.

Similar non monotonous behavior of D_2 band in SiO_2 during isothermal or isochronal annealing has been observed in other studies [5,12,13,21]. For instance, in our prior work [15] similar samples were investigated but with different densification conditions (5 GPa_350°C, 4 GPa_450°C, and 5 GPa_1000°C). As a result of isochronal annealing, both the density and R-band wavenumber decreased monotonically, whereas D_2 band increased in 10^7 Gy samples (especially on the 5 GPa_1000°C) at temperatures between 750-800°C. The higher the compression temperature, the stronger is the anomaly during the relaxation, which could be tentatively attributed to a higher HDA proportion. While in 5 GPa_1000°C 11 GGy silica, D_2 band exhibits a monotonous decrease indicating a "bleaching of the HDA-LDA transitory state" due to such high dose irradiation. In Guerette et al. [4] an increase in the D_2 amplitude was also noticed on the hot-compressed samples during isochronal annealing at 750-800°C. At that time, the authors attributed this to the stress state in the glass network to which the small rings are bonded and in which they vibrate, rather than a change in the concentration of 3-membered rings, as later suggested by Cornet et al. [12]. This last author observed an unexpected D_2 band intensity increase during isothermal annealing of compacted SiO_2 under various conditions (via Belt apparatus or Diamond anvil cell), suggesting the existence of an amorphous-amorphous transition between HDA and LDA energy states. In their following study [13], they further investigated this question and observed large structural disorder by SAXS and WAXS, which tends to confirm the existence of such a transitional state.

In this paper, the unirradiated (5 GPa, 1000°C) and 10^7 Gy irradiated samples exhibited both a bimodal activation energy distribution, with a narrow component attributed to the HDA-LDA transitory state while the wider component ($FWHM_1$, E_1) of the distribution is likely related to the relaxation pathway of LDA phase.

First, this result means that (5 GPa, 1000°C) and 5 GPa_1000°C 10^7 Gy glass samples are constituted by a HDA and LDA states whereas it seems that the metamict phase is characterized by an absence of HDA. Secondly, we have to underline that both components display higher E_d values indicating more stable phases in the pristine densified sample. This is likely due to ionizing irradiation at 10^7 Gy that induces bond breaking and a high amount of point defects (E', NBOHC, ODC) [19] resulting in a more depolymerized network, while the vibrational structure is not strongly affected [7]. This nevertheless creates new

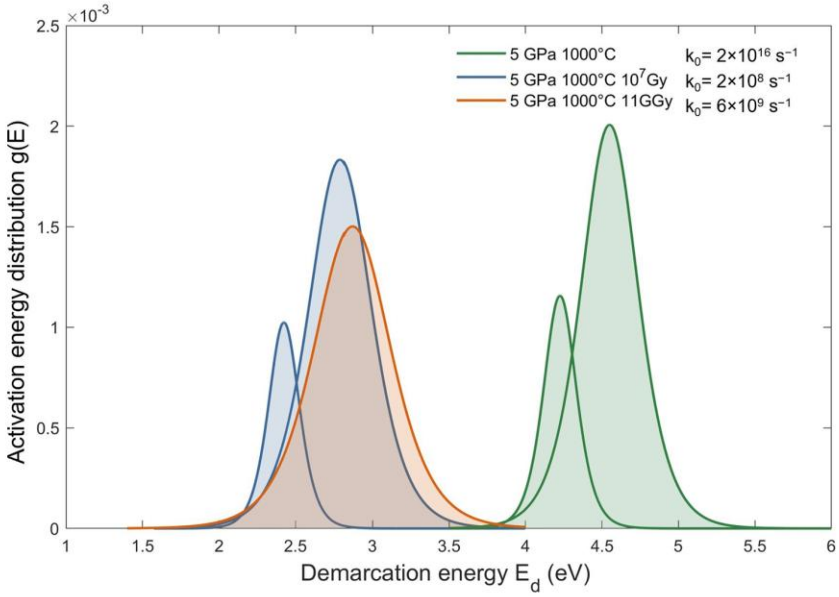

Fig. 5. Activation energy distributions for HPHT silica samples: unirradiated 5 GPa_1000°C, irradiated at 10^7 Gy and 11 GGy.

relaxation pathways for structural evolution linked to densification that tends to reduce its thermal stability thus lowering the measured E_d.

In contrast, the 11 GGy sample experienced a more severe decrease of density under high-dose irradiation, thus reaching a metamict like phase [8]. This in turn leads to a monotonous decrease of D_2(t,T) supported by the presence of a single component. The distribution is slightly wider but the demarcation energy that is quite similar to the one attributed to LDA phase relaxation pathway seen in the 5 GPa_1000°C 10^7 Gy irradiated sample. The absence of HDA signature in 5 GPa_1000°C 11 GGy explains the results obtained in [15] i.e. the absence of non-monotonic variation of D_1 and D_2 bands. It must be highlighted that our results provide an experimental proof for polyamorphism of silica, demonstrating that irradiation can influence the ratio between HDA and LDA phases, similar to the effects of High Pressure, and affect the stability of these states.

In addition, this demonstrates the effect of irradiation on the activation energy distributions attributed to HDA and LDA phases in densified silica. The HDA-LDA transitory state owns a narrow distribution ($\approx 3k_BT$), centered at lower energy compared to LDA, thus relaxing quite easily during thermal annealing as observed in the literature [4,13,21]. Our results suggested that HDA is more prominent in pristine (5GPa, 1000°C) and low irradiated (5GPa, 1000°C 10^7 Gy) than in 11 GGy sample where HDA signature was not apparent. This would suggest that the metamict like phase can be defined as a "unique" phase of silica.

5. Conclusion

In conclusion, we have investigated the thermal stability of densified silica glass samples with different irradiation levels, focusing on the non monotonous behavior of the D_2 Raman band and the underlying activation energy distributions. Our results suggest that the presence of the high-density amorphous (HDA) transition phase in the silica glass samples is responsible for the non monotonous behavior of the D_2 local density indicator and that ionizing irradiation may minimize the HDA states, leading to a transition to a lower density amorphous (LDA) structure. These findings provide important insights into the structural properties and thermal stability of densified silica glass under different irradiation conditions. The implications of this research extend to various fields, including the development of high-performance, radiation-resistant optical devices for space exploration and nuclear power applications.

CRediT authorship contribution statement

N. Shchedrina: Investigation, Data curation, Formal analysis, Writing – original draft, Visualization. **N. Ollier:** Validation, Methodology, Investigation, Resources, Writing – review & editing, Supervision. **M. Mobasher:** Investigation. **M. Lancry:** Validation, Conceptualization, Methodology, Writing – review & editing, Supervision, Funding acquisition.

Declaration of Competing Interest

The authors declare that they have no known competing financial interests or personal relationships that could have appeared to influence the work reported in this paper.

Data availability

Data will be made available on request.

Acknowledgments

The authors express their gratitude for the support received from the EMIR&A French network (FR CNRS 3618) on the platform SIRIUS. We also extend our appreciation to Pavel Varlamov (LSI, École polytechnique) for his assistance with the calculations. Pr. Ludovic Bellot-Gurlet (MONARIS) is warmly acknowledged for his help during Raman experiments.

References

[1] C.Z. Tan, J. Arndt, H.S. Xie, Optical properties of densified silica glasses, Phys. B Condens. Matter. 252 (1998) 28.
[2] M. Ono, S. Aoyama, M. Fujinami, S. Ito, Significant suppression of rayleigh scattering loss in silica glass formed by the compression of its melted phase, Opt. Express 26 (2018) 7942.
[3] G.C. Kahandawa, J. Epaarachchi, H. Wang, K.T. Lau, Use of FBG sensors for SHM in aerospace structures, Photonic. Sens. 2 (2012) 203.
[4] M. Guerette, M.R. Ackerson, J. Thomas, F. Yuan, E. Bruce Watson, D. Walker, L. Huang, Structure and properties of silica glass densified in cold compression and hot compression, Sci. Rep. 5 (2015) 15343.
[5] M. Guerette, M.R. Ackerson, J. Thomas, E.B. Watson, L. Huang, Thermally induced amorphous to amorphous transition in hot-compressed silica glass, J. Chem. Phys. 148 (2018), 194501.
[6] C. Martinet, A. Kassir-Bodon, T. Deschamps, A. Cornet, S.Le Floch, V. Martinez, B. Champagnon, Permanently densified SiO_2glasses: a structural approach, J. Phys. Condens. Matter 27 (2015), 325401.
[7] F. Piao, W.G. Oldham, E.E. Haller, The mechanism of radiation-induced compaction in vitreous silica, J. Non Cryst. Solids 276 (2000) 61.
[8] I. Reghioua, M. Lancry, O. Cavani, S.L. Floch, D.R. Neuville, N. Ollier, Unique silica polymorph obtained under electron irradiation, Appl. Phys. Lett. 115 (2019), 251101.
[9] N.M. Trease, T.M. Clark, P.J. Grandinetti, J.F. Stebbins, S. Sen, Bond length-bond angle correlation in densified silica—results from ^{17}O NMR spectroscopy, J. Chem. Phys. 146 (2017), 184505.
[10] L. Huang, L. Duffrène, J. Kieffer, Structural transitions in silica glass: thermo-mechanical anomalies and polyamorphism, J. Non Cryst. Solids 349 (2004) 1.
[11] C. Weigel, M. Mebarki, S. Clément, R. Vacher, M. Foret, B. Rufflé, Pressure-induced densification of vitreous silica: insight from elastic properties, Phys. Rev. B 100 (2019).
[12] A. Cornet, V. Martinez, D. de Ligny, B. Champagnon, C. Martinet, Relaxation processes of densified silica glass, J. Chem. Phys. 146 (2017), 094504.
[13] A. Cornet, C. Martinet, V. Martinez, D. de Ligny, Evidence of polyamorphic transitions during densified SiO2 glass annealing, J. Chem. Phys. 151 (2019), 164502.
[14] N. Ollier, S. Girard, S. Peuget, Radiation effects in glass, in: P. Richet (Ed.), Encyclopedia of Glass Science, Technology, History, and Culture, John Wiley & Sons, Ltd, Hoboken, NJ, USA, 2021, pp. 405–414.
[15] W. Primak, Fast-neutron-induced changes in quartz and vitreous silica, Phys. Rev. 110 (1958) 1240.
[16] B. Humbert, A. Burneau, J.P. Gallas, J.C. Lavalley, Origin of the raman bands, D1 and D2, in high surface area and vitreous silicas, J. Non Cryst. Solids 143 (1992) 75.
[17] M. Lancry, B. Poumellec, S. Costes, J. Magné, Reliable lifetime prediction for passivated fiber bragg gratings for telecommunication applications, Fibers 2 (2014) 92.
[18] Y. Wang, M. Cavillon, N. Ollier, B. Poumellec, M. Lancry, An overview of the thermal erasure mechanisms of femtosecond laser-induced nanogratings in silica glass, Phys. Status Solidi A 218 (2021), 2100023.
[19] N. Ollier, K. Piven, C. Martinet, T. Billotte, V. Martinez, D.R. Neuville, M. Lancry, Impact of glass density on the green emission and NBOHC formation in silica glass: A combined high pressure and 2.5 MeV electron irradiation, J. Non Cryst. Solids 476 (2017) 81.
[20] C. Guillon, J. Burgin, P. Langot, F. Vallée, B. Hehlen, Femtosecond spectroscopy of defect modes in silica glasses, Appl. Phys. Lett. 86 (2005), 081909.
[21] M. Mobasher, M. Lancry, J. Lu, D. Neuville, L. Bellot Gurlet, N. Ollier, Thermal relaxation of silica phases densified under electron irradiation, J. Non Cryst. Solids 597 (2022), 121917.
[22] N. Ollier, M. Lancry, C. Martinet, V. Martinez, S.Le Floch, D. Neuville, Relaxation study of pre-densified silica glasses under 2.5 MeV electron irradiation, Sci. Rep. 9 (2019) 1227.
[23] M. Heili, B. Poumellec, E. Burov, C. Gonnet, C.Le Losq, D.R. Neuville, M. Lancry, The dependence of raman defect bands in silica glasses on densification revisited, J. Mater. Sci. 51 (2016) 1659.
[24] Y. Wang, M. Lancry, M. Cavillon, B. Poumellec, Lifetime prediction of nanogratings inscribed by a femtosecond laser in silica glass, Opt. Lett. 47 (2022) 1242.
[25] B. Poumellec, Links between writing and erasing (or stability) of bragg gratings in disordered media, J. Non Cryst. Solids 239 (1–3) (1998) 108–115.
[26] W. Primak, Kinetics of processes distributed in activation energy, Phys. Rev. 100 (1955) 1677.

III.3 IMPACT OF THE SILICA GLASS INITIAL STATE ON THE THERMAL AND STRUCTURAL PROPERTIES OF METAMICT-LIKE SILICA GLASS

Journal of Non-Crystalline Solids 655 (2025) 123463

Contents lists available at ScienceDirect

Journal of Non-Crystalline Solids

journal homepage: www.elsevier.com/locate/jnoncrysol

Impact of the silica glass initial state on the thermal and structural properties of metamict-like silica glass

N. Shchedrina [a,b,*], M. Lancry [a], T. Charpentier [c], D. Neuville [d], N. Ollier [b]

[a] Institut de Chimie Moléculaire et des Matériaux d'Orsay, Université Paris-Saclay, Rue du doyen Georges Poitou, 91405 Orsay Cedex, France
[b] Laboratoire des Solides Irradiés, École polytechnique-CEA-CNRS, 91128 Palaiseau, Cedex, France
[c] Université Paris-Saclay, CEA, CNRS, NIMBE, CEA Saclay, Gif-sur-Yvette 91191, Cedex, France
[d] Institut de Physique du Globe de Paris, CNRS-Géomatériaux, Université Paris Cité, 1 rue Jussieu, 75005 Paris, France

ARTICLE INFO

Keywords:
Silica glass
Polyamorphism
Electron irradiation
Metamict phase

ABSTRACT

This study investigates the structural and thermal stability of metamict-like silica glass samples prepared through different thermomechanical pathways and then subjected to the same high dose of electron irradiation (11 GGy). Specifically, we compared Suprasil F300 silica glass samples treated with high-pressure high-temperature (HPHT) conditions followed by irradiation to those solely irradiated. Additionally, Suprasil CG samples were analyzed to investigate the effect of silica impurities (e.g. OH) on the resulting state. Using Raman and FTIR spectroscopy, along with photoluminescence spectroscopy, we analyzed the vibrational structure and point defects changes. The activation energy distribution of the densification relaxation process was calculated to assess its thermal stability in a reliable manner. The results demonstrate that, despite achieving similar densities and vibrational structures in the metamict-like state, the initial structure of silica significantly influences the thermal stability and the resulting point defects population.

1. Introduction

Silica glass, well-known for its wide range of uses in optics, electronics, and materials science, possesses distinctive characteristics that drive it essential in these fields. One of the intriguing features of silica glass is its anomalous thermo-mechanical properties, such as exhibiting negative thermal expansion within specific temperature ranges [1] and an increase in elastic moduli with rising temperature [2,3]. Another important property is its ability to undergo irreversible densification under pressure for $P > 12$ GPa [4–7], affecting not only its structure but also impacting its optical and mechanical traits [8], thus expanding its potential for applications.

One particularly interesting property in silica glass is polyamorphism [9,10], which refers to the ability of a material to exist in multiple amorphous states. For silica glass, there are known high-density amorphous (HDA) and low-density amorphous (LDA) phases obtained in densified silica [5,11]. Despite the absence of long-range order, each phase demonstrates distinct structural and physical properties. The transition from HDA to LDA during annealing is a widely discussed topic, even highlighting their coexistence under specific conditions [12].

Furthermore, another phase of silica glass with distinct structural properties can be achieved when intensively exposed to various types of irradiations, including neutron, ion, and electron irradiation [13–15]. At high doses, silica glass transitions into a "steady" state referred to as the "metamict-like" phase, associated with density of 2.26 g/cm^3 [16]. This term "metamict "comes from geology and is used to describe the amorphization of minerals under irradiation. It was also used to describe the quartz damaged by radioactive decay, reflecting the disordered state of post-irradiation quartz [17]. Due to the similar vibrational signature between quartz and silica exposed to very high dose neutrons ($2 \bullet 10^{20}$ neutrons/cm^2) [18], silica glass in this state was also termed metamict or metamict-like. However, the connection between this "medium density" metamict phase with the LDA or HDA phases remains poorly understood.

The study of the metamict phase in silica glass is relevant due to its profound implications on material applications and performance. In the realm of photonics applications, radiation-induced transformations are critical as they can alter the optical properties of silica glass, such as its refractive index and light transmission capabilities [14]. This is especially relevant for optical fiber sensors containing densified silica zones.

* Corresponding author at: Institut de Chimie Moléculaire et des Matériaux d'Orsay, Université Paris-Saclay, Rue du doyen Georges Poitou, 91405 Orsay Cedex, France.
E-mail address: nadezhda.shchedrina@universite-paris-saclay.fr (N. Shchedrina).

https://doi.org/10.1016/j.jnoncrysol.2025.123463
Received 14 December 2024; Received in revised form 3 February 2025; Accepted 19 February 2025
Available online 22 February 2025

These ones are created by UV light and based on point defects accumulation [19,20] as well as by fs-laser type II and type III modifications similar to high-pressure high-temperature (HPHT) conditions or even shock waves [21]. A deeper understanding of how silica behaves under electron irradiation, whether densified or not, could lead to enhanced strategies for improving the radiation resistance of optical fiber sensors in harsh environments such as nuclear reactors, their next generation or tokamaks.

As a result, irrespective of the initial density of the silica glass or the irradiation method (neutrons, lasers, ions, or electrons), exposure to high doses consistently drives the structure towards a uniform density, typically nearing 2.26 g/cm^3 [22]. This phenomenon was first documented by Primak in 1958 following extensive neutron irradiation, where both quartz and silica exhibited almost equivalent densities and amorphous structures [17]. However, electron diffraction, scanning electron microscopy and electron paramagnetic resonance investigations [23,24] have demonstrated that the structure of the metamict phase slightly varies depending on its origin, whether derived from different polymorphs such as quartz, cristobalite, or tridymite, or induced by different types of irradiation, such as fast neutrons or electrons. This variability indicates that there is no singular, uniform metamict state of SiO_2, highlighting the complexity of this phenomenon. Note the specific mechanisms of densification or its relaxation, however, differ according to the type of irradiation. For neutron and heavy ion irradiation, amorphization occurs through knock-on effects resulting in atomic displacement. In contrast, electron irradiation leads to the accumulation of bond-breaking [14,25,26], catalyzed by the creation of point defects. These processes collectively result in the disruption of Si-O-Si bonds and the formation of defect centers, thereby affecting the glass configurational disorder.

Studies on silica glass irradiated to 11 GGy, using high-energy electrons (2.5 MeV), have revealed that both non-densified and densified samples exhibit similar EPR spectra and a comparable number of E' defects upon reaching a saturated state. These E' centers demonstrate consistent line shapes, quantities, and hyperfine coupling parameters, indicating a similar defect structure and distribution across different initial glass densities [27]. However, the dynamics of E' centers formation with dose differ between the non-densified and densified samples. In non-densified silica, the irradiation progressively increases the density of E' centers [26], with the material able to sustain continuous growth in defect concentration without rapid saturation. In contrast, densified silica experiences an expedited saturation of E' centers at considerably lower irradiation doses. The densified structure, characterized by a compacted network formed under high-pressure conditions, likely impedes the migration and interaction of defect sites, thereby limiting the formation and longevity of these defects. Additionally, interstitial O_2 in pre-densified silica saturates rapidly and is destroyed with further irradiation, while non-densified silica, owing with greater free volume [28], supports a more sustained increase in O_2 concentration. Notably, the free volume configuration in the metamict phase of densified silica resembles that of non-densified silica. Indeed, the study showed that the configuration of intertetrahedral voids in metamict phase is close to that of non-densified silica [27]. This disparity highlights the influence of the initial structural state of silica on its radiation response. Additionally, independent of the initial density, electron-irradiated silica glass consistently shows an increased presence of non-bridging oxygen hole centers (NBOHC) and enhanced green luminescence [22,29,30].

To complete such a view, Raman spectroscopy is an essential tool for analyzing the vibrational structure of silica [31]. The main band peaking at 440 cm^{-1} corresponds to the bending motion of SiO_2 tetrahedra involving n-membered rings ($n \geq 5$) and reflects the average Si-O-Si angle. The D_1 and D_2 bands, located at 490 and 605 cm^{-1} respectively, arise from the collective breathing motion of oxygen atoms within 3-membered and 4-membered rings. In electron-irradiated silica, an increase in the D_2 band is observed with higher irradiation doses, although this increase does not correlate linearly with density since beyond a certain point (2.26 g/cm^3), it decreases, making metamict state the one with the highest D_2 band intensity [32,33].

The central question of this work is studying to what extent the metamict phase is universal and up to what point the thermo-mechanical pathway of silica glass impacts the final metamict-like state. While we observe that different initial densities of the same silica type result in identical Raman signatures after irradiation, it remains unclear whether subtle structural differences persist beyond spectroscopy detection. To explore this, we have characterized two types of suprasil F300 silica samples: one pristine non-densified, and the other pre-densified under HPHT conditions. We investigated their thermal stability by calculating the activation energy distribution during isothermal annealing. Moreover, a Suprasil CG differing mainly in their OH content will be compared after 11 GGy electrons irradiation.

2. Experimental details

The experiments employed Type III silica rods from Heraeus Suprasil F300, characterized by high chlorine content (typ. 2000–2500 ppm) and extremely low hydroxyl group content (<1 ppm, typ. 0.2 ppm). Additionally, Heraeus Suprasil CG silica, with a higher hydroxyl group content (400–1000 ppm) and low chlorine content (typ. 50 ppm). Most of the research, including densification and activation energy analysis, was conducted on Suprasil F300, while Suprasil CG was used for comparative purposes. Densification process was achieved using high pressure-high temperature (HP-HT) conditions of 5 GPa and 1000 °C in a belt press as described elsewhere [6]. Samples were irradiated with high-energy electrons at an energy of 2.5 MeV using the SIRIUS facility at LSI/CEA/Ecole Polytechnique. The current was around 25 μA with a temperature not exceeding 60 °C and we reach the total dose of 11 GGy. The different sample characteristics are detailed in Table 1 below.

Density was assessed using the Archimedean sink-float method, measuring the samples' weights in air (m_a) and when submerged in toluene (m_l). We employed the equation $d = (m_a \times \rho_{toluene})/(m_a - m_l)$ to calculate the density, where $\rho_{toluene}$ is the density of toluene, determined by its temperature-dependent equation (density (T) = 0.8845 − 0.9159 × 10^{-3} × T + 0.368 × 10^{-6} × T^2, T in°C) [34]. The density values are provided in Table 1.

Time-resolved photoluminescence experiments were conducted using the 266 nm excitation lines of an Indi Nd: YAG laser, which has a pulse duration of 10 ns at a repetition rate of 10 Hz. Emission detection was carried out using an Andor Shamrock 193 spectrometer connected to an Intensified Charge-Coupled Device camera. Additional experiments utilized a 488 nm continuous line from a doubled diode laser (Spectra Physics), with the same detection scheme. The 488 nm laser was focused using a × 20 objective through a Renishaw Raman probe.

A SiO_2 glass enriched with 90 % of ^{17}O, synthesized according to the process explained in [35], and irradiated at 11 GGy with 2.5 MeV

Table 1
Summary of sample characteristics: material type, irradiation dose, and density changes.

Sample name	Material	Irradiation dose	Density before irradiation, g/cm^3	Density after irradiation, g/cm^3
F300 11 GGy	Suprasil F300	11 GGy	2.207	2.261
HPHT F300 11 GGy	Suprasil F300	11 GGy	2.589	2.267
Pristine F300	Suprasil F300	unirradiated	2.207	NA
CG 11 GGy	Suprasil CG	11 GGy	2.202	2.245
Pristine CG	Suprasil CG	unirradiated	2.202	NA

electrons, was analyzed by Magic Angle Spinning (MAS) NMR and Multiple Quantum MAS (MQMAS) NMR [36] to investigate the structural changes at the atomic level. The spectra were collected on a Bruker Avance IV NEO solid-state NMR spectrometer operating at a magnetic field of 11.72 T (500WB Bruker magnet) using a 4 mm (o.d. of the ZrO_2 rotor) CPMAS Bruker probe head at a spinning frequency of 12.5 kHz. 29Si spectra were obtained using a CPMG pulse sequence [37] and variable recycle delay values from 2s to 3600s. ^{17}O MAS spectra were acquired using a rotor-synchronized spin echo delay (of one rotor period, 80us) with recycle delays ranging from 0.5s to 8s (no change in line shape were observed). ^{17}O MQMAS spectra were obtained using a shifted-echo three pulses sequence [38] with an echo delay of 2 ms and recycle delay of 1 s. The spectra were processed with in-house code (T. Charpentier). ^{29}Si spectra were referenced to an external TKS sample for which the highest-intensity peak is situated at 9.9 ppm from that of TMS. For ^{17}O external frequency reference was 17O-enriched (40 %) H_2O (0 ppm).

IR spectra were obtained using a Thermo Fisher Nicolet 5700 FTIR spectrometer with a Nicolet continuum microscope. Raman spectra were collected in MONARIS Lab (PLASVO platform, Sorbonne university) utilizing a Horiba Jobin Yvon LabRam HR800 spectrometer equipped with a 600 lines/mm grating and a Peltier-cooled CCD detector. An argon-ion laser at 458 nm served as the excitation source and spectra were collected with an Olympus long working distance x50 microscope objective. *In situ* Raman spectra for the activation energy distribution calculation were then monitored during the isothermal annealing process using a Linkam TS1500 heating stage. Samples were annealed at 825 °C, 885 °C, and 950 °C. These annealing temperatures were selected to ensure measurable erasure at each temperature and a complete erasure at the highest temperature after 18 h. Then the intensity of the D_2 band was chosen as a densification indicator. The analysis was conducted using a custom MATLAB algorithm to extract the D_2 band amplitude from the normalized spectra. Spectral normalization involved the total integrated area, with the D_2 band amplitude extracted by fitting the background within the 550–650 cm^{-1} range using polynomial functions and identifying the peak of the fitted curves. The VAREPA framework [39] was used to estimate the thermal stability of the densification process in terms of activation energy and its distribution. This approach involves using accelerated aging data to feed the chosen model. The model assumes a single relaxation pathway based on a 1st order Arrhenius kinetic that is thermally activated with activation energy, E_a, which is distributed according to a temperature and time-independent function and due to glass configurational disorder. The activation energy can be then calculated using $\boldsymbol{E_d = k_B T ln(k_0 t)}$, where E_d is demarcation energy (eV), k_B is Boltzmann constant (eV/K), T is annealing temperature (K), k_0 is the constant rate of the densification relaxation (s^{-1}), t is the annealing time (s). This experimental procedure is described in more details in our earlier publication [12].

3. Results

In this study, we will compare two metamict-like samples created from initial F300 silica but having different thermo-mechanical pathways. The first sample is a pristine silica glass irradiated with 11 GGy (F300 11 GGy), while the second one is pre-densified under high pressure and high temperature (HPHT) conditions at 5 GPa and 1000 °C, and subsequently irradiated with 11 GGy (HPHT F300 11 GGy). Initially, they have different densities: 2.20 g/cm^3 for pristine glass and 2.59 g/cm^3 for the HPHT sample. High-energy electron irradiation provides the necessary energy to overcome distributed energy barriers, facilitating the transition to a stable metamict-like phase. Both pristine silica and HPHT-densified silica, despite their initial density differences, converge towards a common metamict-like density of approximately 2.26 g/cm^3 (see Table 1).

3.1. Vibrational spectroscopy analysis of metamict-like silica F300

Fig. 1a presents the Raman spectra for pristine silica and two metamict-like samples – silica and HPHT-densified silica, both irradiated with 11 GGy. The Raman signatures of the two metamict samples are remarkably similar, displaying a significant increase in the intensity of the D_2 band around 605 cm^{-1}. This enhancement indicates a higher concentration of 3-membered rings in the structure, a characteristic feature of metamict silica. Consistently, both they also exhibit a higher D_1 band intensity at 490 cm^{-1} (4-membered rings) compared to the pristine glass. Furthermore, both irradiated samples exhibit a narrower main band centered around 440 cm^{-1}, indicating a lower average Si-O-Si bond angle compared to pristine silica. This observation aligns with previous literature findings and agrees with their higher macroscopic density.

Fig. 1b displays FTIR spectra of the samples. The primary characteristic of the silica glass infrared spectrum originates from the collective asymmetric stretching vibration of Si-O-Si subunits in its structure. This infrared active phonon band is located between 900–1300 cm^{-1}. The wavenumber of the Si-O-Si asymmetric stretching band, denoted as $\nu_{as}^{Si-O-Si}$, is linearly decreasing with the silica density [8]. For the F300 11 GGy and HPHT F300 11 GGy sample, this peak is respectively positioned at 1110 cm^{-1} and 1109 cm^{-1} whereas it is centered at 1117 cm^{-1} in pristine silica. The shifts of 7–8 cm^{-1} correspond to a density change of

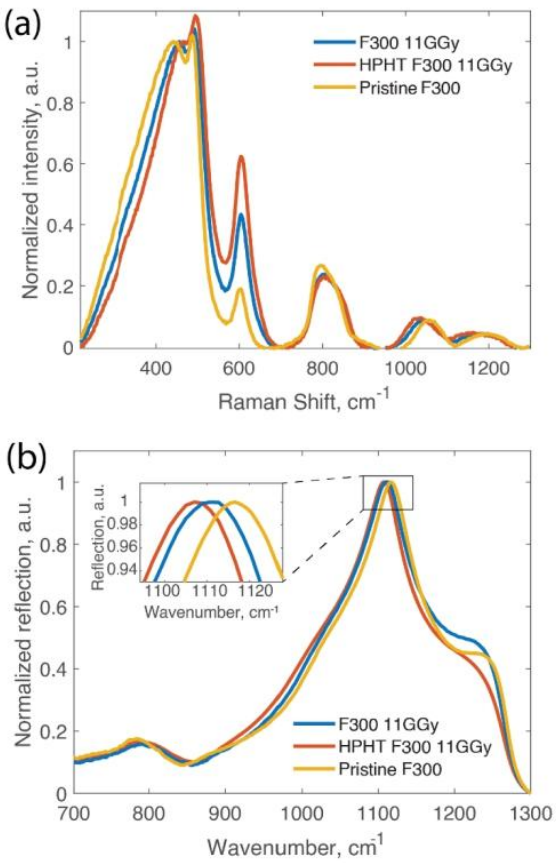

Fig. 1. Vibrational spectra of pristine silica glass (yellow), and two metamict-like samples: silica irradiated with 11 GGy (blue), and HPHT densified silica irradiated with 11 GGy (red): a) Raman spectra. b) FTIR spectra. The spectra are normalized for comparison by the maximum of the main band; The inset shows a close-up peaks.

approximately 0.07–0.08, aligning well with the measured densities of the samples. Differences in the shape of the right shoulder of the peak, attributed to LO mode of asymmetric stretching vibrations, are highly sensitive to the incident light angle. Variations in the roughness and geometrical unevenness of the samples may account for these differences in peak shape [40,41].

Also, we observe in Fig. 1a that the 1100 cm^{-1} Raman band follows the same trend as the FTIR $\nu_{as}^{Si-O-Si}$ band in Fig. 1b, with HPHT F300 11 GGy showing the most pronounced shift, followed by F300 11 GGy and then pristine F300, confirming a consistent densification trend across both spectroscopic techniques.

3.2. ^{29}Si and ^{17}O MAS NMR investigation

To gain deeper insight into the structural modifications induced by electron irradiation, we also conducted ^{29}Si and ^{17}O MAS NMR measurements on the pristine SiO_2 glass and the sample irradiated with 11 GGy of electrons.

Fig. 2 compares the ^{29}Si MAS NMR spectra of the pristine and irradiated samples.

In the irradiated sample, we observe a shift of the chemical shift by 2.4 ppm towards lower values compared to the pristine glass. Additionally, there is noticeable broadening of the spectral band towards lower chemical shifts. Furthermore, the ^{17}O MQMAS NMR spectra are presented in Fig. 3a, with Fig. 3b showing the one-dimensional projection onto the MAS isotropic shift dimension.

The 2D ^{17}O MQMAS NMR isotropic pattern for the irradiated sample exhibits significant broadening towards lower isotropic shifts.

3.3. Photoluminescence emission spectra of metamict-like silica F300 samples

Insert on Fig. 4 presents the photoluminescence emission spectra under 266 nm excitation, normalized by their maximum for sake of comparison. Two main emission bands are observed in both metamict samples. The first peak at 475 nm corresponds to the triplet-singlet transition of Oxygen Deficient Centers, ODC (II) [42]. The second peak at 650 nm is associated with the charge transfer transition in Non-Bridging Oxygen Hole Centers (NBOHC), occurring between the half-filled non-bonding 2p π orbital of the non-bridging oxygen atom and the lone-pair 2p orbital of one of the ligand oxygen atoms [43]. Both samples exhibit approximately the same ratio of these two emission bands.

Fig. 4 presents the photoluminescence emission spectra of these samples under 488 nm excitation, normalized to the amplitude of the

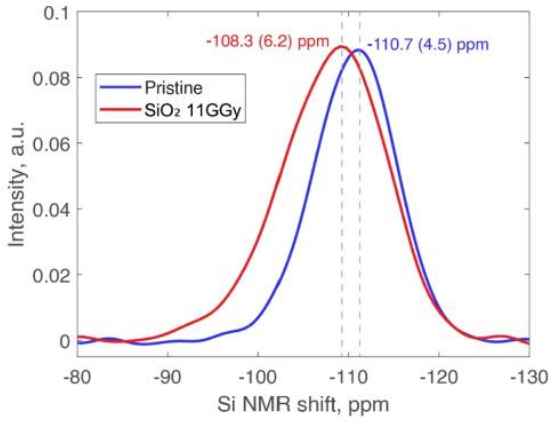

Fig. 2. ^{29}Si MAS NMR spectra of pristine SiO_2 glass (blue line) and SiO_2 glass irradiated with 11 GGy electrons (red line).

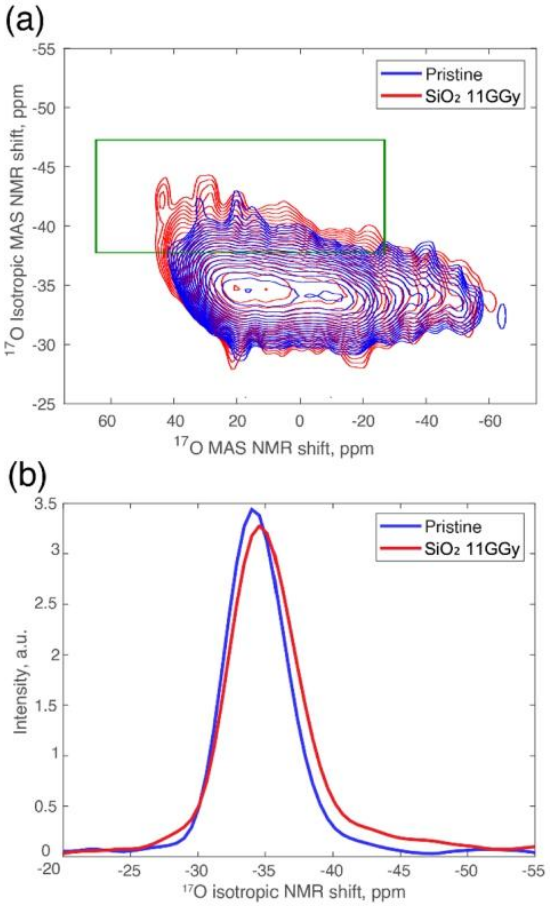

Fig. 3. a) 2D ^{17}O MQ MAS NMR spectra of pristine SiO_2 glass (blue) and SiO_2 glass irradiated with 11 GGy electrons (red); b) 1D projection onto the MAS isotropic shift dimension for both samples.

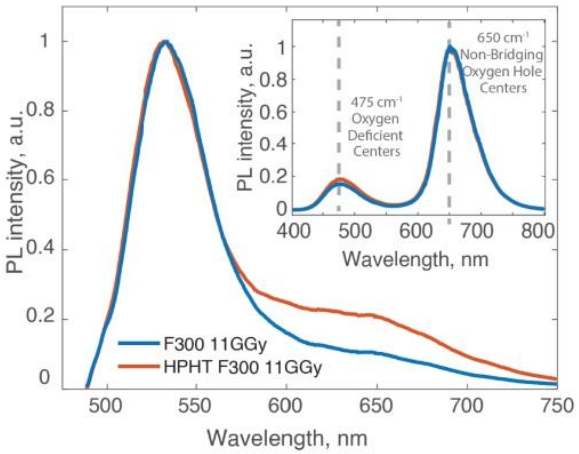

Fig. 4. Photoluminescence emission spectra of metamict-like samples: irradiated with 11 GGy (blue) and HPHT densified silica irradiated with 11 GGy (red) under 488 nm excitation. Insert: spectra obtained after a 500 ns delay time and a gate width of 10 ms at an excitation wavelength of 266 nm.

emission band peaking at 545 nm. This prominent emission band at 545 nm is labeled "green luminescence". The exact nature of the defects responsible for this green luminescence remains unknown; however, it has been demonstrated that these defects are enhanced in silica glasses that are densified [30]. The spectra indicate that both metamict-like samples exhibit similar luminescence characteristics despite a small difference in NBOHC point defects while they both show a huge green luminescence.

3.4. Activation energy distribution of metamict-like silica F300 samples

Next, we assessed the thermal stability and related activation energy distribution of the densification processes in the two metamict samples. To calculate the activation energy, we investigated the relaxation kinetic of the densification. This relaxation is thermally activated, and its energy distribution is influenced by the inherent glass disorder. Raman spectroscopy, particularly the D_2 band, was used as an indicator to track the local density changes within the silica network.

We thus performed in situ Raman spectroscopy during the isothermal annealing process at three different temperatures: 825 °C, 885 °C, and 950 °C. Spectra were recorded every 4 min during the first 2 h, and every 15 min for a total duration of 16 h. This approach allowed us to monitor the structural changes in "real-time" as the samples underwent thermal treatments. This experimental procedure was similar to our previous study, as described in our earlier publication [12]. The recorded Raman spectra were normalized by the total integrated area, and the amplitude of the D_2 band (between 550 and 650 cm^{-1}) was extracted. We obtained two sets of isotherms that follow the evolution of the normalized D_2 intensity over time. Figure SI_1 in Supplementary Information shows the isotherms for F300 11 GGy sample.

Next, a master curve was obtained by rescaling the normalized evolution of D_2 against the demarcation energy, E_d, and adjusting the reaction rate constant, k_0, in such a way we can collapse the three isotherms into a single curve i.e. the so-called master curve. Figure SI_2 in Supplementary Information shows the master curve for F300 11 GGy sample. The optimal value of k_0 was determined through least squares optimization. The best k_0 values were significantly different for the two samples, with $k_0=6.8\times10^9 s^{-1}$ for the HPHT F300 11 GGy sample and $k_0=3.9\times10^5 s^{-1}$ for the F300 11 GGy sample, indicating differing relaxation rates.

Subsequently, the master curve was fitted using a sigmoidal function, and the first derivative of this fit was taken to obtain the distribution of activation energy, $g(E)$, for each sample. Figure SI_3 in Supplementary Information presents the master curve fitting along with activation energy distribution g(E) for F300 11 GGy sample. The distributions of activation energy are shown in Fig. 5. The distribution for the HPHT F300 11 GGy sample is centered at 2.87 eV with a full width at half maximum (FWHM) of 0.59 eV, while the distribution for the F300 11 GGy sample is centered at 1.89 eV with a similar FWHM of 0.59 eV. This reveals the much higher thermal stability of the densification process induced in HPHT sample whereas both samples have already reached the metamict state.

3.5. Effect of silica glass composition on metamict state formation

An important question to address is whether the presence impurities and thus point defects and glass viscosity to some extend affect the resultant metamict state in silica glass. To investigate this, we compared wet and dry silica. Suprasil F300 pristine, with low OH content (typ. 0,2 ppm), and Suprasil CG, with higher OH content (400–1000 ppm). Specifically, we compared F300 11 GGy and CG 11 GGy, both irradiated with the same dose.

Raman spectroscopy (Fig. 6) revealed that pristine CG initially has a different shape compared to pristine F300, there showing lower D_1 and D_2 band intensities. This is because pristine CG has a slightly lower density, attributed to its higher OH content [44]. After irradiation, CG

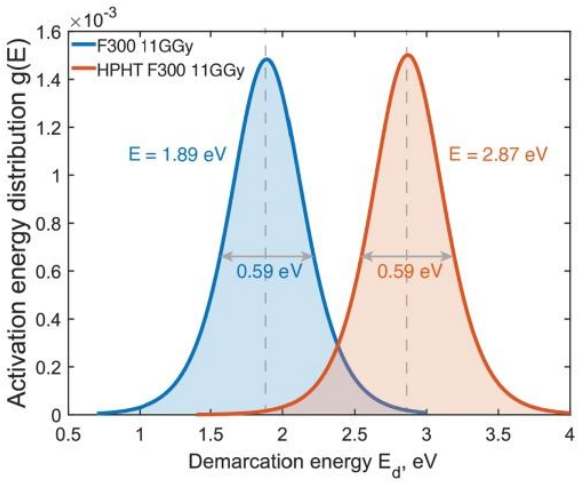

Fig. 5. Activation energy distributions of the densification process in metamict-like silica samples: HPHT F300 11 GGy (orange) and F300 11 GGy (blue).

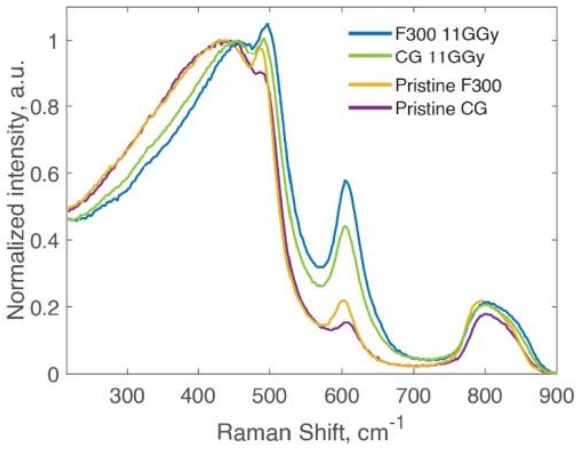

Fig. 6. Raman spectra two unirradiated (Pristine F300 and Pristine CG) and two metamict-like samples (F300 11 GGy and CG 11 GGy).

11 GGy exhibited a lower D_2 band intensity and a narrower full width at half maximum (FWHM) of the main band compared to F300 11 GGy. These changes indicate that CG 11 GGy is less densified. This is corroborated by the post-irradiation densities, with CG 11 GGy having a density of 2.24 g/cm^3 compared to 2.26 g/cm^3 for F300 11 GGy.

Photoluminescence spectra showed that ODC(II)/NBOHC ratio is lower in CG 11 GGy compared to F300 11 GGy sample (Fig. 7 insert). More prominently, the emission band at 545 nm (green luminescence) is very intense in F300 11 GGy contrary to CG 11 GGy displaying almost no emission (Fig. 7). Double integration of the EPR signal was used to evaluate the concentration of E' centers, revealing that F300 11 GGy contains approximately twice as many E' centers as CG 11 GGy. The corresponding EPR spectrum is provided in Supplementary Materials, Figure SI_4. These comparisons demonstrate a significant difference between the two silica metamict-like samples, dependent on their impurities content (mostly OH species) relative to their ring distribution and Si-O-Si angles as well as their point defects population.

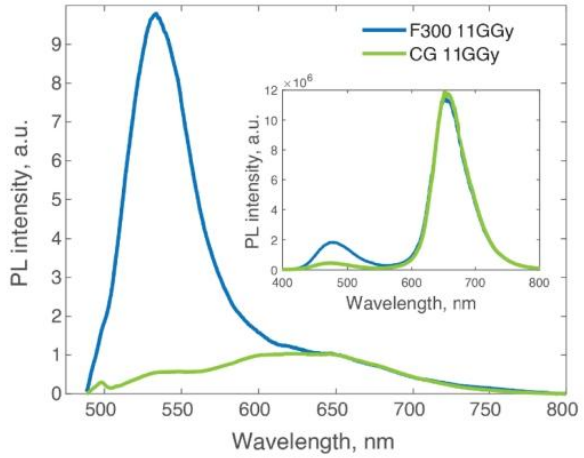

Fig. 7. Photoluminescence emission spectra of metamict-like samples (F300 11 GGy and CG 11 GGy) under 488 nm excitation; insert: photoluminescence emission spectra obtained after a 500 ns delay time and a gate width of 10 ms at an excitation wavelength of 266 nm.

4. Discussion

In this study, we compare the metamict-like structural transformations in silica glass under high-energy electron irradiation, focusing on the effects of different initial densities, specific thermo-mechanical histories, and impurities content (OH amount over 3 orders of magnitude).

The vibrational spectroscopy results from Raman and FTIR analyses provide insights into the structural transformations of silica glass under high-energy electron irradiation. The Raman spectra of the F300 and HPHT-densified F300 post-irradiation 11 GGy displayed significant modifications, particularly an increase in the D_2 band intensity around 605 cm^{-1} and the D_1 band at 490 cm^{-1}, indicative of higher concentrations of three- and four-membered rings, respectively [31] in agreement with [22]. Additionally, the main Raman band at 440 cm^{-1} showed narrowing and a shift towards lower wavenumbers, reflecting a reduced Si-O-Si bond angle and increased network density [45]. The NMR results obtained with ^{29}Si nucleus fully support those changes. We can report the values of Trease et al. [46] of -108.9 ppm for a 8 GPa densified silica close to the value found for the metamict one (-108.3 ppm). Based on the variation of about 1.6°/ppm in shift reported in [46,47], we can estimate a Si-O-Si average angle narrower of 3.8° compared to the pristine silica. Additionally, the main Raman band shifts by approximately 17 cm^{-1} after irradiation, and according to the relationship proposed in [48], a 5.5 cm^{-1} shift corresponds to ~1° change in the average Si–O–Si bond angle. This results in approximately 3° decrease from the pristine sample, which is consistent with the 3.8° narrowing estimated from our ^{29}Si NMR data. The broadening of the ^{29}Si MAS spectrum is consistent with a significant increase of 3 and 4 membered rings as demonstrated by the simulated ^{29}Si MAS NMR spectra of 3 and 4 membered rings by Charpentier et al. [49]. This interpretation is supported by the narrowing of the main Raman band, meaning that a larger dispersion of the Si-O-Si angle is not occurring. Concerning the ^{17}O NMR, the MQMAS NMR spectra displayed in Fig. 3 show a shift towards more negative isotropic shifts upon irradiation. This spectral region is reflective of lower quadrupolar interaction values and higher isotropic chemical shift values. As was discussed in detail in Ref. [49] (see Fig. 4) this spectral region is characteristic of small-membered rings (3- and 4-membered rings). The change in NMR parameters were mainly caused by a decrease of the Si-O-Si angle (Fig. 6 of [49]) in agreement with the ^{29}Si NMR shifts variations.

The CG 11 GGy sample exhibited less pronounced changes in the Raman spectrum compared to F300 11 GGy, with reduced D_1 and D_2 band intensities, indicating fewer three- and four-membered rings and a lower level of densification. This is consistent with its lower final density (2.245 g/cm^3), due to the much higher OH content in CG, which limits the structural reorganization under irradiation and favors bond breaking.

The primary distinction between pristine F300 and pristine CG silica glass lies in their OH content, which is 3 orders of magnitude higher in the latter. This OH content strongly influences the defects formation kinetics, which is a key mechanism behind silica glass densification under electron irradiation [14,25,26]. While both irradiated samples show prominent NBOHC emission, the ODC(II)/NBOHC ratio is significantly lower in CG 11 GGy compared to F300 11 GGy (Fig. 7 insert). This reduced ODC(II)/NBOHC ratio could be explained by a decrease of ODC (II) point defect in CG and/or an increase of NBOHC point defects. The first point can be explained by a bleaching effect caused by hydrogen released from SiOH (silanol) groups during irradiation. In silica with high OH content (Suprasil CG), electron irradiation releases hydrogen atoms from SiOH, which combine into H_2 molecules. These H_2 molecules interact with excited ODC(II)*, causing emission bleaching and forming SiH_2 [50–52]. The second hypothesis is fully consistent with the well-known impact of Si-OH bonds on the increased amount of NBOHC [53].

Furthermore, the higher OH content in CG introduces H_2O molecular into the glass, which can break Si–O bonds through hydrolysis. The bond-breaking depolymerizes the network, reducing the formation of three- and four-membered rings under electron irradiation, which leads to less densification and lower D_1 and D_2 band intensities in CG 11 GGy compared to F300 11 GGy. Additionally, the lower green emission observed in CG 11 GGy (Fig. 7 insert) aligns with the less intense D_2 band and the reduced glass density in agreement with [30].

FTIR spectroscopy provided additional quantitative information on density, particularly regarding the Si-O-Si asymmetric stretching vibrations. The $\nu_{as}^{Si-O-Si}$ band shifted linearly with sample density: it was at 1110 cm^{-1} in the F300 11 GGy sample and slightly lower at 1109 cm^{-1} in the HPHT F300 11 GGy sample, compared to 1117 cm^{-1} in the unirradiated sample, reflecting its lower density. This observation aligns with the findings of Awazu et al. [54], who noted a shift in IR absorption peaks post-heavy-ion irradiation on thin layer silica which they attributed to the formation of three- and four-member rings. Although their observed shift was much higher (35 cm^{-1}), this can be explain with the different IR band shapes and SEM images revealing that heavy-ion irradiation causes structural damage at microscale (conical holes) that could lead to IR large variations [54]. Tan et al. [8] established a calibration curve between density and IR band position for HPHT densified silica. Our results follow a similar trend, with the IR band shifting to lower wavenumbers as density increases from 2.2 g/cm^3 for pristine to 2.26 g/cm^3 for metamict-like samples. The shift of 7–8 cm^{-1} corresponds to a density change of approximately 0.06–0.08 g/cm^3. Despite potential overestimation of density using the calibration curve from this work [8] due to differing densification mechanisms under electron irradiation, the overall trend remains consistent.

The mechanism of silica compaction upon reaching the metamict-like phase differs significantly from HPHT densification. Under HPHT conditions, compaction primarily occurs through the densification of existing ring structures without substantial changes in their sizes with a reduction of free volume [55]. In contrast, when subjected to high doses of electron irradiation, bond breaking accumulation via the formation of point defects leads to a complete reorganization of the silica structure. This reorganization is clearly evidenced by the significant increases in the Raman D_1 and D_2 bands, which indicate the formation of three- and four-membered rings. Additionally, the high levels of defects observed in the photoluminescence data further confirm the structural changes induced by electron irradiation.

To additionally compare the metamict samples, we assessed their

thermal stability. Using the VAREPA framework [56], we extracted the underlying activation energy distribution. The results revealed that while the activation energy distribution width was similar for both samples (approximately 0.6 eV) but the central energy was significantly higher for the HPHT-treated sample (2.87 eV) compared to the solely irradiated sample (1.89 eV). This indicates that despite similar structure, the predensified sample HPHT F300 11 GGy displays a much higher thermal stability compared to the sample obtained by irradiation alone (SiO_2 F300 11 GGy).

Contrarily to previous work [12] made in unirradiated samples or irradiated at low dose (typ. 10^7 Gy), neither of our samples (F300 11 GGy and HPHT F300 11 GGy) exhibited a double distribution, suggesting the absence of the HDA phase when starting from the metamict-like state. This indicates that HDA phase has been relaxed under high-dose electron irradiation. This finding agrees with step isochronal annealing of the metamict phase where local density indicators, D_1 and D_2 bands decreased quasi-monotonously under thermal treatment along with the glass density [16]. It is worth emphasizing that the difference of E_a center values is 2.87 vs 1.89 eV between HPHT F300 11 GGy and F300 11 GGy respectively. These differences in the activation energy distribution demonstrate that silica glass "retains the memory" of its initial thermomechanical pathway even when subjected to high doses of electron irradiation.

This result can be associated to the behavior of HPHT under thermal annealing, where densified silica glass, prepared at higher temperatures, exhibits slower relaxation rates compared to glasses densified at lower temperatures [11].

Furthermore, we observed that both F300 11 GGy and HPHT F300 11 GGy samples, prepared seven years ago, have maintained their Raman signatures and densities unchanged over this period, demonstrating the long-term stability of the metamict phase.

Regarding Suprasil CG and F300, despite significant irradiation, the two samples do not fully converge into an identical phase. Both samples differ in their fictive temperature and viscosity, but we showed previously [22,29], the fictive temperature was not impacting the final density and structure of the metamict-like phase. To explain the final structure, we are rather prone to the point defects formation mechanisms due to the high OH content. It is worth noticing the quasi absence of green emission in the metamict like CG silica. This suggests an inhibition of this defect due to the presence of OH groups that may minimize the precursor of this defect. A second point is that the higher OH amount leads to a pristine silica with less strained bonds attested by a less intense D_2 band (Fig. 6). This reduced amount of strain bonds could explain also why we observed less E' centers and a final D_2 band less intense for CG compared to F300.

Understanding the impact of initial thermomechanical pathways and OH content on silica glass is crucial for developing advanced sensors for nuclear reactors and space environments. These sensors must endure high radiation and temperature while maintaining functionality. Comparing 11 GGy, analogous to sensors made using light and defect accumulation (by UV lasers [57,58]), with sensors fabricated via HPHT processes like fs-laser Type II modifications (which have the same densification mechanism [59]), reveals important insights. We can predict that sensors made with HPHT (like fs-laser Type II), even after being subjected to high levels of irradiation, can have higher thermal stability and show better performance and durability in harsh environments.

5. Conclusion

Our findings indicate that similarly to what happens under thermal relaxation, the thermomechanical pathway of silica densification influences its relaxation under exposure to high doses of electrons, preventing the samples from fully converging into an identical metamict phase.

In particular this study demonstrates that the thermal stability of metamict-like SiO_2 samples is highly dependent on their initial thermomechanical preparation pathways. Samples treated with high-pressure high-temperature (HPHT) followed by irradiation showed significantly greater thermal stability than those solely subjected to irradiation. Activation energy distribution analysis demonstrated that HPHT-treated samples possess a more stable structure. This suggests that sensors fabricated under processes involving HPHT, such as with fs-laser Type II or Type III modifications [60,61], will likely exhibit enhanced thermal stability and improved performance and durability in harsh environments, even after exposure to high levels of radiation, compared to sensors prepares only by defects accumulation or a cold compaction. These results emphasize the importance of initial thermomechanical conditions in determining the thermal resilience of metamict-like silica glass and more generally silica densification process and related optical devices.

CRediT authorship contribution statement

N. Shchedrina: Writing – review & editing, Writing – original draft, Visualization, Software, Investigation, Formal analysis, Data curation. **M. Lancry:** Writing – review & editing, Validation, Supervision, Resources, Methodology, Funding acquisition, Data curation, Conceptualization. **T. Charpentier:** Writing – review & editing, Visualization, Software, Investigation, Formal analysis. **D. Neuville:** Resources. **N. Ollier:** Writing – review & editing, Validation, Supervision, Resources, Project administration, Methodology, Investigation, Formal analysis.

Declaration of competing interest

The authors declare that they have no known competing financial interests or personal relationships that could have appeared to influence the work reported in this paper.

Acknowledgements

The authors express their gratitude for the support received from the EMIR&A French Network (FR CNRS 3618) on the platform SIRIUS. We also thank the "Plateforme de spectroscopies vibrationnelles et optiques (PLASVO, Sorbonne Université)" for access to the HR800 Raman spectrometer and to Assia Hessani and Ludovic Bellot-Gurlet (MONARIS laboratory) for their technical assistance in performing the measurements.

Supplementary materials

Supplementary material associated with this article can be found, in the online version, at doi:10.1016/j.jnoncrysol.2025.123463.

References

[1] J.G. Collins, G.K. White, Chapter IX thermal expansion of solids. Progress in Low Temperature Physics, Elsevier, 1964, pp. 450–479.
[2] A. Polian, D. Vo-Thanh, P. Richet, Elastic properties of a-SiO 2 up to 2300 K from Brillouin scattering measurements, EPL 57 (2002) 375–381.
[3] M. Fukuhara, A.S.A. Fukuhara Mikio, High temperature-elastic moduli and internal dilational and shear frictions of fused quartz, Jap. J. Appl. Phys. 33 (1994).
[4] M. Guerette, M.R. Ackerson, J. Thomas, F. Yuan, E. Bruce Watson, D. Walker, L. Huang, Structure and properties of silica glass densified in cold compression and hot compression, Sci. Rep. 5 (2015) 15343.
[5] M. Guerette, M.R. Ackerson, J. Thomas, E.B. Watson, L. Huang, Thermally induced amorphous to amorphous transition in hot-compressed silica glass, J. Chem. Phys. 148 (2018) 194501.
[6] C. Martinet, A. Kassir-Bodon, T. Deschamps, A. Cornet, S. Le Floch, V. Martinez, B. Champagnon, Permanently densified SiO2 glasses: a structural approach, J. Phys. Condens. Matter 27 (2015) 325401.
[7] R.J. Hemley, Raman spectroscopy of si o 2 glass at high pressure, Phys. Rev. Lett. 57 (1986).
[8] C.Z. Tan, J. Arndt, H.S. Xie, Optical properties of densified silica glasses, Phys. B Condens. Matter 252 (1998) 28–33.
[9] L. Huang, L. Duffrène, J. Kieffer, Structural transitions in silica glass: thermomechanical anomalies and polyamorphism, J. Non Cryst. Solids 349 (2004) 1–9.

[10] C. Weigel, M. Mebarki, S. Clément, R. Vacher, M. Foret, B. Rufflé, Pressure-induced densification of vitreous silica: insight from elastic properties, Phys. Rev. B 100 (2019), https://doi.org/10.1103/physrevb.100.094102.
[11] A. Cornet, C. Martinet, V. Martinez, D. de Ligny, Evidence of polyamorphic transitions during densified SiO2 glass annealing, J. Chem. Phys. 151 (2019) 164502.
[12] N. Shchedrina, N. Ollier, M. Mobasher, M. Lancry, Investigating densification processes of amorphous silica phases through activation energy distribution, J. Non Cryst. Solids 617 (2023) 122491.
[13] F. Piao, W.G. Oldham, E.E. Haller, The mechanism of radiation-induced compaction in vitreous silica, J. Non Cryst. Solids 276 (2000) 61–71.
[14] N. Ollier, S. Girard, S. Peuget, Radiation effects in glass, encyclopedia of glass science (2021). https://onlinelibrary.wiley.com/doi/abs/10.1002/9781118801017.ch3.13.
[15] L. Douillard, J.P. Duraud, Amorphization of α-quartz under irradiation, J. Phys. III 6 (1996) 1677–1687.
[16] M. Mobasher, M. Lancry, J. Lu, D. Neuville, L. Bellot Gurlet, N. Ollier, Thermal relaxation of silica phases densified under electron irradiation, J. Non Cryst. Solids 597 (2022) 121917.
[17] W. Primak, Fast-neutron-induced changes in quartz and vitreous silica, Phys. Rev. 110 (1958) 1240–1254.
[18] J.B. Bates, R.W. Hendricks, L.B. Shaffer, Neutron irradiation effects and structure of noncrystalline SiO2, J. Chem. Phys. 61 (1974) 4163–4176.
[19] T. Erdogan, V. Mizrahi, P.J. Lemaire, D. Monroe, Decay of ultraviolet-induced fiber Bragg gratings, J. Appl. Phys. 76 (1994) 73–80.
[20] A. Morana, E. Marin, L. Lablonde, T. Blanchet, T. Robin, G. Cheymol, G. Laffont, A. Boukenter, Y. Ouerdane, S. Girard, Radiation effects on fiber bragg gratings: vulnerability and hardening studies, Sensors (Basel) 22 (2022) 8175.
[21] S. Mihailov, D. Grobnic, C. Hnatovsky, R. Walker, P. Lu, D. Coulas, H. Ding, Extreme environment sensing using femtosecond laser-inscribed fiber Bragg gratings, Sensors (Basel) 17 (2017) 2909.
[22] I. Reghioua, M. Lancry, O. Cavani, S.L. Floch, D.R. Neuville, N. Ollier, Unique silica polymorph obtained under electron irradiation, Appl. Phys. Lett. 115 (2019).
[23] L.W. Hobbs, The role of topology and geometry in the irradiation-induced amorphization of network structures, J. Non Cryst. Solids 182 (1995) 27–39.
[24] L. Douillard, J.P. Duraud, Amorphization of ?-quartz under irradiation, J. Phys. III 6 (1996) 1677–1687.
[25] R.A.B. Devine, Macroscopic and microscopic effects of radiation in amorphous SiO2, Nucl. Instrum. Methods Phys. Res. B 91 (1994) 378–390.
[26] G. Buscarino, S. Agnello, F.M. Gelardi, R. Boscaino, Polyamorphic transformation induced by electron irradiation ina-SiO2glass, Phys. Rev. B Condens. Matter Mater. Phys. 80 (2009), https://doi.org/10.1103/physrevb.80.094202.
[27] N. Ollier, I. Reghioua, O. Cavani, M. Mobasher, A. Alessi, S. le Floch, L. Skuja, Probing densified silica glass structure by molecular oxygen and E' center formation under electron irradiation, Sci. Rep. 13 (2023) 13657.
[28] M. Zanatta, G. Baldi, R.S. Brusa, W. Egger, A. Fontana, E. Gilioli, S. Mariazzi, G. Monaco, L. Ravelli, F. Sacchetti, Structural evolution and medium range order in permanently densified vitreous SiO2, Phys. Rev. Lett. 112 (2014) 045501.
[29] N. Ollier, M. Lancry, C. Martinet, V. Martinez, S. Le Floch, D. Neuville, Relaxation study of pre-densified silica glasses under 2.5 MeV electron irradiation, Sci. Rep. 9 (2019).
[30] N. Ollier, K. Piven, C. Martinet, T. Billotte, V. Martinez, D.R. Neuville, M. Lancry, Impact of glass density on the green emission and NBOHC formation in silica glass: a combined high pressure and 2.5 MeV electron irradiation, J. Non Cryst. Solids 476 (2017) 81–86.
[31] B. Humbert, A. Burneau, J.P. Gallas, J.C. Lavalley, Origin of the Raman bands, D1 and D2, in high surface area and vitreous silicas, J. Non Cryst. Solids 143 (1992) 75–83.
[32] B. Boizot, S. Agnello, B. Reynard, R. Boscaino, G. Petite, Raman spectroscopy study of β-irradiated silica glass, J. Non Cryst. Solids 325 (2003) 22–28.
[33] T. Gavenda, O. Gedeon, K. Jurek, Irradiation induced densification and its correlation with three-membered rings in vitreous silica, J. Non Cryst. Solids 425 (2015) 61–66.
[34] D.R. Lide, CRC Handbook of Chemistry and physics, 82nd Edition, 82nd ed., CRC Press, Boca Raton, FL, 2001.
[35] F. Angeli, O. Villain, S. Schuller, S. Ispas, T. Charpentier, Insight into sodium silicate glass structural organization by multinuclear NMR combined with first-principles calculations, Geochim. Cosmochim. Acta 75 (2011) 2453–2469.
[36] A. Medek, J.S. Harwood, L. Frydman, Multiple-quantum magic-angle spinning NMR: a new method for the study of quadrupolar nuclei in solids, J. Am. Chem. Soc. 117 (1995) 12779–12787.
[37] F.H. Larsen, I. Farnan, 29Si and 17O (Q)CPMG-MAS solid-state NMR experiments as an optimum approach for half-integer nuclei having long T1 relaxation times, Chem. Phys. Lett. 357 (2002) 403–408.
[38] D. Massiot, B. Touzo, D. Trumeau, J.P. Coutures, J. Virlet, P. Florian, P. J. Grandinetti, Two-dimensional magic-angle spinning isotropic reconstruction sequences for quadrupolar nuclei, Solid State Nucl. Magn. Reson. 6 (1996) 73–83.
[39] B. Poumellec, Links between writing and erasure (or stability) of Bragg gratings in disordered media, J. Non-Cryst. Solids 239 (1998) 108–115.
[40] M. Tomozawa, J.-W. Hong, S.-R. Ryu, Infrared (IR) investigation of the structural changes of silica glasses with fictive temperature, J. Non Cryst. Solids 351 (2005) 1054–1060.
[41] M. Lancry, E. Régnier, B. Poumellec, Fictive temperature in silica-based glasses and its application to optical fiber manufacturing, Prog. Mater. Sci. 57 (2012) 63–94.
[42] L. Skuja, Optically active oxygen-deficiency-related centers in amorphous silicon dioxide, J. Non Cryst. Solids 239 (1998) 16–48.
[43] L. Skuja, The origin of the intrinsic 1.9 eV luminescence band in glassy SiO2, J. Non Cryst. Solids 179 (1994) 51–69.
[44] Shelby, 2004 densité dépend de OH, J. Non-Cryst. Solids 349 (2004) 331–336.
[45] B.T. Poe, C. Romano, G. Henderson, Raman and XANES spectroscopy of permanently densified vitreous silica, J. Non Cryst. Solids 341 (2004) 162–169.
[46] N.M. Trease, T.M. Clark, P.J. Grandinetti, J.F. Stebbins, S. Sen, Bond length-bond angle correlation in densified silica—results from 17O NMR spectroscopy, J. Chem. Phys. 146 (2017) 184505.
[47] K.J.D. Mackenzie, M.E. Smith, Multinuclear Solid-State NMR of Inorganic Materials, Pergamon, 2002.
[48] M. Okuno, B. Reynard, Y. Shimada, Y. Syono, C. Willaime, A Raman spectroscopic study of shock-wave densification of vitreous silica, Phys. Chem. Miner. 26 (1999) 304–311.
[49] T. Charpentier, P. Kroll, F. Mauri, First-principles nuclear magnetic resonance structural analysis of vitreous silica, J. Phys. Chem. C Nanomater. Interf. 113 (2009) 7917–7929.
[50] NATO Advanced Study Institute on Defects in SiO_2 and Related Dielectrics: Science and Technology (2000 : Erice, Italy), Defects in SiO2 and Related dielectrics: Science and Technology, 2000th ed., Springer, Dordrecht, Netherlands, 2012.
[51] G. Pacchioni, G. Ierańo, Ab initio theory of optical transitions of point defects inSiO2, Phys. Rev. B Condens. Matter 57 (1998) 818–832.
[52] L. Skuja, M. Hirano, H. Hosono, K. Kajihara, Defects in oxide glasses, Phys. Status Solidi C 2 (2005) 15–24.
[53] J. Wang, J. Cheng, C. Shao, W. Chen, C. Yu, L. Hu, M. Guzik, G. Boulon, Analysis of red-luminescence lifetime components of non-bridging oxygen hole centers in γ-ray irradiated silica glasses, Opt. Mater. Exp. 13 (2023) 3616.
[54] K. Awazu, S. Ishii, K. Shima, S. Roorda, J.L. Brebner, Structure of latent tracks created by swift heavy-ion bombardment of amorphousSiO2, Phys. Rev. B Condens. Matter 62 (2000) 3689–3698.
[55] P.S. Salmon, A. Zeidler, M. Shiga, Y. Onodera, S. Kohara, Ring compaction as a mechanism of densification in amorphous silica, Phys. Rev. B 107 (2023), https://doi.org/10.1103/physrevb.107.144203.
[56] B. Poumellec, Links between writing and erasing (or stability) of Bragg gratings in disordered media. Bragg Gratings, Photosensitivity, and Poling in Glass Fibers and Waveguides: Applications and Fundamentals, Optica Publishing Group, Washington, D.C., 1997, https://doi.org/10.1364/bgppf.1997.jmf.5.
[57] N.F. Borrelli, C. Smith, D.C. Allan, T.P. Seward, Densification of fused silica under 193-nm excitation, J. Opt. Soc. Am. B 14 (1997) 1606.
[58] M. Lancry, B. Poumellec, UV laser processing and multiphoton absorption processes in optical telecommunication fiber materials, Phys. Rep. 523 (2013) 207–229.
[59] N. Shchedrina, G. Nemeth, F. Borondics, N. Ollier, M. Lancry, Nano-FTIR spectroscopy reveals SiO2 densification within fs-laser induced nanogratings, Nanoscale Adv. 6 (2024) 5164–5170.
[60] S. Girard, A. Morana, A. Ladaci, T. Robin, L. Mescia, J.-J. Bonnefois, M. Boutillier, J. Mekki, A. Paveau, B. Cadier, E. Marin, Y. Ouerdane, A. Boukenter, Recent advances in radiation-hardened fiber-based technologies for space applications, J. Opt. 20 (2018) 093001.
[61] J. He, B. Xu, X. Xu, C. Liao, Y. Wang, Review of femtosecond-laser-inscribed fiber Bragg gratings: fabrication technologies and sensing applications, Photon. Sens. 11 (2021) 203–226.

III.4 The influence of high-temperature during electron irradiation on silica structure

The influence of high-temperature during electron irradiation on silica structure

SHCHEDRINA N.[1,2], LANCRY M.[1], ALESSI A.[2,3], CAVANI O.[2], OLLIER N.[2]

[1] *Institut de Chimie Moléculaire et des Matériaux d'Orsay, Université Paris-Saclay, Rue du doyen Georges Poitou, 91405 Orsay cedex, France*
[2] *Laboratoire des solides irradiés, CEA/DRF/IRAMIS, CNRS, École Polytechnique, Institut Polytechnique de Paris, F-91128, Palaiseau, France*
[3] *Department of Physics and Chemistry Emilio Segrè, University of Palermo, Via Archirafi 36, 90123 Palermo, Italy*

**Corresponding author: nadezhda.shchedrina@universite-paris-saclay.fr*

Received XX Month XXXX; revised XX Month, XXXX; accepted XX Month XXXX; posted XX Month XXXX (Doc. ID XXXXX); published XX Month XXXX

Abstract
This study explores the combined effects of high-dose electron irradiation and elevated temperature on silica glass, focusing on its vibrational structural evolution and defect formation. A systematic investigation was carried out on both pristine and pre-densified at high pressure high temperature conditions silica samples. Electron irradiation was performed at doses up to 8.8 GGy, with combined heating up to 1000 K. Structural changes were characterized through Raman spectroscopy and photoluminescence measurements (to identify defect populations). Results show that while densification is promoted around room temperatures by irradiation, increasing temperature above 600 K activates significant defect annealing and glass network relaxation back toward a pristine-like SiO_2 structure. These findings provide new insights into the dynamic behavior of silica under real-world extreme conditions and help guide the design of silica-based components and sensors for high-dose, high-temperature applications, particularly in next-generation nuclear reactors.

INTRODUCTION

Silica is known for its exceptional optical transparency, mechanical stability, and chemical durability, making it a critical material for advanced technological applications including in harsh environments such as high radiation and elevated temperatures [1,2]. In particular, applications such as Fiber Bragg Grating (FBG) or Fabry-Pérot sensors are exposed to the simultaneous effects of radiation and high temperature, conditions often encountered in next-generation of sodium cooled nuclear reactors or Tokamaks [3]. While the individual effects of radiation or heat on silica are well studied, their combined impact can lead to other tendencies in structural modifications, radiation-induced attenuation, and mechanical degradation, potentially compromising or improving long term operation. Despite its significance, this combination of conditions remains less explored, highlighting the need for further investigation in the light of real-world operating conditions.

Radiation-induced effects on silica were largely studied and include structural rearrangements leading to densification or relaxation (depending on the initial density state), defects formation, and changes in thermal stability of the densification. Although the mechanisms may vary with the type of irradiation (neutrons, gammas, ions or electrons, etc.), the resulting effects are broadly similar. The evolution of silica density under irradiation is strongly dependent on its initial level: pristine silica and silica showing density lower than 2.26 densify whereas much densified silica tends to relax [4], both converging towards a so-called metamict phase at very high doses (around 11 GGy for electron irradiation), characterized by a density near 2.26 g/cm^3 [5,6]. During electron irradiation, bond breaking events happen and charges trapping leading to the formation of point defects, which in turn promote further reorganization and compaction (or its relaxation) of the glass network with significant structural rearrangements. The increase of three-membered rings is evidenced by an increased D_2 band intensity in Raman spectra and is further accompanied by the narrowing (with a redshift) of the main band at 440 cm^{-1}, reflecting a decrease in the average Si–O–Si bond angle. Additionally, irradiation generates in silica various point defects, including E′ centers, non-bridging oxygen hole centers (NBOHCs), oxygen deficient centers (ODC), Peroxy radicals (POR) , interstitial molecular oxygen (O_2) [7], and other defects that lead to phenomena such as green light emission in compacted silica [8]. In silica based optical fibers, these defects are critical contributors to radiation-induced attenuation (RIA), in the near-infrared (IR), ultraviolet, visible spectral ranges, thereby degrading optical transmission.

The thermal relaxation of densified silica glass has been widely studied, particularly in samples prepared via high-pressure (HP) and high-pressure, high-temperature (HPHT) treatments. Silica densified under HPHT conditions exhibits greater homogeneity and stability, requiring longer annealing times to relax, whereas cold compressed samples relax more quickly at lower temperatures [9]. This process involves a transient state marked by an increase in D_2 band intensity in Raman spectra, a behavior linked to the high-density amorphous (HDA) to low-density amorphous (LDA) phase transition, that can coexist attributed to polyamorphism [10,11]. Meanwhile, the electron irradiation can significantly reduce the thermal stability of the densified glasses and change the ratio of the LDA and HDA phases [12,13].

However, the combined influence of radiation and temperature on silica can produce unexpected behaviors that are not fully studied. In fiber-based glasses, as well as on bulk silica, simultaneous exposure to radiations (such as neutron [14] or gamma) and high temperatures (500-1080 K) generally reduces RIA and radiation-induced compaction (RIC) [14–20]. This is partly

due to some thermally activated counter reaction leading to a decrease of defects population. For low-OH optical fibers, at sufficiently high temperatures (higher than 670 K [15]), thermal effects alone induce additional attenuation at 1300 and 1550 nm. Notably, the increase in temperatures (from 670 K) tend to diminish the influence of radiation dose on phenomena such as the Bragg wavelength shift [3,17,21]. However, most researches have focused on limited range of doses (for radiation from 10 kGy up to about 3.8 GGy) and fiber properties, leaving a significant knowledge gap regarding the fundamental mechanisms underlying structural modifications and defects evolution under such high-dose, high-temperature conditions.

To address this gap, it is essential to identify the dependences of the individual contributions of radiation dose and temperature (T) on the silica structure evolution. This study will systematically examine the structural modifications in silica using Raman spectroscopy and track point defect formation while varying both the radiation doses and the temperatures applied (300-1000 K). The main objective is thus to investigate the structural changes in silica subjected to combined electron irradiation and high-temperature conditions, thereby advancing our understanding of its behavior under extreme operational environments.

1. Experimental Details

Silica samples were prepared using Type III silica rods (Heraeus Suprasil F300), notable for their high chlorine content (approximately 2000–2500 ppm) and minimal hydroxyl impurities (<1 ppm, typically around 0.2 ppm). Densification was achieved via high pressure-high temperature (HP-HT) treatments performed in a belt press. Specifically, conditions of 5 GPa at 1000 °C and 5 GPa/350 °C were applied, as detailed in the previous study [22]. Additionally, for comparison, four irradiated samples (pristine silica at 5 and 11 GGy 300K, plus 5 GPa at 1000°C at 5 and 11 GGy 300K) after the irradiation were first annealed at 885 °C for 18 hours and then at 1100 °C for 15.5 hours.

Consequently, 3 samples were prepared: pristine silica and 2 densified samples (5 GPa at 350°C, and 5 GPa at 1000°C). Prior to electron irradiation, the densities of these samples were determined to be 2.203 ± 0.001, 2.408 ± 0.013, and 2.609 ± 0.006, respectively, where the error represents the standard deviation from three separate measurements. Density measurements were conducted using the Archimedean-based sink-float method using toluene as the immersion liquid at ILM, Université Lyon 1.

For the irradiation experiments, samples were exposed to high-energy electrons (2.5 MeV) at the SIRIUS facility (LSI/CEA/Ecole Polytechnique). The electron beam current was maintained at approximately 25 µA. A range of total doses was administered, spanning from 0.1 GGy to 11 GGy, with intermediate dose levels set at 0.6, 1, 3, 4.9–5, 7, 8.2 and 8.8 GGy. These irradiations were carried out under in-situ heating conditions with temperatures controlled at 300 K, 450 K, 600 K, and 1000 K.

The irradiations performed at temperatures up to 600 K were carried out using the "Cirano" irradiation cell [23], with adjustments made to the cooling method. For example, irradiations at 300 K were conducted by actively cooling the sample holder using water maintained at approximately 290 K, whereas those at 600 K relied solely on electron beam heating without water cooling. For irradiations at 1000 K, a commercial heating cell was modified and adapted to meet the operational constraints of the electron accelerator. Preliminary tests were conducted to ensure stable experimental conditions (temperature close to 1000 K and beam current approximately 25 µA) prior to sample irradiation.

Figure 1 illustrates typical temperature profiles during irradiation experiments, showing temperature increases (panel a) and decreases (panel b) as functions of time. For irradiations at 450 K and 600 K, the observed changes in temperature correspond directly to the start and end of electron beam exposure. In contrast, for irradiations at 1000 K, the electron beam exposure started once the sample temperature reached approximately 600 K through initial heating by the irradiation setup's integrated heater. The initiation of irradiation at this point resulted in a rapid increase in heating rate due to the electron beam energy deposition. Subsequently, the irradiation setup's heater was actively controlled to stabilize and maintain the sample at the desired temperature. The conclusion of irradiation at 1000 K coincided with a rapid and pronounced temperature decrease. It should be noted that since the samples cool from their set-point temperature in roughly 25 min, it allows a limited amount of post-irradiation annealing and defect loss in all the samples. Although future fully in-situ isothermal measurements are needed to isolate this contribution, the overall trends we report remain consistent with prior high-temperature studies [14–18], as will be shown in discussion section. In all experiments, the irradiation cell was electrically isolated and functioned as a Faraday cup, allowing direct measurement of the electron beam current.

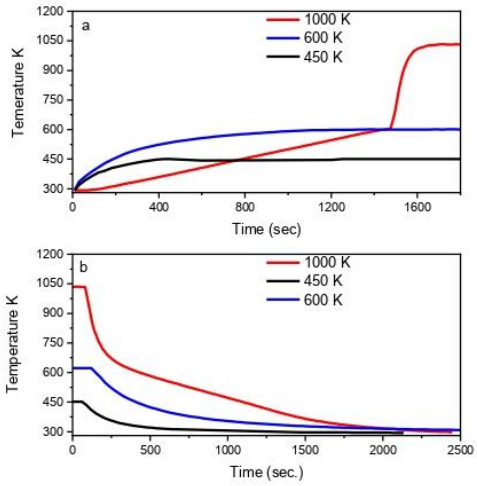

Figure 1. Typical temperature profiles measured during irradiation experiments: (a) Temperature increase from approximately 300 K to the target irradiation temperatures. (b) Temperature decrease upon end of irradiation. Temperatures were monitored using a thermocouple placed near the samples, but positioned outside of the direct path of the electron beam.

Structural characterization was performed using Raman spectroscopy at the MONARIS Lab (Sorbonne University). Measurements were obtained with a Horiba LabRam HR800 spectrometer equipped with a 600 lines/mm grating and a Peltier-cooled CCD detector, employing an argon-ion laser (458 nm) as the excitation source.

Time-resolved photoluminescence experiments were executed using a 266 nm excitation line from an Nd:YAG laser (Indi) with a pulse duration of 10 ns and a repetition rate of 10 Hz. Emission

signals were captured with an Andor Shamrock 193 spectrometer coupled to an intensified CCD camera. Complementary photoluminescence studies utilized a 488 nm continuous-wave diode laser (Spectra Physics), focused through a ×20 objective and collected via a Renishaw Raman probe.

For the data analysis, Raman spectra were baseline-corrected, then normalized by the total integrated area. The D_2 area was calculated between two peak minima, after linear baseline subtraction, using trapezoidal integration. FWHM was determined by identifying the width at half maximum of the main band. Uncertainties were estimated by Monte Carlo resampling: noise, assessed from a flat region (900–1000 cm^{-1}), was added to the spectra, and peak parameters were recalculated multiple times. The standard deviation of these iterations was used as the measurement error. To account for experimental reproducibility, standard deviations among samples measured under identical conditions were combined in quadrature with individual errors to obtain total uncertainties.

In this study, we systematically investigated silica samples with varying initial densities prepared under different pre-densification conditions (pressure and temperature). Samples included pristine silica as well as those densified at various conditions (5 GPa at 1000 °C and 5 GPa at 350 °C), subsequently subjected to electron irradiation at doses ranging from 0.1 to 11 GGy and irradiation temperatures from 300 K to 1000 K. Multiple data points were acquired under each experimental condition, allowing clear trends in structural modifications to be identified as a function of both radiation dose and temperature.

2. Results

2.1 Vibrational structural evolution from Raman spectroscopy

We first consider Raman spectroscopy, as it directly reveals the vibrational structural modifications within silica glass and is closely related to the local density indicators. Figure 2 presents representative Raman spectra of HPHT pre-densified silica samples under conditions of 5 GPa and 1000 °C, subsequently subjected to electron irradiation at a total dose of 5 GGy at different temperatures. A pristine i.e. non-densified silica sample was added for sake of comparison. The non-irradiated densified silica exhibits the narrowest full-width at half maximum (FWHM) of the main Raman band and the lowest intensity of the D_2 band, both characteristic features of silica densified up to 20% under HPHT conditions, indicating a narrowed Si-O-Si bond angle distribution and low number of three-membered rings [22].

Upon irradiation at 300 K, there is a pronounced increase in D_2 band intensity, along with a widening of the main Raman band, indicative of slight density relaxation and structural modification towards so-called metamict state [6]. Samples irradiated at 450 K exhibit a similar spectral evolution. However, irradiation at higher temperature (i.e. 600 K) results in a smaller intensity of the D_2 band (compared to 300K and 450K) and a significant broadening of the main Raman band. Under these conditions, the structure appears to relax, shifting the overall vibrational characteristics toward those observed in pristine, non-densified silica glass.

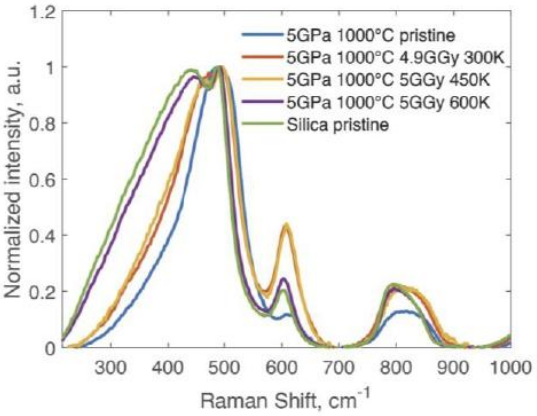

Figure 2. Raman spectra of pre-densified silica samples at 5 GPa and 1000 °C, after electron irradiation at 5 GGy and various temperatures.

2.2 Dose and temperature dependence of Raman parameters

To further quantify these structural modifications, two key Raman parameters were analyzed: the D_2 band area, which correlates with the population of three-membered rings, and FWHM of the main Raman band, associated with the Si–O–Si bond angle distribution. Both parameters were examined as function of irradiation dose made under various temperature conditions (Figure 3).

Figure 3a and 3b presents the evolution of the D2 band area with increasing irradiation dose for non-densified silica and pre-densified silica samples at 5 GPa and 1000 °C. At 300 K, the D2 area increases steadily with dose, consistent with previously reported findings [4,6]. However, increasing irradiation temperature notably alters this behavior. At the intermediate temperature of 450 K, the D2 band area exhibits a slightly lower initial increase and subsequently reaches a plateau at higher doses (from 7 GGy), suggesting a kinetic equilibrium between defects generation and thermally activated annealing processes. At 600 K, the D2 band area initially rises, peaking at approximately 1-3 GGy, and then decreases toward values comparable to pristine silica, indicating substantial thermal annealing effect (i.e. a thermally activated reverse reaction) at higher doses. At 1000 K, the D2 band area shows only a modest increase at a low dose (~0.02 GGy) for pre-densified sample, followed by rapid relaxation towards pristine level.

The FWHM of the main Raman band for predensifed sample (Figure 3c) demonstrates analogous trends. At 300 K, the FWHM decreases with dose, stabilizing at approximately 154 cm^{-1}, reflecting structural evolution towards a metamict-like state. At 450 K, the broadening effect is slightly more pronounced, and the FWHM stabilizes around 163 cm^{-1}. For irradiation at 600 K, the relaxation is notably accelerated, with the FWHM approaching the value of silica (~193 cm^{-1} versus ~200 cm^{-1} for pristine silica). At the highest investigated temperature (1000 K), complete relaxation occurs rapidly, even at low irradiation dose (0.1 GGy), and the FWHM becomes slightly broader (~210 cm^{-1}) than that observed in pristine silica.

For comparison, pristine non-densified silica and a reference sample that was annealed post irradiation (at 885 °C for 18 hours and then at 1100 °C for 15.5 hours), displayed in grey in Figure 3, exhibit minimal D2 band intensities and broader main bands, serving as baseline references indicative of a structurally relaxed state.

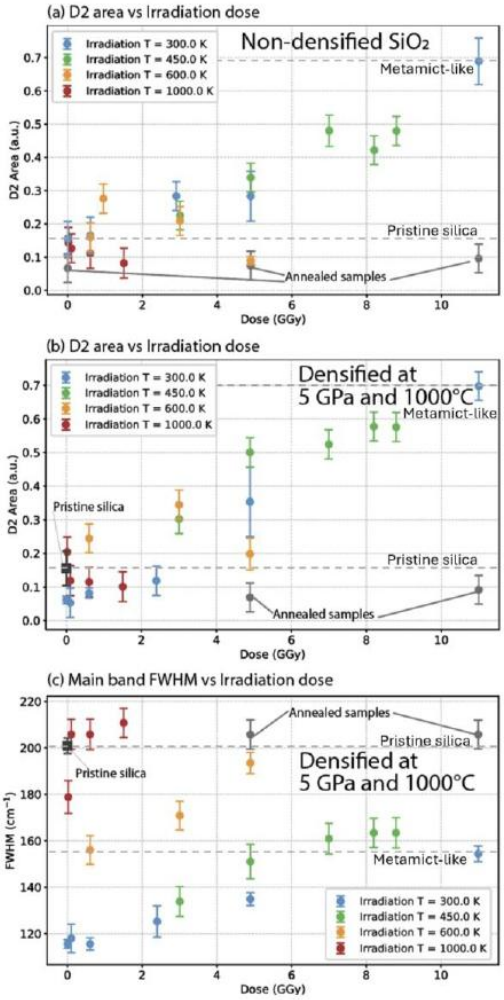

Figure 3. Evolution of Raman spectral parameters with increasing irradiation dose at various temperatures. For non-densified silica SiO_2: (a) D_2 band area as a function of irradiation dose. For HPHT pre-densified silica samples at 5 GPa and 1000 °C: (b) D_2 band area as a function of irradiation dose. (c) FWHM of the main Raman band as a function of irradiation dose. Pristine silica and annealed samples (grey) are included as references.

2.3 Density measurements

The evolution of samples density under electron irradiation follows trends consistent with those observed in Raman spectroscopy. At high temperatures (1000 K), both non-densified and pre-densified silica irradiated samples exhibit minimal change in density, indicating significant relaxation of the glass network. Specifically, for irradiation doses of 0.6 and 1.5 GGy, the density of all samples converges toward the pristine value, measured at 2.20 ± 0.05, regardless of initial compaction state. Similarly, at 600 K 5 GGy, the non-densified silica glass maintains a density of 2.20 ± 0.02, confirming that for long term irradiation exposure at this temperature a measurable densification does not remain. The HPHT pre-densified sample (5 GPa, 1000 °C), initially at 2.60, exhibits a significant decrease in density to 2.23 ± 0.04 after irradiation at 600 K 5 GGy, showing the relaxation toward the pristine state. By comparison, at 300 K and the same dose of 5 GGy, relaxation is slower, with the density decreasing only to 2.41 ± 0.06.

At 450 K, however, the densification trend diverges, though it remains consistent with the Raman data. Electron irradiation at this temperature causes a notable increase in the density of non-densified silica, reaching 2.24 ± 0.02 at a dose of 7 GGy, and remains the same at 8.8 GGy. For pre-densified SiO_2, direct density measurements at 450 K were not feasible for the 5 GPa, 1000 °C condition due to the small weight of the samples resulting in high uncertainties. However, the alternative pre-densified sample (5 GPa, 350 °C), which exhibits a similar vibrational signature to the (5GPa, 1000 °C) condition at 8.8 GGy, reaches a final density of 2.27 ± 0.04 g/cm^3, a value also achieved by 7 GGy. This indicates that for irradiation at 450 K, the reaction stabilizes showing a densified structure near a metastable density plateau, aligned with the intermediate Raman characteristics observed in this regime.

2.4 Vibrational structure evolution at 8.8 GGy 450 K

It is helpful to compare the Raman spectra of samples with different initial densities at a very high dose (8.8 GGy 450K) (Figure 4) with the metamict-like state (11 GGy 300K). Typically, at comparable high doses (9-11 GGy) at room temperature, silica reaches the metamict-like state.

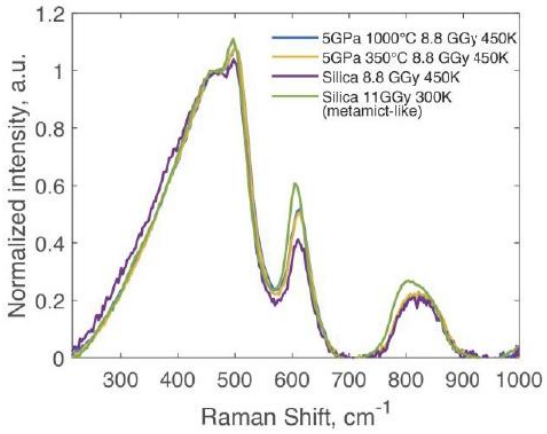

Figure 4. Raman spectra of pre-densified silica samples (5 GPa at 1000 °C and 5 GPa at 350 °C) and non-densified silica, after electron irradiation at 8.8 GGy and 450 K. A reference spectrum of non-densified silica irradiated at 11 GGy and 300 K is included for comparison.

So here, for 8.8 GGy 450K, at first we notice the intense D_2 band compared to pristine silica. The two pre-densified silica samples (5 GPa/1000 °C and 5 GPa/350 °C) exhibit broadly similar profiles, suggesting that they have a similar realxation pathway. These samples irradiated at 8.8 GGy 450K, shows a less intense D_1 and D_2 bands than metamict phase. The non-densified silica spectrum remains distinct with even smaller intensities of D_1 and D_2 bands.

Notably, although the Raman signatures differ, the PL data under 266 nm exitation (not shown) reveal the same ratio of ODC(II) and NBOHCs emissions for all samples at 8.8 GGy 450 K, implying that some aspects of their defect populations converge even if their structural (Raman) features do not fully align.

2.5 Point defects analysis by photoluminescence

Figure 5 presents the photoluminescence (PL) spectra (under 266 nm excitation) of 5 GPa/1000 °C densified silica samples irradiated at 0.6 GGy at three temperatures (300 K, 600 K, and 1000 K). Although all samples exhibit two primary emission bands, one peaking near 465 nm (attributed to $T_1 \rightarrow S_0$ transition of oxygen-deficient centers, ODC(II)) and another around 650 nm (arising from non-bridging

oxygen hole centers, NBOHCs), the relative intensities of these peaks differ. At 300 K, the 650 nm band dominates, suggesting enhanced generation of NBOHCs at room temperature. For the sample irradiated at 600 K, the ratio is similar with a 650 nm band being more narow and shifted towards higher wavenuber. The band at 475 nm is however less pronounced, suggesting partial annealing or transformation of ODC(II) defects. Strikingly, the emission spectrum for the sample irradiated at 1000 K is characterized by a stronger 475 nm band, reflecting a change in ratio of defect population from NBOHC-like toward ODC(II) species under high-temperature irradiation.

Figure 5 insert shows the PL emission spectra under 488 nm excitation of 5 GPa/1000 °C densified silica samples exposed to a 0.6 GGy electron irradiation at three different temperatures: 300 K, 600 K, and 1000 K. Under this excitation wavelength we can observe strong green luminescence near 545 nm, whose underlying defect origin remains unknown, though previous studies indicate that densified silica often exhibits an enhanced green emission [8]. Samples, irradiated at 300 K, exhibits the highest PL intensity in the ~550 nm region, suggesting a larger population of green-emitting defects. At 600 K, the overall PL signal diminishes, implying a partial annealing of the defects population Meanwhile, the 1000 K spectrum shows a very low level of green emission, indicating that the higher irradiation temperature might suppress or relax these luminescent centers.

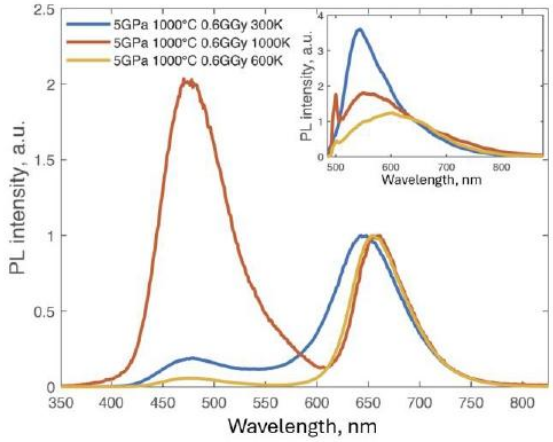

Figure 5. Photoluminescence emission spectra of pre-densified silica samples at 5 GPa and 1000 °C, after electron irradiation at 0.6 GGy and various temperatures obtained after a 500 ns delay time and a gate width of 10 ms at an excitation wavelength of 266 nm. Insert: PL emission spectra under 488 nm continuous-wave excitation.

3. Discussion

In this work, we have systematically investigated how 2.5 MeV electron irradiation at different temperatures impacts the structural properties of both HPHT pre-densified and pristine silica samples. In the following discussion, we examine the underlying mechanisms that drive these changes and explore the dependencies among network densification, defects formation/erasure, and the effect of temperature on their kinetics. Specifically, we analyse the competitive interplay between temperature dependent radiation-induced defects generation and thermally activated relaxation processes, and assess how these physico-chemical reactions govern the overall behaviour of silica glass under such extreme conditions.

In general, the observed results can be seen as the balance between two concurrent temperature-dependent reactions: (i) a forward reaction of electron-driven defect production (and associated densification or relaxation towards metamict), whose rate constant $k_1(dose,T)$ changes with both dose and temperature, and (ii) a backward-erasure reaction i.e. a thermally activated defects annihilation with a rate constant $k_{-1}(T)$. The observed density and spectroscopic plateau at 450 K therefore correspond to the dynamic equilibrium established between these forward-generation and back-annealing pathways, the position of which shifts continuously as the temperature is raised. With this in mind, we now revisit and interpret our experimental observations in this section.

Several other studies have investigated the impact of elevated temperature and irradiation dose on silica-based materials, using different irradiation types (neutron, gamma, X-ray) and focusing on doses ranging from a few kGy to 3.8 GGy [14–20]. For instance, experiments conducted in the 573-1073 K range commonly observe that increasing temperature reduces RIC and promotes faster recovery of optical properties, happening when the dose surpasses a few MGy. This effect is frequently linked to the thermal recombination or annealing of radiation-induced point defects such as E′ centers and NBOHCs, which dominate absorption in the UV–visible range [14,16]. Similarly, measurements on fiber Bragg gratings reveal that at temperatures beyond 873-973 K, thermal annealing can minimize defects accumulation, suppressing substantial Bragg wavelength shifts [17,21]. Other research using 10 kGy of X-ray exposure at temperature up to 573 K finds that visible-range RIA remains comparatively stable below 473 K but diminishes at higher temperatures, again highlighting the role of thermally assisted Al-OHC (aluminum-oxygen hole center) recombination and reduced formation of AlE′ centers [18]. Likewise, at doses exceeding GGy, both low-OH and high-OH fibers show less compaction when irradiated at 1273 K, although some additional thermal attenuation may appear if temperatures exceed 673 K, partly due to thermally released hydrogen interacting with defect precursors [15]. Our study targets more the structural evolution of silica rather than the optical fiber properties (RIA, for example). Furthermore, we are interested here in a higher dose regime up to 9 GGy. Indeed, this is a dose range interesting for polyamorphism with possibly the formation of the "metamict-like phase". During electron irradiation at room temperature, the silica network undergoes substantial structural reconfiguration driven by bond breakage events [24–26], which lead either to enhanced densification or relaxation depending on the sample's initial density (higher or lower than 2.26). In pristine silica, high-energy electrons induce the formation of point defects that promote compaction, reflected in a narrower and blue-shifted Raman main band and a smaller Si-O-Si bond angle distribution [27]. By contrast, in HPHT pre-densified silica glass, the same ionization-induced processes tend to relax the structure, causing main-band broadening in Raman spectra. In both cases, intensification of the D_1 and D_2 bands is a characteristic of newly formed three- and four-membered ring structures [27–29]. These trends are clearly observed in present results as well, for both non-densified and pre-densified silica irradiated at room temperature, as shown in Figure 3.

However, as irradiation temperature rises, the trends in D_2 band intensity and main-band FWHM notably shift. At moderate temperatures (450 K), the D_2 band initially shows a less pronounced increase suggesting that a defect formation is counter-balanced by their partial thermal annealing. Then it follows a "plateau", with a stabilization from 7GGy for all silica type glasses,

indicating an equilibrium between forward reaction and backward-erasure reaction.

At higher temperatures >600 K, the D_2 peak first grows and then recedes, converging toward values similar to pristine silica. Likewise, the FWHM of the main Raman band follows an analogous pattern: at 300 K, it stabilizes at 154 cm^{-1}, indicating a metamict-like state, whereas at 600 K and at 1000 K, the material exhibits an expected faster thermally-assisted relaxation and approaches the broader FWHM characteristic of pristine silica. These observations imply the dominant role of thermal effects avoiding three-membered ring formation, mediated by "an annihilation" of the point defects formation at higher temperatures (i.e. the limiting process). These results are consistent with the previous study reported above reporting RIC and RIA decreases for increased temperature irradiation [14–16].

Speaking about defects behaviour, PL results indicate that increasing irradiation temperature substantially alters the balance between NBOHCs and ODC(II). At moderate temperatures (600 K), for instance, we observe a reduced ODC(II)/NBOHC ratio compared to 300 K. By contrast, at 1000 K an overall higher ODC(II) content emerges, implying that extreme thermal conditions can shift defect pathways in favour of ODC formation or reduce NBOHC-s defects. The 650 nm band itself becomes narrower and shifts to higher wavenumbers at 600 K and 1000K. This modification must be linked to a previous result evidenced in [8]. We have shown there a broadening of the NBOHC emission band in densified silica that may be linked to NBOHC variants. This band width change is thus consistent with the Raman trend showing the relaxation towards silica. Simultaneously, the green emission diminishes significantly at elevated temperatures, somehow mirroring the decrease in densification revealed by Raman spectroscopy and density measurements. The PL trends reinforce the kinetic picture proposed above: a temperature-dependent forward reaction that produces point defects is counter-balanced by a thermally activated erasure reaction, so the defect population, depends on the k_1/k_{-1} ratio set by temperature. With the increase of the irradiation dose, the cumulative defects can transform the material toward a metamict-like phase, regardless of initial density or irradiation type [25,30,31]. Numerous reports indicate that beyond a sufficiently high dose, silica converges toward a universal density near 2.26 g/cm^3 [13,32].

From the literature, high-dose neutron irradiation experiments on amorphous fused silica [33] provide additional insight into the temperature dependence of volumetric compaction. In that study, silica samples were irradiated to fast neutron fluences of 2.4×10^{21} n/cm^2 at temperatures of 368, 571, and 961 K. The results showed that at 368 K, the compaction approached approximately 2.2%, while at 571 K, it was significantly reduced (around 1.8%). At the highest temperature tested (961 K), the compaction decreased further to roughly 0.5%. These findings clearly indicate that elevated irradiation temperatures promote thermally activated annealing mechanisms, which mitigate the build-up of permanent densification.

Although our electron-irradiated samples involve a different mechanism based on ionization, we observe a parallel trend. At 300 K, both pristine and pre-densified silica move toward a metamict-like state near 2.26 (2.7% densification). By 450 K, pristine silica only reaches 2.24 (1.8% densification), while pre-densified samples relax from 2.61 to 2.27. It seems that at 450 K all samples may converge toward the metamict like phase but at this dose (8.8 GGy) they do not yet reach it. Above 600 K, thermal effects dominate: pristine silica remains near 2.20, showing negligible further densification, and HPHT pre-densified silica reverts more swiftly toward pristine density. These results highlight how higher temperatures accelerate defects recombination, thus avoiding further compaction in pristine glass while driving a fast relaxation of initially densified samples.

Our results suggest that three regimes emerge depending on the irradiation temperature. At room temperature (~300 K), silica tends towards a metamict-like state: defects formation and bond breaking accumulate, as also evidenced by a pronounced increase in the D_2 band and narrowing of the main Raman band. At moderate temperatures (~450 K), defects still form (forward reaction) but are partially balanced by the backward thermally activated erasure reaction, producing somewhat a "sub-metamict" state at high doses (around 7-9 GGy) and a saturation of all associated properties. It is worth emphasizing that the two densified glasses evolve toward the same vibrational signature. Compared to the metamict one, D_2 and D_1 are a bit less intense but the main band remains comparable. The Raman signature for non-densified silica does not converge fully to this phase, implying that higher doses (i.e 10-11 GGy) could be required to push the system further along its compaction trajectory and reach the metamict-like phase.

Finally, at 600 K and above (notably 1000 K), the backward-erasure reaction of relaxation dominates. While we see a short-lived D_2 increase at moderate doses, the system quickly relaxes back toward the pristine silica. This result was inferred by the NBOHC band narrowing at 600 and 1000 K (Figure 4) indicating a suppression of some NBOHC and species relative to the green emission found in densified silica [8]. After irradiating at 1000 K, the Raman spectral features are close to those of the solely annealed sample at 1000°C, indicating change in the glass fictive temperature.

These trends are consistent with our earlier findings that electron irradiation decreases activation energies underpinning network rearrangement [12], enhancing the material's sensitivity to thermal relaxation at moderate or high temperatures. As we continue to irradiate, newly formed defects and partial densification states may transiently appear (reflected in short-lived D_2 growth), but their reduced thermal stability accelerates the structural relaxation and moves the structure closer to a pristine-like state. Furthermore, the complex interplay of low density amorphous (LDA) and high density amorphous (HDA) phases is known to cause non-monotonic changes in D_2 intensity under thermal annealing of HPHT densified silica glass [10,11,13,34]. Remarkably, we capture moments of rising D_2 intensity for pre-densified samples at 600 K and 1000 K prior to a final reversion toward the pristine signature, showcasing the "transient, disordered" state previously reported during HPHT glass relaxation [11,34].

Altogether, these observations underscore a kinetics competition between two major processes: a forward chemical reaction with constant rate k_1 related to defects formation (and consequent structural changes in density) promoted by electron irradiation, and the backward reaction i.e. the thermally activated erasure with a constant rate noted $k_{-1}(T)$. This backward reaction reverses or suppresses (through defects annihilation) compaction at high temperatures. In addition, the above observations indicate that the constant rate of defects formation appears to be not only dependent on the dose but also T dependent i.e. k_1(dose, T). At

lower temperatures (300-450 K), the defect formation pathway prevails, driving the network toward metamict states; at higher temperatures (600-1000 K), annealing outpaces compaction, leading to partial or complete relaxation back toward the pristine domain.

These findings have direct connection with the design and deployment of silica-based components and sensors, such as optical fibers, and FBGs sensors, in harsh environments where both high-dose irradiation and elevated temperatures are expected, for instance in advanced sodium cooled nuclear reactors or Tokamaks. Because elevated temperatures irradiation drives structural relaxation in densified silica, it may revert toward a lower-density state, altering both optical and mechanical properties (e.g., refractive index, dimensional stability) during long term operation. In contrast, initially non-densified silica would remain closer to its pristine structure at high temperature, minimizing further compaction. This insight suggests that a careful "preconditioning" of silica (partial densification, controlled thermal treatments or irradiation exposure) might mitigate undesirable long-term drift under harsh conditions. Importantly, the accumulated dose, and thus the irradiation time, must also be considered, because temperature-assisted relaxation continues over some time and proceeds faster as the temperature rises. Consequently, an improved understanding of how electron irradiation, temperature, and initial density intersect to shape silica's structural evolution enables more predictive engineering of silica-based devices, ensuring they remain functional and reliable in extreme environments.

4. Conclusion

In this work, we show that electron irradiation at high doses, combined with in-situ heating, triggers competing processes in silica glass, namely, density changes (densification or relaxation), and point-defect generation or annihilation. The specific response depends strongly on both the initial density of the glass and the irradiation temperature. At lower temperatures (300-450 K), radiation-driven changes towards metamict phase happen and defect formation accumulate more readily. In contrast, higher temperatures (≥600 K) promote defects annealing and network relaxation that tend to compensate for irradiation-induced densification. Overall, higher in-situ irradiation temperatures decrease many of the radiation-induced property changes, suggesting that, for nuclear applications, controlling or exploiting elevated temperature during irradiation can reduce the radiation induced modifications that degrade performance of the non-densified silica glass. In contrast for densified silica (e.g. fs laser imprinted optical sensors), the increase in temperature during the high dose irradiation can accelerate the overall structural relaxation resulting in significant drift of such derived optical components.

Acknowledgements. We thank the "Plateforme de spectroscopies vibrationnelles et optiques (PLASVO, Sorbonne Université)" for access to the HR800 Raman spectrometer and to Assia Hessani and Ludovic Bellot-Gurlet (MONARIS laboratory) for their technical assistance in performing the measurements. Finally, we are grateful to Thierry Deschamps (Institut Lumière Matière, Université Claude Bernard Lyon 1) for kindly providing access to the density-measurement setup used in this study.

Disclosures. The authors declare no conflicts of interest.

Data availability. Data underlying these results may be obtained from the authors upon reasonable request.

References

1. A. V. Bondarenko, A. P. Dyad'kin, Y. A. Kashchuk, A. V. Krasil'nikov, G. A. Polyakov, I. N. Rastyagaev, D. A. Skopintsev, S. N. Tugarinov, V. P. Yartsev, V. A. Bogatyrev, A. L. Tomashuk, S. N. Klyamkin, and S. E. Bender, Instrum. Exp. Tech. **49**, 190 (2006).
2. S. J. Mihailov, Sensors (Basel) **12**, 1898 (2012).
3. G. Laffont, R. Cotillard, N. Roussel, R. Desmarchelier, and S. Rougeault, Sensors (Basel) **18**, 1791 (2018).
4. N. Ollier, M. Lancry, C. Martinet, V. Martinez, S. Le Floch, and D. Neuville, Sci. Rep. **9**, 1227 (2019).
5. N. Shchedrina, M. Lancry, T. Charpentier, D. Neuville, and N. Ollier, Social Science Research Network (2024).
6. I. Reghioua, M. Lancry, O. Cavani, S. L. Floch, D. R. Neuville, and N. Ollier, Appl. Phys. Lett. **115**, 251101 (2019).
7. N. Ollier, I. Reghioua, O. Cavani, M. Mobasher, A. Alessi, S. le Floch, and L. Skuja, Sci. Rep. **13**, 13657 (2023).
8. N. Ollier, K. Piven, C. Martinet, T. Billotte, V. Martinez, D. R. Neuville, and M. Lancry, J. Non Cryst. Solids **476**, 81 (2017).
9. M. Guerette, M. R. Ackerson, J. Thomas, F. Yuan, E. Bruce Watson, D. Walker, and L. Huang, Sci. Rep. **5**, 15343 (2015).
10. M. Guerette, M. R. Ackerson, J. Thomas, E. B. Watson, and L. Huang, J. Chem. Phys. **148**, 194501 (2018).
11. A. Cornet, C. Martinet, V. Martinez, and D. de Ligny, J. Chem. Phys. **151**, 164502 (2019).
12. N. Shchedrina, N. Ollier, M. Mobasher, and M. Lancry, J. Non Cryst. Solids **617**, 122491 (2023).
13. M. Mobasher, M. Lancry, J. Lu, D. Neuville, L. Bellot Gurlet, and N. Ollier, J. Non Cryst. Solids **597**, 121917 (2022).
14. B. W. Morgan, M. P. Van Zile, C. M. Petrie, P. Sabharwall, M. Burger, and I. Jovanovic, J. Nucl. Mater. **570**, 153945 (2022).
15. C. M. Petrie, D. P. Hawn, W. Windl, and T. E. Blue, J. Non Cryst. Solids **409**, 88 (2015).
16. D. P. Hawn, C. M. Petrie, T. E. Blue, and W. Windl, J. Non Cryst. Solids **379**, 192 (2013).
17. L. Remy, G. Cheymol, A. Gusarov, A. Morana, E. Marin, and S. Girard, IEEE Trans. Nucl. Sci. **63**, 2317 (2016).
18. C. Campanella, V. De Michele, A. Morana, A. Guttilla, F. Mady, M. Benabdesselam, E. Marin, A. Boukenter, Y. Ouerdane, and S. Girard, IEEE Trans. Nucl. Sci. **69**, 1515 (2022).
19. G. Cheymol, L. Remy, A. Gusarov, D. Kinet, P. Mégret, G. Laffont, T. Blanchet, A. Morana, E. Marin, and S. Girard, EPJ Web Conf. **170**, 04004 (2018).
20. R. Desmarchelier, R. Cotillard, M. Lancry, S. Breaud, A. Gusarov, C. Destouches, and G. Laffont, in *Advanced Photonics Congress 2024* (Optica Publishing Group, 2024), p. BTu3A.2.
21. M. A. S. Zaghloul, M. Wang, S. Huang, C. Hnatovsky, D. Grobnic, S. Mihailov, M.-J. Li, D. Carpenter, L.-W. Hu, J. Daw, G. Laffont, S. Nehr, and K. P. Chen, Opt. Express **26**, 11775 (2018).
22. C. Martinet, A. Kassir-Bodon, T. Deschamps, A. Cornet, S. Le Floch, V. Martinez, and B. Champagnon, J. Phys. Condens. Matter **27**, 325401 (2015).
23. "L'installation SIRIUS," https://portail.polytechnique.edu/lsi/fr/equipements/linstallation-sirius.html.
24. R. A. B. Devine, Nucl. Instrum. Methods Phys. Res. B **91**, 378 (1994).
25. N. Ollier, S. Girard, and S. Peuget, Encyclopedia of Glass Science (2021).
26. G. Buscarino, S. Agnello, F. M. Gelardi, and R. Boscaino, Phys. Rev. B Condens. Matter Mater. Phys. **80**, (2009).

27. B. Boizot, S. Agnello, B. Reynard, R. Boscaino, and G. Petite, J. Non Cryst. Solids **325**, 22 (2003).
28. T. Gavenda, O. Gedeon, and K. Jurek, J. Non Cryst. Solids **425**, 61 (2015).
29. J.-M. Delaye, S. Peuget, G. Bureau, and G. Calas, J. Non Cryst. Solids **357**, 2763 (2011).
30. F. Piao, W. G. Oldham, and E. E. Haller, J. Non Cryst. Solids **276**, 61 (2000).
31. L. Douillard and J. P. Duraud, Journal de physique III **6**, 1677 (1996).
32. I. Reghioua, M. Lancry, O. Cavani, S. L. Floch, D. R. Neuville, and N. Ollier, Applied Physics Letters **115**, (2019).
33. C. M. Petrie, A. Birri, and T. E. Blue, J. Non Cryst. Solids **525**, 119668 (2019).
34. A. Cornet, V. Martinez, D. de Ligny, B. Champagnon, and C. Martinet, J. Chem. Phys. **146**, 094504 (2017).

III.5 CONCLUSION

In this chapter, we investigated the effects of electron irradiation on silica glass, examining, metamict-like transformations. We also study how high-temperature combined with irradiation jointly influences the silica glass network in terms of vibrational structure and point defects centers i.e. bond breaking and charges trapping.

By employing *in situ* Raman spectroscopy during thermal annealing, we could determine activation energy distributions that govern the relaxation of densified states. The results confirm that silica's thermomechanical history has a pivotal role in its subsequent response to irradiation: samples that underwent HPHT treatment before irradiation consistently display higher thermal stability than those subjected only to irradiation. A key finding is that HPHT densified and pre-densified and low-irradiated silica exhibits a bimodal activation energy distribution, reflecting the presence of a HDA "transition phase" whose partial erasure is revealed through the non-monotonic behavior of the D_2 Raman band along isothermal annealing in agreement with the literature on HPHT densified silica.

Increasing the dose up to 11 GGy effectively removes that bimodality and diminishes the HDA contribution, pushing the glass into a largely LDA and metamict-like state. Nevertheless, even within this metamict-like regime, the exact thermal stability and structural details depend strongly on the sample's thermomechanical preparation pathway and impurity levels. Higher OH content (e.g. 1000 ppm instead of 0.1 ppm) in the initial silica composition can slow the metamictization process, indicating that such small compositional changes affect long-term performance. From an applications perspective, the enhanced thermal stability observed in HPHT-densified silica hints that sensors or optical components fabricated through similar densification pathways, such as femtosecond-laser Type II as was shown in the previous chapter, would be more resilient under extreme radiation.

Finally, examining irradiations performed at elevated temperatures clarified how thermal and radiative processes connect. At (300-450K) temperatures, the structure of both pristine and densified silica glass moves towards a metamict-like state with the increase of temperature, slowing the process. At sufficiently high temperatures, irradiation-driven densification gives way to simultaneous thermal relaxation effects. For instance, at 600 K, a total dose of 5 GGy essentially fully relaxes pre-densified samples, while at 1000 K the same phenomenon occurs even faster, below 1 GGy. These observations emphasize the need to account for both radiation dose and temperature when engineering silica-based components for harsh environments. Overall, our findings underscore the critical importance of thermomechanical history, dose, temperature, and composition in shaping the structure and stability of irradiated silica glass.

Chapter IV. DENSIFICATION MECHANISMS AFTER FS-LASER INTERACTION AND THE EFFECT OF COMBINED ELECTRON IRRADIATION

IV.1 INTRODUCTION

Building on the methodology developed in Chapter 2 and findings of Chapter 3, this chapter delves deeper and at large extent into the densification mechanisms of fs laser modifications in silica glass for types I, II, III and then explores how these modifications, particularly nanogratings, respond when subjected to high electron irradiation doses.

In the first part, we extend our nanoscale spectroscopic approach, s-SNOM and nano-FTIR measurements, to investigate all three main fs-laser-induced modification types (namely Type I, Type II, and Type III). Although each modification type is known to exhibit varying degrees of densification, detailed assessments of the density levels have remained challenging especially due to the intimate composite nature of these modifications at sub-micrometer scale. By reviewing existing knowledge and incorporating our new synchrotron-based nanoscale data, we clarify how and why silica densifies differently across these three modification types and relate those changes to the underlying laser light-induced mechanisms.

In the second part, we shift our focus back to Type II nanogratings, which play an important role in numerous photonic and sensing applications due to their high birefringence and robust thermal stability. As we found, these periodic structures can reach very high densities, similar to HPHT densification. It is thus interesting to test how these fs modifications behave under electron irradiation in silica. Prior studies have shown that electron doses can either densify initially "low-density" silica or relax densified material (above ~2.26). We therefore expose nanogratings to a 5 GGy electron dose and track changes in both optical (e.g., retardance, phase) and structural (periodicity, pore size, Raman D_2 band intensity) properties using SEM, Raman spectroscopy, s-SNOM, and nano-FTIR. Significantly, we find that the nanograting morphology (the periodicity, pore diameters) remains intact, but the dense interlayers relax. This relaxation lowers the birefringent properties, reinforcing both our earlier findings on the structure and density of Type II modifications and the impact of electron irradiation on densified silica. Finally, we analyze this result within the framework of the known relationship between the D_2 band intensity and density, highlighting the non-linear behavior above 2.26. This observation underscores how three-membered rings in silica (probed via Raman D_2 band) do not simply increase with density beyond the density of 2.26. From an applied point of view, these findings also have broad implications for sensors made via Type II modifications used in environments with high radiation, providing insights into their long-term stability and performance in harsh environments.

IV.2 PROPERTIES, MECHANISMS, AND PERSPECTIVES OF ULTRAFAST LASER MODIFICATIONS IN SILICATE GLASS VOLUME

Properties, mechanisms, and perspectives of ultrafast laser modifications in silicate glass volume

Nadezhda Shchedrina [1,2], Matilde Sosa [1,3], Maxime Cavillon [1], Matthieu Lancry [1]

[1] Institut de Chimie Moléculaire et des Matériaux d'Orsay, Université Paris-Saclay, CNRS, 17 avenue des Sciences, 91400 Orsay, France

[2] Laboratoire des Solides Irradiés, École polytechnique-CEA-CNRS, 91128 Palaiseau Cedex, France

[3] Université Paris-Saclay, CEA, List, F-91120, Palaiseau, France

Abstract

Ultrafast laser irradiation of glass enables highly localized structural transformations within the material's bulk, unlocking diverse applications in photonics, data storage, and microfabrication. Here, we provide a concise yet comprehensive overview of the main types of femtosecond laser-induced modifications in silica-based glasses (Type I, II, III, X, and related crystalline transformations), highlighting their distinct features and underlying thermal- and pressure-driven mechanisms. This review offers a current state-of-the-art perspective on various modifications, while also presenting new nanoscale insights through advanced scattering scanning near-field optical microscopy (s-SNOM) and nano-Fourier transform infrared (nano-FTIR) spectroscopy, discussing the densification mechanisms behind. Finally, we outline broader perspectives, from fundamental research directions to industry developments, to inspire future advances in next-generation optical technologies.

1. Introduction

Ultrafast laser interactions with a material can yield a diversity of localized modifications both on its surface and within its volume. Relying more specifically on glasses, such interactions have been an extraordinary research topic over almost 30 years. Both laser "parameters" and glass composition offer virtually unlimited combinations, therefore becoming a vast playground to the Glass science community and engineering their properties. Moreover, a significant potential for diverse applications has allowed advancements in fields such as photonics, data storage [1,2], biomedical devices, and microfabrication [3–7]. The interaction between ultrashort laser pulses and glass is a complex, multi-stage process involving several physico-chemical mechanisms. Laser-induced modifications in glass can occur within the bulk material and on its surface as reviewed recently (e.g., refs. [8,9]). Initially, an intense incident laser light is focused inside a glass material. The conditions are such that intensities on the order of TW/cm² are reached within the focal volume. This induces electronic excitation within the glass through a series of nonlinear processes, such as multiphoton ionization, tunnelling, and avalanche ionization [10–14].

Subsequently, a high-density free electron plasma (over or under critical depending on the chosen conditions) is created, which thus transfers a part of its gained energy to the glass lattice via electron-phonon coupling associated to various relaxation phenomena. The rapid energy deposition generates temperature and pressure gradients, which can cause structural rearrangements within the glass matrix. For instance, elevation reaching 1000s of °C can be experimentally measured in silica and silicate glasses using time resolved Raman spectroscopy [15]. Moreover, pressure shockwaves on the order of few 10s of GPa have been recently verified [16] and higher values are predicted in strong focusing conditions [17]. In these extreme conditions, a variety of processes occur including cavitation, micro-explosion, densification/expansion, recrystallization, chemical migrations, etc. Ultimately, this leads to permanent glass modifications exploitable in various fields [4,7,14,18].

Surface modifications are demonstrated by laser-induced periodic surface structures (LIPSS), which are nanoscale ripple patterns formed on the material's surface [19]. LIPSS are generally categorized into low-spatial frequency LIPSS (LSFL) and high-spatial frequency LIPSS (HSFL) [20,21]. LSFL often exhibit spatial periods in dielectric materials close to the laser wavelength λ or λ/n, where n represents the material's refractive index. The orientation of LSFL is typically perpendicular to the laser beam polarization, or parallel in the case of large band gap materials such as SiO_2 and BaF_2 [22]. The formation of LSFL is attributed to a spatially modulated energy deposition resulting from the interference between the incident laser radiation and excited surface electromagnetic waves. Applications of LIPSS in surface structuring are continually being explored, particularly in tailoring surface-specific properties such as absorption, reflection, and wettability [23].

Transitioning from surface to volume modifications, which will be the focus of this article, ultrashort laser pulses can induce a variety of structural changes within the bulk of glass materials. These volume modifications are generally categorized as “Types” of transformations, each one corresponding to different levels / conditions of energy deposition, and resulting to structural transformations within the material [7]. There exist many of them (Types I, II, III, A, X etc. or a combination thereof), their properties and applications have been partially reviewed [4,24]. The resulting modified structures strongly depend on laser parameters [25] (such as energy, pulse duration, repetition rate, wavelength, polarization (state and orientation), numerical aperture, depth of focus, and writing speed), and on the material's properties [26], including band gap, viscosity, density, heat capacity, thermal conductivity, and their temperature dependencies. Figure 1 chronologically highlights the first reported discovery, to the best of our knowledge, of different types of modifications induced in optical glasses in volume. We purposely renamed some types of modifications (see caption of Fig. 1) to make the nomenclature more consistent and meaningful.

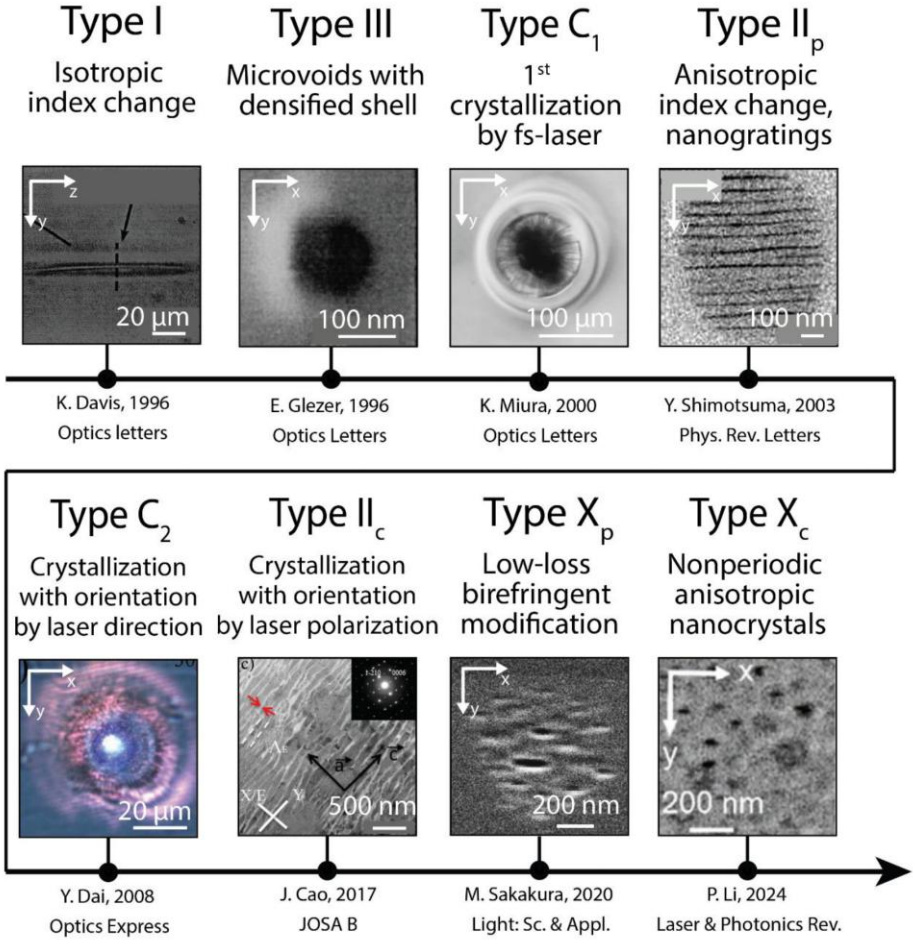

Figure 1. Main types of laser-induced structural modifications in glass volume presented in a chronological order of discovery. Type I: Isotropic refractive index change [27]. Type III: Microvoid formation with a densified shell [28]. Type C_1: First laser-induced crystallization in glass (C for crystalline) [29]. Type II_p: Anisotropic refractive index changes due to nanogratings (p indicates porous layers) [30]. Type C_2: Crystallization oriented by laser writing direction [31]. Type II_c: Lamellar crystallization oriented by laser polarization (II + c for crystallization) [32]. Type X_p: Low-loss birefringent modifications with porous structures [33]. Type X_c: Low-loss birefringent modifications with nonperiodic anisotropic nanocrystals [34].

With the different types of transformations that exist in mind, and principal mechanisms and features of laser induced transformation succinctly described about, the goal of this article is first to provide an overview of the different types of modifications that are typically encountered in glass using femtosecond laser, including their key features / characteristics in term of optical and mechanical properties, main structural changes and underlying mechanisms. We do not aim to be fully exhaustive, as the literature on the topic is extremely vast. However, we expect this overview to be a brief compilation of important aspects of volume modifications by femtosecond laser in glasses, with up-to-date results from, and for, the community. Subsequently, a focus on nanoscale densification processes for the main types of transformations encountered in silica glass (namely Types I, II, III) is given in light of recent results exploiting scattering near-field optical microscopy (s-SNOM) and nano-Fourier transform infrared spectroscopy (Nano-FTIR) measurements performed at Synchrotron Soleil. Finally, we present an extended section about perspectives for future research and applications on this topic.

2. State-of-the-art overview of transformation Types

In this section, we present a brief review of fs-laser induced main transformation types in glasses and in particular Type I, II, III and X in SiO_2. We examine key optical properties (such as refractive index changes, linear and circular optical anisotropy, absorption, light scattering), mechanical parameters (like variations in Young's modulus and Poisson's ratio), as well as structural changes (such as defects formation, densification identified through Raman and Fourier transform infrared (FTIR) spectroscopy, etc.). Finally, we discuss the underlying mechanisms driving these transformations.

2.1. Type I modifications

Type I modifications are characterized by isotropic change in the refractive index with minimal structural transformation [27,35]. The refractive index change of Type I modifications is permanent (associated with the increase in density), quite transparent and has higher thermal stability compared to UV-induced changes, though it remains moderate since it fully erases within 30min at 1000°C [36]. In fused silica, the maximum index change (Δn) observed ranges typically between $3\text{-}6\times10^{-3}$ [35,37], which is significantly larger than the UV laser-induced index change limited to 3×10^{-4} using 193 nm excimer (ns) laser writing [38]. These modifications are typically achieved under laser parameters involving lower energy levels, visible or near IR laser light and shorter pulse durations (typ. <10 ps). While multiscan helps to increases the refractive index contrast up to 10^{-2} as reported recently [39], and a record has been achieved with $\Delta n = 2.2\times10^{-2}$ [40], taking advantage of a high repetition rate regime but leading to additional damage and light scattering.

The origin of index contrast (Δn) in the Type I regime arises from different contributions, including specific volume changes Δn_V, related stress field and point defects Δn_D, but also elemental migration Δn_M in specific glasses like soda-lime silicate, borate [41] or phosphate glasses when mobile species have been introduced [42]. The Δn_D can be described using the Kramers-Kroning relation and remains moderate (typ. 10^{-4}) [43–46]. The main defects in Type I are E' centers and non-bridging oxygen hole centers (NBOHC) [47,48], which can be completely erased in conditions as 2 hour annealing at 450°C [49,50]. As a results Type I modification exhibit low optical losses and most optical absorption remains located in the UV and VUV while light scattering remains very low [49]. Δn_V origin is plural, including fast quenching [4,51], significant pressures may be developed at short time scale, bond breaking accumulation or a combination thereof resulting in a glass restructuration and eventually coordination changes. This permanent index change is related to the relative volume change of the material ($\Delta V/V$) through the Lorentz-Lorenz expression but one should also associate the elastic strain which brings an additional index change (of opposite sign) through photo-elastic effect.

Apart from point defects centers, structural changes of Type I modifications can be observed in Raman and Fourier transform infrared (FTIR) spectroscopy. Raman spectra of the laser modified areas show a narrowing of the main band's full width at half maximum (FWHM), meaning a decrease in the average Si-O-Si angle and an increase in the D_1 and D_2 bands, which correspond to vibrations in 4- and 3-membered silica rings, respectively [48,51–53]. Additionally, the Si-O-Si antisymmetric stretching band, centered at 1120 cm^{-1}, shifts to lower frequencies, reflecting increased glass density due to changes in inter-tetrahedral Si-O-Si bridges [54,55]. FTIR spectra for Type I modifications showed a 6 cm^{-1} shift in the main IR band [56], indicating a localized glass densification in SiO_2 but a volume expansion in many other glasses.

Changes in structure inevitably result in the modified mechanical properties of the Type I modifications. Mechanical investigations such as surface topography changes due to permanent strain relaxation is a direct way to probe the presence of a glass densification/expansion [57,58]. In addition, such permanents strain and related elastic response may affect the local mechanical properties. For example, cantilever deflection experiments correlate sample upward bending with a localized reduction of volume and equivalent average tensile stress of

around 40 MPa [59] in post-mortem measurements, while nanoindentation measurements indicate a 2-3 GPa rise in the local Young's modulus (from ~72 GPa in pristine silica to 74–75 GPa in the modified zones) [60]. This type of modification decreases the coefficient of thermal expansion (CTE) compared to pristine fused silica, lowering the CTE by about a factor of 2 for deposited energies above 100 J/mm² [61].

All the aspects discussed (refractive index, spectroscopy, and mechanical properties) confirm the permanent densification in Type I modifications. In simple terms, the transfer of energy from free electrons to the glass network generates extremely high local temperatures, reaching several thousand of degrees [62] at the focal point, constrained by thermal conduction [63,64], and accompanied by high pressures. This can lead to a localized increase of the glass fictive temperature (T_f) by several hundred of degrees above the pristine (i.e., non-irradiated) value [55]. Upon rapid cooling, these conditions result in permanent structural changes [48,51,65]. The mechanisms underlying densification will be discussed in detail alongside insights from new measurements in Section 3.

2.2. Type II_p modifications

Type II_p modifications, often referred to as nanogratings, are characterized by a highly anisotropic change in the refractive index within the glass material mostly due to form birefringence [66,67] with a significant contribution of stress induced birefringence depending on the writing geometry [68–70]. The refractive index change can be substantial, reaching magnitudes up to -2×10^{-2} [39,71], and is notable for its exceptional thermal stability, the modifications remain stable even after exposure to temperatures as high as 1000 °C for at least two hours [36,72–74] and even 100's hours after a thermal stabilization as made in fiber Bragg gratings [36] or as predicted in bulk silica [74]. The main feature – form birefringence – comes from the structure of nanogratings [30,75], which consist of periodic layers containing oblate nanopores [76,77] and an densified interlayer material. These porous nanolayers are aligned perpendicular to the laser beam polarization [30,71], resulting in a negative uniaxial birefringent response, where the fast (slow) axis is also parallel (perpendicular) to the polarization orientation [71]. In addition to form birefringence, the overall linear birefringence in Type II_p modifications includes contributions from stress-induced birefringence (arising from permanent volume changes during laser writing, which adds elastic strain and thus stress within the material [78,79]), point defects, and the densified background matrix [80].

The process formation can be decomposed into a series of steps. First, inhomogeneities are present inside the dielectric domain, that can already exist in the glass or formed during laser writing. The formation of nanoplasma from them has been suggested in the literature, originating from defects (including transient ones like self-trapped excitons (STE) or self-trapped holes (STH)) or color centers [76,81–83], or from available free volume in the glass matrix [84], nanometer size inhomogeneities [85,86], with subsequent scattered waves interference [87] resulting in spatio-temporal structuring into nanogratings. Following this, formation of nanopores occurs, assisted by temperature and pressure [88]. Likewise, the nanocavitation process is in principle a global approach since all the glass compositions [26,76] would experience a stress field upon heat deposition inside the focal volume. However, a recent theorical approach has pointed out the existence of large electric field produced by light excitation leading to consider electrostriction or inverse piezoelectricity [89]. These effects may also trigger strain fields and thus contribute to, or even seed, the nanocavitation process.

These nanopores are associated with a formation of molecular O_2 (free within nanopores and interstitial inside glass matrix [77]). In silica and silicates, the existence of nanogratings is a function of laser parameters (including number of pulses [76]). They would not form if the nanopores are unstable during irradiation process (for instance too high temperatures at high repetition rate [90,91] or not enough available intermolecular free volume as we investigated very recently in densified silica under high pressure [84]).

In these Type II_p modifications, the contribution of point defects to the refractive index difference (between porous and densified interlayers) and their contribution to birefringence remains low. Key photo-induced defects, similar to those in Type I, include E' centers [92] and NBOHC, which are produced by self-trapped exciton decay [81,93] but within Type II_p there are additional defects such as oxygen defects centers (ODC) and O_2. NBOHC can react with E' centers at critical concentrations to form ODC(II) [25,63,94]. E' and ODC defects can be bleached after 30 minutes of annealing at 600°C [95], while NBOHC requires for example 10 hours of annealing at 300°C for removal [96]. Notably, once the defects are fully bleached, the overall birefringence in the visible to near-IR spectral range decreases by less than 5 % [49].

From structural changes point of view, vibrational spectroscopy has been extensively used. The Raman signature of Type II_p modifications in silica glass reveals an increase in D_1 and D_2 band intensities, narrowing of the R-band's FWHM, and the presence of O_2 molecules. Raman spectroscopy has also been employed to estimate densification in fs-laser inscribed tracks [52,53,59,78,95,97]. An 8% densification in glass by comparing Raman signatures with high-pressure, high-temperature (HPHT) treated samples has been reported [53]. Further studies

estimated glass density post-irradiation at 2.25–2.27, based on D_2 band intensity and R-band FWHM [95], though the D_2 band intensity is not the most reliable density indicator above 2.3, as it decreases for densities beyond this point [98]. Recent work also explored fs-laser-induced shock waves, estimating pressures of tens of GPa using silica's Raman signature [97]. Since Type I modifications have a relatively homogeneous structure, micro-characterization techniques like Raman and classical FTIR can be applied for analysis. In contrast, Type II_p, with their layered composite nanostructure, are challenging to be investigated at nanoscale using the same techniques. Recently, we have utilized nano-FTIR and IR s-SNOM measurements to correlate the shift of the main IR vibrational structural band of silica glass with density and estimated values ranging from 2.4 to 2.5 within laser tracks and between nanolayers [80,99].

Specific volume changes and mechanical properties in Type II_p modifications were similarly analyzed through micro-cantilever deflections [59,61,78,100]. While Type I modifications cause upward deflection due to volume reduction and densification, Type II_p induce downward deflection from nanopore formation and overall net volume expansion [59,78]. These studies highlight stress-state inversion in silica glass [59], where the dense interlayer material, resembling Type I, shows an increased Young's modulus (around 80 GPa), contrasting with the porous layers' significantly lower modulus [59,61,100]. Furthermore, the coefficient of thermal expansion (CTE) also depends on the modification type: whereas densified (Type I) zones exhibit a decrease in the CTE, Type II_p display the opposite trend compared to pristine silica [61]. Additionally, Type II_p modifications exhibit a decrease in the temperature coefficient of elasticity (TCE) by more than 50%, attributed to submicron densified layers within the nanograting structure [101]. A recent study using grid nano-indentation revealed a bimodal stiffness distribution along the laser-affected zones in silica, with a porous region where nanogratings form and a more densified region further along the laser track [102].

In addition to mechanical changes, Type II_p modifications exhibit distinct optical properties. They typically maintain relatively high transparency in the visible spectrum (74% transmission at 550 nm) [103], with a laser damage threshold of 0.31 ± 0.05 μJ/pulse in pure silica (800 nm, 160 fs, 0.5 NA, 100 kHz) [25]. However, due to imperfections, anisotropic light scattering can result in 10–50% of incident light being scattered in the visible range [49]. Nanogratings also display linear dichroism [49,103], as well as engineered circular properties such as optical rotation and circular dichroism [103,104], offering potential for advanced photonic applications.

For readers who are looking more extensive details about these transformations, we can propose some recent review papers about nanogratings, related applications [9,105], and some generalization in term of chemical composition dependence in oxide glasses and recent perspectives in non-oxide glasses [26].

2.3. Type III modifications

Type III modifications are characterized by the formation of nano or micro-voids within the material due to very high energy deposition [28,106–108]. Morphological studies using scanning electron microscopy (SEM) [59,62] report void sizes ranging from 100 to 400 nm, which depend on focusing conditions, laser parameters and whose length can be engineered as well to form complex objects such as gradient-index metaphotonic structure [109]. At this level of energy input, the material undergoes a micro-explosion resulting in the formation of a void surrounded by a densified shell. These modifications exhibit exceptional thermal stability: high-temperature annealing experiments reveal that voids shrink between 1050°C and ~1150°C, followed by expansion and deformation above 1200°C, while the densified shell remains present [110]. This high thermal stability is particularly advantageous for applications that require materials to maintain their properties under harsh thermal conditions such as sensors for structural health monitoring, laser additive manufacturing or nuclear applications [94,111,112].

Similar to Types I and II, Raman spectroscopy indicates the presence of a densified shell surrounding micro-voids in Type III modifications in SiO_2 and GeO_2 [113]. Additionally, using quantitative phase microscopy (QPM) in optical fibers, negative phase variations inside the void and positive variations around it could be observed, confirming the presence of densified matter and permanent strain [110,114]. Furthermore, atomic force microscopy (AFM) combined with s-SNOM measurements at 1130 cm^{-1} unambiguously attribute this positive phase shell to local densification [110].

An original model explaining micro-void formation attributed it to a Coulomb explosion [106,115]: when the density of excitations becomes extremely high, electrostatic repulsion between ions surpasses their binding energies, pushing ions into interstitial positions. However, this scenario is unlikely under typical irradiation conditions. The model was subsequently revised: energy absorbed in a small volume generates intense pressure, launching a spherical shock wave that compresses the surrounding material while a rarefaction wave reduces density at the energy deposition center [116]. The shock wave continues to propagate until the pressure behind it approaches the Young's modulus of the material (up to 200 GPa), at which point it stabilizes [17,117–120]. Furthermore, the void formation threshold in glasses is inversely proportional to the concentration of glass

formers such as Si, P, and B, as higher concentrations of these elements lead to a stronger bond network [121]. Figure 2 summarizes the main characteristics of Type I, Type II and Type III modifications.

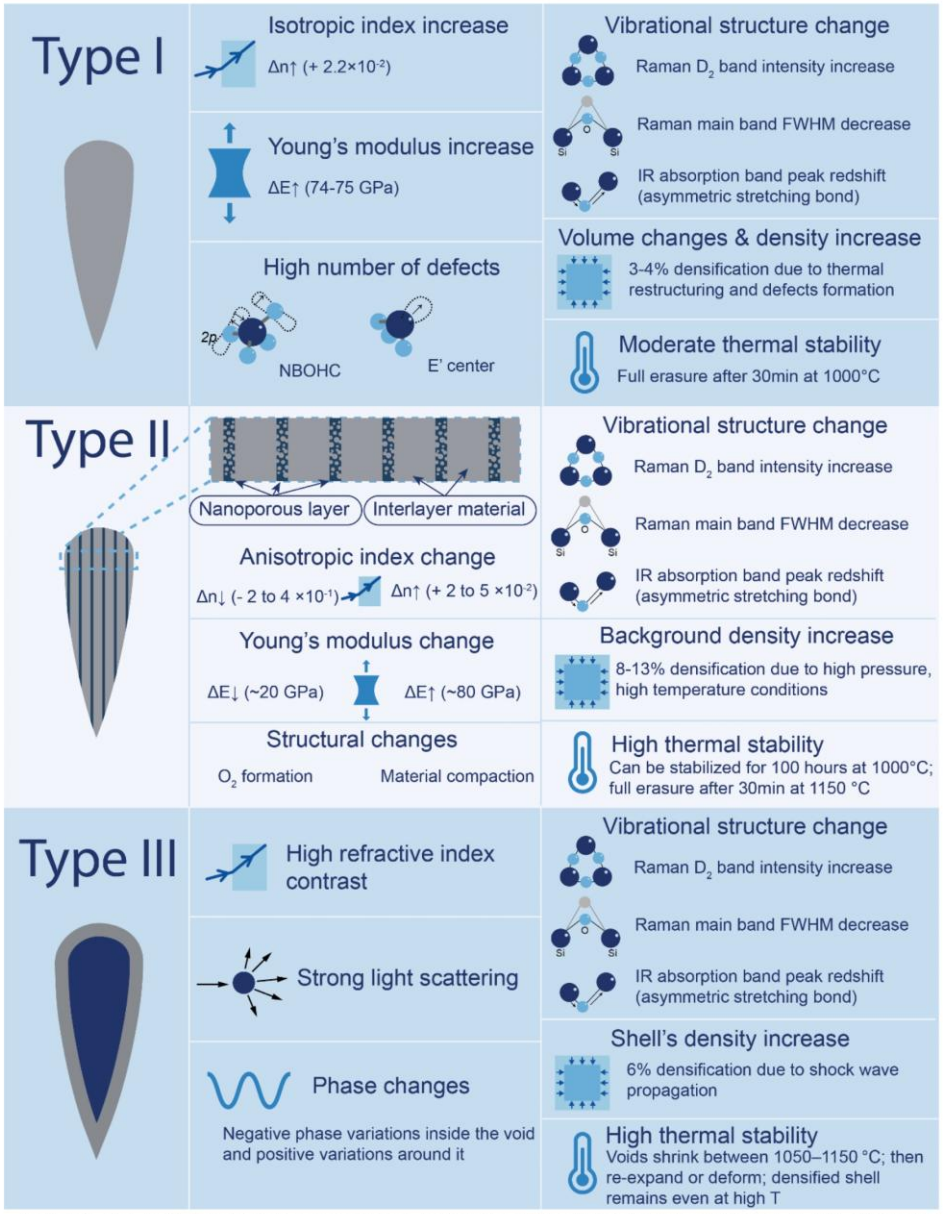

Figure 2. Comparison of femtosecond laser-induced modifications in a glass (Types I, II, III), summarizing key structural, optical, mechanical, and thermal characteristics.

2.4. Type X modifications

Aside from pure silica and the three main types of aforementioned transformations, some other induced modifications are noteworthy. One other kind of interesting transformations, present in silica has recently been discovered [33]. It is so-called Type X (Type X_p on Figure 1) and corresponds to the formation of oblate nanopores typically observed at low pulse density, with a time duration >220 fs. Counterintuitively, decreasing energy density by increasing the scanning speed can enhance the strength of Type X (and Type I) modification in silica glass due to the nonlocality of light-matter interaction [122]. Temporal contrast of the fs-laser pulses also plays

an important role in Type X_p formation: high-contrast pulses from a Yb:KGW laser promote the formation of Type X_p, while low-contrast pulses from a Yb fiber laser mostly lead to Type II modifications [123].

Type X_p enables very high transparency (up to 99% in visible spectrum) which somehow compensates from its lower retardance values (typ. below 50nm) that leads to the necessity of multilayers writing. Type X_p birefringence is typically in the order of 10^{-4} to 10^{-3} [33,124]) achieved compared to Type II which can reach 10^{-2} [71]. The refractive index contrast is moderate and comes from a balance between densification and formation of nanopores. This formation originates from the clustering of STH, which generates regions of high positive charge density that expel oxygen, creating the nanopores [125]. The elongation of the nanopores in one direction during the laser writing is attributed to the near-field enhancement around the nanopore perpendicularly to the laser polarization. At the same time, it was shown that elliptical polarization is more efficient for creating anisotropic nanopores than linear polarization, as circular component enhances nanopore formation and concentration while circular polarization leads to spherical nanopores [83,126].

From applied side, apart its high transparency, type X_p modifications in silica glass exhibit a higher optical damage threshold (1.56 J/cm^2 for 300 fs pulses at 1030 nm) compared to Type II modifications (0.96 J/cm^2 for 300 fs pulses at 1030 nm) due to a lower concentration of laser-induced defects and the different formation mechanisms and stress-induced effects [127]. Since Type X_p modifications in silica glass exhibit very high transmission and can be written with few pulses only, they have been successfully demonstrated as a promising approach for low loss 3D geometric phases optics [33] but also for optical data storage, achieving high data writing speed (from 8 kB s^{-1} to several MBs^{-1}) [122,124], an interesting prospect within the framework of ambient temperature data storage [128].

2.5. Other types – Others glass systems

Now, considering glass systems other than silica but staying in the oxide families, a series of other types of transformations must be considered. Since it is now not a unary composition, transformations such as chemical migration, phase separation, and crystallization (sometimes oriented) are to be expected [129–132]. For instance, it becomes possible to develop rounded laser tracks with tuned refractive index in commercial optical glasses [133], very useful to design 3D glass embedded optical waveguides, or to induce tunable oriented second harmonic generation through laser polarization-oriented nanocrystals like $LiNbO_3$ [134,135]. Most recently, a combination of crystallization and Type X, another type of transformation has been identified in a lithium aluminosilicate glass (LAS), called Type A (or Type X_c, Figure 1) [34]. The resulting optical properties resemble Type X_p in the sense that an elongated structure, oriented perpendicular to the laser polarization, induces a tunable birefringence response with reduced transmission losses. However, as opposed to Type X_p, the structure is composed of elongated nanocrystals (in this case Spodumene $LiAlSi_2O_6$). Considering spherical crystal seeds, the local field enhancement is more pronounced parallel to the light polarization. The authors suggested that at the early stage of the induced crystallization, the nanocrystal aspect ratio is dictated by the nanoplasma formation and field enhancement around it. Several contributions to the formation of crystalline structures and phase separation are worth mentioning. First, the temperature distribution and evolution during laser writing is a key aspect [136]. For instance, the laser writing conditions must ensure that the time-temperature profile penetrates the crystallization domain (or crystallization nose). Moreover, elemental migration can be dictated by thermal gradients (Soret effect [137,138] or electrostatic force [89]).

Beyond “conventional” oxide glasses, laser-induced transformations are also of significant interest in other glass systems, particularly those designed for infrared applications, such as chalcogenides, heavy oxides, and fluoride glasses.

Femtosecond laser direct writing (FLDW) enables precise, localized modifications, facilitating the fabrication of compact, lightweight optical components for IR applications. It has been effectively used to induce controlled transformations in materials such as chalcogenide glasses, oxide-based glasses, and sapphire [139–142]. Chalcogenide glasses, in particular, are well-known for their suitability in mid-infrared (mid-IR) applications [143–146]. Compared to oxide-based glasses, they exhibit high refractive indices, strong nonlinear optical effects, and extended infrared transparency windows, reaching up to 28 µm, due to the low phonon energy of their heavy chalcogen elements [147–149]. However, these advantages come with certain limitations, such as high return loss when integrated into photonic circuits and increased bulk index-induced losses. To address these challenges, alternative glass families like heavy oxides [150–155] and fluorides [150,156–161] have gained attention, offering lower return losses for wavelengths up to 6 µm. In terms of refractive index modification, significant changes on the order of 5×10^{-2} have been reported in GeS_2-based chalcogenide glasses [151,162], surpassing the maximum index variation observed in silica, being approximately 2.2×10^{-2} [27,40,163].

The following sections will summarize the current understanding of the structural modifications associated with each of the three types of laser-induced changes in glass – Type I, Type II, and Type III. We will explore the densification levels specific to each modification type and investigate the corresponding densification mechanisms, presenting new insights that contribute to a deeper comprehension of these laser-induced structural transformations in glass materials.

3. Comparative densification study between Type I, II, and III in silica at nanoscale

In the previous section, fs-laser-induced modifications in glass were reported, with a focus on silica as the major constituent of glass-based materials, and the resulting structural changes and densification. Although earlier studies have confirmed densification in all three types of fs-laser-induced volume modifications in silica glass using Raman spectroscopy [52,53,59,78,95,97], mechanical property measurements [59,61,78,100], and refractive index assessments [37,71], the densification levels and mechanisms consistency across different of this process remain uncertain. Moreover, these methods usually lack nanoscale resolution. To overcome this limitation, nano-FTIR and IR s-SNOM techniques [164], which can probe the asymmetric stretching vibration Si-O-Si band [165], linked to density changes [54,55], offer nanoscale insights into the densification mechanisms occurring within the modified regions.

3.1. s-SNOM and nano-FTIR

Below, we investigate three silica samples, each corresponding to one of the three primary modification types: Type I, Type II, and Type III. These samples were prepared using specific fs-laser parameters to achieve the desired structural changes within the glass. Type I modifications were inscribed in SuprasilCG silica glass using 800 nm, 160 fs pulses at 0.23 µJ/pulse and 100 kHz repetition rate, with a writing speed of 100 µm/s and NA = 0.6. Type II modifications were formed in SuprasilCG silica at 1030 nm, 250 fs, 1 µJ/pulse, 100 kHz, 10 µm/s, NA = 0.6, as described in details in [80]. Type III modifications were created in GeO_2-doped SMF-28e single-mode optical fibers (Corning) at 515 nm, 170 fs, 50 nJ/pulse, 1 pulse, NA = 1.4 [110]. After the inscription, all samples were cleaved to expose the XY cross-sectional plane of the modified regions for analysis.

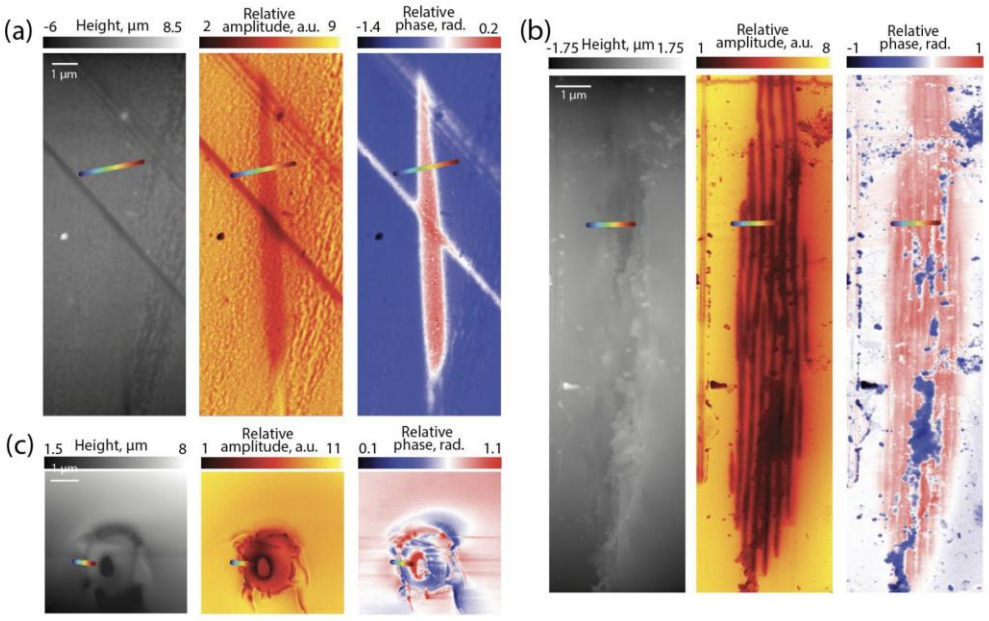

Figure 3. S-SNOM images of silica samples with laser-induced modifications. Each part corresponds to a different modification type: (a) Type I, (b) Type II_p, and (c) Type III. For Types I and II_p, the AFM surface topography is presented alongside the near-field amplitude and phase maps at 1130 cm^{-1}; for Type III, the maps are shown at 1120 cm^{-1}. Lines on the maps indicate the linescan measurements presented in Figure 4.

Subsequently, at Synchrotron Soleil (SMIS beamline), we performed s-SNOM measurements to obtain amplitude and phase maps at fixed wavenumbers. We selected the wavenumbers of 1120 cm^{-1} and 1130 cm^{-1}, corresponding to the peak position of the Si-O-Si asymmetric stretching absorption band in silica glass, which is very sensitive to permanent strain [165]. When densification occurs, this band undergoes a redshift, leading to a decrease in amplitude (as the measurements move on the right shoulder of the spectrum) and variations in the phase spectra (either increases or decreases), depending on the chosen wavenumber and its position relative to the shifted band. These changes are shown in the s-SNOM amplitude and phase maps presented in Figure 3 for all types of modifications. Notably, AFM height maps, particularly for Type I modifications (Figure 3a), do not reveal the laser-induced track indicating the densification level should remain quite low. However, Type I related laser track is clearly visible in the amplitude and phase maps obtained from s-SNOM measurements. This enhancement is less pronounced for Type II_p modifications (Figure 3b) but remains noticeable. For Type III modifications (Figure 3c), the amplitude and phase maps reveal the structural changes in the area surrounding the void itself.

Afterwards, we measured the nano-FTIR spectra, both amplitude and phase, at pristine silica areas and laser-modified regions for each modification type. For all samples, we observed a significant redshift in the position of the main IR band corresponding to the asymmetric stretching vibrations of the Si-O-Si bonds, indicative of permanent densification.

For Type I modifications, the peak position of the asymmetric stretching band in the amplitude spectra is located at 1117 cm^{-1} for the pristine material and 1110 cm^{-1} within the laser-modified region, indicating a shift of approximately 7 cm^{-1}, as can be seen in Figure 4a and similarly in phase spectra in Figure 4b. To gain a more detailed understanding, we performed nano-FTIR measurements by conducting point-by-point scans along the rainbow lines indicated in Figure 2 on the maps. By following the band position of the amplitude and phase spectra across the laser track, we clearly observed a rapid shift to lower wavenumbers from the surroundings into the interior of the laser track (Figure 4c and 4d). The shape of the peak position pattern remains quite smooth, indicating a uniform densification within the laser-modified region.

In contrast, for Type II_p modifications, we observed a variation in the band position which mirrors the periodic structure of the nanogratings (Figure 4e and 4f). The peak position outside the laser track is 1124 cm^{-1}. Within the laser-modified region, a pattern of fluctuating peak positions appears, decreasing and increasing in correspondence with the nanogratings' alternating interlayers (around 1112 cm^{-1}) and nanoporous layers. The lowest points in the graph, around 1103 cm^{-1}, represent areas where the densification is at its highest degree, near the porous nanolayers. Interestingly, the nanogratings evolve within a densified background. In our previous work [80], we studied a laser track corresponding more closely to Type X_p modifications (with only few pulse at low energy), where no nanogratings are yet formed but a strongly densified background exists, with the peak position shifting from 1121 cm^{-1} to 1107 cm^{-1} thus indicating that Type X_p (and likely Type II_p) are somehow written within a Type I affected area.

For Type III modifications, we measured the nano-FTIR spectra of the SiO_2 fiber cladding and the GeO_2-doped core. The peak position of the IR band is located at 1119 cm^{-1} for the cladding and 1114 cm^{-1} for the core. The incorporation of GeO_2 into the core results in a shift of 5 cm^{-1} to lower wavenumbers, as expected due to alterations in the glass network structure [110]. Within the void region created by the laser, the peak position further shifts to 1106 cm^{-1}, indicating an additional shift of approximately 8 cm^{-1}. For the point-by-point scans, the chosen line traverses both the densified nanolayer surrounding the void and the undisturbed core material, enabling a direct comparison of their vibrational properties. By tracking the peak positions of the Si-O-T (T = Si or Ge) asymmetric stretching band, we observed that the peak position in the densified shell decreased to as low as 1100 cm^{-1}, compared to 1114 cm^{-1} in the core material (Figure 4e). A similar trend was observed in the phase spectra (Figure 4f).

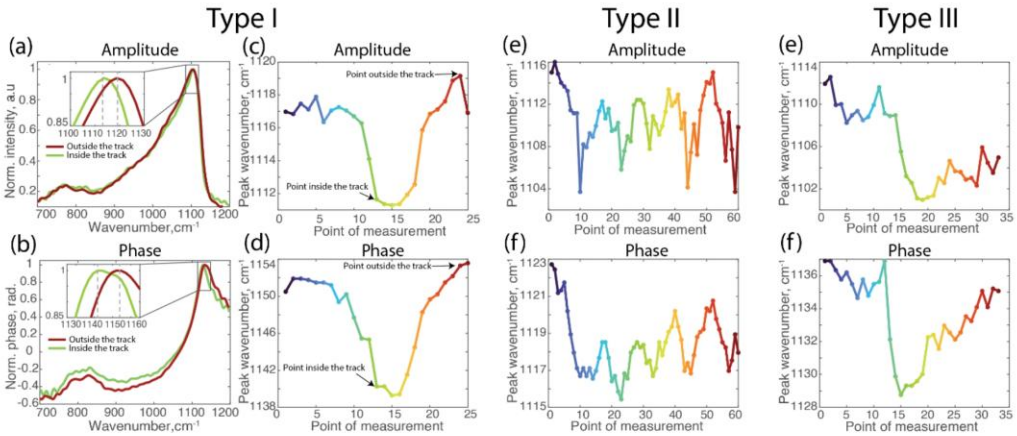

Figure 4. a) synchrotron nano-FTIR amplitude and (b) phase spectra for pristine material and irradiated area inside of the laser track for the Type I modification. (c) amplitude peak position and (d) phase peak position along the line profile for Type I; (c) amplitude peak position and (d) phase peak position (measured at 80% of its maximum) along the line profile for Type II; (c) amplitude peak position and (d) phase peak position along the line profile for Type III.

3.2. Discussion of the densification mechanisms and related nanoscale investigations

Type I

As has been seen from the state-of-art overview, it has been shown Type I modification exhibits densification of the material leading to structural and optical changes. An interesting possibility is to estimate the level of the densification and the mechanisms driving this densification. A shift towards lower wavenumbers in the IR spectra is indicative of densification in silica glass [54,55]. Specifically, the decrease in the resonance frequency of the Si-O-Si asymmetric stretching band is associated with increased glass density due to changes in the Si-O-Si intertetrahedral bridges. The relationship between this resonance frequency and the density for pure silica glass is given by the linear equation:

$$\nu_{as}^{(Si\text{-}O\text{-}Si)} = (1332 \pm 13) - (95 \pm 5)\rho, \quad (1)$$

where $\nu_{as}^{(Si\text{-}O\text{-}Si)}$ is the resonance frequency in cm^{-1}, and ρ is the silica glass density [54].

The nano-FTIR measurements reveal a shift of 7 cm^{-1} in the $\nu_{as}^{(Si\text{-}O\text{-}Si)}$ band, corresponding to a densification of approximately 3-4% according to equation 1. This observation aligns with previous results reported in [56], where a shift of 6 cm^{-1} was noted for Type I modifications. In agreement with microscale mechanical measurements and Raman spectroscopy, this confirms the presence of densification inside the laser tracks. It is important to note that our analysis focuses on the relative shift of the Si-O-Si vibrational band within each sample (between background and fs-irradiate zone) rather than the absolute peak positions between different samples. It is quite difficult to compare absolute values within different samples using this technique, when changing each sample and especially the SNOM tip and surface roughness affect the values of the peak.

What drives densification in Type I modifications? In fused silica, it is well-established that the density and refractive index increase when the glass is quenched from a considerably high temperature [48,51,65], which partly happens in the focal volume due to laser irradiation. However, if there was a local melt-quenching resulting in fictive temperature changes, the imprinted densification would be thermally stable above T_g which is actually not the case. So, it was suggested that the Type I densification is solely attributed to defect accumulation [18]. Indeed, even the level of densification of 3% is similar to the magnitude of the densification achieved by electron irradiation [166] (with the accumulation of bond-breaking, catalyzed by the creation of point defects [167–169]). However, the high thermal stability of Type I modifications suggests otherwise. For instance, E′ and NBOHC defects in waveguides are erased at 400°C, yet they remain stable up to 900°C [47]. This indicates that color centers alone are unlikely to drive such a level of densification. Instead, a combination of thermal effects and defect processes is more likely [170]. Laser irradiation can heat the glass near, or above, its transition temperature, enabling rapid quenching that elevate the fictive temperature [55], and favoring a defects assisted structural relaxation. Meanwhile, point defects can persist even under extreme thermal conditions, as observed

in optical fiber drawing above 2000 °C, where additional defects such as E′ centers are generated [171]. Thus, both thermal restructuring and the formation or persistence of point defects due to high strain collectively contribute to the permanent densification observed in Type I modifications.

Type II_p

For Type II_p modifications, our previous work using nano-FTIR and IR s-SNOM has provided density estimates and insights into the underlying mechanisms [80]. Here, we briefly summarize those findings and present new numerical estimations. Previously we showed that at 2 pulses/µm, we see formation of elongated nanopores within a densified "bed", Type I-like matrix, with density approximately of 2.400±0.186. Increasing the pulse density to 200 pulses/µm stabilizes the foundational densification while nanogratings evolve through a pulse-by-pulse mechanism, suggesting densification precedes and accompanies nanograting formation [59]. The density of the interlayer nanogratings material was around 2.316±0.183, going as high as about 2.495±0.190. Notably, the most densified areas appear closer to the nanoporous layers, showing that densification occurs throughout the laser track, between nanolayers but also likely around the nanopores. In another study we showed that electron irradiation can reduce nanograting anisotropy by relaxing the interlayer material without altering the morphology [99]. For tracks written with 10,000 pulses/µm, we estimated similar densities (~2.49), using same nano-FTIR approach as well as by modeling the retardance changes after electron irradiation. Here, we measured shifts of 13 cm^{-1} inside the laser track, with maximum shifts of 22 cm^{-1}, corresponding to densities of about 2.316±0.183 and 2.41±0.185, respectively. Thus, the overall densification precent of Type II modifications is about 8-13%.

Laser-induced densification in Type II modifications reaches levels similar to those achieved under HPHT conditions, indicating that both elevated temperature and dynamic pressure are likely developed at short time scale. While high-temperature quenching (i.e. glass fictive temperature increase) alone yields only about 3% densification in silica [55,172], the much higher densification observed here requires simultaneous high pressures. Similarly, pressure without heat would be ineffective on femtosecond timescales, confirming the need for a combined high pressure and high temperature presence. High temperatures enable rapid and homogeneous densification along the laser track, mirroring the beam's shape and thermal profile. This process, activated by a rapid temperature rise from light-matter interaction, induces thermal expansion and initiates a strain wave. This leads to a wave compressing the material ahead, promoting densification, while a rarefaction wave behind that may trigger this plasma-mediated nanocavitation process [76] thus leading to nanopores formation.

Direct evidence of these high-pressure contributions comes from polariscopic observations of femtosecond laser-induced stress waves in fused silica, which reveal the potential formation of a weak shockwave that rapidly transitions to a sub-sonic strain wave traveling at about 5.5 µm/ns [16]. These shockwaves generate stresses of around 10 GPa, aligning with simulation data [173]. Using a static high-pressure Hugoniot relationship [174–178], a density near 2.5 implies estimated pressure of 7 GPa, while during the shock wave pressure a ~13.6% densification ratio corresponds to ~14 GPa [178]. Additional investigations comparing Raman spectra of shockwave-densified silica with hydrostatic loading experiments indicate pressures ranging from 13 to 15 GPa [97]. Collectively, these findings emphasize the key roles of high temperature, high pressure in driving densification during Type II_p femtosecond laser modifications.

Type III

In Type III modifications, micro/nano-void formation is characterized by a measured $\nu_{as}^{(Si\text{-}O\text{-}Si)}$ peak shift of about 8-13 cm^{-1}, corresponding to roughly 6% densification. Initially, the fs-laser pulse drives a micro-explosion and a shock wave traveling slightly faster than the speed of sound, creating high local pressure and compressing the surrounding silica network. However, once the shock wave passes, the region behind it experiences a significant temperature rise due to subsequent relaxation wave. At these elevated temperatures, the glass structure partially relaxes from its densified state, causing a reduction in overall densification [179,180]. Densification in silica by shock wave can reach up to around 13% at 18-20 GPa, but further increases in pressure raise the temperature enough to trigger additional structural relaxation, lowering the final density. According to pressure-densification correlations [178], the observed 6% densification could correlate with a shock pressure up to 28 GPa, implying that the initial densification exceeded its maximum before temperature-driven relaxation partially reversed it. Early research suggested that transient pressures inside the micro-explosion could exceed 10 TPa [181]. However, more recent research and modeling utilizing a 3D Maxwell propagator found that plasma shielding limited the peak pressure in the warm dense matter state of sapphire to about 200 GPa and a similar effect is expected in SiO_2 [17]. While lower than initially thought, this pressure is still high enough to produce an

internal void within the transparent material and cause phase transformations. The pressure generated in these processes is consistent with the shock wave nature of the densification process.

4. Conclusions and perspectives

In this work, we have provided a concise overview of fs-laser-induced modifications in optical glasses, emphasizing how different transformation types (I, II, III, X, and C) arise from the interplay between laser parameters and material properties. We have shown that each modification type exhibits unique structural, optical, and mechanical characteristics, ranging from isotropic refractive index changes to anisotropic birefringence and voids formation, and that these differences stem from distinct energy-deposition mechanisms. Recently deeper investigations around fs-induced structural changes and mechanisms using nanoscale techniques such as nano-FTIR and s-SNOM were performed to investigate structural changes at a 10 nm scale using vibrational spectroscopy. From these experiments we have estimated the density levels of these main modifications and confirmed how the mechanisms across the types: Type I modifications are largely governed by thermal quenching and defect processes, Type II_p densification requires coupled HPHT conditions, and Type III is strongly influenced by shock wave dynamics.

Towards a new paradigm – To go beyond a simple energy deposition to develop optical forces

Understanding how a material behaves at the nanoscale under intense laser excitation is crucial for advancing future laser processing technologies. Mechanical, thermal, optical, structural and compositional properties of materials could be tailored for optical data storage, micro/nano fluidic devices, optical devices, novel alloy formation, catalytic and sensor applications, etc. A classical effect of a light beam is a thermal effect (laser cutting, melting). However, it is possible to go far beyond a simple deposition of laser energy in the matter and we can develop forces and torques, after non-linear energetic excitation of the transparent matter by intense ultrashort laser light.

What one can imagine with a sub-picosecond laser available nowadays would also be realized more efficiently with a "true" femtosecond laser (pulse durations << 100 fs) appearing on the market. One should develop a few-cycle ultrafast pulses processing that may result in an "avalanche-free mode" for a more efficient and highly localized energy deposition, a more effective manipulation of spatial-temporal coupling and a better control of nanogratings seeding process. The time for a half period in the IR at a wavelength of 1 µm is 1.7fs. In that case, opposite charges can be more easily separated using appropriate pulse shaping. Ultimately, this will pave the way to materials science by few or single-cycle laser pulses. Future modeling would investigate which laser parameters are needed to develop forces and torques, mechanical fields that are large enough to imprint twisted inorganic glasses. These future works will boost our knowledge of non-linear action involving the interaction of intense and ultrashort laser light with matter. This new knowledge will apply to any structuring of dielectric materials to functionalize them, in integrated optics and more generally in solid-state chemistry.

Exploring vectorial aspects of light matter interaction processes

Light polarization is an effective parameter for controlling energy delivery in laser structuring of surfaces and volumes. The results reported over the last 20 years bring evidence of a polarization-impacted light-matter interaction process. One fascinating prospect is to combine the time and spatial distribution of light polarization, intensity, and phase inside a dielectric material. By doing so, it will become possible to efficiently control the non-linear force distribution and orientation in the excited solid state (e.g., the induced plasma) and, thus, the final effect in the matter, exerting thermo-mechanical actions. This is possible only for significantly high intensity and short pulse durations when electrons can be excited in delocalized states independently of the ionic motion.

The proposed ideas boil down to the following sentence: "match the processing tool (i.e. laser and its spatial-temporal shaping) to a given task". For instance, an exciting result would be to create complex nanogratings by combining several laser beams with different polarization states. Such laser beams, i.e., circularly polarized or optical vortices, can carry spin and orbital angular momentum (SAM and OAM). These experiments would help answering the early question of whether SAM and OAM are equivalent concerning light absorption or if a vortex beam can imprint chirality at the molecular level in materials. Among vector beams there are a class of solutions to the vector wave equation defined by a spatially varying direction of polarization e.g. cylindrical vector beams obey axial symmetry, such as radial and azimuthal polarization or generalized Poincaré beam, e.g., a coaxial superposition of two optical vortices. Vector beams are of interest because of their unique focusing properties, which allow a significant amount of control over the electric field shape near the focus, including the potential for tighter focusing than regular beams. As a result, we can develop novel birefringent optical elements and expand our knowledge on ultrafast laser beam focus control under tight focusing. For instance, a radially

polarized laser beam focused with a high NA objective will exhibit a longitudinal electric field, which could even accelerate charged particles while a hybrid Poincaré beam can create an orbital Hall effect and a longitudinal SAM component alternating its sign along radius [182]. These possibilities of focal spot polarization engineering can benefit both anisotropic circular/linear or nonlinear effects imprinting in glasses. Another example is Bessel beams, which already allow the fabrication of high aspect ratio structures. Indeed, fs imprinting can be explored to generate known laser beams such as Bessel, Hermite-Gaussian, and Laguerre-Gaussian modes and to enable not only the engineering of intensity but also of the polarization distribution at the focus and even along the focus [183] of the beam.

Exploring other glass systems and nanocrystals photo-precipitation

Nanogratings can be composed of nanopores or nanocrystals and amorphous phase separation. Compared to nanopores, nanocrystals pocess more properties, e.g., photoluminescence, high thermal stability, second harmonic generation, etc. For instance, the photoluminescence property of nanocrystals is useful in multi-dimensional information encoding and as microscale LEDs inside glass or solid. We also point out that crystallographic structure is controllable by acting on the electromagnetic field morphology in the beam focal volume focused inside a transparent glass. One can think about the photo-precipitation of chiral crystals from suitable glasses, where we expect to get racemic nanocrystal assemblies when the beam is axis-symmetric while getting enantiomeric excesses when the beam is not axis-symmetric. The latter may lead to the controlled generation of circular optical properties to develop passive optical isolators or alignment free optical rotators. At the same time, we expect the orientation of the induced optical properties to be controllable with the orientation of the vector properties of light (polarization, gradients of intensity and phase). Results in this direction will represent a step forward in understanding the non-linear interaction of light with glasses. In that way, we will abandon the classical view in elaboration chemistry that the laser is only an energy source for a new paradigm in which light can shape matter at the microscopic level in many ways and even at the molecular scale.

Towards applications

Besides the fundamental interest, the ability to control the optical phase, birefringence slow/fast axis and even to induce circular optical properties lead to the engineering of unique integrated optical devices with 3D spatially varying birefringence and refractive index changes. From this perspective, this 3D manufacturing technique allows the fabrication of compact and low-cost optical components in Vis and near-IR transparent materials like SiO_2 glasses. This has drawn attention to applications/fields, including birefringent optical devices, 3D geometric phase optics, optical data storage, microfluidic, structural health monitoring, and high-temperature sensing. However, intrinsic parameters (nanogratings period, rotation in 3D, nanoporosity, nanocrystals size/symmetry and their orientation) of femtosecond laser-induced modifications are still not fully controlled. An ongoing major problem is to quantitatively establish the role played by each laser parameters including spatiotemporal beam distortions. The ability to manipulate them would open possibilities for 3D engineering the optical properties of a given material. As a result, people will be able to develop reliable freeform phase optics or birefringent-based devices operating in a broad spectral range, including super-achromatic components, for applications ranging from polarimetry, spectroscopy, attosecond pulse generation, THz, imaging.

Additionally, recent works plan to extend these overall results in the UV range and towards the IR, i.e. mid-IR, using heavy oxide glass materials and later in the far IR using non-oxide glasses like fluorides and chalcogenides [184]. Indeed, in mid and far-IR instrumentation, there is a need for miniaturized, weight and low-cost optical systems for civil (domotics, smartphone, automobile, spatial) but also security and military applications (vehicle steering, survey, weapons guidance, unmasking, countermeasure identification). The constraints on the size and weight of optical systems are so demanding that traditional optical systems with a single optical axis are reaching their limits. Therefore, breakthroughs in optical design have been proposed to develop bio-inspired multichannel and multiaxis architectures and integrate multiple optical functions using planar optical components. In addition, the possibility of making 3D direct shaping using femtosecond lasers enlarges the panel of optical functions we could encode into a small device.

From Industry perspective

From the very beginning, the industrial community working in FLDW has strongly been influenced by the development of ultrafast laser systems, which are, in fact, the critical part of the ultrafast laser direct writing setup. For example, the initial demonstration of waveguides writing was implemented after introducing Ti: Sapphire laser systems with high operation stability. Thus, future trends in this field should also be determined by the evolution of femtosecond laser systems. We can already see that high average power femtosecond laser

systems operating at more than 100 W reached industrial-scale applications, where requirements are raised for quality and to increase the processing speed. Several commercial systems based on compact and reliable fiber lasers were introduced for two-photon polymerization and glass processing. The flexibility of this technique in terms of materials and its ability to implement 3D geometries with subwavelength precision turned into an ideal low-cost platform for rapid prototyping, which was explored in the fields of microfluidics and quantum optics. However, for unlocking industrial applications, implementing parallel processing or at least increasing the volumetric writing speed in ultrafast laser direct writing remains crucial. Commonly, even nJ laser pulses can modify the material under strong focusing or high repetition rate; however, conventional focusing techniques do not allow exploitation of the whole power capacity of a laser system. Adding adaptive optics elements or variants into the laser direct writing system has already demonstrated the potential of process parallelization (e.g. multi-focii), increasing writing speed (surface and volumetric) using extended beams (e.g. Bessel), and reducing production cost. Adequate spatial shaping (e.g. truncated Airy, truncated Bessel beams etc.), should also enhance the spatial uniformity of imprinted optical properties and reduce overall optical losses while temporal ones such as GHz burst machining can be used for enhancing writing speed.

Acknowledgments

We acknowledge the support of the SMIS beamline from synchrotron SOLEIL.

References

1. Gao, J.; Zhao, X.-J.; Yan, Z.; Fu, Y.; Qiu, J.; Wang, L.; Zhang, J. Multi-dimensional Shingled Optical Recording by Nanostructuring in Glass. *Adv. Funct. Mater.* **2024**, *34*, doi:10.1002/adfm.202306870.
2. Lei, Y.; Sakakura, M.; Wang, L.; Yu, Y.; Wang, H.; Shayeganrad, G.; Kazansky, P.G. High Speed Ultrafast Laser Anisotropic Nanostructuring by Energy Deposition Control via Near-Field Enhancement. *Optica* **2021**, *8*, 1365.
3. Piacentini, S.; Bragheri, F.; Corrielli, G.; Martínez Vázquez, R.; Paiè, P.; Osellame, R. Advanced Photonic and Optofluidic Devices Fabricated in Glass via Femtosecond Laser Micromachining [Invited]. *Opt. Mater. Express* **2022**, *12*, 3930.
4. Stoian, R. Volume Photoinscription of Glasses: Three-Dimensional Micro- and Nanostructuring with Ultrashort Laser Pulses. *Appl. Phys. A Mater. Sci. Process.* **2020**, *126*, doi:10.1007/s00339-020-03516-3.
5. Gattass, R.R.; Mazur, E. Femtosecond Laser Micromachining in Transparent Materials. *Nat. Photonics* **2008**, *2*, 219–225.
6. Qiu, J.; Miura, K.; Hirao, K. Femtosecond Laser-Induced Microfeatures in Glasses and Their Applications. *J. Non Cryst. Solids* **2008**, *354*, 1100–1111.
7. Itoh, K.; Watanabe, W.; Nolte, S.; Schaffer, C.B. Ultrafast Processes for Bulk Modification of Transparent Materials. *MRS Bull.* **2006**, *31*, 620–625.
8. Stoian, R.; Colombier, J.-P. Advances in Ultrafast Laser Structuring of Materials at the Nanoscale. *Nanophotonics* **2020**, *9*, 4665–4688.
9. Gao, L.; Zhang, Q.; Gu, M. Femtosecond Laser Micro/Nano Processing: From Fundamental to Applications. *Int. J. Extrem. Manuf.* **2025**, *7*, 022010.
10. Mao, S.S.; Quéré, F.; Guizard, S.; Mao, X.; Russo, R.E.; Petite, G.; Martin, P. Dynamics of Femtosecond Laser Interactions with Dielectrics. *Appl. Phys. A Mater. Sci. Process.* **2004**, *79*, 1695–1709.
11. Keldysh, L.V. Ionization in the Field of a Strong Electromagnetic Wave. In *Selected Papers of Leonid V Keldysh*; World scientific, 2023; pp. 56–63 ISBN 9789811279454.
12. Couairon, A.; Mysyrowicz, A. Femtosecond Filamentation in Transparent Media. *Phys. Rep.* **2007**, *441*, 47–189.
13. Couairon, A.; Sudrie, L.; Franco, M.; Prade, B.; Mysyrowicz, A. Filamentation and Damage in Fused Silica Induced by Tightly Focused Femtosecond Laser Pulses. *Phys. Rev. B Condens. Matter Mater. Phys.* **2005**, *71*, doi:10.1103/physrevb.71.125435.
14. Schaffer, C.B.; Brodeur, A.; Mazur, E. Laser-Induced Breakdown and Damage in Bulk Transparent Materials Induced by Tightly Focused Femtosecond Laser Pulses. *Meas. Sci. Technol.* **2001**, *12*, 1784–1794.
15. Yoshino, T.; Ozeki, Y.; Matsumoto, M.; Itoh, K. In Situ Micro-Raman Investigation of Spatio-Temporal Evolution of Heat in Ultrafast Laser Microprocessing of Glass. *Jpn. J. Appl. Phys. (2008)* **2012**, *51*, 102403.
16. Koritsoglou, O.; Duchateau, G.; Utéza, O.; Mouskeftaras, A. Quantitative Assessment of Femtosecond Laser-Induced Stress Waves in Fused Silica. *Phys. Rev. B.* **2024**, *110*, doi:10.1103/physrevb.110.054112.
17. Rudenko, A.; Moloney, J.V.; Polynkin, P. Ionization Clamping in Ultrafast Optical Breakdown of Transparent Solids. *Phys. Rev. Appl.* **2023**, *20*, 064035.

18. Mishchik, K.; D'Amico, C.; Velpula, P.K.; Mauclair, C.; Boukenter, A.; Ouerdane, Y.; Stoian, R. Ultrafast Laser Induced Electronic and Structural Modifications in Bulk Fused Silica. *J. Appl. Phys.* **2013**, *114*, 133502.
19. Gräf, S.; Kunz, C.; Müller, F.A. Formation and Properties of Laser-Induced Periodic Surface Structures on Different Glasses. *Materials* **2017**, *10*, 933.
20. Bonse, J. Quo Vadis LIPSS?-Recent and Future Trends on Laser-Induced Periodic Surface Structures. *Nanomaterials* **2020**, *10*, 1950.
21. Bonse, J.; Gräf, S. Ten Open Questions about Laser-Induced Periodic Surface Structures. *Nanomaterials* **2021**, *11*, 3326.
22. Bonse, J.; Krüger, J.; Höhm, S.; Rosenfeld, A. Femtosecond Laser-Induced Periodic Surface Structures. *J. Laser Appl.* **2012**, *24*, 042006.
23. Bonse, J.; Hohm, S.; Kirner, S.V.; Rosenfeld, A.; Kruger, J. Laser-Induced Periodic Surface Structures— A Scientific Evergreen. *IEEE J. Sel. Top. Quantum Electron.* **May-June 2017**, *23*, doi:10.1109/jstqe.2016.2614183.
24. Tan, D.; Sharafudeen, K.N.; Yue, Y.; Qiu, J. Femtosecond Laser Induced Phenomena in Transparent Solid Materials: Fundamentals and Applications. *Prog. Mater. Sci.* **2016**, *76*, 154–228.
25. Poumellec, B.; Lancry, M.; Chahid-Erraji, A.; Kazansky, P.G. Modification Thresholds in Femtosecond Laser Processing of Pure Silica: Review of Dependencies on Laser Parameters [Invited]. *Opt. Mater. Express* **2011**, *1*, 766.
26. Yao, H.; Xie, Q.; Cavillon, M.; Dai, Y.; Lancry, M. Materials Roadmap for Inscription of Nanogratings inside Transparent Dielectrics Using Ultrafast Lasers. *Prog. Mater. Sci.* **2024**, *142*, 101226.
27. Davis, K.M.; Miura, K.; Sugimoto, N.; Hirao, K. Writing Waveguides in Glass with a Femtosecond Laser. *Opt. Lett.* **1996**, *21*, 1729–1731.
28. Glezer, E.N.; Milosavljevic, M.; Huang, L.; Finlay, R.J.; Her, T.H.; Callan, J.P.; Mazur, E. Three-Dimensional Optical Storage inside Transparent Materials. *Opt. Lett.* **1996**, *21*, 2023–2025.
29. Miura, K.; Qiu, J.; Mitsuyu, T.; Hirao, K. Space-Selective Growth of Frequency-Conversion Crystals in Glasses with Ultrashort Infrared Laser Pulses. *Opt. Lett.* **2000**, *25*, 408–410.
30. Shimotsuma, Y.; Kazansky, P.G.; Qiu, J.; Hirao, K. Self-Organized Nanogratings in Glass Irradiated by Ultrashort Light Pulses. *Phys. Rev. Lett.* **2003**, *91*, 247405.
31. Dai, Y.; Ma, H.; Lu, B.; Yu, B.; Zhu, B.; Qiu, J. Femtosecond Laser-Induced Oriented Precipitation of Ba2TiGe2O8 Crystals in Glass. *Opt. Express* **2008**, *16*, 3912–3917.
32. Cao, J.; Mazerolles, L.; Lancry, M.; Brisset, F.; Poumellec, B. Modifications in Lithium Niobium Silicate Glass by Femtosecond Laser Direct Writing: Morphology, Crystallization, and Nanostructure. *J. Opt. Soc. Am. B* **2017**, *34*, 160.
33. Sakakura, M.; Lei, Y.; Wang, L.; Yu, Y.-H.; Kazansky, P.G. Ultralow-Loss Geometric Phase and Polarization Shaping by Ultrafast Laser Writing in Silica Glass. *Light Sci. Appl.* **2020**, *9*, 15.
34. Li, P.; Yan, Z.; Wang, L.; Xu, Y.; Lu, P.; Zhang, J. Advanced Transparent Glass-ceramics via Laser Anisotropic Nanocrystallization. *Laser Photon. Rev.* **2024**, *18*, doi:10.1002/lpor.202301403.
35. Miura, K.; Qiu, J.; Inouye, H.; Mitsuyu, T.; Hirao, K. Photowritten Optical Waveguides in Various Glasses with Ultrashort Pulse Laser. *Appl. Phys. Lett.* **1997**, *71*, 3329–3331.
36. Grobnic, D.; Smelser, C.W.; Mihailov, S.J.; Walker, R.B. Long-Term Thermal Stability Tests at 1000 °C of Silica Fibre Bragg Gratings Made with Ultrafast Laser Radiation. *Meas. Sci. Technol.* **2006**, *17*, 1009–1013.
37. Royon, M.; Marin, E.; Girard, S.; Boukenter, A.; Ouerdane, Y.; Stoian, R. X-Ray Preconditioning for Enhancing Refractive Index Contrast in Femtosecond Laser Photoinscription of Embedded Waveguides in Pure Silica. *Opt. Mater. Express* **2019**, *9*, 65.
38. Lancry, M.; Poumellec, B. UV Laser Processing and Multiphoton Absorption Processes in Optical Telecommunication Fiber Materials. *Phys. Rep.* **2013**, *523*, 207–229.
39. Fernandez, T.T.; Johnston, B.; Mahmodi, H.; Privat, K.; Kabakova, I.; Gross, S.; Withford, M.; Fuerbach, A. Thermally Stable High Numerical Aperture Integrated Waveguides and Couplers for the 3 μm Wavelength Range. *APL Photonics* **2022**, *7*, 126106.
40. Eaton, S.M.; Ng, M.L.; Osellame, R.; Herman, P.R. High Refractive Index Contrast in Fused Silica Waveguides by Tightly Focused, High-Repetition Rate Femtosecond Laser. *J. Non Cryst. Solids* **2011**, *357*, 2387–2391.
41. Dias, A.; Muñoz, F.; Alvarez, A.; Moreno-Zárate, P.; Atienzar, J.; Urbieta, A.; Fernandez, P.; Pardo, M.; Serna, R.; Solis, J. Femtosecond Laser Writing of Photonic Devices in Borate Glasses Compositionally Designed to Be Laser Writable. *Opt. Lett.* **2018**, *43*, 2523–2526.

42. Macias-Montero, M.; Moreno-Zárate, P.; Muñoz, F.; Sotillo, B.; Garcia-Pardo, M.; Serna, R.; Fernandez, P.; Solis, J. Competition Effects during Femtosecond Laser Induced Element Redistribution in Ba- and La-Migration Based Laser Written Waveguides. *Materials* **2021**, *14*, 3185.
43. Hirao, K.; Miura, K. Writing Waveguides and Gratings in Silica and Related Materials by a Femtosecond Laser. *J. Non Cryst. Solids* **1998**, *239*, 91–95.
44. Streltsov, A.M.; Borrelli, N.F. Study of Femtosecond-Laser-Written Waveguides in Glasses. *J. Opt. Soc. Am. B* **2002**, *19*, 2496–2504.
45. Saliminia, A.; Vallée, R.; Chin, S.L. Waveguide Writing in Silica Glass with Femtosecond Pulses from an Optical Parametric Amplifier at 1.5µm. *Opt. Commun.* **2005**, *256*, 422–427.
46. Dekker, P.; Ams, M.; Marshall, G.D.; Little, D.J.; Withford, M.J. Annealing Dynamics of Waveguide Bragg Gratings: Evidence of Femtosecond Laser Induced Colour Centres. *Opt. Express* **2010**, *18*, 3274–3283.
47. Saliminia, A.; Vallée, R.; Chin, S.L. Waveguide Writing in Silica Glass with Femtosecond Pulses from an Optical Parametric Amplifier at 1.5um. *Optics Communications* **2005**, *256*, 422–427.
48. Chan, J.W.; Huser, T.R.; Risbud, S.H.; Krol, D.M. Modification of the Fused Silica Glass Network Associated with Waveguide Fabrication Using Femtosecond Laser Pulses. *Appl. Phys. A Mater. Sci. Process.* **2003**, *76*, 367–372.
49. Beresna, M.; Gecevičius, M.; Lancry, M.; Poumellec, B.; Kazansky, P.G. Broadband Anisotropy of Femtosecond Laser Induced Nanogratings in Fused Silica. *Appl. Phys. Lett.* **2013**, *103*, 131903.
50. Royon, M. Ingénierie de Verres de Silice : Influence de Pré-Traitements Sur La Variation d'indice de Réfraction de Guides d'ondes Photo-Inscrits Par Laser Femtoseconde, Université Jean Monnet: Lyon, 2018.
51. Bressel, L.; de Ligny, D.; Sonneville, C.; Martinez, V.; Mizeikis, V.; Buividas, R.; Juodkazis, S. Femtosecond Laser Induced Density Changes in GeO_2 and SiO_2 Glasses: Fictive Temperature Effect [Invited]. *Opt. Mater. Express* **2011**, *1*, 605.
52. Chan, J.W.; Huser, T.; Risbud, S.; Krol, D.M. Structural Changes in Fused Silica after Exposure to Focused Femtosecond Laser Pulses. *Opt. Lett.* **2001**, *26*, 1726–1728.
53. Bellouard, Y.; Barthel, E.; Said, A.A.; Dugan, M.; Bado, P. Scanning Thermal Microscopy and Raman Analysis of Bulk Fused Silica Exposed to Lowenergy Femtosecond Laser Pulses. *Opt. Express* **2008**, *16*, 19520.
54. Tan, C.Z.; Arndt, J.; Xie, H.S. Optical Properties of Densified Silica Glasses. *Physica B Condens. Matter* **1998**, *252*, 28–33.
55. Lancry, M.; Régnier, E.; Poumellec, B. Fictive Temperature in Silica-Based Glasses and Its Application to Optical Fiber Manufacturing. *Prog. Mater. Sci.* **2012**, *57*, 63–94.
56. Kawamura, K.-I.; Sarukura, N.; Hirano, M.; Hosono, H. Holographic Encoding of Fine-Pitched Micrograting Structures in Amorphous SiO2 Thin Films on Silicon by a Single Femtosecond Laser Pulse. *Appl. Phys. Lett.* **2001**, *78*, 1038–1040.
57. Bhardwaj, V.R.; Corkum, P.B.; Rayner, D.M.; Hnatovsky, C.; Simova, E.; Taylor, R.S. Stress in Femtosecond-Laser-Written Waveguides in Fused Silica. *Opt. Lett.* **2004**, *29*, 1312–1314.
58. Poumellec, B.; Sudrie, L.; Franco, M.; Prade, B.; Mysyrowicz, A. Femtosecond Laser Irradiation Stress Induced in Pure Silica. *Opt. Express* **2003**, *11*, 1070–1079.
59. Bellouard, Y.; Champion, A.; McMillen, B.; Mukherjee, S.; Thomson, R.R.; Pépin, C.; Gillet, P.; Cheng, Y. Stress-State Manipulation in Fused Silica via Femtosecond Laser Irradiation. *Optica* **2016**, *3*, 1285.
60. Bellouard, Y.; Colomb, T.; Depeursinge, C.; Dugan, M.; Said, A.A.; Bado, P. Nanoindentation and Birefringence Measurements on Fused Silica Specimen Exposed to Low-Energy Femtosecond Pulses. *Opt. Express* **2006**, *14*, 8360–8366.
61. Vlugter, P.; Block, E.; Bellouard, Y. Local Tuning of Fused Silica Thermal Expansion Coefficient Using Femtosecond Laser. *Phys. Rev. Mater.* **2019**, *3*, doi:10.1103/physrevmaterials.3.053802.
62. Eaton, S.; Zhang, H.; Herman, P.; Yoshino, F.; Shah, L.; Bovatsek, J.; Arai, A. Heat Accumulation Effects in Femtosecond Laser-Written Waveguides with Variable Repetition Rate. *Opt. Express* **2005**, *13*, 4708–4716.
63. Lancry, M.; Poumellec, B.; Chahid-Erraji, A.; Beresna, M.; Kazansky, P.G. Dependence of the Femtosecond Laser Refractive Index Change Thresholds on the Chemical Composition of Doped-Silica Glasses. *Opt. Mater. Express* **2011**, *1*, 711.
64. Lancry, M.; Poumellec, B.; Chahid-Erraji, A.; Beresna, M.; Kazansky, P.G. Dependence of the Femtosecond Laser Refractive Index Change Thresholds on the Chemical Composition of Doped-Silica Glasses. *Opt. Mater. Express* **2011**, *1*, 711–723.
65. Brückner, R. Properties and Structure of Vitreous Silica. I. *J. Non Cryst. Solids* **1970**, *5*, 123–175.

66. Kazansky, P.G.; Inouye, H.; Mitsuyu, T.; Miura, K.; Qiu, J.; Hirao, K.; Starrost, F. Anomalous Anisotropic Light Scattering in Ge-Doped Silica Glass. *Phys. Rev. Lett.* **1999**, *82*, 2199–2202.
67. Bricchi, E.; Mills, J.D.; Kazansky, P.G.; Klappauf, B.G.; Baumberg, J.J. Birefringent Fresnel Zone Plates in Silica Fabricated by Femtosecond Laser Machining. *Opt. Lett.* **2002**, *27*, 2200–2202.
68. Champion, A.; Beresna, M.; Kazansky, P.; Bellouard, Y. Stress Distribution around Femtosecond Laser Affected Zones: Effect of Nanogratings Orientation. *Opt. Express* **2013**, *21*, 24942–24951.
69. McMillen, B.; Athanasiou, C.; Bellouard, Y. Femtosecond Laser Direct-Write Waveplates Based on Stress-Induced Birefringence. *Opt. Express* **2016**, *24*, 27239–27252.
70. Tian, J.; Yao, H.; Cavillon, M.; Garcia-Caurel, E.; Ossikovski, R.; Stchakovsky, M.; Eypert, C.; Poumellec, B.; Lancry, M. A Comparison between Nanogratings-Based and Stress-Engineered Waveplates Written by Femtosecond Laser in Silica. *Micromachines* **2020**, *11*, 131.
71. Bricchi, E.; Klappauf, B.G.; Kazansky, P.G. Form Birefringence and Negative Index Change Created by Femtosecond Direct Writing in Transparent Materials. *Opt. Lett.* **2004**, *29*, 119–121.
72. Zhang, J.; Gecevičius, M.; Beresna, M.; Kazansky, P.G. Seemingly Unlimited Lifetime Data Storage in Nanostructured Glass. *Phys. Rev. Lett.* **2014**, *112*, 033901.
73. Bricchi, E.; Kazansky, P.G. Extraordinary Stability of Anisotropic Femtosecond Direct-Written Structures Embedded in Silica Glass. *Appl. Phys. Lett.* **2006**, *88*, 111119.
74. Wang, Y.; Lancry, M.; Cavillon, M.; Poumellec, B. Lifetime Prediction of Nanogratings Inscribed by a Femtosecond Laser in Silica Glass. *Opt. Lett.* **2022**, *47*, 1242–1245.
75. Sudrie, L.; Franco, M.; Prade, B.; Mysyrowicz, A. Writing of Permanent Birefringent Microlayers in Bulk Fused Silica with Femtosecond Laser Pulses. *Opt. Commun.* **1999**, *171*, 279–284.
76. Xie, Q.; Shchedrina, N.; Cavillon, M.; Poumellec, B.; Lancry, M. Nanoscale Investigations of Femtosecond Laser Induced Nanogratings in Optical Glasses 2023.
77. Lancry, M.; Poumellec, B.; Canning, J.; Cook, K.; Poulin, J.-C.; Brisset, F. Ultrafast Nanoporous Silica Formation Driven by Femtosecond Laser Irradiation. *Laser Photon. Rev.* **2013**, *7*, 953–962.
78. Champion, A.; Bellouard, Y. Direct Volume Variation Measurements in Fused Silica Specimens Exposed to Femtosecond Laser. *Opt. Mater. Express* **2012**, *2*, 789.
79. Wang, Y.; Cavillon, M.; Ollier, N.; Poumellec, B.; Lancry, M. An Overview of the Thermal Erasure Mechanisms of Femtosecond Laser-induced Nanogratings in Silica Glass. *Phys. Status Solidi (A)* **2021**, *218*, 2100023.
80. Shchedrina, N.; Nemeth, G.; Borondics, F.; Ollier, N.; Lancry, M. Nano-FTIR Spectroscopy Reveals SiO2 Densification within Fs-Laser Induced Nanogratings. *Nanoscale Adv.* **2024**, *6*, 5164–5170.
81. Richter, S.; Jia, F.; Heinrich, M.; Döring, S.; Peschel, U.; Tünnermann, A.; Nolte, S. The Role of Self-Trapped Excitons and Defects in the Formation of Nanogratings in Fused Silica. *Opt. Lett.* **2012**, *37*, 482–484.
82. Taylor, R.; Hnatovsky, C.; Simova, E. Applications of Femtosecond Laser Induced Self-Organized Planar Nanocracks inside Fused Silica Glass. *Laser Photon. Rev.* **2008**, *2*, 26–46.
83. Lei, Y.; Shayeganrad, G.; Wang, H.; Sakakura, M.; Yu, Y.; Wang, L.; Kliukin, D.; Skuja, L.; Svirko, Y.; Kazansky, P.G. Efficient Ultrafast Laser Writing with Elliptical Polarization. *Light Sci. Appl.* **2023**, *12*, 74.
84. Shchedrina, N.; Cavillon, M.; Ari, J.; Ollier, N.; Lancry, M. Impact of Glass Free Volume on Femtosecond Laser-Written Nanograting Formation in Silica Glass. *Materials* **2024**, *17*, 502.
85. Buschlinger, R.; Nolte, S.; Peschel, U. Self-Organized Pattern Formation in Laser-Induced Multiphoton Ionization. *Phys. Rev. B Condens. Matter Mater. Phys.* **2014**, *89*, doi:10.1103/physrevb.89.184306.
86. Rudenko, A.; Colombier, J.-P.; Itina, T.E. From Random Inhomogeneities to Periodic Nanostructures Induced in Bulk Silica by Ultrashort Laser. *Phys. Rev. B.* **2016**, *93*, doi:10.1103/physrevb.93.075427.
87. Rudenko, A.; Colombier, J.-P.; Itina, T.E.; Stoian, R. Genesis of Nanogratings in Silica Bulk via Multipulse Interplay of Ultrafast Photo-excitation and Hydrodynamics. *Adv. Opt. Mater.* **2021**, *9*, 2100973.
88. Rudenko, A.; Colombier, J.-P.; Itina, T. Nanopore-Mediated Ultrashort Laser-Induced Formation and Erasure of Volume Nanogratings in Glass. *Phys. Chem. Chem. Phys.* **2018**, *20*, 5887–5899.
89. Poumellec, B.; Cavillon, M.; Lancry, M. Electrostatic Interpretation of Phase Separation Induced by Femtosecond Laser Light in Glass. *Crystals* **2023**, *13*, 393.
90. Xie, Q.; Cavillon, M.; Poumellec, B.; Lancry, M. Upper Temperature Limit for Nanograting Survival in Oxide Glasses: Publisher's Note. *Appl. Opt.* **2023**, *62*, 7156.
91. Xie, Q.; Cavillon, M.; Lancry, M. Modeling Nanogratings Erasure at High Repetition Rate in Commercial Optical Glasses. *Ceram. Int.* **2024**, doi:10.1016/j.ceramint.2024.09.257.
92. Zoubir, A.; Rivero, C.; Grodsky, R.; Richardson, K.; Richardson, M.; Cardinal, T.; Couzi, M. Laser-Induced Defects in Fused Silica by Femtosecond IR Irradiation. *Phys. Rev. B Condens. Matter Mater. Phys.* **2006**, *73*, doi:10.1103/physrevb.73.224117.

93. Saeta, P.N.; Greene, B.I. Primary Relaxation Processes at the Band Edge of SiO 2. *Physical review letters* **1993**, *70*.
94. Martinez, A.; Khrushchev, I.Y.; Bennion, I. Thermal Properties of Fibre Bragg Gratings Inscribed Point-by-Point by Infrared Femtosecond Laser. *Electron. Lett.* **2005**, *41*, 176–178.
95. Wang, Y.; Cavillon, M.; Ollier, N.; Poumellec, B.; Lancry, M. An Overview of the Thermal Erasure Mechanisms of Femtosecond Laser-Induced Nanogratings in Silica Glass". *Physica status solidi* **2021**.
96. Witcher, J.J.; Reichman, W.J.; Fletcher, L.B.; Troy, N.W.; Krol, D.M. Thermal Annealing of Femtosecond Laser Written Structures in Silica Glass. *Opt. Mater. Express* **2013**, *3*, 502.
97. Radhakrishnan, A.; Gateau, J.; Vlugter, P.; Bellouard, Y. Femtosecond Laser-Shockwave Induced Densification in Fused Silica. *Opt. Mater. Express* **2022**, *12*, 2886.
98. Ollier, N.; Lancry, M.; Martinet, C.; Martinez, V.; Le Floch, S.; Neuville, D. Relaxation Study of Pre-Densified Silica Glasses under 2.5 MeV Electron Irradiation". *Scientific Reports* **2019**, *9*.
99. Shchedrina, N.; Allaoui, R.; Sosa, M.; Nemeth, G.; Borondics, F.; Ollier, N.; Lancry, M. The Effect of Combining Femtosecond Laser and Electron Irradiation on Silica Glass. *Nanomaterials* **2024**, *14*, 1909.
100. Vlugter, P.; Bellouard, Y. Elastic Properties of Self-Organized Nanogratings Produced by Femtosecond Laser Exposure of Fused Silica. *Phys. Rev. Mater.* **2020**, *4*, doi:10.1103/physrevmaterials.4.023607.
101. Vlugter, P.; Bellouard, Y. Abnormal Temperature Dependent Elastic Properties of Fused Silica Irradiated by Ultrafast Lasers. *Phys. Rev. Mater.* **2022**, *6*, doi:10.1103/physrevmaterials.6.033602.
102. Gaillard, Y.; Radhakrishnan, A.; Bellouard, Y.; Amiot, F. Sub-Micron Elastic Properties Measurement of Single Laser-Affected Volume in Fused Silica. *J. Non Cryst. Solids* **2025**, *652*, 123399.
103. Lu, J.; Tian, J.; Poumellec, B.; Garcia-Caurel, E.; Ossikovski, R.; Zeng, X.; Lancry, M. Tailoring Chiral Optical Properties by Femtosecond Laser Direct Writing in Silica. *Light Sci. Appl.* **2023**, *12*, 46.
104. Lu, J.; Garcia-Caurel, E.; Ossikovski, R.; Courvoisier, F.; Zeng, X.; Poumellec, B.; Lancry, M. Femtosecond Laser Direct Writing Multilayer Chiral Waveplates with Minimal Linear Birefringence. *Opt. Lett.* **2023**, *48*, 271–274.
105. Yao, H.; Pugliese, D.; Lancry, M.; Dai, Y. Ultrafast Laser Direct Writing Nanogratings and Their Engineering in Transparent Materials. *Laser Photon. Rev.* **2024**, *18*, doi:10.1002/lpor.202300891.
106. Schaffer, C.B.; Brodeur, A.; Nishimura, N.; Mazur, E. Laser-Induced Microexplosions in Transparent Materials: Microstructuring with Nanojoules. In Proceedings of the Commercial and Biomedical Applications of Ultrafast Lasers; Reed, M.K., Neev, J., Eds.; SPIE, June 4 1999.
107. Varkentina, N.; Dussauze, M.; Royon, A.; Ramme, M.; Petit, Y.; Canioni, L. High Repetition Rate Femtosecond Laser Irradiation of Fused Silica Studied by Raman Spectroscopy. *Opt. Mater. Express* **2016**, *6*, 79–90.
108. Watanabe, W.; Toma, T.; Yamada, K.; Nishii, J.; Hayashi, K.; Itoh, K. Optical Seizing and Merging of Voids in Silica Glass with Infrared Femtosecond Laser Pulses. *Opt. Lett.* **2000**, *25*, 1669–1671.
109. Datta, S.; Clady, R.; Grojo, D.; Utéza, O.; Sanner, N. Scalable Nanophotonic Structures inside Silica Glass Laser-machined by Intense Shaped Beams. *Laser Photon. Rev.* **2024**, *18*, doi:10.1002/lpor.202301365.
110. Sosa, M.; Cavillon, M.; Blanchet, T.; Nemeth, G.; Borondics, F.; Laffont, G.; Lancry, M. Micro-to-Nanoscale Characterization of Femtosecond Laser Photo-Inscribed Microvoids. *Nanomaterials* **2024**, *14*, 1228.
111. Lerner, A.; Blanchet, T.; Cotillard, R.; Sosa, M.; Roussel, N.; Bouwmans, G.; Laffont, G. High Temperature Annealing Behavior of Femtosecond Written FBGs in Ge-Doped Fused Silica Optical Fibers. In Proceedings of the European Workshop on Optical Fibre Sensors (EWOFS 2023); Wuilpart, M., Caucheteur, C., Eds.; SPIE, May 23 2023; p. 61.
112. Marshall, G.D.; Withford, M.J. Annealing Properties of Femtosecond Laser Inscribed Point-by-Point Fiber Bragg Gratings. In Proceedings of the Bragg Gratings, Photosensitivity, and Poling in Glass Waveguides; OSA: Washington, D.C., 2007.
113. Bressel, L.; De Ligny, D.; Sonneville, C.; Martinez, V.; Mizeikis, V.; Buividas, R.; Juodkazis, S. Femtosecond Laser Induced Density Changes in GeO2 and SiO2 Glasses: Fictive Temperature Effect. *Opt. Mater. Expres*.
114. Martinez, A.; Dubov, M.; Khrushchev, I. Bennion, I. Photoinduced Modifications in Fiber Gratings Inscribed Directly by Infrared Femtosecond Irradiation. *IEEE Photonics Technol*.
115. Fleischer, R.L.; Price, P.B.; Walker, R.M. Solid-State Track Detectors: Applications to Nuclear Science and Geophysics. *Annu. Rev. Nucl. Sci.* **1965**, *15*, 1–28.
116. Gamaly, E.G.; Juodkazis, S.; Nishimura, K.; Misawa, H.; Luther-Davies, B.; Hallo, L.; Nicolai, P.; Tikhonchuk, V.T. Laser-Matter Interaction in the Bulk of a Transparent Solid: Confined Microexplosion and Void Formation. *Phys. Rev. B Condens. Matter Mater. Phys.* **2006**, *73*, doi:10.1103/physrevb.73.214101.

117. Stoian, R.; Mishchik, K.; Cheng, G.; Mauclair, C.; D'Amico, C.; Colombier, J.P.; Zamfirescu, M. Investigation and Control of Ultrafast Laser-Induced Isotropic and Anisotropic Nanoscale-Modulated Index Patterns in Bulk Fused Silica. *Opt. Mater. Express* **2013**, *3*, 1755.
118. Glezer, E.N.; Mazur, E. Ultrafast-Laser Driven Micro-Explosions in Transparent Materials. *Appl. Phys. Lett.* **1997**, *71*, 882–884.
119. Juodkazis, S.; Misawa, H.; Hashimoto, T.; Gamaly, E.G.; Luther-Davies, B. Laser-Induced Microexplosion Confined in a Bulk of Silica: Formation of Nanovoids. *Appl. Phys. Lett.* **2006**, *88*, 201909.
120. Mermillod-Blondin, A.; Bonse, J.; Rosenfeld, A.; Hertel, I.V.; Meshcheryakov, Y.P.; Bulgakova, N.M.; Audouard, E.; Stoian, R. Dynamics of Femtosecond Laser Induced Voidlike Structures in Fused Silica. *Appl. Phys. Lett.* **2009**, *94*, 041911.
121. Hashimoto, T.; Juodkazis, S.; Misawa, H. Void Formation in Glasses. *New J. Phys.* **2007**, *9*, 253–253.
122. Wang, H.; Lei, Y.; Shayeganrad, G.; Svirko, Y.; Kazansky, P.G. Increasing Efficiency of Ultrafast Laser Writing via Nonlocality of Light-matter Interaction. *Laser Photon. Rev.* **2024**, *18*, doi:10.1002/lpor.202301143.
123. Lei, Y.; Wang, H.; Shayeganrad, G.; Svirko, Y.; Kazansky, P.G. Controlling Ultrafast Laser Writing in Silica Glass by Pulse Temporal Contrast. *Opt. Lett.* **2024**, *49*, 2385–2388.
124. Wang, H.; Lei, Y.; Wang, L.; Sakakura, M.; Yu, Y.; Shayeganrad, G.; Kazansky, P.G. 100-layer Error-free 5D Optical Data Storage by Ultrafast Laser Nanostructuring in Glass. *Laser Photon. Rev.* **2022**, *16*, 2100563.
125. Lei, Y.; Wang, H.; Skuja, L.; Kühn, B.; Franz, B.; Svirko, Y.; Kazansky, P.G. Ultrafast Laser Writing in Different Types of Silica Glass. *Laser Photon. Rev.* **2023**, *17*, 2200978.
126. Li, X.; Xie, W. Efficient Ultrafast Laser Writing with Appropriate Polarization. *Light Sci. Appl.* **2023**, *12*, 112.
127. Shayeganrad, G.; Chang, X.; Wang, H.; Deng, C.; Lei, Y.; Kazansky, P.G. High Damage Threshold Birefringent Elements Produced by Ultrafast Laser Nanostructuring in Silica Glass. *Opt. Express* **2022**, *30*, 41002–41011.
128. Anderson, P.; Aranas, E.B.; Assaf, Y.; Behrendt, R.; Black, R.; Caballero, M.; Cameron, P.; Canakci, B.; De Carvalho, T.; Chatzieleftheriou, A.; et al. Project Silica: Towards Sustainable Cloud Archival Storage in Glass. In Proceedings of the Proceedings of the 29th Symposium on Operating Systems Principles; ACM: New York, NY, USA, October 23 2023.
129. Fernandez, T.T.; Sakakura, M.; Eaton, S.M.; Sotillo, B.; Siegel, J.; Solis, J.; Shimotsuma, Y.; Miura, K. Bespoke Photonic Devices Using Ultrafast Laser Driven Ion Migration in Glasses. *Prog. Mater. Sci.* **2018**, *94*, 68–113.
130. Komatsu, T. Design and Control of Crystallization in Oxide Glasses. *J. Non Cryst. Solids* **2015**, *428*, 156–175.
131. Komatsu, T.; Honma, T. Laser Patterning and Growth Mechanism of Orientation Designed Crystals in Oxide Glasses: A Review. *J. Solid State Chem.* **2019**, *275*, 210–222.
132. Veenhuizen, K.; McAnany, S.; Nolan, D.; Aitken, B.; Dierolf, V.; Jain, H. Fabrication of Graded Index Single Crystal in Glass. *Sci. Rep.* **2017**, *7*, 44327.
133. Fernandez, T.T.; Gross, S.; Privat, K.; Johnston, B.; Withford, M. Designer Glasses—Future of Photonic Device Platforms. *Adv. Funct. Mater.* **2022**, *32*, 2103103.
134. Cao, J.; Poumellec, B.; Brisset, F.; Helbert, A.-L.; Lancry, M. Tunable Angular-Dependent Second-Harmonic Generation in Glass by Controlling Femtosecond Laser Polarization. *J. Opt. Soc. Am. B* **2016**, *33*, 741–747.
135. Cao, J.; Lancry, M.; Brisset, F.; Mazerolles, L.; Saint-Martin, R.; Poumellec, B. Femtosecond Laser-Induced Crystallization in Glasses: Growth Dynamics for Orientable Nanostructure and Nanocrystallization. *Cryst. Growth Des.* **2019**, *19*, 2189–2205.
136. Que, R.; Lancry, M.; Cavillon, M.; Poumellec, B. How to Crystallize Glass with a Femtosecond Laser. *Crystals* **2024**, *14*, 606.
137. Nishida, Y.; Shimizu, M.; Okuno, T.; Matsuoka, J.; Shimotsuma, Y.; Miura, K. Ultra-High Temperature Soret Effect in a Silicate Melt: SiO2 Migration to Cold Side. *arXiv [physics.chem-ph]* 2023.
138. Macias-Montero, M.; Muñoz, F.; Sotillo, B.; Del Hoyo, J.; Ariza, R.; Fernandez, P.; Siegel, J.; Solis, J. Femtosecond Laser Induced Thermophoretic Writing of Waveguides in Silicate Glass. *Sci. Rep.* **2021**, *11*, 8390.
139. Mcmillen, B.W. Ultrafast Laser Fabrication of Waveguides in Glasses and Crystalline Materials, University of Pittsburgh, 2012.
140. Le Coq, D.; Carcreff, J.; Masselin, P. Direct Femtosecond Laser Writing of Low-Loss Waveguides in Chalcogenide Glasses for Mid-Infrared Applications. In Proceedings of the SPIE Micro + Nano Materials, Devices, and Applications 2019; Simpson, M.C., Juodkazis, S., Eds.; SPIE, December 31 2019.
141. Choi, J.; Schwarz, C. Advances in Femtosecond Laser Processing of Optical Material for Device Applications. *Int. J. Appl. Glass Sci.* **2020**, *11*, 480–490.

142. Yang, W.; Corbari, C.; Kazansky, P.G.; Sakaguchi, K. Fabrication of Photonic Devices in Heavy Metal Oxide Glass by Femtosecond Laser Direct Writing. In Proceedings of the 2007 European Conference on Lasers and Electro-Optics and the International Quantum Electronics Conference; IEEE, June 2007.
143. Nazabal, V.; Adam, J.-L.; B. Bureau; Colas, F.; Rinnert, E.; De la Chapelle, M.L.; Toury, T.; Michel, K.; Compere, C.; Marre, S.; et al. Chalcogenide Glasses for Mid-IR Photonic Applications. In Proceedings of the 2014 IEEE Photonics Society Summer Topical Meeting Series; IEEE, July 2014.
144. Eggleton, B.J.; Luther-Davies, B.; Richardson, K. Chalcogenide Photonics. *Nat. Photonics* **2011**, *5*, 141–148.
145. Bruno Bureau; Boussard, C.; Cui, S.; Chahal, R.; Anne, M.L.; Nazabal, V.; Sire, O.; Loréal, O.; Lucas, P.; Monbet, V.; et al. Chalcogenide Optical Fibers for Mid-Infrared Sensing. *Opt. Eng.* **2014**, *53*, 027101.
146. Sanghera, J.S.; Shaw, L.B.; Busse, L.E.; Talley, D.B.; Aggarwal, I.D. Infrared-Transmitting Fiber Optics for Biomedical Applications. In Proceedings of the Specialty Fiber Optics for Medical Applications; Katzir, A., Harrington, J.A., Eds.; SPIE, April 21 1999.
147. Zhang, X.; Bureau, B.; Lucas, P.; Boussard-Pledel, C.; Lucas, J. Glasses for Seeing beyond Visible. *Chemistry* **2008**, *14*, 432–442.
148. Adam, J.-L.; Zhang, X. *_Chalcogenide Glasses : Preparation, Properties and Applications_*; Woodhead Publishing: Oxford, 2014;
149. Serna, S.; Lin, H.; Alonso-Ramos, C.; Yadav, A.; Le Roux, X.; Richardson, K.; Cassan, E.; Dubreuil, N.; Hu, J.; Vivien, L. Nonlinear Optical Properties of Integrated GeSbS Chalcogenide Waveguides. *Photonics Res.* **2018**, *6*, B37.
150. Arriola, A.; Gross, S.; Ams, M.; Gretzinger, T.; Le Coq, D.; Wang, R.P.; Ebendorff-Heidepriem, H.; Sanghera, J.; Bayya, S.; Shaw, L.B.; et al. Mid-Infrared Astrophotonics: Study of Ultrafast Laser Induced Index Change in Compatible Materials. *Opt. Mater. Express* **2017**, *7*, 698.
151. Delullier, P.; Calvez, L.; Druart, G.; De La Barrière, F.; Humbert, C.; Poumellec, B.; Lancry, M. Photosensitivity of Infrared Glasses under Femtosecond Laser Direct Writing for Mid-IR Applications. *Appl. Sci.* **2022**, *12*, 8813.
152. Bai, J.; Long, X.; Liu, X.; Huo, G.; Zhao, W.; Stoian, R.; Hui, R.; Cheng, G. Embedded Optical Waveguides Fabricated in SF10 Glass by Low-Repetition-Rate Ultrafast Laser. *Appl. Opt.* **2013**, *52*, 7288–7294.
153. Yao, H.; Zaiter, R.; Cavillon, M.; Sapaly, B.; Calzavara, F.; Delullier, P.; Cardinal, T.; Dai, Y.; Poumellec, B.; Lancry, M. Photosensitivity of Barium Germano-Gallate Glasses under Femtosecond Laser Direct Writing for Mid-IR Applications. *Ceram. Int.* **2021**, *47*, 34235–34241.
154. Khalid, M.; Chen, G.Y.; Ebendorff-Heidepreim, H.; Lancaster, D.G. Femtosecond Laser Induced Low Propagation Loss Waveguides in a Lead-Germanate Glass for Efficient Lasing in near to Mid-IR. *Sci. Rep.* **2021**, *11*, 10742.
155. Guérineau, T.; Dupont, A.; Lapointe, J.; Vallée, R.; Messaddeq, Y. Investigation of Ga_2O_3-BaO-GeO_2 Glasses for Ultrafast Laser Inscription. *Opt. Mater. Express* **2023**, *13*, 2036.
156. Bérubé, J.-P.; Bernier, M.; Vallée, R. Femtosecond Laser-Induced Refractive Index Modifications in Fluoride Glass. *Opt. Mater. Express* **2013**, *3*, 598.
157. Gross, S.; Lancaster, D.G.; Ebendorff-Heidepriem, H.; Monro, T.M.; Fuerbach, A.; Withford, M.J. Femtosecond Laser Induced Structural Changes in Fluorozirconate Glass. *Opt. Mater. Express* **2013**, *3*, 574.
158. Heck, M.; Nolte, S.; Tünnermann, A.; Vallée, R.; Bernier, M. Femtosecond-Written Long-Period Gratings in Fluoride Fibers. *Opt. Lett.* **2018**, *43*, 1994–1997.
159. Miura, K.; Qiu, J.; Mitsuyu, T.; Hirao, K. Preparation and Optical Properties of Fluoride Glass Waveguides Induced by Laser Pulses. *J. Non Cryst. Solids* **1999**, *256–257*, 212–219.
160. Dupont, A.; Lapointe, J.; Pouliot, S.; Vallée, R. From Near-UV to Long-Wave Infrared Waveguides Inscribed in Barium Fluoride Using a Femtosecond Laser. *Opt. Lett.* **2021**, *46*, 3925–3928.
161. Lancaster, D.G.; Gross, S.; Ebendorff-Heidepriem, H.; Kuan, K.; Monro, T.M.; Ams, M.; Fuerbach, A.; Withford, M.J. Fifty Percent Internal Slope Efficiency Femtosecond Direct-Written Tm^{3+}:ZBLAN Waveguide Laser. *Opt. Lett.* **2011**, *36*, 1587–1589.
162. Petit, L.; Carlie, N.; Anderson, T.; Choi, J.; Richardson, M.; Richardson, K.C. Progress on the Photoresponse of Chalcogenide Glasses and Films to Near-Infrared Femtosecond Laser Irradiation: A Review. *IEEE J. Sel. Top. Quantum Electron.* **2008**, *14*, 1323–1334.
163. Hughes, M.; Yang, W.; Hewak, D. Fabrication and Characterization of Femtosecond Laser Written Waveguides in Chalcogenide Glass. *Appl. Phys. Lett.* **2007**, *90*, 131113.
164. Ocelic, N.; Huber, A.; Hillenbrand, R. Pseudoheterodyne Detection for Background-Free near-Field Spectroscopy. *Appl. Phys. Lett.* **2006**, *89*, doi:10.1063/1.2348781.

165. Bell, R.J.; Bird, N.F.; Dean, P. The Vibrational Spectra of Vitreous Silica, Germania and Beryllium Fluoride. *J. Phys.* **1968**, *1*, 299–303.
166. Reghioua, I.; Lancry, M.; Cavani, O.; Floch, S.L.; Neuville, D.R.; Ollier, N. Unique Silica Polymorph Obtained under Electron Irradiation". *Applied Physics Letters* **2019**, *115*.
167. Devine, R.A.B. Macroscopic and Microscopic Effects of Radiation in Amorphous SiO2. *Nucl. Instrum. Methods Phys. Res. B* **1994**, *91*, 378–390.
168. Ollier, N.; Girard, S.; Peuget, S. Radiation Effects in Glass. *Encyclopedia of Glass Science* **2021**.
169. Buscarino, G.; Agnello, S.; Gelardi, F.M.; Boscaino, R. Polyamorphic Transformation Induced by Electron Irradiation Ina-SiO2glass. *Phys. Rev. B Condens. Matter Mater. Phys.* **2009**, *80*, doi:10.1103/physrevb.80.094202.
170. Shcheblanov, N.S.; Povarnitsyn, M.E. Bond-Breaking Mechanism of Vitreous Silica Densification by IR Femtosecond Laser Pulses. *EPL* **2016**, *114*, 26004.
171. Hanafusa, H.; Hibino, Y.; Yamamoto, F. Formation Mechanism of Drawing-Induced *E'* Centers in Silica Optical Fibers. *J. Appl. Phys.* **1985**, *58*, 1356–1361.
172. Agarwal, A.; Davis, K.M.; Tomozawa, M. A Simple IR Spectroscopic Method for Determining Fictive Temperature of Silica Glasses. *J. Non Cryst. Solids* **1995**, *185*, 191–198.
173. Beuton, R.; Chimier, B.; Breil, J.; Hébert, D.; Mishchik, K.; Lopez, J.; Maire, P.H.; Duchateau, G. Thermo-Elasto-Plastic Simulations of Femtosecond Laser-Induced Multiple-Cavity in Fused Silica. *Appl. Phys. A Mater. Sci. Process.* **2018**, *124*, doi:10.1007/s00339-018-1743-x.
174. Sugiura, H.; Kondo, K.; Sawaoka, A. Dynamic Response of Fused Quartz in the Permanent Densification Region. *J. Appl. Phys.* **1981**, *52*, 3375–3382.
175. Alexander, C.S.; Chhabildas, L.C.; Reinhart, W.D.; Templeton, D.W. Changes to the Shock Response of Fused Quartz Due to Glass Modification. *Int. J. Impact Eng.* **2008**, *35*, 1376–1385.
176. Wackerle, J. Shock-Wave Compression of Quartz. *J. Appl. Phys.* **1962**, *33*, 922–937.
177. Renou, R.; Soulard, L.; Lescoute, E.; Dereure, C.; Loison, D.; Guin, J.-P. Silica Glass Structural Properties under Elastic Shock Compression: Experiments and Molecular Simulations. *J. Phys. Chem. C Nanomater. Interfaces* **2017**, *121*, 13324–13334.
178. Sugiura, H.; Ikeda, R.; Kondo, K.; Yamadaya, T. Densified Silica Glass after Shock Compression. *J. Appl. Phys.* **1997**, *81*, 1651–1655.
179. Zel'dovich, Y.B.; Raizer, Y.P. *Physics of Shock Waves and High-Temperature Hydrodynamic Phenomena*; Courier Corporation, 2002; ISBN 9780486420028.
180. Dereure, C. Comportement Mécanique Des Verres Sous Choc Produit Par Interaction Laser-Matière : Une Approche Expérimentale et Numérique Multi-Échelles. PhD, Université de Rennes: France, 2019.
181. Juodkazis, S.; Nishimura, K.; Tanaka, S.; Misawa, H.; Gamaly, E.G.; Luther-Davies, B.; Hallo, L.; Nicolai, P.; Tikhonchuk, V.T. Laser-Induced Microexplosion Confined in the Bulk of a Sapphire Crystal: Evidence of Multimegabar Pressures. *Phys. Rev. Lett.* **2006**, *96*, 166101.
182. Kotlyar, V.V.; Kovalev, A.A.; Telegin, A.M. Generalized Poincaré Beams in Tight Focus. *Photonics* **2023**, *10*, 218.
183. Lu, J.; Hassan, M.; Courvoisier, F.; Garcia-Caurel, E.; Brisset, F.; Ossikovski, R.; Zeng, X.; Poumellec, B.; Lancry, M. 3D Structured Bessel Beam Polarization and Its Application to Imprint Chiral Optical Properties in Silica. *APL Photonics* **2023**, *8*, doi:10.1063/5.0140843.
184. Yao, H.; Zaiter, R.; Cavillon, M.; Delullier, P.; Lu, B.; Cardinal, T.; Dai, Y.; Poumellec, B.; Lancry, M. Formation of Nanogratings Driven by Ultrafast Laser Irradiation in Mid-IR Heavy Oxide Glasses. *Ceram. Int.* **2022**, *48*, 31363–31369.

IV.3 THE EFFECT OF COMBINING FEMTOSECOND LASER AND ELECTRON IRRADIATION ON SILICA GLASS

nanomaterials

MDPI

Article

The Effect of Combining Femtosecond Laser and Electron Irradiation on Silica Glass

Nadezhda Shchedrina [1,2,*], Roqya Allaoui [1], Matilde Sosa [1,3], Gergely Nemeth [4], Ferenc Borondics [4], Nadege Ollier [2] and Matthieu Lancry [1,*]

[1] Institut de Chimie Moléculaire et des Matériaux d'Orsay, Université Paris-Saclay, Rue du Doyen Georges Poitou, 91405 Orsay, France; allaouiroqya@gmail.com (R.A.); matilde.sosa-marti@universite-paris-saclay.fr (M.S.)
[2] Laboratoire des Solides Irradiés, École Polytechnique-CEA-CNRS, 91128 Palaiseau, France; nadege.ollier@polytechnique.edu
[3] Université Paris-Saclay, CEA, List, 91120 Palaiseau, France
[4] SMIS Beamline, SOLEIL Synchrotron, L'Orme des Merisiers, RD128, 91190 Saint Aubin, France; gergely.nemeth@synchrotron-soleil.fr (G.N.); ferenc.borondics@synchrotron-soleil.fr (F.B.)
* Correspondence: nadezhda.shchedrina@universite-paris-saclay.fr (N.S.); matthieu.lancry@universite-paris-saclay.fr (M.L.)

Abstract: This study investigates the structural and optical responses of silica glass to femtosecond (fs) laser irradiation followed by high-energy electron (2.5 MeV, 4.9 GGy) irradiation. Using optical microscopy and spectroscopy techniques, we analyzed retardance, phase shifts, nanograting periodicity, and Raman D_2 band intensity, which is an indicator of local glass densification. S-SNOM and nano-FTIR measurements further revealed changes in the Si–O–Si vibrational bands, indicating partial relaxation of the densified nanolayers under electron irradiation. Our findings reveal significant optical modifications due to subsequent electron irradiation, including reduced retardance and phase values, which are in agreement with the relaxation of the local densification. SEM analysis confirmed the preservation of nanogratings' morphology including their periodicity. Apart from revealing fundamental aspects related to glass densification within nanogratings, this study also underscores the potential of combined fs-laser and electron irradiation techniques in understanding silica glass behavior under high radiation conditions, which is crucial for applications in harsh environments.

Keywords: femtosecond laser; electron irradiation; silica glass; nanogratings; birefringence; type II modifications; metamict phase; density

Citation: Shchedrina, N.; Allaoui, R.; Sosa, M.; Nemeth, G.; Borondics, F.; Ollier, N.; Lancry, M. The Effect of Combining Femtosecond Laser and Electron Irradiation on Silica Glass. *Nanomaterials* **2024**, *14*, 1909. https://doi.org/10.3390/nano14231909

Academic Editors: Óscar Barro and Mohamed Boutinguiza

Received: 18 October 2024
Revised: 23 November 2024
Accepted: 27 November 2024
Published: 28 November 2024

1. Introduction

Silica glass, with its unique network of interconnected SiO_4 tetrahedra [1], is an essential material in fields such as optics [2] and technologies designed for harsh environments [3]. When irradiated with infrared (IR) femtosecond (fs) laser pulses, silica glass can exhibit the formation of various types of structural modifications, namely Type I [4], Type II [5–7], and Type III [8], determined by the energy deposition and laser processing parameters [1]. Type I modifications alter the refractive index mostly isotropically [4]; Type II modifications, known as nanogratings, introduce strong linear birefringence [9]; and Type III modifications create nano/micro-voids with a densified shell [8].

Of particular interest, Type II modifications play a crucial role in advancing optical and photonic technologies due to their controllable form birefringence, which makes them easily identifiable through optical measurements [10–12]. They also exhibit exceptional thermal resilience and chemical stability, capable of withstanding temperatures above 800 °C for years [9,13,14]. These nanogratings are widely applied in various fields, including optical data storage [2,15], optofluidic [16,17], sensors [3,5], and various optical components, such as 3D optical waveguides, space-variant birefringent devices, or geometric phase optics [18].

Nanogratings in silicate glasses form when laser intensity exceeds a threshold, generating high-density electron plasma through multiphoton ionization [10,19,20]. Periodic modulations of electron plasma density and temperature caused by the interference of incident and scattered waves on dielectric constant inhomogeneity lead to the formation of these nanostructures [21]. This leads to localized glass decomposition through a plasma-mediated nanocavitation process, resulting in porous layers made of oblate nanopores oriented perpendicular to the laser's linear polarization [22,23].

Although the regions between nanoporous layers are believed to be densified, their precise structural changes remain unclear. Several studies have attempted to estimate indirectly the density changes in laser-modified silica, providing insights into potential densification within nanogratings. For instance, it was reported that the material between nanoporous layers exhibits a higher Young's modulus (around 80 GPa) compared to pristine silica, suggesting local densification in these areas [24]. Radhakrishnan et al. investigated femtosecond laser-shockwave-induced densification in fused silica [25], reporting a significant 12% increase in density, resulting in a value of 2.464 g/cm^3. In an earlier study, Bellouard et al. exploited scanning thermal microscopy coupled to a micro-Raman analysis [26], observing an 8% densification in silica, corresponding to a density of approximately 2.38 g/cm^3. Recently, using nano-FTIR measurements, the correlation of the shift of the main IR vibrational structural band of silica glass with density estimated values ranging from 2.4 to 2.5 g/cm^3 within laser tracks and between nanolayers [27].

Meanwhile, silica glass exhibits polymorphism in different structural forms, such as low-density amorphous (LDA), high-density amorphous (HDA), and so-called metamict phases [28,29]. The irradiation of silica glass with different types of radiation (such as electron and neutron beams) can induce structural changes, and under high doses of irradiation, it is possible to reach a metamict phase whose density tends to approach 2.26 g/cm^3, regardless of its initial value [28,30]. Under irradiation, low-density silica glass (less than 2.26 g/cm^3) increases in density, while highly densified glasses (higher than 2.26 g/cm^3) or even quartz relax from values as high as 2.6 g/cm^3 [28]. This metamictization process is key to understanding silica glass's behavior in extreme conditions, with important applications in harsh environments such as nuclear reactors [31,32] and space environments [33,34].

One of the significant uses of silica in these extreme conditions is to design fiber Bragg gratings (FBGs) as optical sensors, particularly using IR-fs-lasers [35]. Some previous studies have explored the effects of electron and neutron irradiation on IR-fs FBGs [32,34,36–39], thus revealing partial erasure and wavelength drift attributed to changes in refractive index and density, as well as point defect center formation. However, these works do not address how high radiation doses impact the structural and optical properties of fs-laser-induced modifications beyond FBG. Understanding the behavior of fs-laser-inscribed nanogratings under high-dose irradiation is thus essential for expanding their applicability in extreme environments and for advancing knowledge of their lifetime and underlying structural evolution.

In this study, we investigate the "relaxation kinetics" of fs-laser-inscribed nanogratings in silica glass under a high electron irradiation dose of 4.9 GGy, focusing on the resulting changes in their optical properties and vibrational structure. Furthermore, we intend to estimate the density levels within the nanolayers of the nanogratings by using electron irradiation as a probing mechanism. Given the known behavior of silica glass under such irradiation [30], we can estimate density changes based on observed alterations in optical properties, nano-FTIR, and Raman signature.

2. Materials and Methods

All the glass samples employed in this work are synthetic fused Type III silica glass (Suprasil CG, Heraeus, Hanau, Germany) with a thickness of 1 mm. An ultrafast laser system (Satsuma, Amplitude Systemes Ltd., Pessac, France) was used to irradiate each sample with a wavelength centered at 1030 nm and a pulse duration of 350 fs, focused using a 0.6 numerical aperture (NA) to a depth of 200 µm (at the ICMMO, Paris-Saclay

University) with a theoretical spot diameter of approximately 1.585 µm. However, during high-intensity femtosecond laser irradiation, nonlinear optical effects such as self-focusing and plasma defocusing can significantly affect the beam propagation within the material. These effects tend to increase the effective focal spot size beyond the theoretical value calculated for linear propagation, and this increase becomes more pronounced at higher pulse energies, as reported in previous studies [40,41].

Afterward, the samples were subsequently irradiated with high-energy electrons at 2.5 MeV with a dose of 4.9 GGy at the SIRIUS facility (LSI/CEA/École Polytechnique). The density of the pristine silica Suprasil CG glass was 2.203 g/cm^3.

Two sets of experimental conditions were applied. In the first set of experiments, energy was varied with a repetition rate of 100 kHz; the energy applied ranged from 0.05 to 2 µJ, and a scanning speed of about 100 µm/s, which corresponds to typical conditions to imprint nanogratings. In the second set, the number of pulses per micron was varied while keeping the energy constant at 1 µJ. The frequency spanned from 10 to 1000 kHz, and the scanning speed varied from 0.002 to 0.1 µm/s, which corresponds to several pulse densities ranging from 2 to 50,000 pulses per micron. Two different laser polarization orientations were used to write lines: perpendicular (called Xy configuration) and parallel (Xx configuration) to the laser scanning direction (X-axis).

Characterizations began with retardance measurements conducted using a Sénarmont compensator, an instrument involving a quarter wavelength birefringent, a quartz plate, and a rotating analyzer. Relative retardance is defined by the equation: $\Gamma = (546 \times \theta)/180$, where θ is the rotation angle of the analyzer, and Γ is the relative retardation or optical path difference. By coupling this technique with a full waveplate, one can reveal the polarization-dependent birefringence and, in particular, slow/fast axis rotation when changing the writing configuration. The next step was phase determination using quantitative phase microscopy (QPM, from Iatia Vision Science) with an optical microscope (BX60, Olympus Co., Tokyo, Japan). A 20× objective and a defocus of $+/-$ 3 microns were used to measure the phase quantitative shift in natural light at 550 nm going through the irradiated sample.

To investigate the morphology and periodicity of nanogratings, the samples were cleaved perpendicularly to the laser scanning direction, allowing the laser track cross-sections to be observed using a field emission gun scanning electron microscope (FEG-SEM, ZEISS SUPRA 55 VP, Zeiss, Oberkochen, Germany). Additionally, Raman spectroscopy was performed to analyze the structural changes in MONARIS Lab (Sorbonne University). Horiba Jobin Yvon LabRam HR 800 spectrometer, equipped with edge filters, a 600 lines/mm grating, and a Peltier-cooled CCD detector, was used. The excitation wavelength was 456 nm from an Ar^+ laser, with a laser power at the sample of 5.19 mW using a 100× objective lens. For data treatment, each Raman spectrum was first baseline-corrected by fitting a third-order polynomial over the range of 200 to 1000 cm^{-1} using points at the minimum; then, the spectra were normalized to their maximum intensity. Following normalization, a third-order polynomial fit was applied to each spectrum ranging from 500 cm^{-1} to 700 cm^{-1} to extract the maximum value of the D_2 band.

Infrared (IR) analyses were conducted at the SMIS beamline of synchrotron SOLEIL (Saint Aubin, France). We employed scattering-type scanning near-field optical microscopy (s-SNOM) using an IR-neaSCOPE instrument (Attocube Systems AG, Haar, Germany). The s-SNOM operated in tapping mode with the optical signal demodulated at the second harmonic of the tip oscillation frequency [42]. For the nano-FTIR spectroscopy, broadband synchrotron radiation enabled us to collect near-field amplitude and phase spectra from various sample regions. Then, using a quantum cascade laser, we performed high-resolution single-wavelength s-SNOM imaging. The primary infrared characteristic of silica glass is the Si–O–Si asymmetric stretching vibrational band between 900 and 1300 cm^{-1} [43]. We selected a wavenumber of 1130 cm^{-1} from the high-frequency edge of this band due to its sensitivity to femtosecond laser-induced structural changes.

3. Results

3.1. Effects of Electron Irradiation on Retardance

Silica glass samples were first inscribed with fs-laser-induced nanogratings, and their initial retardance was characterized. Following this, the samples were exposed to a high-energy electron irradiation of 4.9 GGy. Subsequently, we conducted measurements to observe changes in these two experimental series, varying both the energy values and the number of pulses per micron (i.e., pulse-to-pulse overlap).

Figure 1 presents the variation in retardance for samples processed with fs-laser writing alone and for samples that underwent subsequent electron irradiation. The data represent average values across both writing configurations, Xx and Xy.

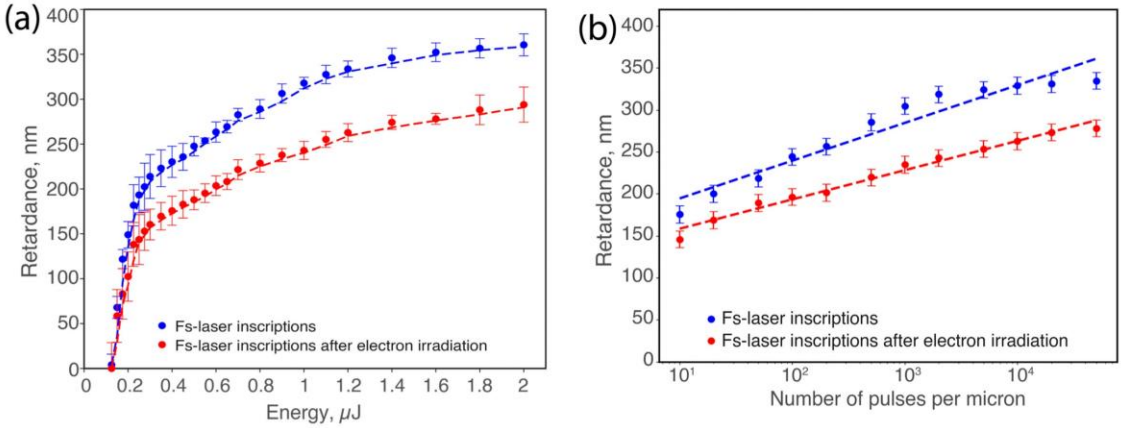

Figure 1. Retardance variation at 550 nm before (blue dots) and after electron irradiation (red dots), showing (**a**) dependence on pulse energy and (**b**) dependence on number of pulses per micron (logarithmic scale). Experimental conditions: λ = 1030 nm; τ = 250 fs; repetition rate f = 100 kHz; and scanning speed v = 100 μm/s. For (**a**), the number of pulses per micron is fixed at 1000; for (**b**), pulse energy E = 1 μJ was fixed.

When varying energy, as seen in Figure 1a, we observed that the retardance increases rapidly and then tends to stabilize before reaching a maximum. This trend is observed in both sets of samples: those with only fs-laser writing and those that were subsequently irradiated with electrons. At lower energy levels, changes in retardance are minimal, with minor differences between the two sets of samples. However, as energy increases, a significant decrease in retardance is observed after electron irradiation, with a reduction of approximately 20% at higher energies. When comparing the saturation values, the retardance is 353 nm for the fs-laser alone; conversely, with fs-laser writing followed by electron irradiation, retardance at the saturation is 283 nm. Regarding the slope at the origin, it starts at 2240 nm/μJ for fs only, whereas it decreases to 1410 nm/μJ in samples post-irradiated with electrons.

Similarly, after varying the number of pulses, as seen in Figure 1b, the retardance exhibits a monotonic growth in the log scale. The distinction between fs-laser writing and fs-laser writing followed by electron irradiation becomes significant at a high number of pulses (typ. above 100 pulses/μm), with a retardance difference at the saturation of approximately 60 nm. Comparing the saturation values again, the retardance reaches 332 nm for the fs-laser writing alone and 272 nm when followed by electron irradiation. For the slope, the initial step of fs-laser writing yields 58 nm/pulse. After substantial electron exposure, a much smaller slope is observed, decreasing to 32 nm/pulse, revealing a much lower efficiency in the generation of the form birefringence.

3.2. Effect of Electron Irradiation on Phase Shift

To complement the retardance measurements, we analyzed the phase variations in the fs-laser inscribed nanogratings (before and after electron irradiation) using QPM in natural light, thus probing the average refractive index changes Δn_{mean} within the nanogratings composite structure.

Overall negative phase values are observed in Figure 2 because the laser-written tracks exhibit a smaller optical path length compared to the pristine regions. This decrease in optical path length is the result of a net volume expansion [44] and a reduction in the refractive index within the irradiated areas that are attributed to the formation of porous nanolayers [45]. This trend is true for both the fs-laser writing and the subsequent electron irradiation.

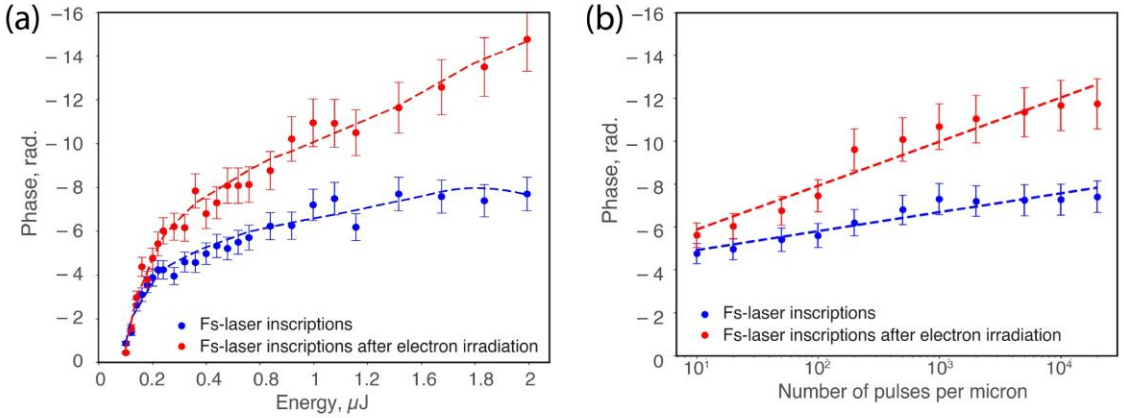

Figure 2. Phase variation (in radians) at 550 nm before (blue dots) and after electron irradiation (red dots), showing (**a**) dependence on pulse energy and (**b**) dependence on number of pulses per micron (logarithmic scale). Experimental conditions: λ = 1030 nm; τ = 250 fs; repetition rate f = 100 kHz; and scanning speed v = 100 μm/s. For (**a**), the number of pulses per micron is fixed at 1000; for (**b**), pulse energy E = 1 μJ was fixed.

Figure 2 illustrates the quantitative phase variation in samples of both fs-laser writing and fs-laser writing followed by electron irradiation. As the energy varied, Figure 2a, the phase exhibited a fast initial decrease and then a more moderate monotonous decay, a trend consistently observed across the two sets of measurements. Noticeable differences emerged between fs-laser writing alone and fs-laser writing followed by electron irradiation samples. However, at low pulse energies, phase changes were subtle, indicating minimal impact. With increasing energy, a more pronounced negative phase shift occurred post-irradiation; we observe that the phase decreased up to 50% after electron irradiation. Likewise, when adjusting the number of pulses per micron, as seen in Figure 2b, a comparable pattern emerges. Initially, there is a decrease in phase, followed by a linear decrease (higher negative values) in the log scale, mirroring the observed trend. Notably, the difference between fs-laser writing alone and fs-laser writing followed by electron irradiation becomes quite visible with a higher number of pulses, where the difference between the two is about −4 rad, i.e., a much negative phase shift for the latter case. This likely reflects a higher net volume expansion.

3.3. Effect of Electron Irradiation on Nanogratings' Morphology

SEM analysis was performed to investigate the effects of electron irradiation on the morphology of the fs-laser inscribed nanogratings in both silica samples. Apart from certifying the formation of nanogratings, the analysis included measurements of the periodicity

and porosity filling factor of the nanolayers. In the Xx configuration, nanopores exhibited sizes in the tens of nanometers and showed a uniform distribution across the nanolayer areas. Conversely, in the Xy configuration, the nanoplanes demonstrated a high density of planar structures with a well-defined orientation perpendicular to the laser polarization. Note that slight tilting of the nanogratings may occur due to variations in the local material response [46]. Importantly, the period of the nanogratings did not show significant variation after electron irradiation, regardless of the laser energy used. For instance, at a pulse energy of 1 μJ, the periodicity remained approximately 225 nm. This consistency suggests that electron irradiation does not significantly alter the morphological characteristics of the nanogratings, such as their periodicity and porosity.

3.4. Effect of Electron Irradiation on Nanoscale IR Vibrational Signature

To gain deeper insights into the structural modifications induced by fs-laser irradiation and subsequent electron irradiation, we performed IR s-SNOM imaging measurements as well as nano-FTIR spectroscopy. These techniques allow for high-resolution imaging and spectroscopic analysis of the material's optical properties at the ~10 nm scale, providing valuable information on local changes in glass structure.

Through near-field amplitude mapping at 1130 cm^{-1}, significant structural modifications were observed in the fs-laser and electron-irradiated samples, as shown in Figure 3a. The map clearly highlights an extensive area within the irradiated track where the amplitude is notably reduced compared to the unaltered surrounding regions. This reduction indicates a shift of the main IR vibrational band toward lower wavenumbers, considering that 1130 cm^{-1} is on the higher-frequency side of this well-known Si–O–Si band. Similarly, the near-field phase map in Figure 3b reveals substantial phase variations, displaying an increase in relative phase within the irradiated volume.

Figure 3c,d presents the nano-FTIR amplitude and phase spectra for both the fs-laser irradiated sample and the one followed by electron irradiation. The analysis focuses on the relative shift of the Si–O–Si vibrational band within each sample, which is more reliable. In Figure 3c, the blue solid curve represents the amplitude spectrum of pristine silica (silica glass pristine), showing the main Si–O–Si stretching vibrational band peak at 1138 cm^{-1}. The blue dashed curve corresponds to a point inside the laser track of the same sample (fs-laser inscriptions), where the peak position shifts to 1104 cm^{-1}, indicating a significant redshift of 34 cm^{-1}. This substantial shift suggests a high degree of densification within the laser-modified region due to fs-laser irradiation [12,27].

For the sample subjected to fs-laser irradiation followed by electron irradiation, the red solid curve in Figure 3c depicts the amplitude spectrum outside the laser track (silica glass after electron irradiation). Here, the peak position is at 1121 cm^{-1}, reflecting a redshift compared to pristine silica, which indicates that electron irradiation alone induces densification in the silica glass [1,29]. The red dashed curve represents the spectrum inside the laser track after subsequent electrons, showing a peak at 1108 cm^{-1}. This corresponds to a redshift of 13 cm^{-1} compared to outside the laser track within the same sample.

Comparing each sample, we observe that the shift inside the laser track relative to the surrounding material decreases from 34 cm^{-1} in the fs-laser-only sample to 13 cm^{-1} after electron irradiation. This suggests that electron irradiation causes partial relaxation of the densified interlayers. These observations are consistent with the nano-FTIR phase spectra shown in Figure 3d, which display similar trends in peak positions and shifts. The combined amplitude and phase spectra confirm that electron irradiation affects laser-modified regions, leading to the relaxation of densified nanolayers.

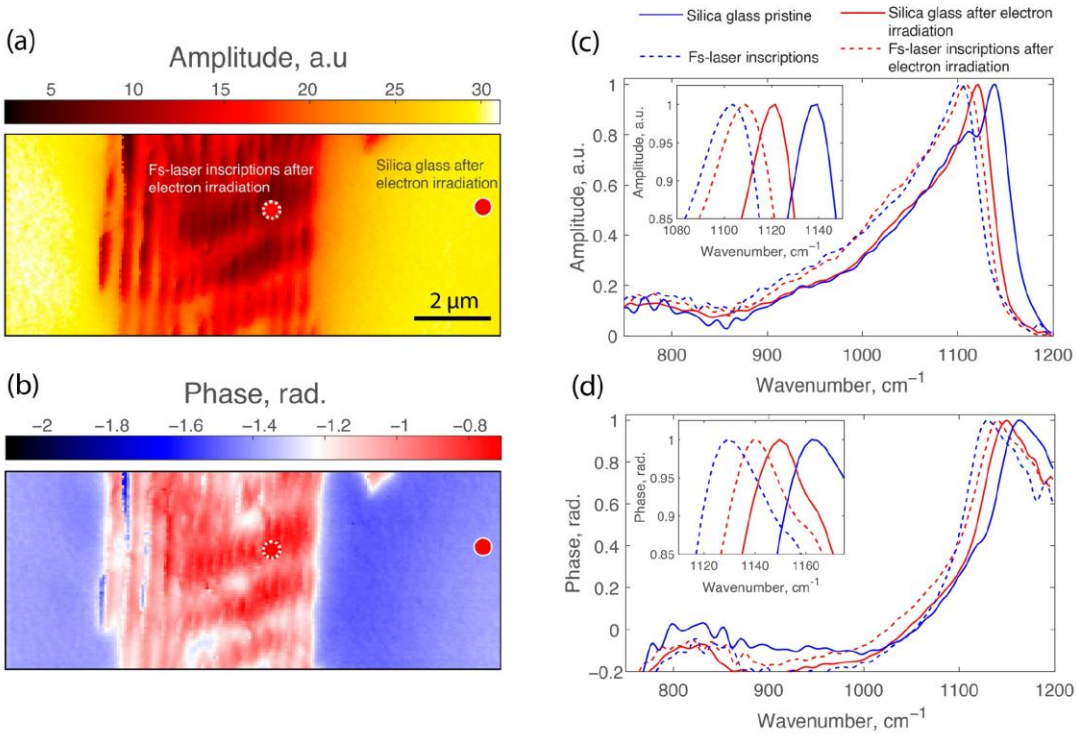

Figure 3. (**a**) Near-field amplitude map at 1130 cm^{-1} and (**b**) near-field phase map at 1130 cm^{-1} of a laser track written with 10,000 pulses per micron, after femtosecond laser and electron irradiation (4.9 GGy). (**c**) Nano-FTIR amplitude spectra and (**d**) nano-FTIR phase spectra of silica glass samples.

3.5. Effect of Electron Irradiation on Raman Vibrational Signature

Figure 4 illustrates three distinct Raman spectra corresponding to a sample written at a pulse density of 5000 pulses per micron. The first spectrum (blue) represents glass that has been subjected only to fs-laser irradiation. The second spectrum (red) pertains to glass that was initially exposed to fs-laser irradiation and subsequently treated with a high dose of electrons (4.9 GGy). The third spectrum (gray) is from a pristine, untreated glass sample taken for comparison.

Our primary focus is to analyze the intensity of the D_2 band, peaking prominently at 600 cm^{-1} and associated with three-membered rings [47–49], under varying pulse-to-pulse overlap. In agreement with the literature [14,26], the D_2 band intensity increases under fs-laser irradiation. In the sample irradiated with fs-laser followed by electron irradiation, the D_2 band intensity increases even more significantly. Furthermore, we observed that the main band, the corresponding bending motion of n-membered rings (n > 4) around 440 cm^{-1}, becomes narrower and shifts to higher wavenumbers after electron irradiation. Additionally, the D_1 band at approximately 490 cm^{-1}, associated with four-membered ring structures, increases significantly, consistent with previous results [29].

The insert in Figure 4 illustrates the changes in the normalized intensity of the D_2 band as a function of the pulse density. It is observed that the D_2 band intensity is consistently higher in the sample that underwent both fs-laser and electron irradiation compared to the one that was solely exposed to fs-laser treatment. This trend persists across all pulse densities from 2 to 10,000 pulses per micron, demonstrating that electron irradiation significantly enhances the amount of three-membered rings, which will be further discussed

in the next section. The dashed lines in the inset represent the average values of the D_2 band intensity for each condition.

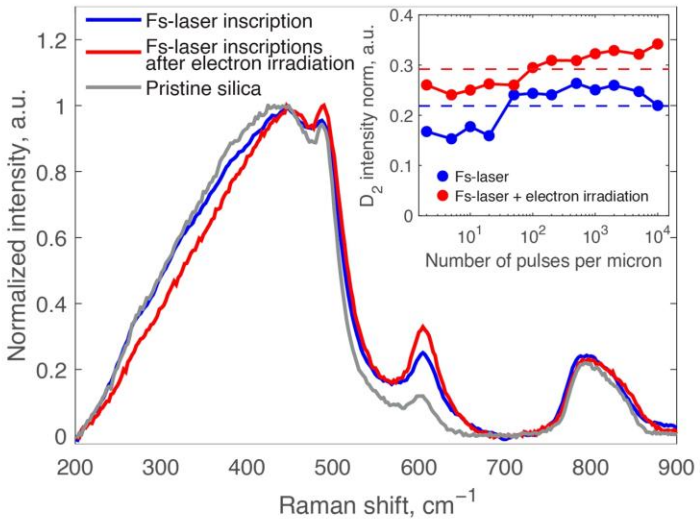

Figure 4. Raman spectra of silica glass samples: pristine (gray line), irradiated with a fs-laser at 5000 pulses per micron (blue line), and irradiated with a fs-laser at 5000 pulses per micron followed by electron irradiation of 4.9 GGy (red line). Insert: normalized D_2 intensity as a function of the number of pulses for the two samples.

4. Discussion

Our study demonstrates that high-dose electron irradiation significantly affects the optical properties and the background density of fs-laser-inscribed nanogratings in silica glass. Specifically, we observed a notable decrease in retardance (proportional to birefringence) and a more negative phase shift after electron irradiation, indicating a reduction in optical anisotropy and in the average refractive index changes within the nanogratings.

It is well-established that electron irradiation induces density modifications in silica glass, as pristine silica increases in density up to 2.26 g/cm^3 with increasing electron dose, while strongly densified silica or even quartz relaxes from higher densities toward this value corresponding to the so-called metamict state [29]. Electron irradiation decreased glass density due to the accumulation of bond-breaking events in the silica network and the creation of point defects. Based on this behavior, we hypothesized that electron irradiation would induce relaxation in the densified interlayer material along the nanogratings, leading to decreased density.

It is important to notice that the hydroxyl content in silica glass can influence its response to irradiation. While prior research indicates that femtosecond laser damage thresholds are almost the same in both high-OH and low-OH silica glasses [50], under high-dose electron irradiation, the hydroxyl content influences defect formation. In high-OH silica, irradiation dissociates silanol groups (SiOH), releasing hydrogen that interacts with excited oxygen-deficient centers (ODC(II)*), reducing their number compared to low-OH silica [51,52]. Despite these differences, the overall trend of densified glass relaxing under high radiation doses (>1 GGy) and the reverse densification remains consistent regardless of hydroxyl content.

To further confirm our interpretations, we can quantify phase measurements. Before electron irradiation, the phase shifts were less negative (by approximately four radians) compared to post-electron irradiation, as depicted in Figure 2. By using the measured

phase shift in radians and equating the optical path length (L) to the wavelength (λ), we apply the following equation:

$$\Delta n_{mean} = \frac{(\Delta\varphi \cdot \lambda)}{(2 \cdot \pi \cdot L)} \quad (1)$$

The average refractive index change (Δn_{mean}) after fs-laser exposure was calculated as -0.0157 ± 0.0006, whereas it decreased down to -0.0284 ± 0.0006 after electron irradiation while nanogratings' morphology was not affected. Although the densified interlayers within the nanogratings exhibit a positive refractive index change due to increased density, the nanoporous layers undergo significant volume expansion [44], resulting in a substantial negative refractive index change. Consequently, the measured average refractive index change Δn_{mean} across the composite probed medium made of these subwavelength nanogratings is negative, reflecting the dominant effect of the nanoporous layers outweighing the positive contribution from the densified interlayers.

This reflects an overall increase in net volume expansion following electron exposure that is attributed to a relaxation of the densified regions under such a very high dose (4.9 GGy) of electrons [30].

In turn, this relaxation reduces the refractive index contrast along nanogratings, leading to a lower form birefringence and, consequently, a decrease in the measured optical retardance. Our overall experimental results confirmed this hypothesis. Initially, fs-laser writing produced well-defined nanogratings with densified layers [27], leading to pronounced optical anisotropy, a high slope, and high saturation values of retardance around 350 nm. However, after subsequent electron irradiation, we observed notable changes, with both the slope and maximum values of retardance decreased significantly.

To interpret the observed decrease in both the retardance and the measured phase shift, let us recall the basic concept behind it. Optical retardance (R) is defined as the product of the linear birefringence (LB) and the thickness (l) of the birefringent object, expressed as R = LB × l. The primary contribution to the overall birefringence is typically attributed to the form birefringence [10,23]. The birefringence B can be determined by the difference between the refractive indices of the ordinary axis (n_0) and the extraordinary axis (n_e) and is given by the following equation [14]:

$$B = n_0 - n_e = \sqrt{\left[1 - \frac{t_1}{(t_1+t_2)}\right] n_2^2 + \frac{t_1}{t_1+t_2} n_1^2} - \left[\sqrt{\left[\frac{1-\frac{t_1}{(t_1+t_2)}}{n_2^2} + \frac{\frac{t_1}{(t_1+t_2)}}{n_1^2}\right]}\right]^{-1} \quad (2)$$

where n_2 represents the refractive index between the porous nanolayers, n_1 is the refractive index of the nanoporous layer, $L = (t_1 + t_2)$ is the total period of nanolayers, t_1 is the nanoporous layer thickness, and t_2 is the interlayer (presumably densified) thickness.

At first, SEM measurements demonstrated that the morphology of nanogratings remained unchanged after electron irradiation, i.e., the periodicity L and the porosity (thus n_1) of the nanoporous material stayed consistent. This indicates that while electron irradiation affects the density and optical properties of the interlayer material, the lower retardance is likely due to a decrease in density between layers rather than nanogratings morphological changes. The corresponding lower index n_2 along the nanogratings naturally results in a smaller form of birefringence.

From this point, one can try to quantify these effects using the form birefringence model fed by experimental data. To calculate the retardance, the thickness of the fs-laser-modified region (l) was measured as 50 µm. The periodicity of the nanogratings was determined from SEM measurements, with the thickness of the porous layer (t_1) being approximately 30 nm and the total period ($t_1 + t_2$) being 225 nm. In our calculations, the filling factor (ff) was set as 0.35, representing the fraction of the total volume occupied by nanopores within nanolayers, as determined from SEM images and previous studies.

The effective refractive index of the porous layers (n_1) was then calculated using the following equation:

$$n_1 = ff \times n_{air} + (1 - ff) \times n_0 \quad (3)$$

assuming n_{air} = 1, we obtain n_1 = 1.299. Finally, the refractive index of the densified layer was adjusted to match the measured optical retardance at the plateau, i.e., approximately 350 nm, resulting in n_2 = 1.499.

Then, to estimate glass density in-between nanolayers, it is possible to utilize the Lorentz–Lorenz relation, which factors in refractive index changes with compaction [41]:

$$\Delta n = \frac{(n_0^2 - 1)(n_0^2 + 2)}{6n_0}(\Omega - 1)\frac{\Delta\rho}{\rho_0}, \quad (4)$$

where $\Omega = (\Delta\alpha/\alpha)/(\Delta V/V_0)$ is the change of polarizability with compaction, n_0 is the refractive index of the unmodified glass (1.46 for silica), $\Delta\rho$ is the change in density, and ρ_0 is the initial density, here taken as 2.202 g/cm^3 for silica. Ω, quantifying the glass polarizability changes due to fs-laser irradiation, was set at 0.2 [53]. As a result, the density of the densified interlayers in the fs-laser-only irradiated sample was found to be 2.49 g/cm^3, aligning with previous studies [27], and it is reported below in Figure 5.

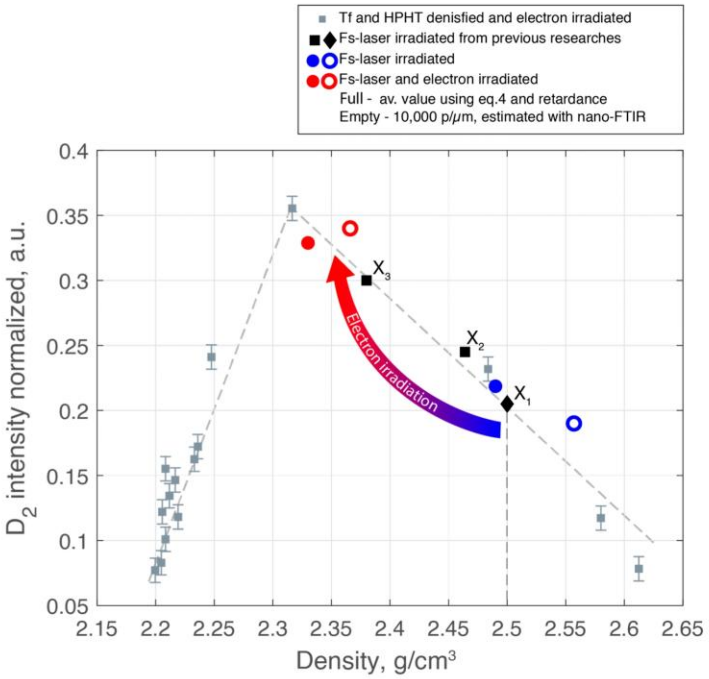

Figure 5. Intensity of the Raman D_2 band as a function of density for various silica glass samples. Gray dots represent Tf and HPHT densified and electron-irradiated silica glass [30]. Black dots correspond to data from fs-laser-irradiated silica glass from previous studies: X1 (d = 2.50 g/cm^3) [27] (X1 was extrapolated on the trendline using only the density value.), X2 (d = 2.464 g/cm^3) [25], and X3 (d = 2.38 g/cm^3) [26]. Blue dots represent the fs-laser irradiated sample, and red dots represent the fs-laser followed by electron-irradiated from the current study. Filled dots correspond to density values estimated using Equation (4) and average D_2 band intensities from the inset in Figure 4. Empty dots represent density values estimated using nano-FTIR measurements for laser tracks inscribed with 10,000 pulses per micron.

Finally, to estimate the density after electron irradiation, we adjusted $\Delta\rho$ in Equation (4), recalculated the retardance, and compared it with the experimental one. By adjusting $\Delta\rho$ and matching the recalculated retardance to the observed value of 280 nm, we estimated the density after electron irradiation to be around 2.33 g/cm^3.

In addition, nano-FTIR results showed that the shift of Si–O–Si asymmetric stretching band inside laser tracks decreased from 34 cm^{-1} in the fs-sample to 13 cm^{-1} after electron irradiation, confirming that such post-irradiation induces partial relaxation of the densified interlayers. According to Tan's calibration curve relating this vibrational band position to density [12], a 34 cm^{-1} shift corresponds to a density of approximately 2.557 g/cm^3 (after fs-irradiation), while a 13 cm^{-1} shift corresponds to a density of about 2.366 g/cm^3 (after subsequent electron irradiation).

Raman spectroscopy is another highly effective tool for assessing the vibrational structure of silica glass. Specifically, the D_2 band is often seen as a local densification indicator as it corresponds to the presence of three-membered rings, which are the most compact structures in silica glass [54]. Despite what might seem intuitive, the correlation between D_2 band intensity and density is not linear. The D_2 band is highly sensitive to its environment, and recent studies indicate that its amplitude does not have a monotonous relationship with silica density. This is illustrated in Figure 5 for silica samples obtained by changing their fictive temperature (T_f) or through high-pressure–high-temperature compression followed by electron irradiation [30]. For the sake of comparison, we also added some data (black dots) obtained under fs-laser irradiation from recent studies [25–27]. For the current study, we indicated the D_2 amplitude for fs-laser irradiation only as blue points and fs-laser followed by electron irradiation as red points.

Figure 5 reveals that for densities below approximately 2.3 g/cm^3, the D_2 band intensity increases linearly with density. Beyond this returning point, the intensity decreases even as macroscopic density follows a monotonous increase. Our results are consistent with this pattern, thus confirming that high pressures combined with high temperatures are clearly involved in nanograting formation. The fs-laser irradiated sample (blue dots) with a higher density exhibits a lower D_2 band intensity compared to the sample that also underwent electron irradiation (red dots) and had a lower density. This confirms that electron irradiation causes relaxation in the densified interlayers, reducing the density and refractive index, yet enhancing the D_2 band intensity.

All these findings confirm that the density of the interlayer nanogratings material is higher than 2.26 g/cm^3 (i.e., metamict state). Within our laser conditions, silica undergoes a densification up to 2.49 g/cm^3 before electron irradiation, in agreement with the literature [25–27], while it partly relaxes down to 2.33 g/cm^3 after irradiation. This decrease in glass density results in a much lower form of birefringence and a more pronounced negative average index change. This overall scheme confirms that high dynamic pressures during femtosecond laser irradiation (experimentally observed stress waves of around 2 GPa at ns time scales and modeled at 10–15 GPa at sub-100 ps [55]) combined to high temperatures are clearly involved within nanogratings formation [25,27].

Thus, we assume that the sequential use of fs-laser and electron irradiation can be viewed similarly to the electron irradiation of high-pressure–high-temperature (HPHT) densified silica glass. The silica glass between nanolayers was initially strongly densified (to an "over metamict" state) by fs-laser due to HPHT conditions developed on a short time scale (ps-ns) within the focal volume. Subsequently, followed by high-dose electron irradiation, these densified interlayers undergo structural relaxation (reducing their density) similar to what is observed in electron-irradiated HPHT bulk silica glass [28,30].

5. Conclusions

This study demonstrates that high-dose (4.9 GGy) electron irradiation induces glass relaxation in the densified interlayers of fs-laser-inscribed nanogratings in silica glass, decreasing their local density. While the nanogratings' morphology under SEM remained unchanged, the form birefringence significantly decreased, accompanied by a larger ap-

parent net volume expansion. This picture confirms that high-dose electron irradiation relaxes regions exhibiting densities above the metamict state (typ. 2.26 g/cm^3) and, thus, created under high temperatures and high dynamic pressures that develop at the sub ns time scale during the fs-laser writing process. This relaxation initiates a decrease in density from approximately 2.49 to 2.33 g/cm^3, as confirmed by vibrational spectroscopy.

Although electron and neutron irradiation differ in mechanism (thermal effects and knocked on atoms with neutrons compared to ionization with electrons), the fact that our studied system is amorphous means that the disorder induced by both types of irradiations is comparable (unlike in crystallized matrix). Moreover, their high-dose effects on silica glass are similar, both reaching the same metamict-like state [28]. Therefore, these findings on the relaxation of fs-laser-densified regions under high-dose electron irradiation may also apply to neutron irradiation. These findings have important implications for optical devices fabricated with fs-Type II modifications, such as IR-fs laser-induced Type II FBGs or Fabry-Pérot sensors used in high-irradiation environments like nuclear reactors, Tokamaks, and high-temperature applications. Based on our results, we anticipate a drift in the optical properties of such components under these conditions. For instance, Type II FBGs would exhibit a blue shift in their Bragg wavelength [38] due to the relaxation of densified interlayers. This relaxation could impact the accuracy and reliability of these sensors over long-term operation, which is crucial for their operation in extreme environments.

Author Contributions: Conceptualization, M.L., N.O. and N.S.; methodology, M.L. and N.O.; validation, M.L., N.O., G.N. and F.B.; formal analysis, N.S. and R.A.; investigation, N.S., R.A., M.S. and G.N.; resources, M.L., N.O. and F.B.; data curation, N.S. and G.N.; writing—original draft preparation, R.A. and N.S.; writing—review and editing, N.S., M.L., N.O., G.N. and F.B.; visualization, N.S. and R.A.; supervision, M.L. and N.O.; project administration, M.L.; funding acquisition, M.L. All authors have read and agreed to the published version of the manuscript.

Funding: This research was funded by ANR grant number ANR-24-CE51-4059-01, OPTOPHAB.

Data Availability Statement: Data underlying the results presented in this paper are not publicly available at this time but may be obtained from the authors upon reasonable request.

Acknowledgments: The authors express their gratitude for the support received from the EMIR&A French network (FR CNRS 3618) on the platform SIRIUS. We acknowledge the support of the SMIS beamline from synchrotron SOLEIL. Ludovic Bellot-Gurlet (MONARIS) is warmly acknowledged for his help during Raman experiments.

Conflicts of Interest: The authors declare no conflicts of interest.

References

1. Ollier, N.; Piven, K.; Martinet, C.; Billotte, T.; Martinez, V.; Neuville, D.R.; Lancry, M. Impact of Glass Density on the Green Emission and NBOHC Formation in Silica Glass: A Combined High Pressure and 2.5 MeV Electron Irradiation. *J. Non-Cryst. Solids* **2017**, *476*, 81–86. [CrossRef]
2. Glezer, E.N.; Milosavljevic, M.; Huang, L.; Finlay, R.J.; Her, T.H.; Callan, J.P.; Mazur, E. Three-Dimensional Optical Storage inside Transparent Materials. *Opt. Lett.* **1996**, *21*, 2023–2025. [CrossRef] [PubMed]
3. Wang, Y.; Cavillon, M.; Ballato, J.; Hawkins, T.; Elsmann, T.; Rothhardt, M.; Desmarchelier, R.; Laffont, G.; Poumellec, B.; Lancry, M. 3D Laser Engineering of Molten Core Optical Fibers: Toward a New Generation of Harsh Environment Sensing Devices. *Adv. Opt. Mater.* **2022**, *10*, 2200379. [CrossRef]
4. Davis, K.M.; Miura, K.; Sugimoto, N.; Hirao, K. Writing Waveguides in Glass with a Femtosecond Laser. *Opt. Lett.* **1996**, *21*, 1729–1731. [CrossRef]
5. Mihailov, S.; Grobnic, D.; Hnatovsky, C.; Walker, R.; Lu, P.; Coulas, D.; Ding, H. Extreme Environment Sensing Using Femtosecond Laser-Inscribed Fiber Bragg Gratings. *Sensors* **2017**, *17*, 2909. [CrossRef]
6. Shimotsuma, Y.; Kazansky, P.G.; Qiu, J.; Hirao, K. Self-Organized Nanogratings in Glass Irradiated by Ultrashort Light Pulses. *Phys. Rev. Lett.* **2003**, *91*, 247405. [CrossRef]
7. Lu, J.; Dai, Y.; Li, Q.; Zhang, Y.; Wang, C.; Pang, F.; Wang, T.; Zeng, X. Fiber Nanogratings Induced by Femtosecond Pulse Laser Direct Writing for In-Line Polarizer. *Nanoscale* **2019**, *11*, 908–914. [CrossRef]
8. Schaffer, C.B.; Brodeur, A.; Nishimura, N.; Mazur, E. Laser-Induced Microexplosions in Transparent Materials: Microstructuring with Nanojoules. In Proceedings of the Commercial and Biomedical Applications of Ultrafast Lasers, San Jose, CA, USA, 23–29 January 1999; Reed, M.K., Neev, J., Eds.; SPIE: Bellingham, WA, USA, 1999.

9. Bricchi, E.; Kazansky, P.G. Extraordinary Stability of Anisotropic Femtosecond Direct-Written Structures Embedded in Silica Glass. *Appl. Phys. Lett.* **2006**, *88*, 111119. [CrossRef]
10. Xie, Q.; Shchedrina, N.; Cavillon, M.; Poumellec, B.; Lancry, M. Nanoscale Investigations of Femtosecond Laser Induced Nanogratings in Optical Glasses. *Nanoscale Adv.* **2023**, *6*, 489–498. [CrossRef]
11. Sakakura, M.; Lei, Y.; Wang, L.; Yu, Y.-H.; Kazansky, P.G. Ultralow-Loss Geometric Phase and Polarization Shaping by Ultrafast Laser Writing in Silica Glass. *Light Sci. Appl.* **2020**, *9*, 15. [CrossRef]
12. Tan, C.Z.; Arndt, J.; Xie, H.S. Optical Properties of Densified Silica Glasses. *Physica B Condens. Matter* **1998**, *252*, 28–33. [CrossRef]
13. Xie, Q.; Cavillon, M.; Pugliese, D.; Janner, D.; Poumellec, B.; Lancry, M. On the Formation of Nanogratings in Commercial Oxide Glasses by Femtosecond Laser Direct Writing. *Nanomaterials* **2022**, *12*, 2986. [CrossRef]
14. Wang, Y.; Cavillon, M.; Ollier, N.; Poumellec, B.; Lancry, M. An Overview of the Thermal Erasure Mechanisms of Femtosecond Laser-Induced Nanogratings in Silica Glass. *Phys. Status Solidi* **2021**, *218*, 2100023. [CrossRef]
15. Hong, M.H.; Luk'yanchuk, B.; Huang, S.M.; Ong, T.S.; Van, L.H.; Chong, T.C. Femtosecond Laser Application for High Capacity Optical Data Storage. *Appl. Phys. A Mater. Sci. Process.* **2004**, *79*, 791–794. [CrossRef]
16. Monat, C.; Domachuk, P.; Eggleton, B.J. Integrated Optofluidics: A New River of Light. *Nat. Photonics* **2007**, *1*, 106–114. [CrossRef]
17. Bellouard, Y.; Said, A.; Dugan, M.; Bado, P. Fabrication of High-Aspect Ratio, Micro-Fluidic Channels and Tunnels Using Femtosecond Laser Pulses and Chemical Etching. *Opt. Express* **2004**, *12*, 2120–2129. [CrossRef]
18. Beresna, M.; Gecevičius, M.; Kazansky, P.G.; Gertus, T. Radially Polarized Optical Vortex Converter Created by Femtosecond Laser Nanostructuring of Glass. *Appl. Phys. Lett.* **2011**, *98*, 201101. [CrossRef]
19. Mao, S.S.; Quéré, F.; Guizard, S.; Mao, X.; Russo, R.E.; Petite, G.; Martin, P. Dynamics of Femtosecond Laser Interactions with Dielectrics. *Appl. Phys. A Mater. Sci. Process.* **2004**, *79*, 1695–1709. [CrossRef]
20. Yao, H.; Xie, Q.; Cavillon, M.; Dai, Y.; Lancry, M. Materials Roadmap for Inscription of Nanogratings inside Transparent Dielectrics Using Ultrafast Lasers. *Prog. Mater. Sci.* **2024**, *142*, 101226. [CrossRef]
21. Liang, F.; Vallée, R.; Chin, S.L. Mechanism of Nanograting Formation on the Surface of Fused Silica. *Opt. Express* **2012**, *20*, 4389–4396. [CrossRef]
22. Lu, Y.; Li, Y.; Xie, X.; Tang, Z.; Li, L.; Li, J.; Ding, Y. Research Advances of Femtosecond Laser-Induced Nanogratings for Transparent Materials. *Front. Chem.* **2022**, *10*, 1082651. [CrossRef]
23. Desmarchelier, R.; Poumellec, B.; Brisset, F.; Mazerat, S.; Lancry, M. In the Heart of Femtosecond Laser Induced Nanogratings: From Porous Nanoplanes to Form Birefringence. *World J. Nano Sci. Eng.* **2015**, *5*, 115–125. [CrossRef]
24. Vlugter, P.; Bellouard, Y. Elastic Properties of Self-Organized Nanogratings Produced by Femtosecond Laser Exposure of Fused Silica. *Phys. Rev. Mater.* **2020**, *4*, 023607. [CrossRef]
25. Radhakrishnan, A.; Gateau, J.; Vlugter, P.; Bellouard, Y. Femtosecond Laser-Shockwave Induced Densification in Fused Silica. *Opt. Mater. Express* **2022**, *12*, 2886. [CrossRef]
26. Bellouard, Y.; Barthel, E.; Said, A.A.; Dugan, M.; Bado, P. Scanning Thermal Microscopy and Raman Analysis of Bulk Fused Silica Exposed to Lowenergy Femtosecond Laser Pulses. *Opt. Express* **2008**, *16*, 19520. [CrossRef]
27. Shchedrina, N.; Nemeth, G.; Borondics, F.; Ollier, N.; Lancry, M. Nano-FTIR Spectroscopy Reveals SiO_2 Densification within Fs-Laser Induced Nanogratings. *Nanoscale Adv.* **2024**, *6*, 5164–5170. [CrossRef] [PubMed]
28. Mobasher, M.; Lancry, M.; Lu, J.; Neuville, D.; Bellot Gurlet, L.; Ollier, N. Thermal Relaxation of Silica Phases Densified under Electron Irradiation. *J. Non-Cryst. Solids* **2022**, *597*, 121917. [CrossRef]
29. Reghioua, I.; Lancry, M.; Cavani, O.; Floch, S.L.; Neuville, D.R.; Ollier, N. Unique Silica Polymorph Obtained under Electron Irradiation. *Appl. Phys. Lett.* **2019**, *115*, 251101. [CrossRef]
30. Ollier, N.; Lancry, M.; Martinet, C.; Martinez, V.; Le Floch, S.; Neuville, D. Relaxation Study of Pre-Densified Silica Glasses under 2.5 MeV Electron Irradiation. *Sci. Rep.* **2019**, *9*, 1227. [CrossRef]
31. Bondarenko, A.V.; Dyad'kin, A.P.; Kashchuk, Y.A.; Krasil'nikov, A.V.; Polyakov, G.A.; Rastyagaev, I.N.; Skopintsev, D.A.; Tugarinov, S.N.; Yartsev, V.P.; Bogatyrev, V.A.; et al. A Study of Radiation Resistance of Silica Optical Fibers under Conditions of Reactor Irradiation. *Instrum. Exp. Tech.* **2006**, *49*, 190–198. [CrossRef]
32. Mihailov, S.J. Fiber Bragg Grating Sensors for Harsh Environments. *Sensors* **2012**, *12*, 1898–1918. [CrossRef] [PubMed]
33. Santiago-Prowald, J.; Drioli, L.S. Space Environment and Materials. In *Space Antenna Handbook*; John Wiley & Sons, Ltd.: Chichester, UK, 2012; pp. 106–132.
34. Girard, S.; Morana, A.; Ladaci, A.; Robin, T.; Mescia, L.; Bonnefois, J.-J.; Boutillier, M.; Mekki, J.; Paveau, A.; Cadier, B.; et al. Recent Advances in Radiation-Hardened Fiber-Based Technologies for Space Applications. *J. Opt.* **2018**, *20*, 093001. [CrossRef]
35. He, J.; Xu, B.; Xu, X.; Liao, C.; Wang, Y. Review of Femtosecond-Laser-Inscribed Fiber Bragg Gratings: Fabrication Technologies and Sensing Applications. *Photonic Sens.* **2021**, *11*, 203–226. [CrossRef]
36. Xu, Y.; Ma, L.; Jiang, S.; He, Z. Effect of KGy Dose Level Gamma Radiation on Ge-Doped FBGs and Femtosecond-Laser-Inscribed Pure-Silica-Core FBGs. In Proceedings of the 2017 16th International Conference on Optical Communications and Networks (ICOCN), Wuzhen, China, 7–10 August 2017; IEEE: Piscataway, NJ, USA, 2017.
37. Henschel, H.; Grobnic, D.; Hoeffgen, S.K.; Kuhnhenn, J.; Mihailov, S.J.; Weinand, U. Development of Highly Radiation Resistant Fiber Bragg Gratings. *IEEE Trans. Nucl. Sci.* **2011**, *58*, 2103–2110. [CrossRef]
38. Morana, A.; Marin, E.; Lablonde, L.; Blanchet, T.; Robin, T.; Cheymol, G.; Laffont, G.; Boukenter, A.; Ouerdane, Y.; Girard, S. Radiation Effects on Fiber Bragg Gratings: Vulnerability and Hardening Studies. *Sensors* **2022**, *22*, 8175. [CrossRef]

39. Cheymol, G.; Remy, L.; Gusarov, A.; Kinet, D.; Megret, P.; Laffont, G.; Blanchet, T.; Morana, A.; Marin, E.; Girard, S. Study of Fiber Bragg Grating Samples Exposed to High Fast Neutron Fluences. *IEEE Trans. Nucl. Sci.* **2018**, *65*, 2494–2501. [CrossRef]
40. Que, R.; Lancry, M.; Cavillon, M.; Poumellec, B. How to Crystallize Glass with a Femtosecond Laser. *Crystals* **2024**, *14*, 606. [CrossRef]
41. Xie, Q.; Cavillon, M.; Lancry, M. Modeling Nanogratings Erasure at High Repetition Rate in Commercial Optical Glasses. *Ceram. Int.* **2024**, *50*, 49157–49164. [CrossRef]
42. Ocelic, N.; Huber, A.; Hillenbrand, R. Pseudoheterodyne Detection for Background-Free near-Field Spectroscopy. *Appl. Phys. Lett.* **2006**, *89*, 101124. [CrossRef]
43. Bell, R.J.; Bird, N.F.; Dean, P. The Vibrational Spectra of Vitreous Silica, Germania and Beryllium Fluoride. *J. Phys.* **1968**, *1*, 299–303. [CrossRef]
44. Bellouard, Y.; Champion, A.; McMillen, B.; Mukherjee, S.; Thomson, R.R.; Pépin, C.; Gillet, P.; Cheng, Y. Stress-State Manipulation in Fused Silica via Femtosecond Laser Irradiation. *Optica* **2016**, *3*, 1285. [CrossRef]
45. Lancry, M.; Poumellec, B.; Canning, J.; Cook, K.; Poulin, J.-C.; Brisset, F. Ultrafast Nanoporous Silica Formation Driven by Femtosecond Laser Irradiation. *Laser Photon. Rev.* **2013**, *7*, 953–962. [CrossRef]
46. Dai, Y.; Ye, J.; Gong, M.; Ye, X.; Yan, X.; Ma, G.; Qiu, J. Forced Rotation of Nanograting in Glass by Pulse-Front Tilted Femtosecond Laser Direct Writing. *Opt. Express* **2014**, *22*, 28500. [CrossRef] [PubMed]
47. Galeener, F.L. Planar Rings in Glasses. *Solid State Commun.* **1982**, *44*, 1037–1040. [CrossRef]
48. Pasquarello, A.; Car, R. Identification of Raman Defect Lines as Signatures of Ring Structures in Vitreous Silica. *Phys. Rev. Lett.* **1998**, *80*, 5145–5147. [CrossRef]
49. Umari, P.; Gonze, X.; Pasquarello, A. Concentration of Small Ring Structures in Vitreous Silica from a First-Principles Analysis of the Raman Spectrum. *Phys. Rev. Lett.* **2003**, *90*, 027401. [CrossRef]
50. Lancry, M.; Groothoff, N.; Guizard, S.; Yang, W.; Poumellec, B.; Kazansky, P.G.; Canning, J. Femtosecond Laser Direct Processing in Wet and Dry Silica Glass. *J. Non-Cryst. Solids* **2009**, *355*, 1057–1061. [CrossRef]
51. Pacchioni, G.; Ierańo, G. Ab Initiotheory of Optical Transitions of Point Defects $InSiO_2$. *Phys. Rev. B Condens. Matter* **1998**, *57*, 818–832. [CrossRef]
52. Skuja, L.; Hirano, M.; Hosono, H.; Kajihara, K. Defects in Oxide Glasses. *Phys. Status Solidi C* **2005**, *2*, 15–24. [CrossRef]
53. Dürr, F. *Laser-Induced Stress Changes in Optical Fibers*; École Polytechnique Fédérale de Lausanne (EPFL): Lausanne, Switzerland, 2005.
54. Cornet, A.; Martinez, V.; de Ligny, D.; Champagnon, B.; Martinet, C. Relaxation Processes of Densified Silica Glass. *J. Chem. Phys.* **2017**, *146*, 094504. [CrossRef]
55. Koritsoglou, O.; Duchateau, G.; Utéza, O.; Mouskeftaras, A. Quantitative Assessment of Femtosecond Laser-Induced Stress Waves in Fused Silica. *Phys. Rev. B* **2024**, *110*, 054112. [CrossRef]

IV.4 CONCLUSION

In this chapter, we investigated the densification mechanisms of femtosecond (fs) laser modifications in silica glass and examined how these modifications, particularly nanogratings, respond to subsequent high-dose electron irradiation.

First, using s-SNOM and nano-FTIR techniques, we quantified the density changes across the three principal fs-laser-induced modification types (Type I, Type II, and Type III). By measuring the redshift of the Si-O-Si asymmetric stretching band inside and outside the modified regions, we converted those shifts into density estimations via a well-established linear relationship. In all investigated samples, the redshift of this band confirms significant densification across Type I, Type II, and Type III modifications. For Type I, a shift of about 7 cm^{-1} corresponds to ~3-4% densification. For the densification mechanism, defect-driven structural modification (e.g., involving E′ centers and NBOHC) combined with thermal quenching likely contributes to the final densified state. Type II modifications, as we also saw in Chapter 2, exhibit more complex periodic shifts that mirror the alternating densified and porous layers of nanogratings, with overall densification reaching 8-13%. These higher values suggest a combined effect of elevated temperatures and high pressures, up to approximately 10-15 GPa as estimated from shock-wave models and the high-pressure Hugoniot relationship. For Type III modifications, which involve micro- or nano-void formation, the surrounding shell exhibits a densification of roughly 6%. Although initial shock-induced pressures may transiently exceed tens of gigapascals before being moderated by plasma shielding, the subsequent temperature rise (due to the strain relaxation wave) leads to partial structural relaxation and a lower densification. This outcome aligns with both hydrostatic and shock-wave pressure studies, where immediate post-shock densities are higher but partly relax due to increased temperature at short time scale.

Second, we demonstrated that high-dose (4.9 GGy) electron irradiation relaxes strongly the densified interlayers that were first photo-induced in fs-laser-written nanogratings (type II) without altering their overall morphology. The local density drops from about 2.49 to 2.33, reducing the form birefringence on 20% and increasing apparent net volume expansion. These results confirm that electron irradiation relaxes silica structure whose density exceeds the metamict threshold (~2.26), mirroring electrons-induced relaxation phenomena observed in other HPHT studies of silica. This finding has significant implications for photonic devices and especially sensors (e.g., Type II FBGs and likely Type III as well) deployed in high-radiation or high-temperature environments, such as nuclear reactors and fusion devices. Over time, electron- or neutron-irradiation-induced relaxation of dense interlayers can alter the Bragg wavelength and refractive index contrast, hence impairing the accuracy and reliability of these sensors. Understanding these relaxation phenomena is therefore critical for predicting long-term device performance in such extreme conditions.

GENERAL CONCLUSION

With these findings, we conclude a thesis dedicated to exploring how silica glass, which is a seemingly simple yet remarkably versatile material and undergoes structural transformations under different types of irradiations. We have studied structural transformations under HPHT conditions and electron irradiation, as well as its response to ultrafast laser irradiation in three distinct modification regimes (Type I, II, and III). Taken together, our analyses highlight the fundamental and application-oriented richness of silica's behavior when subjected to different densification pathways and levels.

Several times throughout this thesis, we have drawn intermediate conclusions, so here we will avoid repeating all details. Instead, we highlight the following key findings:

1. **Glass free volume as a precursor for nanograting formation.**
   We demonstrate that free volume within silica acts as a precursor for nanograting formation under fs-laser irradiation, facilitating the generation of nanoplasma hotspots that evolve into periodic structures aligned perpendicular to the laser polarization [18]. This explains why silica or GeO_2 glasses, naturally rich in free volume, compared to other glasses like alkali alumino-borosilicate, exhibit highest nanograting formation efficiency.

2. **Nanogratings as continuous porous layers.**
   Using high-resolution electron microscopy and advanced spectroscopy, we show that Type II nanogratings are composed of periodically arranged nanoporous layers embedded in a densified matrix, with the porous planes oriented perpendicular to the laser polarization and forming via a plasma-mediated nanocavitation mechanism, which is initiated by a strain assisted cavitation around free volume seeds or nanovoids [19].

3. **Nano-FTIR and s-SNOM for density mapping.**
   We show that advanced near-field microscopies and nano-FTIR techniques offer powerful means to estimate local density variations in such "composite" materials containing nanogratings or voids. These spectroscopic methods revealed that nanogratings reach a local densification of about 8-13%, embedded within a densified background [20].

4. **Densification regimes for the three laser modification types.**

   a. **Type I** experiences about 3-4 % densification, driven predominantly by defect formation and a swift thermal quench.

b. **Type II** exhibits 8-13 % densification, reflecting a combined effect of high localized pressures and temperatures much beyond the glass transition temperature.

c. **Type III** shows ~6 % densification in the shell around voids, likely resulting from shock-wave compression followed by partial relaxation.

5. **Electron irradiation effects HDA-LDA phase ratio.**
   We observe that electron irradiation can shift the ratio of low-density and high-density amorphous phases, while also reducing the thermal stability of these phases in silica compared to their formation through a classical thermos-mechanical pathway [21].

6. **Thermal stability of the metamict-like phase.**
   The stability of metamict-like phases depends on the particular thermo-mechanical pathway followed along its preparation. Additionally, the chemical composition of the glass (here hydroxyl content) can significantly influence the final characteristics and the formation kinetic of the metamict-like state [22].

7. **Elevated temperatures during electron irradiation.**
   Raising the temperature (up to 1000 K) while irradiating silica with electrons slows down the metamictization and structural reorganization, demonstrating how thermally activated relaxation can moderate or even counterbalance the solely radiation-driven processes.

8. **Combined fs-laser and electron irradiation effects.**
   In Type II fs modifications, subsequent electron irradiation partially relaxes the densified interlayers, reducing the optical birefringence, increasing the net apparent volume expansion and modifying the final nanograting optical properties and likely the mechanical ones [23].

Building on these outcomes, we can now look toward implications and perspectives.

FUTURE WORK AND PERSPECTIVES

Industrial-scale fs-laser direct writing:

From its earliest demonstrations, the industrial field of fs-laser direct writing has relied heavily on progress in ultrafast laser systems. Early achievements like waveguide inscription became feasible only after the introduction of stable Ti:Sapphire lasers. Thus, future trends in this field should also be determined by the evolution of fs-laser systems.

Already, high-power fs-lasers exceeding 100 W have begun to meet high industrial demands for speed and quality. Moreover, the emergence of compact and reliable fiber-based laser systems (like Yb based laser developed by Amplitude) has opened new opportunities for two-photon polymerization and 2D-3D glass processing (marking, welding, etc.), providing an economical, 3D platform for rapid prototyping in fast growing areas such as microfluidics and quantum optics.

Despite these advances, scaling fs-laser writing to large-volume industrial use requires further gains in processing speed and parallelization. While even low-energy (nJ-level) pulses can alter silica under tight focusing, conventional focusing strategies rarely employ the full power potential of modern ultrafast lasers. Integrating adaptive optics into laser direct writing systems has already shown promise for increasing process speed and efficiency by enabling parallel processing through multi-focus techniques and extended beam shapes, such as Bessel beams and others vortex beams. Appropriate spatial beam shaping, including truncated Airy or Bessel beams, can also improve the uniformity of optical modifications and minimize optical losses. Additionally, temporal shaping methods, such as GHz burst machining, offer further opportunities to significantly boost writing speed and optimize the quality of the resulting nano/micro-structures.

Our research on silica's densification and structure under ultrafast laser exposure helps towards this investigation and transition. By clarifying how the glass network responds to a range of irradiation conditions, we provide insight into how to better predict and control optical and mechanical properties in the final written structures, using other systems. This knowledge is essential for developing advanced, high-speed fs-laser methods that maintain consistent process quality at industrial scales.

Next-generation photonic devices via fs-laser writing:

One of the most promising directions for applying the insights gained in this work is the design and fabrication of next-generation photonic components. Photonics plays a critical role in numerous technological fields, including healthcare (bioimaging and diagnostics, optofluidics, lab-on-chip), transportation (light-based sensors and optical communication), space exploration (radiation-resistant optical systems), and fundamental research areas such as quantum optics and ultrafast laser science. Traditionally, the production of optical devices for these contexts has relied on bulky, costly, and/or time-consuming fabrication methods. In contrast, fs-laser direct writing offers an innovative alternative, enabling precise and localized micro- and nanoscale modifications within robust materials like silica glass; silicate glasses and recently non-oxide glasses.

To achieve this, Type II modifications can be employed in well-chosen glasses, allowing precise control over their properties and spatial arrangement through careful tuning of laser pulse energy and polarization. This opens the door to rapid, custom fabrication

of miniaturized and versatile 3D photonic elements, such as space-variant waveplates, polarization converters, or 3D geometric phase optics (lenses, gratings, prisms), devices that can drastically simplify optical setups by integrating multiple functions within a single element. Over last 5 years, the early birth of nanogratings formation so-called Type X modifications are also interesting, characterized by a much higher transparency compared to nanogratings, making them helpful for high-performance optical applications such as 5D optical data storage and geometric phase optics.

Using capabilities of fs-laser direct writing for photonic applications demands a precise command of silica's structural responses, like densification and porosity formation, etc., which was systematically investigated in this thesis. However, high scattering losses and slow writing speeds (often below 1mm/s) remain additional challenges, underscoring the need for refined pulse-intensity management and alternative approaches (such as extended focuses or GHz burst modes) that accelerate and stabilize the writing process.

Laser-written optics could soon allow rapid, on-demand creation and customization of optical components, much like what 3D printing did for mechanical details. Researchers could easily produce on-demand specialized lenses, gratings, waveguides, and other photonic elements directly in their labs either in bulk, planar substrate or in optical fiber. This simpler and more accessible method would help create smaller, tougher, and more efficient optical systems for a wide range of scientific and industrial uses.

Irradiation effects on silica-based devices in Generation IV reactor environments:

An important extension of this work lies in high-radiation and high-temperature environments such as those encountered in sodium-cooled fast reactors (SFRs), which is a leading concept within Generation IV nuclear systems. Unlike conventional reactors, SFRs allow neutrons to remain at high energy (so-called "fast" neutrons), thereby expanding fuel options and reducing long-term nuclear waste. Yet this approach inevitably entails intense fluxes of fast neutrons ($E > 1\,MeV$, with fluences up to $10^{23}\,n/cm^2$) and substantial gamma radiation (doses up to 30 kGy/h, often exceeding 1 GGy over five years), all at elevated temperatures near 600 °C. The simultaneous exposure to such extreme irradiation and temperature conditions poses a significant challenge for materials performance.

Despite studying the effects of electron irradiation at elevated temperatures, one open question for the SFRs silica-based sensors applications is the combined effect of neutrons, gamma radiation, and heat. It is particularly important since we know that most of irradiation types (neutrons, ions, etc.) can drive silica toward a metamict-like state. In principle, pre-existing electron-induced defects might influence how the glass responds to subsequent neutron bombardment, while high temperatures could either accelerate or suppress structural relaxation. Such interplay (neutrons, gamma radiation,

and heat) remains unexplored and is crucial for designing reliable silica-based devices that remain stable throughout the reactor's operational lifetime or least for intermediate period of 2 years at least.

Strategies for developing radiation-tolerant silica sensors:

A key application area involves FBG sensors within SFR cores to monitor temperature, pressure, strain, or other parameters in real time. However, typical silica fibers in these environments suffer from radiation-induced densification, leading to drifting Bragg wavelengths and diminishing sensor accuracy. Based on the findings presented in this thesis, we could suggest several approaches to address these issues:

1. **"Metamictizing" or pre-conditioning the silica**
   One potential strategy to enhance the radiation tolerance of silica involves intentionally preparing the glass to metamict-like density (~2.26) prior to its use in reactor environments. By achieving this stable state, it may be possible to significantly reduce subsequent radiation-induced densification or structural relaxation. This approach involves either precise control of laser irradiation parameters to directly attain targeted density levels or a dedicated pre-conditioning procedure. Such pre-conditioning could include electron irradiation or exposure to carefully controlled reactor-like conditions (specific irradiation doses combined with elevated temperatures) to stabilize the material properties before actual use.

2. **Alternative glass compositions**
   Silica's relatively large free volume makes it most susceptible to densification. Replacing or doping it with other network formers, for example, aluminosilicates, or adding alkaline-earth modifiers for charge compensation, can partially "fill" that free volume. Although such compositions must still retain optical clarity and mechanical integrity, a more densely packed initial network could reduce radiation-induced compaction.

3. **Predictive modeling and sensor recalibration**
   Another approach is to accept that some wavelength drift is inevitable and instead build an empirical model that predicts the Bragg shift as a function of accumulated fast-neutron fluence, gamma radiation dose and temperature annealing. By using preliminary-obtained irradiation data, reactor operating conditions, and real-time reference grating signals, these models could provide ongoing predictions of sensor drift. Periodic recalibration or drift corrections based on these predictions would help maintain sensor accuracy over extended reactor operations, transforming unavoidable wavelength drift into a manageable calibration routine.

Ultimately, designing robust optical sensors for SFR environments involves understanding and controlling how silica (or alternative glasses) responds to synergistic effects of fast neutrons, electrons, and high temperatures. The findings of this thesis offer insight into the fundamental mechanisms of densification and defect formation, laying the groundwork for tailored glass compositions, pre-treatments, and device designs that can function reliably in next-generation nuclear reactors.

Mechanical behavior of the metamict state:

Understanding the mechanical and thermodynamic (e.g. viscosity) properties of the metamict-like phase in silica glass is just as critical as characterizing its structure. The metamict state changes the glass network, affecting properties such as hardness, elastic modulus, and fracture toughness. These mechanical characteristics determine the material's durability and resilience in extreme environments. A thorough investigation into the metamict phase's mechanical behavior will be beneficial for design strategies for robust, radiation-tolerant photonic and sensor devices.

APPENDIX – EXPERIMENTAL DETAILS

APPENDIX 1 - FEMTOSECOND LASER DIRECT WRITING SYSTEM

In this thesis, the preparation of samples in silica glass was carried out using a femtosecond fibre laser writing system. Specifically, the setup employs a diode-pumped Ytterbium fibre laser (Satsuma HP from Amplitude Systèmes), operating at a central wavelength of 1030 nm with adjustable repetition rates ranging from 10 kHz to 2 MHz. The main characteristics of the laser system are summarized in Table A-1. Additionally, the system incorporates a pulse picker (acousto-optic modulator), enabling the selection of single pulses if required. With a fixed average power of 10 W, the laser provides pulse energies up to approximately 73 µJ per pulse at 400 kHz, 25 µJ per pulse at higher frequencies, and around 10 µJ per pulse at 1 MHz.

Table A-1. Certificate of Conformance (CoC) for the Satsuma HP laser utilized in this research. The table is adapted from PhD thesis of J. Tian [290].

Laser Parameters	Unit	Target		Measurement	
		400 kHz	2000 kHz	400 kHz	2000 kHz
Energy per pulse	µJ	≥ 25	≥ 5	26.5	27
Average power	W	≥ 10	≥ 10	11.1	11.3
Center wavelength	nm	1030 +/- 5		1032.1	1032.2
Bandwidth FWHM	nm	≤ 10		8.6	8.9
Pulse duration	fs	< 500		220	240
Pulse energy over 12h (Average)	µJ	> 25	> 5	27.8	-
Pulse energy over 12h (RMS)	%	< 2		0.08	
Polarization ratio	-	> 100:1		625:1	
M^2 (Mx)	-	< 1.3		1.10	
M^2 (My)				1.07	
Beam diameter (Wx)	mm	2 +/- 0.5		1.53	
Beam diameter (Wy)				1.50	
Beam ellipticity	%	< 13%		1.9	
Astigmatism		< 50%		27.8	
Waist ellipticity		< 13%		0.1	

After amplification and compression, the typical pulse duration is approximately 250 fs, measured at full width at half maximum (FWHM). To optimize pulse compression at different repetition rates, the intra-cavity spacing between chirped gratings can be adjusted via a motorized translation stage. Figure A-1 provides an example of an autocorrelation measurement for typical output pulses at 1030 nm. The experimental

autocorrelation data was fitted with a Lorentzian function, yielding an autocorrelation FWHM of 341 fs, corresponding to a pulse duration of approximately 221 fs under optimal conditions (prior to the focusing lens). Spatial chirp measurements indicated values of approximately 0.54 nm/mm along the x-axis and 0.02 nm/mm along the y-axis.

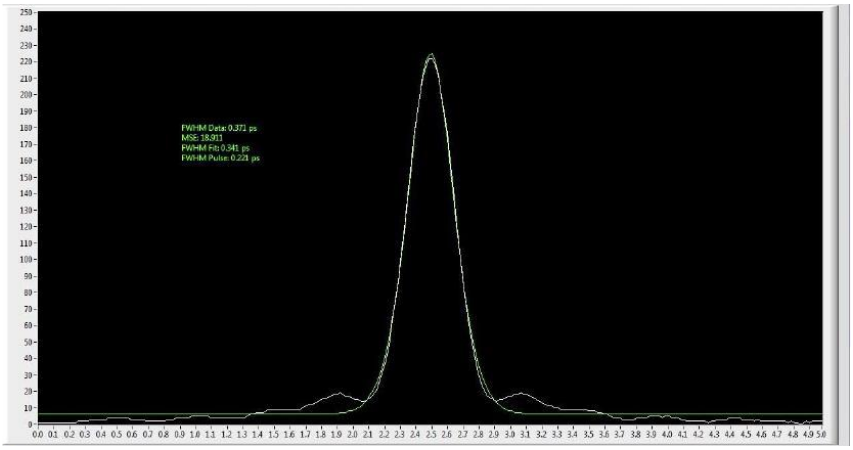

Figure A-1. Measurement of the temporal pulse profile of the laser using an optical autocorrelator. The horizontal axis represents time in picoseconds (ps), and the vertical axis represents power in arbitrary units. The graph is adapted from PhD thesis of J. Tian [290].

The output laser beam is linearly polarized in the horizontal direction (parallel to the optical table surface), perpendicular to the z-axis, as illustrated in Figure A-2. A computer-controlled half-wave plate mounted on a rotation stage (Newport SR50CC) combined with a Glan-Laser polarizer allows precise adjustment of the beam power while ensuring a constant horizontal polarization orientation. At this stage, the polarization is aligned along the x-axis, parallel to the plane defined by the laser compressor. After polarization control, the laser beam path can be directed through one of two routes: either through the acoustic-optic modulator (AOM) path or through the alternative non-AOM path.

The AOM is computer-controlled via a digital radio-frequency (RF) driver, which generates primarily a single first-order diffracted beam. The diffraction efficiency can be precisely adjusted from 0% to 100% of the input beam's total power. In certain experimental conditions, the AOM acts as a rapid on/off switch, reliably operating at modulation frequencies of up to 2 MHz within the current setup. At this stage in the fabrication system depicted in Figure A-2, the laser wavelength is fixed at 1030 nm, with a typical pulse duration of approximately 250 fs. The repetition rate can be varied from 10 kHz to 2 MHz. Additionally, the AOM allows modulation frequencies typically around 100 kHz, down to the selection of individual pulses, and is complemented by a mechanical shutter used for synchronization purposes.

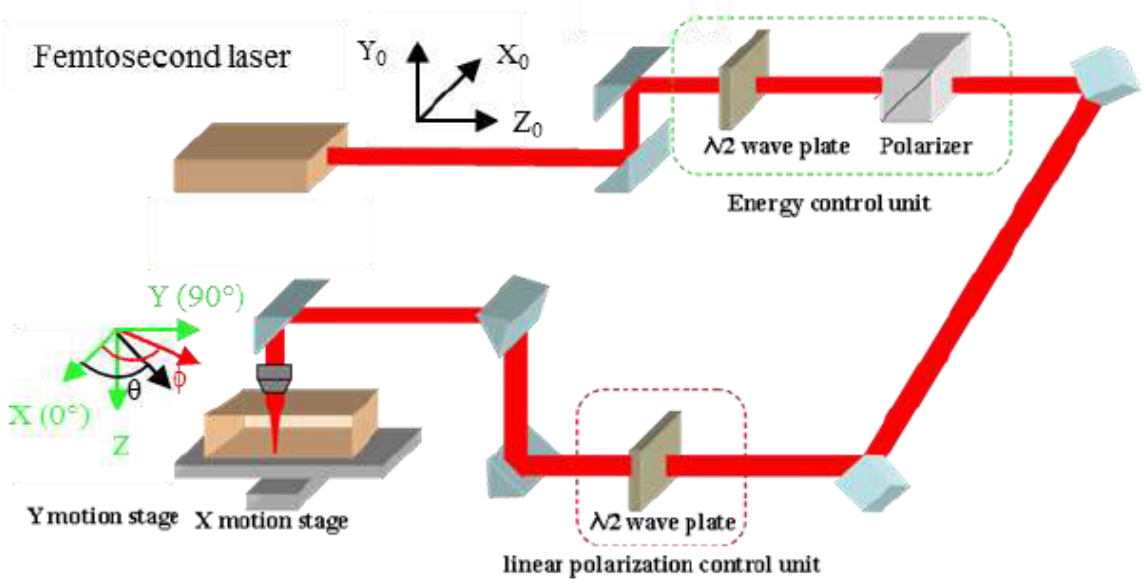

Figure A-2. Schematic diagram of the femtosecond laser direct writing setup. The graph is adapted from PhD thesis of J. Tian [290].

The laser beam is subsequently directed into the target delivery system illustrated in Figure A-3 and focused within the silica glass sample. The sample is secured on computer-controlled XY motion stages (Newport ONE-XY200HA), providing a minimum positioning resolution of 50 nm, bidirectional repeatability of 90 nm, and maximum movement speed of 200 mm/s. The vertical positioning (Z-axis) is managed by a computer-controlled translation stage (Newport UTS100CC), which typically focuses the laser spot approximately 300 µm below the sample's surface.

Focusing is achieved using aspheric lenses with numerical apertures (NA) between 0.16 and 0.65, resulting in focused spot diameters ranging from approximately 4.5 µm down to 1.1 µm (e.g., about 1.3 µm for a 0.55 NA lens). The spot size diameter (measured at $1/e^2$ of the maximum intensity) is calculated using the relationship:

$$\omega_0 = \frac{M^2\lambda}{\pi NA},$$

where ω_0 is the spot radius at the 1030 nm infrared wavelength, assuming a Gaussian intensity distribution and typical beam quality of $M^2 < 1.1$.

Additionally, the system includes a motorized half-wave plate (depicted in Figure A-3), mounted on a rapid belt-driven rotation stage (Newport URB100CC) with a rotation speed up to 720°/s. This allows precise adjustment of the linear polarization orientation at the sample position. Combining this polarization control capability with the adjustable laser power and XYZ positioning enables versatile alignment of the laser polarization (parallel, perpendicular, or at arbitrary angles) with respect to the laser scanning direction within the glass sample.

Figure A-3 illustrates the process of laser focusing into a fused silica sample, where a laser-written line is generated by translating the sample through the stationary laser spot.

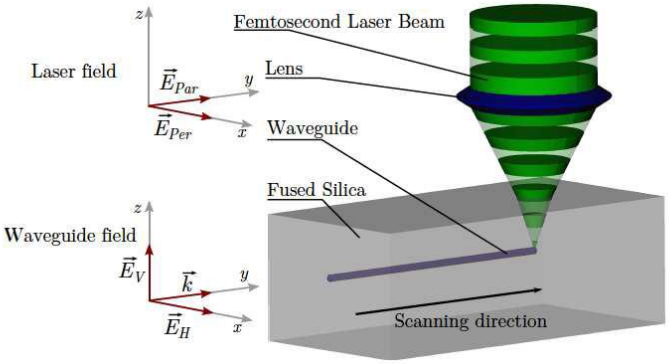

Figure A-3. Schematic diagram representing the fabrication of laser-written lines (waveguide-like structures). Here, EPar and EPer denote the parallel and perpendicular polarizations of the writing laser, respectively, while the scanning direction is fixed along the Y-axis. In the parallel polarization case (EPar, Yy writing configuration), the formed nanogratings induce a birefringence optical fast axis oriented along the y-axis, and a slow axis along the x-axis. Conversely, in the perpendicular polarization case (EPer, Yx writing configuration), the optical fast axis aligns along the x-axis, while the slow axis is along the y-axis. The graph is adapted from PhD thesis of J. Tian [290].

All motorized system components are connected to a computer via an XPS 8-axis motion controller (Newport). Control of the hardware is managed through the dedicated software interface "GOL3D," schematically depicted in Figure A-4. This software centralizes control over all integrated hardware components and translation stages where the sample is positioned. It facilitates performing complex writing trajectories, including spiral patterns and three-dimensional sets of structures, while maintaining a constant scanning speed. Maintaining uniform writing speed throughout the entire trajectory is crucial, as it directly affects the pulse accumulation along the laser-written trace. Consequently, the writing algorithm and synchronization of the shutter operation are carefully optimized.

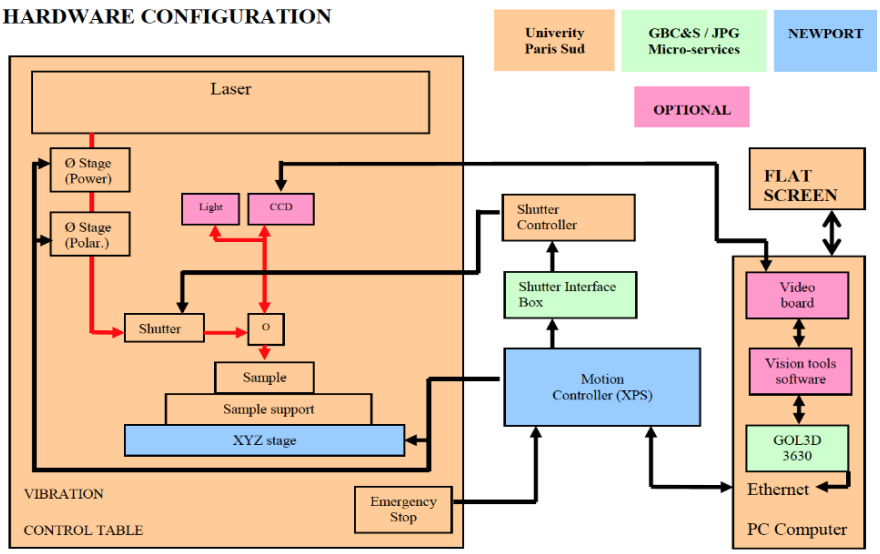

Figure A-4. Schematic overview of the hardware configuration controlled by the custom direct-writing software "GOL3D." The graph is adapted from PhD thesis of J. Tian [290].

APPENDIX 2 - ELECTRON IRRADIATION

The glass samples were irradiated using the SIRIUS electron accelerator (belonging to EMIR&A accelerator French network), manufactured by National Electronics Corporation (NEC) and installed at the Laboratoire des Solides Irradiés (LSI) in Palaiseau, France (Figure A-5a). This Pelletron-type electron accelerator delivers electrons with adjustable energies ranging from 150 keV to 2.5 MeV and beam currents from 150 nA up to 50 µA. The accelerator system consists of four main components: electron production stage, two-stage electron acceleration section, electron beam steering system, scattering chambers.

This accelerator operates by generating an electrostatic charge through a mechanical transport system consisting of a pellet chain. This chain comprises short conductive tubes interconnected by insulating links, used to accumulate charge on high-voltage terminals. The entire system is housed within a pressure vessel filled with sulfur hexafluoride (SF_6), an insulating gas. The accelerator includes an evacuated beamline, where electrons are accelerated between the high-voltage terminals and the grounded end. The electrons exit through scattering chambers (Figure A-5b), after which their trajectories are precisely controlled by a magnetic field (electron steering) up to the final beamline exit (Figure A-5c).

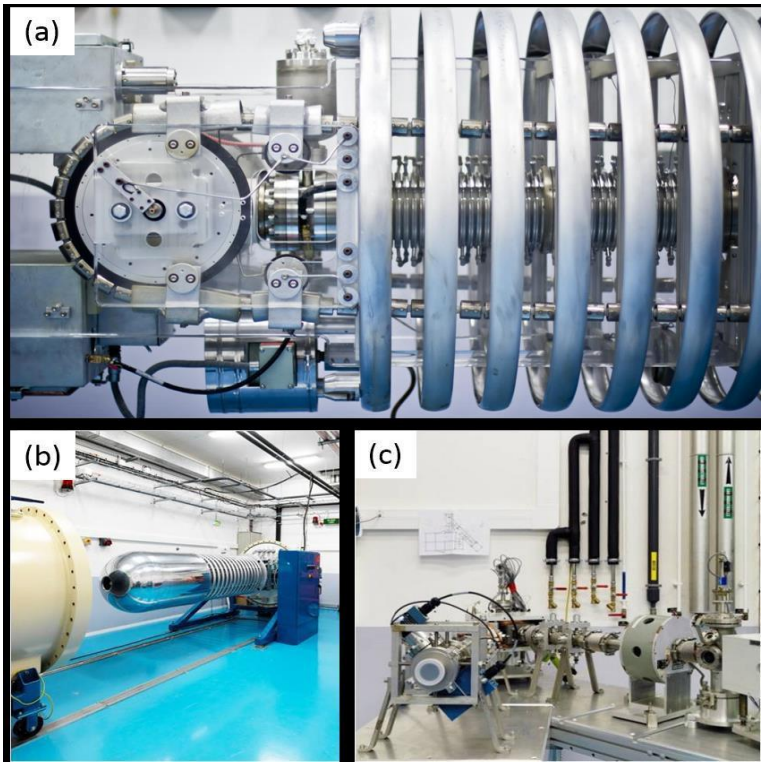

Figure A-5. SIRIUS accelerator in LSI (a) close view of inside – Pelletron charging system, (b) accelerator chamber, and (c) irradiation beam lines.

In this study, the glass samples were irradiated using a 2.5 MeV electron beam under homogeneous irradiation throughout the entire sample volume. The beam current was maintained at approximately 25 µA. The total accumulated doses ranged from 0.02 GGy to 11 GGy, with several intermediate dose levels, including 0.1, 0.6, 1, 3, 4.9–5, 7, 8.2, and 8.8 GGy.

Irradiations were performed at various controlled temperatures: 300 K, 450 K, 600 K, and 1000 K. For temperatures up to 600 K, the experiments were carried out using "Cirano" irradiation cell, with appropriate adjustments made to the cooling system depending on the target temperature. At 300 K, the copper sample holder was actively cooled using a water circulation system maintained around 290 K. In contrast, irradiation at 600 K relied solely on heating by the electron beam, without any active cooling. Irradiations at 1000 K were performed using a recent modified commercial heating cell adapted to the constraints of the accelerator setup (Figure A-6). Prior to irradiation, the system was tested to ensure stable experimental conditions, including a beam current of approximately 25 µA and a temperature close to 1000 K.

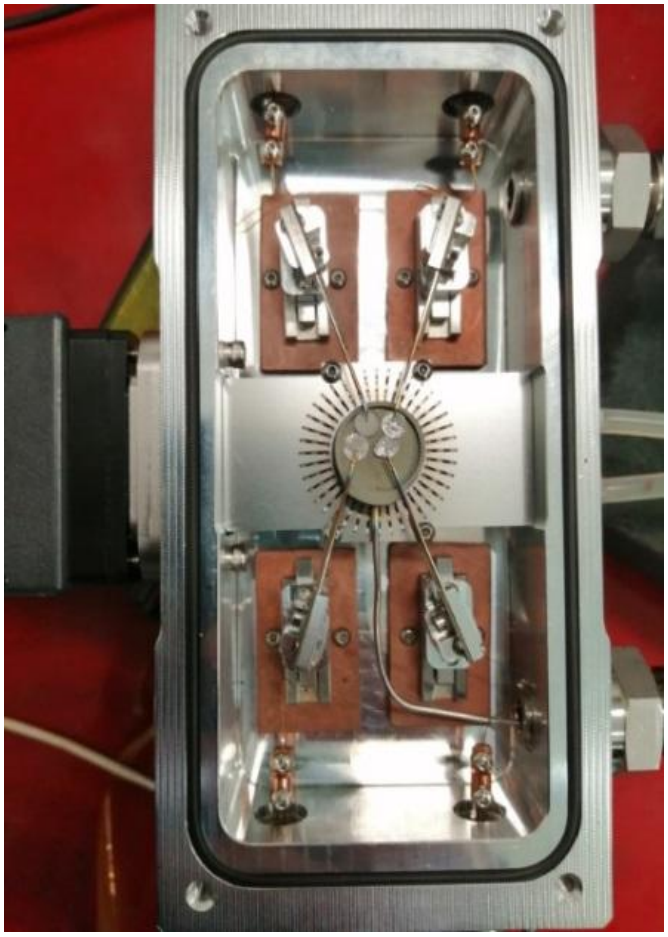

Figure A-6. Modified commercial heating cell for high temperature irradiations.

During irradiations at 450 K and 600 K, electron beam exposure began and ended precisely with the start and stop of the heating phase. In the case of the 1000 K

irradiation, the electron beam was introduced once the sample reached approximately 600 K via preliminary heating with the integrated heater. The initiation of the beam resulted in a rapid temperature increase, after which the heater was actively regulated to maintain the sample at 1000 K. The end of the irradiation coincided with a fast and significant drop in temperature.

Throughout all experiments, the irradiation cell was electrically isolated and functioned as a Faraday cup, allowing for direct and accurate measurement of the beam current reaching the sample. These conditions ensured precise control over both dose delivery and irradiation temperature.

APPENDIX 3 - S-SNOM AND NANO-FTIR

Infrared investigations were carried out at the SMIS beamline of Synchrotron SOLEIL (Saint-Aubin, France) with a commercial scattering-type scanning near-field optical microscopy (s-SNOM) platform (IR-neaSCOPE, Attocube Systems AG, Haar, Germany). S-SNOM combines the topographical precision of an atomic-force microscope (AFM) with the optical contrast of an infrared microscope by focusing light onto a metal-coated AFM tip. When the tip is brought into close proximity of the sample, the near-field interaction results in scattered light. By measuring both the amplitude and the phase of the scattered light s-SNOM is capable of retrieving the complex optical properties of the sample [291].

The optical head of the instrument forms one arm of an asymmetric Michelson interferometer in which the conventional fixed mirror is replaced by the set of focusing mirror, tip and sample (Figure A-6). Half of the incoming beam is directed toward a movable reference mirror, while the remainder is concentrated onto the tip apex. Near-field scattering produced in the tip-sample interactions is collected by the same mirror, recombined with the reference arm and detected by an infrared photodiode. Because the interaction volume is set by the radius of the tip (typically a few tens of nanometres), the technique goes beyond the far-field diffraction limit and provides the signal with true nanoscale resolution [292].

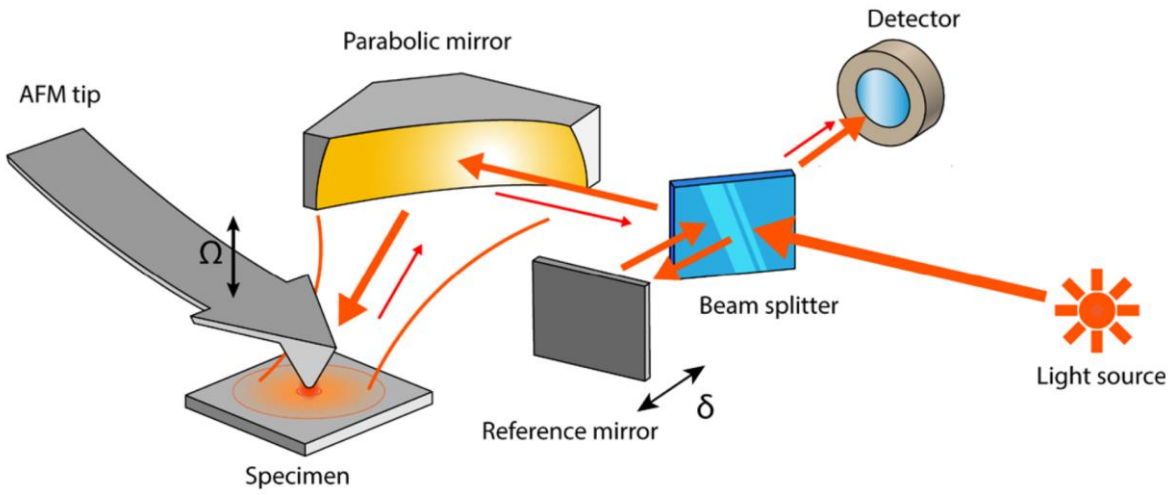

Figure A-6. Schematic representation of a s-SNOM setup. Cited from [292].

The selective detection of the near-field signal is achieved through a combination of mechanical and interferometric modulation. The AFM operates in tapping mode, so that the tip-sample distance oscillates at frequency Ω. The detector output is demodulated at higher harmonics ($n\Omega$, $n \geq 2$). Owing to the non-linear distance dependence of the near-field, these harmonics suppress the much stronger, linearly varying far-field background. Additionally, mixing the back-scattered light with the beam from the reference mirror of the interferometer results in signal level enhancement and phase

modulation in the interference term [292]. With monochromatic illumination, the reference mirror movement is typically modulated at a fixed frequency in a pseudo-heterodyne detection scheme that further suppresses background and extracts the amplitude and phase of the near-field scattering [291]. For broad-band illumination, the reference mirror is moved linearly over a fixed distance and the demodulated signal is recorded as a function of mirror position to collect an interferogram. The subsequent nano-FTIR interferogram is then Fourier-transformed to yield the amplitude and the phase of the scattered light [293].

Two operating modes were used. Broadband synchrotron radiation provided nano-FTIR spectra across regions of interest, producing spatially resolved amplitude and phase information. Single-frequency imaging used the system's integrated quantum-cascade laser to visualise the selected vibrational fingerprints with enhanced signal-to-noise ratios. Throughout the study, all datasets were acquired in tapping mode and demodulated at the second harmonic of the cantilever oscillation [291].

PUBLICATION LIST

Journal papers

1. Shchedrina N., Sosa M., Cavillon M., & Lancry M. (2025). Properties, mechanisms, and perspectives of ultrafast laser modifications in silicate glass volume. International Journal of Applied Glass Science, e16706.
2. Shchedrina, N., Lancry, M., Alessi, A., Cavani, O., Ollier, N. (2025). The influence of high-temperature during electron irradiation on silica structure. Submitted to Journal of Non-Crystalline Solids.
3. Shchedrina N., Lancry M., Charpentier T., Neuville D., & Ollier N. (2025). Impact of the silica glass initial state on the thermal and structural properties of metamict-like silica glass. Journal of Non-Crystalline Solids ,655, 123463.
4. Shchedrina, N., Allaoui, R., Sosa, M., Nemeth, G., Borondics, F., Ollier, N., & Lancry, M. (2024). The Effect of Combining Femtosecond Laser and Electron Irradiation on Silica Glass. Nanomaterials, 14(23), 1909.
5. Shchedrina, N., Nemeth, G., Borondics, F., Ollier, N., & Lancry, M. (2024). Nano-FTIR spectroscopy reveals SiO_2 densification within fs-laser induced nanogratings. Nanoscale Advances, 6(20), 5164-5170.
6. Xie, Q., Shchedrina, N., Cavillon, M., Poumellec, B., & Lancry, M. (2024). Nanoscale investigations of femtosecond laser induced nanogratings in optical glasses. Nanoscale Advances, 6(2), 489-498.
7. Shchedrina, N., Cavillon, M., Ari, J., Ollier, N., & Lancry, M. (2024). Impact of Glass Free Volume on Femtosecond Laser-Written Nanograting Formation in Silica Glass. Materials, 17(2), 502.
8. Shchedrina, N., Ollier, N., Mobasher, M., & Lancry, M. (2023). Investigating densification processes of amorphous silica phases through activation energy distribution. Journal of Non-Crystalline Solids, 617, 122491.

International conferences

1. Oral: Densification evaluation in femtosecond laser modified silica glass of types I, II and III, The 15th International Conference on SiO2, Advanced Dielectrics, and Related Devices, Saint-Etienne, France, June 23-26, 2025.
2. Oral: Exploring densification mechanisms of silica glass in femtosecond laser modifications using Nano-FTIR, XXVII International Congress on Glass ICG, Kolkata, India, January 20-24, 2025
3. Oral: NanoIR spectroscopic analysis revealing densification mechanisms in fs-laser induced nanogratings, The International Symposium on Laser Precision Microfabrication (LPM 2024), San-Sebastian, Spain, June 11-14, 2024.
4. Poster: Impact of glass free volume on femtosecond laser-written nanograting formation in silica glass, Photonics TALANT International Summer School, Bordeaux

(France), July 8-12, 2024

5. Oral: In Situ Raman Spectroscopy during Annealing for Calculation of the Activation Energy Distribution in Densified Silica Glass, RamanFest 2023 International Conference, Paris, November 9, 2023.
6. Oral: Electron irradiation effects on the activation energy distribution in densified silica, EMIR&A user's meeting, EMIRUM, GANIL, Caen, December 14-15, 2023.
7. Oral: Activation energy distribution of densification process in electron-irradiated silica, The 14th International Conference on SiO2, Advanced Dielectrics, and Related Devices, Palermo, Italy, June 12-14, 2023.

Summer schools

1. 14th ICG Montpellier Summer School, 2-7 July 2023, Montpellier.
2. 1st TALANT International Summer School, 8-12 July 2024, Bordeaux.

REFERENCES

1. J. D. Mackenzie, "High-pressure effects on oxide glasses: I, densification in rigid state," J. Am. Ceram. Soc. **46**, 461–470 (1963).
2. H. Sugiura, R. Ikeda, K. Kondo, and T. Yamadaya, "Densified silica glass after shock compression," J. Appl. Phys. **81**, 1651–1655 (1997).
3. M. Guerette, M. R. Ackerson, J. Thomas, E. B. Watson, and L. Huang, "Thermally induced amorphous to amorphous transition in hot-compressed silica glass," J. Chem. Phys. **148**, 194501 (2018).
4. C. Fiori and R. A. B. Devine, "Ultraviolet irradiation induced compaction and photoetching in amorphous, thermal SiO2," Mater. Res. Soc. Symp. Proc. **61**, (1985).
5. W. Primak and R. Kampwirth, "The radiation compaction of vitreous silica," J. Appl. Phys. **39**, 5651–5658 (1968).
6. W. Primak, "Fast-neutron-induced changes in quartz and vitreous silica," Phys. Rev. **110**, 1240–1254 (1958).
7. K. M. Davis, K. Miura, N. Sugimoto, and K. Hirao, "Writing waveguides in glass with a femtosecond laser," Opt. Lett. **21**, 1729–1731 (1996).
8. Y. Shimotsuma, P. G. Kazansky, J. Qiu, and K. Hirao, "Self-organized nanogratings in glass irradiated by ultrashort light pulses," Phys. Rev. Lett. **91**, 247405 (2003).
9. E. N. Glezer, M. Milosavljevic, L. Huang, R. J. Finlay, T. H. Her, J. P. Callan, and E. Mazur, "Three-dimensional optical storage inside transparent materials," Opt. Lett. **21**, 2023–2025 (1996).
10. A. Champion, M. Beresna, P. Kazansky, and Y. Bellouard, "Stress distribution around femtosecond laser affected zones: effect of nanogratings orientation," Opt. Express **21**, 24942–24951 (2013).
11. B. McMillen, C. Athanasiou, and Y. Bellouard, "Femtosecond laser direct-write waveplates based on stress-induced birefringence," Opt. Express **24**, 27239–27252 (2016).
12. P. G. Kazansky, H. Inouye, T. Mitsuyu, K. Miura, J. Qiu, K. Hirao, and F. Starrost, "Anomalous anisotropic light scattering in Ge-doped silica glass," Phys. Rev. Lett. **82**, 2199–2202 (1999).
13. E. Bricchi, J. D. Mills, P. G. Kazansky, B. G. Klappauf, and J. J. Baumberg, "Birefringent Fresnel zone plates in silica fabricated by femtosecond laser machining," Opt. Lett. **27**, 2200–2202 (2002).
14. L. Sudrie, M. Franco, B. Prade, and A. Mysyrowicz, "Writing of permanent birefringent microlayers in bulk fused silica with femtosecond laser pulses," Opt. Commun. **171**, 279–284 (1999).
15. J. He, B. Xu, X. Xu, C. Liao, and Y. Wang, "Review of femtosecond-laser-inscribed fiber Bragg gratings: Fabrication technologies and sensing applications," Photonic Sens. **11**, 203–226 (2021).
16. S. J. Mihailov, "Fiber Bragg grating sensors for harsh environments," Sensors (Basel) **12**, 1898–1918 (2012).
17. G. Laffont, R. Cotillard, N. Roussel, R. Desmarchelier, and S. Rougeault,

"Temperature resistant fiber Bragg gratings for on-line and structural health monitoring of the next-generation of nuclear reactors," Sensors (Basel) **18**, 1791 (2018).
18. N. Shchedrina, M. Cavillon, J. Ari, N. Ollier, and M. Lancry, "Impact of glass free volume on femtosecond laser-written nanograting formation in silica glass," Materials **17**, 502 (2024).
19. Q. Xie, N. Shchedrina, M. Cavillon, B. Poumellec, and M. Lancry, "Nanoscale investigations of femtosecond laser induced nanogratings in optical glasses," (2023).
20. N. Shchedrina, G. Nemeth, F. Borondics, N. Ollier, and M. Lancry, "Nano-FTIR spectroscopy reveals SiO2 densification within fs-laser induced nanogratings," Nanoscale Adv. **6**, 5164–5170 (2024).
21. N. Shchedrina, N. Ollier, M. Mobasher, and M. Lancry, "Investigating densification processes of amorphous silica phases through activation energy distribution," J. Non Cryst. Solids **617**, 122491 (2023).
22. N. Shchedrina, M. Lancry, T. Charpentier, D. Neuville, and N. Ollier, "Impact of the silica glass initial state on the thermal and structural properties of metamict-like silica glass," J. Non Cryst. Solids **655**, 123463 (2025).
23. N. Shchedrina, R. Allaoui, M. Sosa, G. Nemeth, F. Borondics, N. Ollier, and M. Lancry, "The effect of combining femtosecond laser and electron irradiation on silica glass," Nanomaterials **14**, 1909 (2024).
24. I. G. Polyakova, "4. The main silica phases and some of their properties," in *Glass* (DE GRUYTER, 2014), pp. 197–268.
25. L. Lichtenstein, M. Heyde, and H.-J. Freund, "Atomic arrangement in two-dimensional silica: From crystalline to vitreous structures," J. Phys. Chem. C Nanomater. Interfaces **116**, 20426–20432 (2012).
26. K. Mishchik, "Transformation photo-assistee de dielectriques pour l'optique par laser a impulsions ultra-breves: etudes des mecanismes microscopiques," Universite Jean Monnet - Saint-Etienne (2012).
27. NATO Advanced Study Institute on Defects in SiO_2 and Related Dielectrics: Science and Technology (2000 : Erice, Italy), *Defects in SiO2 and Related Dielectrics: Science and Technology*, 2000th ed., NATO Science Series II No. 2 (Springer, 2012).
28. A. C. Hannon, "Basic concepts of network glass structure," Encyclopedia of Glass Science **1**, 129–140 (2021).
29. B. E. Warren, "Summary of work on atomic arrangement in glass," J. Am. Ceram. Soc. **24**, 256–261 (1941).
30. D. I. Grimley, A. C. Wright, and R. N. Sinclair, "Neutron scattering from vitreous silica IV. Time-of-flight diffraction," J. Non Cryst. Solids **119**, 49–64 (1990).
31. F. Liebau, *Structural Chemistry of Silicates: Structure, Bonding, and Classification* (Springer Science & Business Media, 2012).
32. R. J. Bell and P. Dean, "The structure of vitreous silica: Validity of the random network theory," Philos. Mag. **25**, 1381–1398 (1972).
33. C. M. Smith, *Silica, Vitreous," in Kirk-Othmer Encyclopedia of Chemical Technology* (Wiley, 2006), Vol. 22.

34. L. Skuja, M. Hirano, H. Hosono, and K. Kajihara, "Defects in oxide glasses," Phys. Status Solidi C **2**, 15–24 (2005).
35. H. Hosono, Y. Abe, H. Imagawa, H. Imai, and K. Arai, "Experimental evidence for the Si-Si bond model of the 7.6-eV band in SiO2 glass," Phys. Rev. B Condens. Matter **44**, 12043–12045 (1991).
36. L. Skuja, "Optically active oxygen-deficiency-related centers in amorphous silicon dioxide," J. Non Cryst. Solids **239**, 16–48 (1998).
37. M. Guzzi, F. Piot, G. Spinolo, A. Vedda, C. B. Azzoni, and A. Paleari, "Neutron irradiation effects in quartz: optical absorption and electron paramagnetic resonance," J. Phys. Condens. Matter **4**, 8635–8648 (1992).
38. L. Skuja, K. Kajihara, T. Kinoshita, M. Hirano, and H. Hosono, "The behavior of interstitial oxygen atoms induced by F2 laser irradiation of oxygen-rich glassy SiOβ," Nucl. Instrum. Methods Phys. Res. B **191**, 127–130 (2002).
39. Y. Akahama and H. Kawamura, "High-pressure infrared spectroscopy of solid oxygen," Phys. Rev. B Condens. Matter **61**, 8801–8805 (2000).
40. R. A. Weeks, "Paramagnetic resonance of lattice defects in irradiated quartz," J. Appl. Phys. **27**, 1376–1381 (1956).
41. D. L. Griscom, "Characterization of three E′-center variants in X- and γ-irradiated high purity a-SiO2," Nucl. Instrum. Methods Phys. Res. B **1**, 481–488 (1984).
42. G. Buscarino, S. Agnello, and F. M. Gelardi, "Delocalized nature of the E′delta center in amorphous silicon dioxide," Phys. Rev. Lett. **94**, 125501 (2005).
43. S. Agnello, R. Boscaino, G. Buscarino, M. Cannas, and F. M. Gelardi, "Structural relaxation of E′ gamma centers in amorphous silica," arXiv [cond-mat.mtrl-sci] (2002).
44. L. Skuja, "A new intrinsic defect in amorphous SiOβ: twofold coordinated silicon," Solid State Commun **50**, 1069–1072 (1984).
45. M. Stapelbroek, D. L. Griscom, E. J. Friebele, and G. H. Sigel Jr, "Oxygen-associated trapped-hole centers in high-purity fused silicas," J. Non Cryst. Solids **32**, 313–326 (1979).
46. R. A. B. Devine and J. Arndt, "Defect pair creation through ultraviolet radiation in dense, amorphous SiO β," Phys. Rev. B **42**, (1990).
47. S. Munekuni, T. Yamanaka, Y. Shimogaichi, R. Tohmon, Y. Ohki, K. Nagasawa, and Y. Hama, "Various types of nonbridging oxygen hole center in high-purity silica glass," J. Appl. Phys. **68**, 1212–1217 (1990).
48. T. Bakos, S. N. Rashkeev, and S. T. Pantelides, "Optically active defects in Si O β : The nonbridging oxygen center and the interstitial OH molecule," Phys. Rev. B **70**, (2004).
49. E. J. Friebele, D. L. Griscom, M. Stapelbroek, and R. A. Weeks, "Fundamental defect centers in glass: The peroxy radical in irradiated, high-purity, fused silica," Phys. Rev. Lett. **42**, 1346–1349 (1979).
50. D. L. Griscom and M. Mizuguchi, "Determination of the visible range optical absorption spectrum of peroxy radicals in gamma-irradiated fused silica," J. Non Cryst. Solids **239**, 66–77 (1998).
51. H. Hanafusa, Y. Hibino, and F. Yamamoto, "Formation mechanism of drawing-

induced defects in optical fibers," J. Non Cryst. Solids **95–96**, 655–661 (1987).
52. Y. Sasajima and K. Tanimura, "Optical transitions of self-trapped holes in amorphousSiO2," Phys. Rev. B Condens. Matter **68**, (2003).
53. R. T. Williams and K. S. Song, "The self-trapped exciton," J. Phys. Chem. Solids **51**, 679–716 (1990).
54. K. Tanimura, C. Itoh, and N. Itoh, "Transient optical absorption and luminescence induced by band-to-band excitation in amorphous SiO2," J. Phys. **21**, 1869–1876 (1988).
55. N. Itoh, T. Shimizu-Iwayama, and T. Fujita, "Excitons in crystalline and amorphous SiOβ: formation, relaxation and conversion to Frenkel pairs," J. Non-Cryst. Solids **179**, 194–201 (1994).
56. Y. Morimoto, S. Nozawa, and H. Hosono, "Effect ofXe2*light (7.2 eV) on the infrared and vacuum ultraviolet absorption properties of hydroxyl groups in silica glass," Phys. Rev. B Condens. Matter **59**, 4066–4073 (1999).
57. K. Kajihara, L. Skuja, M. Hirano, and H. Hosono, "Formation and decay of nonbridging oxygen hole centers in SiO2 glasses induced by F2 laser irradiation: *In situ* observation using a pump and probe technique," Appl. Phys. Lett. **79**, 1757–1759 (2001).
58. Y. Ikuta, K. Kajihara, M. Hirano, S. Kikugawa, and H. Hosono, "Effects of H2 impregnation on excimer-laser-induced oxygen-deficient center formation in synthetic SiO2 glass," Appl. Phys. Lett. **80**, 3916–3918 (2002).
59. G. Pacchioni, L. Skuja, and D. L. Griscom, *Defects in SiO2 and Related Dielectrics: Science and Technology* (Springer, 2000).
60. L. Skuja, M. Leimane, N. Ollier, and A. Grishchenko, "Paramagnetic point defect in fluorine-doped silica glass: The E^{'}(F) center," Phys. Rev. Lett. **131**, 256903 (2023).
61. S. Girard, J. Kuhnhenn, A. Gusarov, B. Brichard, M. Van Uffelen, Y. Ouerdane, A. Boukenter, and C. Marcandella, "Radiation effects on silica-based optical fibers: Recent advances and future challenges," IEEE Trans. Nucl. Sci. **60**, 2015–2036 (2013).
62. R. Brückner, "Properties and structure of vitreous silica. I," J. Non Cryst. Solids **5**, 123–175 (1970).
63. L. A. Moore and C. M. Smith, "Fused silica as an optical material [Invited]," Opt. Mater. Express **12**, 3043 (2022).
64. G. D. Ulrich and J. W. Rieh, "Aggregation and growth of submicron oxide particles in flames," J. Colloid Interface Sci. **87**, 257–265 (1982).
65. M. Blankenship and C. Deneka, "The outside vapor deposition method of fabricating optical waveguide fibers," IEEE J. Quantum Electron. **18**, 1418–1423 (1982).
66. A. Audsley and R. K. Bayliss, "The induced plasma torch as a high‐temperature chemical reactor. I. Oxidation of silicon tetrachloride," J. Appl. Chem. **19**, 33–38 (1969).
67. FindLight-The New Way to Find Lasers, "Suprasil 300 material grades for the infrared spectrum," https://www.findlight.net/optics/optical-materials/optical-glass/suprasil-300-material-grades-for-the-infrared-spectrum.

68. E. I. Kamitsos, "Infrared spectroscopy of glasses," Modern Glass Characterization 1–42 (2015).
69. F. J. Fraile-Pelaez and A. Macho, "Electromagnetic formalism of the propagation and amplification of light," arXiv [physics.optics] (2019).
70. M. K. Gunde, "Vibrational modes in amorphous silicon dioxide," Physica B Condens. Matter **292**, 286–295 (2000).
71. C. T. Kirk, "Quantitative analysis of the effect of disorder-induced mode coupling on infrared absorption in silica," Phys. Rev. B Condens. Matter **38**, 1255–1273 (1988).
72. R. Kitamura, L. Pilon, and M. Jonasz, "Optical constants of silica glass from extreme ultraviolet to far infrared at near room temperature," Appl. Opt. **46**, 8118–8133 (2007).
73. A. Agarwal and M. Tomozawa, "Correlation of silica glass properties with the infrared spectra," J. Non Cryst. Solids **209**, 166–174 (1997).
74. R. J. Bell, N. F. Bird, and P. Dean, "The vibrational spectra of vitreous silica, germania and beryllium fluoride," J. Phys. **1**, 299–303 (1968).
75. M. Tomozawa, J.-W. Hong, and S.-R. Ryu, "Infrared (IR) investigation of the structural changes of silica glasses with fictive temperature," J. Non Cryst. Solids **351**, 1054–1060 (2005).
76. F. L. Galeener, "Band limits and the vibrational spectra of tetrahedral glasses," Phys. Rev. B Condens. Matter **19**, 4292–4297 (1979).
77. R. A. B. Devine, "Ion implantation- and radiation-induced structural modifications in amorphous SiO2," J. Non Cryst. Solids **152**, 50–58 (1993).
78. C. Z. Tan, J. Arndt, and H. S. Xie, "Optical properties of densified silica glasses," Physica B Condens. Matter **252**, 28–33 (1998).
79. M. Lancry, E. Régnier, and B. Poumellec, "Fictive temperature in silica-based glasses and its application to optical fiber manufacturing," Prog. Mater. Sci. **57**, 63–94 (2012).
80. C.-Y. Li and M. Tomozawa, "Fictive temperature and fictive pressure measurement of silica glasses using FTIR method: For thick samples and samples containing Si–H," J. Non Cryst. Solids **358**, 3365–3371 (2012).
81. D. Neuville, M. Cicconi, W. Blanc, and L. M., "Applications of Raman spectroscopy, a tool to investigate glass structure and glass fiber," (n.d.).
82. B. Hehlen and B. Rufflé, "Atomic Vibrations in Glasses," arXiv [cond-mat.dis-nn] (2019).
83. P. Mcmillan, "Structural studies of silicate glasses and melts-applications and limitations of Raman spectroscopy," American Mineralogist **69**, 622–644 (1984).
84. J. Burgin, C. Guillon, P. Langot, F. Vallée, B. Hehlen, and M. Foret, "Vibrational modes and local order in permanently densified silica glasses: Femtosecond and Raman spectroscopy study," Phys. Rev. B Condens. Matter Mater. Phys. **78**, (2008).
85. F. L. Galeener, "Planar rings in vitreous silica," J. Non Cryst. Solids **49**, 53–62 (1982).
86. F. L. Galeener and A. E. Geissberger, "Vibrational dynamics inSi30-substituted vitreous SiO2," Phys. Rev. B Condens. Matter **27**, 6199–6204 (1983).
87. B. Humbert, A. Burneau, J. P. Gallas, and J. C. Lavalley, "Origin of the Raman bands,

D1 and D2, in high surface area and vitreous silicas," J. Non Cryst. Solids **143**, 75–83 (1992).
88. S. K. Sharma, J. F. Mammone, and M. F. Nicol, "Raman investigation of ring configurations in vitreous silica," Nature **292**, 140–141 (1981).
89. A. Pasquarello and R. Car, "Identification of Raman defect lines as signatures of ring structures in vitreous silica," Phys. Rev. Lett. **80**, 5145–5147 (1998).
90. H. Kragh, "The Lorenz-Lorentz formula: Origin and early history," Substantia **2**, 7–18 (2018).
91. R. E. Schenker and W. G. Oldham, "Ultraviolet-induced densification in fused silica," J. Appl. Phys. **82**, 1065–1071 (1997).
92. J. E. Shelby, "Effect of radiation on the physical properties of borosilicate glasses," J. Appl. Phys. **51**, 2561–2565 (1980).
93. F. Durr, "Laser-induced stress changes in optical fibers," École Polytechnique Fédérale de Lausanne (2005).
94. L. Huang, L. Duffrène, and J. Kieffer, "Structural transitions in silica glass: thermo-mechanical anomalies and polyamorphism," J. Non Cryst. Solids **349**, 1–9 (2004).
95. B. M. Hauke, A. M. Bossen, and J. C. Mauro, "Experimental and computational methods for studying relaxation of aluminosilicate glasses: A review," Journal of the American Ceramic Society **e20440**, 0002–7820 (2025).
96. R. O. Davies and G. O. Jones, "Thermodynamic and kinetic properties of glasses," Adv. Phys. **2**, 370–410 (1953).
97. S. Spinner, "Temperature dependence of elastic constants of vitreous silica," J. Am. Ceram. Soc. **45**, 394–397 (1962).
98. R. Brückner, "Metastable equilibrium density of hydroxyl-free synthetic vitreous silica," J. Non Cryst. Solids **5**, 281–285 (1971).
99. C. Weigel, M. Mebarki, S. Clément, R. Vacher, M. Foret, and B. Rufflé, "Pressure-induced densification of vitreous silica: Insight from elastic properties," Phys. Rev. B. **100**, (2019).
100. L. P. Dávila, M.-J. Caturla, A. Kubota, B. Sadigh, T. Díaz de la Rubia, J. F. Shackelford, S. H. Risbud, and S. H. Garofalini, "Transformations in the medium-range order of fused silica under high pressure," Phys. Rev. Lett. **91**, 205501 (2003).
101. K. Suito, M. Miyoshi, T. Sasakurau, and H. Fujisawa, "Elastic properties of obsidian, vitreous SiO2, and vitreous GeO2under high pressure up to 6 GPa," in *High-Pressure Research: Application to Earth and Planetary Sciences* (American Geophysical Union, 2013), pp. 219–225.
102. C. Sonneville, A. Mermet, B. Champagnon, C. Martinet, J. Margueritat, D. de Ligny, T. Deschamps, and F. Balima, "Progressive transformations of silica glass upon densification," J. Chem. Phys. **137**, 124505 (2012).
103. P. W. Bridgman and I. Simon, "Effects of very high pressures on glass," in *Papers 169-199* (Harvard University Press, 1964), pp. 4291–4299.
104. A. Polian and M. Grimsditch, "Room-temperature densification of a-SiO2 versus pressure," Phys. Rev. B Condens. Matter **41**, 6086–6087 (1990).
105. T. Rouxel, H. Ji, T. Hammouda, and A. Moréac, "Poisson's ratio and the densification of glass under high pressure," Phys. Rev. Lett. **100**, 225501 (2008).

106. T. Deschamps, A. Kassir-Bodon, C. Sonneville, J. Margueritat, C. Martinet, D. de Ligny, A. Mermet, and B. Champagnon, "Permanent densification of compressed silica glass: a Raman-density calibration curve," J. Phys. Condens. Matter **25**, 025402 (2013).
107. C. Dereure, "Comportement mécanique des verres sous choc produit par interaction laser-matière : une approche expérimentale et numérique multi-échelles," L'Universite de Rennes (2019).
108. M. Guerette, M. R. Ackerson, J. Thomas, F. Yuan, E. Bruce Watson, D. Walker, and L. Huang, "Structure and properties of silica glass densified in cold compression and hot compression," Sci. Rep. **5**, 15343 (2015).
109. C. Martinet, A. Kassir-Bodon, T. Deschamps, A. Cornet, S. Le Floch, V. Martinez, and B. Champagnon, "Permanently densified SiO2 glasses: a structural approach," J. Phys. Condens. Matter **27**, 325401 (2015).
110. Y. Onodera, S. Kohara, P. S. Salmon, A. Hirata, N. Nishiyama, S. Kitani, A. Zeidler, M. Shiga, A. Masuno, H. Inoue, S. Tahara, A. Polidori, H. E. Fischer, T. Mori, S. Kojima, H. Kawaji, A. I. Kolesnikov, M. B. Stone, M. G. Tucker, M. T. McDonnell, A. C. Hannon, Y. Hiraoka, I. Obayashi, T. Nakamura, J. Akola, Y. Fujii, K. Ohara, T. Taniguchi, and O. Sakata, "Structure and properties of densified silica glass: characterizing the order within disorder," NPG Asia Mater. **12**, (2020).
111. M. Zanatta, G. Baldi, R. S. Brusa, W. Egger, A. Fontana, E. Gilioli, S. Mariazzi, G. Monaco, L. Ravelli, and F. Sacchetti, "Structural evolution and medium range order in permanently densified vitreous SiO2," Phys. Rev. Lett. **112**, 045501 (2014).
112. R. A. Devine and J. Arndt, "Si-O bond-length modification in pressure-densified amorphous SiO2," Phys. Rev. B Condens. Matter **35**, 9376–9379 (1987).
113. B. T. Poe, C. Romano, and G. Henderson, "Raman and XANES spectroscopy of permanently densified vitreous silica," J. Non Cryst. Solids **341**, 162–169 (2004).
114. M. Heili, B. Poumellec, E. Burov, C. Gonnet, C. Le Losq, D. R. Neuville, and M. Lancry, "The dependence of Raman defect bands in silica glasses on densification revisited," J. Mater. Sci. **51**, 1659–1666 (2016).
115. J. E. Shelby, "Density of vitreous silica," J. Non Cryst. Solids **349**, 331–336 (2004).
116. A. Cornet, C. Martinet, V. Martinez, and D. de Ligny, "Evidence of polyamorphic transitions during densified SiO2 glass annealing," J. Chem. Phys. **151**, 164502 (2019).
117. A. Cornet, V. Martinez, D. de Ligny, B. Champagnon, and C. Martinet, "Relaxation processes of densified silica glass," J. Chem. Phys. **146**, 094504 (2017).
118. M. Mobasher, M. Lancry, J. Lu, D. Neuville, L. Bellot Gurlet, and N. Ollier, "Thermal relaxation of silica phases densified under electron irradiation," J. Non Cryst. Solids **597**, 121917 (2022).
119. M. Ono, Y. Tanabe, M. Fujioka, H. Yamada, K. Ohara, S. Kohara, M. Fujinami, and J. Nishii, "Direct observation of the topological pruning in silica glass network; the key for realizing extreme transparency," NPG Asia Mater. **17**, (2025).
120. S. J. Tracy, S. J. Turneaure, and T. S. Duffy, "In situ X-ray diffraction of shock-compressed fused silica," Phys. Rev. Lett. **120**, (2018).
121. M. B. Boslough, "Postshock temperatures in silica," J. Geophys. Res. **93**, 6477–

6484 (1988).
122. M. Okuno, B. Reynard, Y. Shimada, Y. Syono, and C. Willaime, "A Raman spectroscopic study of shock-wave densification of vitreous silica," Phys. Chem. Miner. **26**, 304–311 (1999).
123. J. Arndt, "Shock-wave densification of silica glass," Physics and Chemistry of Glasses **12**, 1–7 (1971).
124. C. Dereure, R. Hall, F. Baber, D. Loison, E. Lescoute, J.-P. Guin, J.-C. Sangleboeuf, L. Berthe, M. Nivard, and I. Guven, "Laser induced dynamic fracture of fused silica: Experiments and simulations," J. Non Cryst. Solids **511**, 125–139 (2019).
125. A. Radhakrishnan, J. Gateau, P. Vlugter, and Y. Bellouard, "Femtosecond laser-shockwave induced densification in fused silica," Opt. Mater. Express **12**, 2886 (2022).
126. S. Höfler and F. Seifert, "Volume relaxation of compacted SiO2 glass: a model for the conservation of natural diaplectic glasses," Earth Planet. Sci. Lett. **67**, 433–438 (1984).
127. J. Arndt, R. A. B. Devine, and A. G. Revesz, "Anomalous behaviour of the refractive index during the annealing of densified, amorphous SiO2," J. Non Cryst. Solids **131–133**, 1206–1212 (1991).
128. T. Loerting, K. Winkel, M. Seidl, M. Bauer, C. Mitterdorfer, P. H. Handle, C. G. Salzmann, E. Mayer, J. L. Finney, and D. T. Bowron, "How many amorphous ices are there?," Phys. Chem. Chem. Phys. **13**, 8783–8794 (2011).
129. O. Mishima, L. D. Calvert, and E. Whalley, "An apparently first-order transition between two amorphous phases of ice induced by pressure," Nature **314**, 76–78 (1985).
130. M. Grimsditch, "Polymorphism in amorphous SiO2," Phys. Rev. Lett. **52**, 2379–2381 (1984).
131. M. Courtois, A. Berthelot, A. Cornet, S. Le Floch, C. Martinet, and T. Deschamps, "Pressure-induced amorphous-amorphous transition in pre-densified silica glass: an experimental exploration of the potential energy landscape," Sci. Rep. **15**, 6719 (2025).
132. S. Girard, A. Morana, A. Ladaci, T. Robin, L. Mescia, J.-J. Bonnefois, M. Boutillier, J. Mekki, A. Paveau, B. Cadier, E. Marin, Y. Ouerdane, and A. Boukenter, "Recent advances in radiation-hardened fiber-based technologies for space applications," J. Opt. **20**, 093001 (2018).
133. N. Ollier, S. Girard, and S. Peuget, "Radiation Effects in Glass," Encyclopedia of Glass Science, Technology, History, and Culture 405–414 (2021).
134. F. Piao, W. G. Oldham, and E. E. Haller, "The mechanism of radiation-induced compaction in vitreous silica," J. Non Cryst. Solids **276**, 61–71 (2000).
135. R. A. B. Devine, "Macroscopic and microscopic effects of radiation in amorphous SiO2," Nucl. Instrum. Methods Phys. Res. B **91**, 378–390 (1994).
136. N. Ollier, S. Girard, and S. Peuget, "Radiation effects in glass," Encyclopedia of Glass Science (2021).
137. G. Buscarino, S. Agnello, F. M. Gelardi, and R. Boscaino, "Polyamorphic transformation induced by electron irradiation ina-SiO2glass," Phys. Rev. B

Condens. Matter Mater. Phys. **80**, (2009).
138. L. Douillard and J. P. Duraud, "Swift heavy ion amorphization of quartz — a comparative study of the particle amorphization mechanism of quartz," Nucl. Instrum. Methods Phys. Res. B **107**, 212–217 (1996).
139. J.-M. Delaye, S. Peuget, G. Bureau, and G. Calas, "Molecular dynamics simulation of radiation damage in glasses," J. Non Cryst. Solids **357**, 2763–2768 (2011).
140. B. Boizot, S. Agnello, B. Reynard, R. Boscaino, and G. Petite, "Raman spectroscopy study of β-irradiated silica glass," J. Non Cryst. Solids **325**, 22–28 (2003).
141. N. Ollier, M. Lancry, C. Martinet, V. Martinez, S. Le Floch, and D. Neuville, "Relaxation study of pre-densified silica glasses under 2.5 MeV electron irradiation"," Scientific Reports **9**, (2019).
142. T. Gavenda, O. Gedeon, and K. Jurek, "Irradiation induced densification and its correlation with three-membered rings in vitreous silica," J. Non Cryst. Solids **425**, 61–66 (2015).
143. V. K. Malinovsky, V. N. Novikov, N. V. Surovtsev, and A. P. Shebanin, "Investigation of amorphous states of SiO2 by Raman scattering spectroscopy," Phys. Solid State **42**, 65–71 (2000).
144. S. Sugai, H. Sotokawa, D. Kyokane, and A. Onodera, "Bose peak in the Raman spectra of densified SiO2 and GeO2 glass under high pressure," Physica B Condens. Matter **219–220**, 293–295 (1996).
145. Y. A. Kuznetsova and A. N. Kiryakov, "Static and dynamic disorder in ion-implanted silica glass," J. Non Cryst. Solids **631**, 122936 (2024).
146. N. Ollier, K. Piven, C. Martinet, T. Billotte, V. Martinez, D. R. Neuville, and M. Lancry, "Impact of glass density on the green emission and NBOHC formation in silica glass: A combined high pressure and 2.5 MeV electron irradiation," J. Non Cryst. Solids **476**, 81–86 (2017).
147. R. A. Devine, "Radiation-sensitivity enhancement and annealing variation in densified, amorphous SiO2," Phys. Rev. B Condens. Matter **35**, 9783–9789 (1987).
148. R. A. B. Devine, "Radiation damage and the role of structure in amorphous SiO2," Nucl. Instrum. Methods Phys. Res. B **46**, 244–251 (1990).
149. R. A. Devine and J. Arndt, "Correlated defect creation and dose-dependent radiation sensitivity in amorphous SiO2," Phys. Rev. B Condens. Matter **39**, 5132–5138 (1989).
150. M. Hasegawa, M. Saneyasu, M. Tabata, Z. Tang, Y. Nagai, T. Chiba, and Y. Ito, "Positron and positronium studies of irradiation-induced defects and microvoids in vitreous metamict silica," Nucl. Instrum. Methods Phys. Res. B **166–167**, 431–439 (2000).
151. A. V. Bondarenko, A. P. Dyad'kin, Y. A. Kashchuk, A. V. Krasil'nikov, G. A. Polyakov, I. N. Rastyagaev, D. A. Skopintsev, S. N. Tugarinov, V. P. Yartsev, V. A. Bogatyrev, A. L. Tomashuk, S. N. Klyamkin, and S. E. Bender, "A study of radiation resistance of silica optical fibers under conditions of reactor irradiation," Instrum. Exp. Tech. **49**, 190–198 (2006).
152. G. Buscarino, S. Agnello, and F. M. Gelardi, "Structural modifications induced by electron irradiation in SiO 2 glass: Local densification measurements," EPL **87**,

26007 (2009).
153. G. Buscarino, E. Vella, G. Navarra, and R. Boscaino, "A two-component model for the 2260cm−1 infrared absorption band in electron irradiated amorphous SiO2," J. Non Cryst. Solids **357**, 1926–1930 (2011).
154. I. Reghioua, M. Lancry, O. Cavani, S. L. Floch, D. R. Neuville, and N. Ollier, "Unique silica polymorph obtained under electron irradiation”," Applied Physics Letters **115**, (2019).
155. R. A. Devine, "Macroscopic and microscopic efects of radiation in amorphous SiO2," Nucl. Instrum. Methods Phys. Res **91**, 378–390 (1994).
156. N. F. Borrelli, C. Smith, D. C. Allan, and T. P. Seward, "Densification of fused silica under 193-nm excitation," J. Opt. Soc. Am. B **14**, 1606 (1997).
157. S. Hirsch, H. Klein, and P. Jung, "Dimensional changes of silica-, borosilicate- and germania-glasses and quartz under irradiation," J. Non Cryst. Solids **351**, 3279–3288 (2005).
158. W. Primak, "Mechanism for the radiation compaction of vitreous silica," J. Appl. Phys. **43**, 2745–2754 (1972).
159. L. Douillard and J. P. Duraud, "Amorphization of α-quartz under irradiation," Journal de physique III **6**, 1677–1687 (1996).
160. J.-Y. Cheng, M. M. J. Treacy, and P. J. Keblinski, "Metamict transformation of silica," Mater. Res. Soc. Symp. Proc. **762**, (2003).
161. J. B. Bates, R. W. Hendricks, and L. B. Shaffer, "Neutron irradiation effects and structure of noncrystalline SiO2," J. Chem. Phys. **61**, 4163–4176 (1974).
162. J. P. Bonnet, M. Boissier, and A. Ait Gherbi, "The amorphization process of neutron-irradiated crystalline quartz studied by Brillouin scattering," J. Non Cryst. Solids **167**, 199–204 (1994).
163. L. W. Hobbs and M. R. Pascucci, "Radiolysis and defect structure in electron-irradiated α-quartz," J. Phys., Colloq. **41**, C6-237-C6-242 (1980).
164. L. W. Hobbs, "The role of topology and geometry in the irradiation-induced amorphization of network structures," J. Non Cryst. Solids **182**, 27–39 (1995).
165. L. Douillard and J. P. Duraud, "Amorphization of ?-Quartz under Irradiation," J. Phys. III **6**, 1677–1687 (1996).
166. N. Ollier, I. Reghioua, O. Cavani, M. Mobasher, A. Alessi, S. le Floch, and L. Skuja, "Probing densified silica glass structure by molecular oxygen and E’ center formation under electron irradiation," Sci. Rep. **13**, 13657 (2023).
167. R. Stoian, "Volume photoinscription of glasses: three-dimensional micro- and nanostructuring with ultrashort laser pulses," Appl. Phys. A Mater. Sci. Process. **126**, (2020).
168. C. B. Schaffer, J. F. García, and E. Mazur, "Bulk heating of transparent materials using a high-repetition-rate femtosecond laser," Appl. Phys. A Mater. Sci. Process. **76**, 351–354 (2003).
169. M. Lancry, N. Groothoff, B. Poumellec, S. Guizard, N. Fedorov, and J. Canning, "Time-resolved plasma measurements in Ge-doped silica exposed to infrared femtosecond laser," Phys. Rev. B Condens. Matter Mater. Phys. **84**, (2011).
170. S. S. Mao, F. Quéré, S. Guizard, X. Mao, R. E. Russo, G. Petite, and P. Martin,

"Dynamics of femtosecond laser interactions with dielectrics," Appl. Phys. A Mater. Sci. Process. **79**, 1695–1709 (2004).
171. L. Gao, Q. Zhang, and M. Gu, "Femtosecond laser micro/nano processing: from fundamental to applications," Int. J. Extrem. Manuf. **7**, 022010 (2025).
172. T. Yoshino, Y. Ozeki, M. Matsumoto, and K. Itoh, "In situ micro-Raman investigation of spatio-temporal evolution of heat in ultrafast laser microprocessing of glass," Jpn. J. Appl. Phys. (2008) **51**, 102403 (2012).
173. S. Eaton, H. Zhang, P. Herman, F. Yoshino, L. Shah, J. Bovatsek, and A. Arai, "Heat accumulation effects in femtosecond laser-written waveguides with variable repetition rate," Opt. Express **13**, 4708–4716 (2005).
174. O. Koritsoglou, G. Duchateau, O. Utéza, and A. Mouskeftaras, "Quantitative assessment of femtosecond laser-induced stress waves in fused silica," Phys. Rev. B. **110**, (2024).
175. A. Rudenko, J. V. Moloney, and P. Polynkin, "Ionization clamping in ultrafast optical breakdown of transparent solids," Phys. Rev. Appl. **20**, 064035 (2023).
176. Y. Bellouard, A. Champion, B. McMillen, S. Mukherjee, R. R. Thomson, C. Pépin, P. Gillet, and Y. Cheng, "Stress-state manipulation in fused silica via femtosecond laser irradiation," Optica **3**, 1285 (2016).
177. B. Poumellec, L. Sudrie, M. Franco, B. Prade, and A. Mysyrowicz, "Femtosecond laser irradiation stress induced in pure silica," Opt. Express **11**, 1070–1079 (2003).
178. V. R. Bhardwaj, P. B. Corkum, D. M. Rayner, C. Hnatovsky, E. Simova, and R. S. Taylor, "Stress in femtosecond-laser-written waveguides in fused silica," Opt. Lett. **29**, 1312–1314 (2004).
179. K. Mishchik, C. D'Amico, P. K. Velpula, C. Mauclair, A. Boukenter, Y. Ouerdane, and R. Stoian, "Ultrafast laser induced electronic and structural modifications in bulk fused silica," J. Appl. Phys. **114**, 133502 (2013).
180. K. Itoh, W. Watanabe, S. Nolte, and C. B. Schaffer, "Ultrafast processes for bulk modification of transparent materials," MRS Bull. **31**, 620–625 (2006).
181. C. B. Schaffer, A. Brodeur, and E. Mazur, "Laser-induced breakdown and damage in bulk transparent materials induced by tightly focused femtosecond laser pulses," Meas. Sci. Technol. **12**, 1784–1794 (2001).
182. S. Guizard, P. Martin, G. Petite, P. D'Oliveira, and P. Meynadier, "Time-resolved study of laser-induced colour centres in," J. Phys. Condens. Matter **8**, 1281–1290 (1996).
183. H. S. Carslaw, J. C. Jaeger, L. R. Ingersoll, O. J. Zobel, A. C. Ingersoll, and J. H. Van Vleck, "*conduction of heat in solids* and *heat conduction*," Phys. Today **1**, 24–24 (1948).
184. C. B. Schaffer and A. Brodeur, "Laser-induced breakdown and damage in bulk transparent materials induced by tighly focused femtosecond laser pulses," Measurement Science Technology **12**, 1784–1794 (2001).
185. Q. Xie, M. Cavillon, and M. Lancry, "Modeling nanogratings erasure at high repetition rate in commercial optical glasses," Ceram. Int. (2024).
186. R. Que, M. Lancry, and B. Poumellec, "Useable analytical expressions for temperature distribution induced by ultrafast laser pulses in dielectric solids,"

Micromachines **15**, (2024).
187. A. M. Streltsov and N. F. Borrelli, "Study of femtosecond-laser-written waveguides in glasses," J. Opt. Soc. Am. B **19**, 2496 (2002).
188. M. Lenzner, J. Krüger, W. Kautek, and F. Krausz, "Incubation of laser ablation in fused silica with 5-fs pulses," Appl. Phys. A Mater. Sci. Process. **69**, 465–466 (1999).
189. D. Ashkenasi, M. Lorenz, R. Stoian, and A. Rosenfeld, "Surface damage threshold and structuring of dielectrics using femtosecond laser pulses: the role of incubation," Appl. Surf. Sci. **150**, 101–106 (1999).
190. R. Stoian, "Investigations of the dynamics of material removal in ultrashort pulsed laser ablation of dielectrics," (2001).
191. J. Cao, M. Lancry, F. Brisset, L. Mazerolles, R. Saint-Martin, and B. Poumellec, "Femtosecond laser-induced crystallization in glasses: Growth dynamics for orientable nanostructure and nanocrystallization," Cryst. Growth Des. **19**, 2189–2205 (2019).
192. X. He, C. Fan, B. Poumellec, F. Brisset, Q. Liu, H. Zeng, G. Chen, X. Zhao, and M. Lancry, "Controllable 3D crystallization in SiO2-based glasses by femtosecond laser," MATEC Web Conf. **8**, 02009 (2013).
193. F. Zimmermann, M. Lancry, A. Plech, S. Richter, T. Ullsperger, B. Poumellec, A. Tünnermann, and S. Nolte, "Ultrashort pulse laser processing of silica at high repetition rates—from network change to residual strain," Int. J. Appl. Glass Sci. **8**, 233–238 (2017).
194. D. Tan, K. N. Sharafudeen, Y. Yue, and J. Qiu, "Femtosecond laser induced phenomena in transparent solid materials: Fundamentals and applications," Prog. Mater. Sci. **76**, 154–228 (2016).
195. B. Poumellec, M. Lancry, A. Chahid-Erraji, and P. G. Kazansky, "Modification thresholds in femtosecond laser processing of pure silica: review of dependencies on laser parameters [Invited]," Opt. Mater. Express **1**, 766 (2011).
196. K. Miura, J. Qiu, H. Inouye, T. Mitsuyu, and K. Hirao, "Photowritten optical waveguides in various glasses with ultrashort pulse laser," Appl. Phys. Lett. **71**, 3329–3331 (1997).
197. C. Hnatovsky, R. S. Taylor, P. P. Rajeev, E. Simova, V. R. Bhardwaj, D. M. Rayner, and P. B. Corkum, "Pulse duration dependence of femtosecond-laser-fabricated nanogratings in fused silica," Appl. Phys. Lett. **87**, 014104 (2005).
198. S. Juodkazis, K. Nishimura, S. Tanaka, H. Misawa, E. G. Gamaly, B. Luther-Davies, L. Hallo, P. Nicolai, and V. T. Tikhonchuk, "Laser-induced microexplosion confined in the bulk of a sapphire crystal: evidence of multimegabar pressures," Phys. Rev. Lett. **96**, 166101 (2006).
199. P. P. Rajeev, M. Gertsvolf, P. B. Corkum, and D. M. Rayner, "Field dependent avalanche ionization rates in dielectrics," Phys. Rev. Lett. **102**, 083001 (2009).
200. S. Onda, W. Watanabe, K. Yamada, K. Itoh, and J. Nishii, "Study of filamentary damage in synthesized silica induced by chirped femtosecond laser pulses," J. Opt. Soc. Am. B **22**, 2437 (2005).
201. M. Sakakura, Y. Lei, L. Wang, Y.-H. Yu, and P. G. Kazansky, "Ultralow-loss geometric phase and polarization shaping by ultrafast laser writing in silica glass,"

Light Sci. Appl. **9**, 15 (2020).
202. Y. Lei, H. Wang, L. Skuja, B. Kühn, B. Franz, Y. Svirko, and P. G. Kazansky, "Ultrafast laser writing in different types of silica glass," Laser Photon. Rev. **17**, 2200978 (2023).
203. Y. Lei, G. Shayeganrad, H. Wang, M. Sakakura, Y. Yu, L. Wang, D. Kliukin, L. Skuja, Y. Svirko, and P. G. Kazansky, "Efficient ultrafast laser writing with elliptical polarization," Light Sci. Appl. **12**, 74 (2023).
204. G. Shayeganrad, X. Chang, H. Wang, C. Deng, Y. Lei, and P. G. Kazansky, "High damage threshold birefringent elements produced by ultrafast laser nanostructuring in silica glass," Opt. Express **30**, 41002–41011 (2022).
205. H. Wang, Y. Lei, G. Shayeganrad, Y. Svirko, and P. G. Kazansky, "Increasing efficiency of ultrafast laser writing via nonlocality of light - matter interaction," Laser Photon. Rev. **18**, (2024).
206. H. Wang, Y. Lei, L. Wang, M. Sakakura, Y. Yu, G. Shayeganrad, and P. G. Kazansky, "100 - layer error - free 5D optical data storage by ultrafast laser nanostructuring in glass," Laser Photon. Rev. **16**, 2100563 (2022).
207. C. B. Schaffer and E. Mazur, "Micromachining using ultrashort pulses from a laser oscillator," Opt. Photonics News **12**, 20 (2001).
208. A. Couairon, L. Sudrie, M. Franco, B. Prade, and A. Mysyrowicz, "Filamentation and damage in fused silica induced by tightly focused femtosecond laser pulses," Phys. Rev. B Condens. Matter Mater. Phys. **71**, (2005).
209. I. Zergioti, K. D. Kyrkis, D. G. Papazoglou, and S. Tzortzakis, "Structural modifications in fused silica induced by ultraviolet fs laser filaments," Appl. Surf. Sci. **253**, 7865–7868 (2007).
210. D. Grobnic, C. W. Smelser, S. J. Mihailov, and R. B. Walker, "Long-term thermal stability tests at 1000 °C of silica fibre Bragg gratings made with ultrafast laser radiation," Meas. Sci. Technol. **17**, 1009–1013 (2006).
211. M. Royon, E. Marin, S. Girard, A. Boukenter, Y. Ouerdane, and R. Stoian, "X-ray preconditioning for enhancing refractive index contrast in femtosecond laser photoinscription of embedded waveguides in pure silica," Opt. Mater. Express **9**, 65 (2019).
212. T. T. Fernandez, B. Johnston, H. Mahmodi, K. Privat, I. Kabakova, S. Gross, M. Withford, and A. Fuerbach, "Thermally stable high numerical aperture integrated waveguides and couplers for the 3 μm wavelength range," APL Photonics **7**, 126106 (2022).
213. S. M. Eaton, M. L. Ng, R. Osellame, and P. R. Herman, "High refractive index contrast in fused silica waveguides by tightly focused, high-repetition rate femtosecond laser," J. Non Cryst. Solids **357**, 2387–2391 (2011).
214. K. Hirao and K. Miura, "Writing waveguides and gratings in silica and related materials by a femtosecond laser," J. Non Cryst. Solids **239**, 91–95 (1998).
215. A. M. Streltsov and N. F. Borrelli, "Study of femtosecond-laser-written waveguides in glasses," J. Opt. Soc. Am. B **19**, 2496–2504 (2002).
216. A. Saliminia, R. Vallée, and S. L. Chin, "Waveguide writing in silica glass with femtosecond pulses from an optical parametric amplifier at 1.5µm," Opt. Commun.

256, 422–427 (2005).
217. P. Dekker, M. Ams, G. D. Marshall, D. J. Little, and M. J. Withford, "Annealing dynamics of waveguide Bragg gratings: evidence of femtosecond laser induced colour centres," Opt. Express **18**, 3274–3283 (2010).
218. A. Saliminia, R. Vallée, and S. L. Chin, "Waveguide writing in silica glass with femtosecond pulses from an optical parametric amplifier at 1.5um," Optics Communications **256**, 422–427 (2005).
219. J. W. Chan, T. R. Huser, S. H. Risbud, and D. M. Krol, "Modification of the fused silica glass network associated with waveguide fabrication using femtosecond laser pulses," Appl. Phys. A Mater. Sci. Process. **76**, 367–372 (2003).
220. M. Beresna, M. Gecevičius, M. Lancry, B. Poumellec, and P. G. Kazansky, "Broadband anisotropy of femtosecond laser induced nanogratings in fused silica," Appl. Phys. Lett. **103**, 131903 (2013).
221. M. Royon, "Ingénierie de verres de silice : influence de pré-traitements sur la variation d'indice de réfraction de guides d'ondes photo-inscrits par laser femtoseconde," Université Jean Monnet (2018).
222. L. Bressel, D. de Ligny, C. Sonneville, V. Martinez, V. Mizeikis, R. Buividas, and S. Juodkazis, "Femtosecond laser induced density changes in GeO_2 and SiO_2 glasses: fictive temperature effect [Invited]," Opt. Mater. Express **1**, 605 (2011).
223. J. W. Chan, T. Huser, S. Risbud, and D. M. Krol, "Structural changes in fused silica after exposure to focused femtosecond laser pulses," Opt. Lett. **26**, 1726–1728 (2001).
224. Y. Bellouard, E. Barthel, A. A. Said, M. Dugan, and P. Bado, "Scanning thermal microscopy and Raman analysis of bulk fused silica exposed to lowenergy femtosecond laser pulses," Opt. Express **16**, 19520 (2008).
225. K.-I. Kawamura, N. Sarukura, M. Hirano, and H. Hosono, "Holographic encoding of fine-pitched micrograting structures in amorphous SiO2 thin films on silicon by a single femtosecond laser pulse," Appl. Phys. Lett. **78**, 1038–1040 (2001).
226. Y. Bellouard, T. Colomb, C. Depeursinge, M. Dugan, A. A. Said, and P. Bado, "Nanoindentation and birefringence measurements on fused silica specimen exposed to low-energy femtosecond pulses," Opt. Express **14**, 8360–8366 (2006).
227. M. Lancry, B. Poumellec, A. Chahid-Erraji, M. Beresna, and P. G. Kazansky, "Dependence of the femtosecond laser refractive index change thresholds on the chemical composition of doped-silica glasses," Opt. Mater. Express **1**, 711 (2011).
228. M. Lancry, B. Poumellec, A. Chahid-Erraji, M. Beresna, and P. G. Kazansky, "Dependence of the femtosecond laser refractive index change thresholds on the chemical composition of doped-silica glasses," Opt. Mater. Express **1**, 711–723 (2011).
229. J. Tian, H. Yao, M. Cavillon, E. Garcia-Caurel, R. Ossikovski, M. Stchakovsky, C. Eypert, B. Poumellec, and M. Lancry, "A comparison between nanogratings-based and stress-engineered waveplates written by femtosecond laser in silica," Micromachines **11**, 131 (2020).
230. E. Bricchi, B. G. Klappauf, and P. G. Kazansky, "Form birefringence and negative index change created by femtosecond direct writing in transparent materials," Opt.

Lett. **29**, 119–121 (2004).
231. J. Zhang, M. Gecevičius, M. Beresna, and P. G. Kazansky, "Seemingly unlimited lifetime data storage in nanostructured glass," Phys. Rev. Lett. **112**, 033901 (2014).
232. E. Bricchi and P. G. Kazansky, "Extraordinary stability of anisotropic femtosecond direct-written structures embedded in silica glass," Appl. Phys. Lett. **88**, 111119 (2006).
233. Y. Wang, M. Lancry, M. Cavillon, and B. Poumellec, "Lifetime prediction of nanogratings inscribed by a femtosecond laser in silica glass," Opt. Lett. **47**, 1242–1245 (2022).
234. M. Lancry, B. Poumellec, J. Canning, K. Cook, J.-C. Poulin, and F. Brisset, "Ultrafast nanoporous silica formation driven by femtosecond laser irradiation," Laser Photon. Rev. **7**, 953–962 (2013).
235. Y. Shimotsuma, M. Sakakura, P. G. Kazansky, M. Beresna, J. Qiu, K. Miura, and K. Hirao, "Ultrafast manipulation of self-assembled form birefringence in glass," Adv. Mater. **22**, 4039–4043 (2010).
236. A. Champion and Y. Bellouard, "Direct volume variation measurements in fused silica specimens exposed to femtosecond laser," Opt. Mater. Express **2**, 789 (2012).
237. Y. Wang, M. Cavillon, N. Ollier, B. Poumellec, and M. Lancry, "An overview of the thermal erasure mechanisms of femtosecond laser‐induced nanogratings in silica glass," Phys. Status Solidi (A) **218**, 2100023 (2021).
238. Q. Xie, "Mécanismes de formation et effacement des nanoréseaux dans les verres d'oxyde par écriture directe laser femtoseconde," Université Paris-Saclay (2024).
239. J. Lu, J. Tian, B. Poumellec, E. Garcia-Caurel, R. Ossikovski, X. Zeng, and M. Lancry, "Tailoring chiral optical properties by femtosecond laser direct writing in silica," Light Sci. Appl. **12**, 46 (2023).
240. J. Lu, E. Garcia-Caurel, R. Ossikovski, F. Courvoisier, X. Zeng, B. Poumellec, and M. Lancry, "Femtosecond laser direct writing multilayer chiral waveplates with minimal linear birefringence," Opt. Lett. **48**, 271–274 (2023).
241. H. Yao, Q. Xie, M. Cavillon, Y. Dai, and M. Lancry, "Materials roadmap for inscription of nanogratings inside transparent dielectrics using ultrafast lasers," Prog. Mater. Sci. **142**, 101226 (2024).
242. A. Rudenko, J.-P. Colombier, T. E. Itina, and R. Stoian, "Genesis of nanogratings in silica bulk via multipulse interplay of ultrafast photo‐excitation and hydrodynamics," Adv. Opt. Mater. **9**, 2100973 (2021).
243. S. Richter, F. Jia, M. Heinrich, S. Döring, U. Peschel, A. Tünnermann, and S. Nolte, "The role of self-trapped excitons and defects in the formation of nanogratings in fused silica," Opt. Lett. **37**, 482–484 (2012).
244. R. Taylor, C. Hnatovsky, and E. Simova, "Applications of femtosecond laser induced self-organized planar nanocracks inside fused silica glass," Laser Photon. Rev. **2**, 26–46 (2008).
245. R. Buschlinger, S. Nolte, and U. Peschel, "Self-organized pattern formation in laser-induced multiphoton ionization," Phys. Rev. B Condens. Matter Mater. Phys. **89**, (2014).

246. A. Rudenko, J.-P. Colombier, and T. E. Itina, "From random inhomogeneities to periodic nanostructures induced in bulk silica by ultrashort laser," Phys. Rev. B. **93**, (2016).
247. E. Gribaudo, M. Deckart, P. Vlugter, and Y. Bellouard, "Sub-wavelength femtosecond laser based nanostructuring of complex patterns in the bulk of fused silica," Opt. Express **33**, 11529 (2025).
248. Y. Liao, W. Pan, Y. Cui, L. Qiao, Y. Bellouard, K. Sugioka, and Y. Cheng, "Formation of in-volume nanogratings with sub-100-nm periods in glass by femtosecond laser irradiation," Opt. Lett. **40**, 3623–3626 (2015).
249. Y. Liao, J. Ni, L. Qiao, M. Huang, Y. Bellouard, K. Sugioka, and Y. Cheng, "High-fidelity visualization of formation of volume nanogratings in porous glass by femtosecond laser irradiation," Optica **2**, 329 (2015).
250. Y. Liao, Y. Shen, L. Qiao, D. Chen, Y. Cheng, K. Sugioka, and K. Midorikawa, "Femtosecond laser nanostructuring in porous glass with sub-50 nm feature sizes," Opt. Lett. **38**, 187–189 (2013).
251. V. R. Bhardwaj, E. Simova, P. P. Rajeev, C. Hnatovsky, R. S. Taylor, D. M. Rayner, and P. B. Corkum, "Optically produced arrays of planar nanostructures inside fused silica," Phys. Rev. Lett. **96**, 057404 (2006).
252. P. P. Rajeev, M. Gertsvolf, C. Hnatovsky, E. Simova, R. S. Taylor, P. B. Corkum, D. M. Rayner, and V. R. Bhardwaj, "Transient nanoplasmonics inside dielectrics," J. Phys. B At. Mol. Opt. Phys. **40**, S273–S282 (2007).
253. J. Canning, M. Lancry, K. Cook, A. Weickman, F. Brisset, and B. Poumellec, "Anatomy of a femtosecond laser processed silica waveguide [Invited]," Opt. Mater. Express **1**, 998 (2011).
254. S. Richter, A. Plech, M. Steinert, M. Heinrich, S. Döring, F. Zimmermann, U. Peschel, E. B. Kley, A. Tünnermann, and S. Nolte, "On the fundamental structure of femtosecond laser-induced nanogratings," Laser Photon. Rev. **6**, 787–792 (2012).
255. M. Lancry, J. Canning, K. Cook, M. Heili, D. R. Neuville, and B. Poumellec, "Nanoscale femtosecond laser milling and control of nanoporosity in the normal and anomalous regimes of GeO_2-SiO_2 glasses," Opt. Mater. Express **6**, 321 (2016).
256. A. Rudenko, J.-P. Colombier, and T. Itina, "Nanopore-mediated ultrashort laser-induced formation and erasure of volume nanogratings in glass," Phys. Chem. Chem. Phys. **20**, 5887–5899 (2018).
257. F. Zimmermann, M. Lancry, A. Plech, S. Richter, B. H. Babu, B. Poumellec, A. Tünnermann, and S. Nolte, "Femtosecond laser written nanostructures in Ge-doped glasses," Opt. Lett. **41**, 1161–1164 (2016).
258. F. Zimmermann, A. Plech, S. Richter, A. Tünnermann, and S. Nolte, "Ultrashort laser pulse induced nanogratings in borosilicate glass," Appl. Phys. Lett. **104**, 211107 (2014).
259. Q. Xie, M. Cavillon, B. Poumellec, and M. Lancry, "Upper temperature limit for nanograting survival in oxide glasses: publisher's note," Appl. Opt. **62**, 7156 (2023).
260. A. Zoubir, C. Rivero, R. Grodsky, K. Richardson, M. Richardson, T. Cardinal, and M. Couzi, "Laser-induced defects in fused silica by femtosecond IR irradiation,"

Phys. Rev. B Condens. Matter Mater. Phys. **73**, (2006).
261. P. N. Saeta and B. I. Greene, "Primary relaxation processes at the band edge of SiO 2," Physical review letters **70**, (1993).
262. A. Martinez, I. Y. Khrushchev, and I. Bennion, "Thermal properties of fibre Bragg gratings inscribed point-by-point by infrared femtosecond laser," Electron. Lett. **41**, 176–178 (2005).
263. Y. Wang, M. Cavillon, N. Ollier, B. Poumellec, and M. Lancry, "An Overview of the Thermal Erasure Mechanisms of Femtosecond Laser-Induced Nanogratings in Silica Glass"," Physica status solidi (2021).
264. J. J. Witcher, W. J. Reichman, L. B. Fletcher, N. W. Troy, and D. M. Krol, "Thermal annealing of femtosecond laser written structures in silica glass," Opt. Mater. Express **3**, 502 (2013).
265. P. Vlugter, E. Block, and Y. Bellouard, "Local tuning of fused silica thermal expansion coefficient using femtosecond laser," Phys. Rev. Mater. **3**, (2019).
266. P. Vlugter and Y. Bellouard, "Elastic properties of self-organized nanogratings produced by femtosecond laser exposure of fused silica," Phys. Rev. Mater. **4**, (2020).
267. P. Vlugter and Y. Bellouard, "Abnormal temperature dependent elastic properties of fused silica irradiated by ultrafast lasers," Phys. Rev. Mater. **6**, (2022).
268. Y. Gaillard, A. Radhakrishnan, Y. Bellouard, and F. Amiot, "Sub-micron elastic properties measurement of single laser-affected volume in fused silica," J. Non Cryst. Solids **652**, 123399 (2025).
269. C. B. Schaffer, A. Brodeur, N. Nishimura, and E. Mazur, "Laser-induced microexplosions in transparent materials: microstructuring with nanojoules," in *Commercial and Biomedical Applications of Ultrafast Lasers*, M. K. Reed and J. Neev, eds. (SPIE, 1999).
270. N. Varkentina, M. Dussauze, A. Royon, M. Ramme, Y. Petit, and L. Canioni, "High repetition rate femtosecond laser irradiation of fused silica studied by Raman spectroscopy," Opt. Mater. Express **6**, 79–90 (2016).
271. W. Watanabe, T. Toma, K. Yamada, J. Nishii, K. Hayashi, and K. Itoh, "Optical seizing and merging of voids in silica glass with infrared femtosecond laser pulses," Opt. Lett. **25**, 1669–1671 (2000).
272. S. Datta, R. Clady, D. Grojo, O. Utéza, and N. Sanner, "Scalable nanophotonic structures inside silica glass laser - machined by intense shaped beams," Laser Photon. Rev. **18**, (2024).
273. M. Sosa, M. Cavillon, T. Blanchet, G. Nemeth, F. Borondics, G. Laffont, and M. Lancry, "Micro-to-nanoscale characterization of femtosecond laser photo-inscribed microvoids," Nanomaterials **14**, 1228 (2024).
274. A. Lerner, T. Blanchet, R. Cotillard, M. Sosa, N. Roussel, G. Bouwmans, and G. Laffont, "High temperature annealing behavior of femtosecond written FBGs in Ge-doped fused silica optical fibers," in *European Workshop on Optical Fibre Sensors (EWOFS 2023)*, M. Wuilpart and C. Caucheteur, eds. (SPIE, 2023), p. 61.
275. G. D. Marshall and M. J. Withford, "Annealing properties of femtosecond laser inscribed point-by-point fiber Bragg gratings," in *Bragg Gratings, Photosensitivity,*

and Poling in Glass Waveguides (OSA, 2007).
276. L. Bressel, D. De Ligny, C. Sonneville, V. Martinez, V. Mizeikis, R. Buividas, and S. Juodkazis, "Femtosecond laser induced density changes in GeO2 and SiO2 glasses: Fictive temperature effect," Opt. Mater. Expres (n.d.).
277. A. Martinez, M. Dubov, and I. Khrushchev, "Bennion, I. Photoinduced Modifications in Fiber Gratings Inscribed Directly by Infrared Femtosecond Irradiation," IEEE Photonics Technol (n.d.).
278. R. L. Fleischer, P. B. Price, and R. M. Walker, "Solid-state track detectors: Applications to nuclear science and geophysics," Annu. Rev. Nucl. Sci. **15**, 1–28 (1965).
279. E. G. Gamaly, S. Juodkazis, K. Nishimura, H. Misawa, B. Luther-Davies, L. Hallo, P. Nicolai, and V. T. Tikhonchuk, "Laser-matter interaction in the bulk of a transparent solid: Confined microexplosion and void formation," Phys. Rev. B Condens. Matter Mater. Phys. **73**, (2006).
280. R. Stoian, K. Mishchik, G. Cheng, C. Mauclair, C. D'Amico, J. P. Colombier, and M. Zamfirescu, "Investigation and control of ultrafast laser-induced isotropic and anisotropic nanoscale-modulated index patterns in bulk fused silica," Opt. Mater. Express **3**, 1755 (2013).
281. E. N. Glezer and E. Mazur, "Ultrafast-laser driven micro-explosions in transparent materials," Appl. Phys. Lett. **71**, 882–884 (1997).
282. S. Juodkazis, H. Misawa, T. Hashimoto, E. G. Gamaly, and B. Luther-Davies, "Laser-induced microexplosion confined in a bulk of silica: Formation of nanovoids," Appl. Phys. Lett. **88**, 201909 (2006).
283. A. Mermillod-Blondin, J. Bonse, A. Rosenfeld, I. V. Hertel, Y. P. Meshcheryakov, N. M. Bulgakova, E. Audouard, and R. Stoian, "Dynamics of femtosecond laser induced voidlike structures in fused silica," Appl. Phys. Lett. **94**, 041911 (2009).
284. J. Lu, Y. Dai, Q. Li, Y. Zhang, C. Wang, F. Pang, T. Wang, and X. Zeng, "Fiber nanogratings induced by femtosecond pulse laser direct writing for in-line polarizer," Nanoscale **11**, 908–914 (2019).
285. M. Beresna, M. Gecevičius, P. G. Kazansky, and T. Gertus, "Radially polarized optical vortex converter created by femtosecond laser nanostructuring of glass," Appl. Phys. Lett. **98**, 201101 (2011).
286. M. Beresna, M. Gecevičius, and P. G. Kazansky, "Ultrafast laser direct writing and nanostructuring in transparent materials," Adv. Opt. Photonics **6**, 293 (2014).
287. A. Rowstron, "Rethinking data storage for the zettabyte cloud era: The journey from metal to glass," in *Advanced Photonics 2018 (BGPP, IPR, NP, NOMA, Sensors, Networks, SPPCom, SOF)* (OSA, 2018).
288. S. Mihailov, D. Grobnic, C. Hnatovsky, R. Walker, P. Lu, D. Coulas, and H. Ding, "Extreme environment sensing using femtosecond laser-inscribed fiber Bragg gratings," Sensors (Basel) **17**, 2909 (2017).
289. Y. Wang, M. Cavillon, J. Ballato, T. Hawkins, T. Elsmann, M. Rothhardt, R. Desmarchelier, G. Laffont, B. Poumellec, and M. Lancry, "3D laser engineering of molten core optical fibers: Toward a new generation of harsh environment sensing devices," Adv. Opt. Mater. **10**, 2200379 (2022).

290. J. Tian, "Femtosecond laser direct writing of circular optical properties in silica glass," Université Paris-Saclay (2020).
291. N. Ocelic, A. Huber, and R. Hillenbrand, "Pseudoheterodyne detection for background-free near-field spectroscopy," Appl. Phys. Lett. **89**, (2006).
292. G. Németh, H. A. Bechtel, and F. Borondics, "Origins and consequences of asymmetric nano-FTIR interferograms," Opt. Express **32**, 15280–15294 (2024).
293. F. Huth, M. Schnell, J. Wittborn, N. Ocelic, and R. Hillenbrand, "Infrared-spectroscopic nanoimaging with a thermal source," Nat. Mater. **10**, 352–356 (2011).